

Effect of Deformation History on Punching Resistance of Reinforced Concrete Slabs

THÈSE N° 6472 (2015)

PRÉSENTÉE LE 5 FÉVRIER 2015

À LA FACULTÉ DE L'ENVIRONNEMENT NATUREL, ARCHITECTURAL ET CONSTRUIT
LABORATOIRE DE CONSTRUCTION EN COMPOSITES
PROGRAMME DOCTORAL EN GÉNIE CIVIL ET ENVIRONNEMENT

ÉCOLE POLYTECHNIQUE FÉDÉRALE DE LAUSANNE

POUR L'OBTENTION DU GRADE DE DOCTEUR ÈS SCIENCES

PAR

Robert KOPPITZ

acceptée sur proposition du jury:

Prof. A. Nussbaumer, président du jury
Prof. T. Keller, directeur de thèse
Prof. E. Brühwiler, rapporteur
Prof. A. Kenel, rapporteur
Prof. V. Sigrist, rapporteur



ÉCOLE POLYTECHNIQUE
FÉDÉRALE DE LAUSANNE

Suisse
2015

To my parents

Preface

Reinforced concrete (RC) flat slabs used for buildings are sensitive to punching shear failure. Recent years have shown that many RC flat slabs, particularly of those built between the 1960s and 1980s, exhibit insufficient punching shear resistance and thus need to be strengthened. Several strengthening systems exist on the market; however, their efficiency is generally limited since they do not allow significant prestressing and thus effective unloading of the punching region of the slab. Furthermore, already at small rotations, slabs may fail before really activating non-prestressed strengthening systems.

In this work, a prestressed carbon fiber-reinforced polymer (CFRP) strap strengthening system was experimentally investigated and further developed. Sixteen full-scale punching shear experiments were performed, from which analytical models were derived to predict the load-rotation behavior and rotation-dependent punching shear resistance of prestressed punching shear-strengthened RC flat slabs. The positive effect of significant prestressing could be clearly demonstrated.

Particular aspects related to the strengthening of RC flat slabs against punching shear failure were further investigated, such as the effect of the prestressing level, the deformation history caused by unloading/reloading cycles (the former may be required to install the strengthening system) or shear on the deformation behavior and thus punching shear resistance.

I would like to acknowledge the support for this research project provided by the Commission for Technology and Innovation CTI (Project-No. 11569.2 PFIW-IW) and industry partner E.J. Aschwanden AG, Lyss, Switzerland. The support of Carbo-Link AG in Fehraltorf, Switzerland (supplier of the CFRP straps), and Sika AG in Zurich, Switzerland (supplier of the CFRP plates and adhesives), is also gratefully acknowledged.

Prof. Dr. Thomas Keller
EPFL-CCLab

Acknowledgments

The present doctoral thesis was developed in close collaboration between the Composite Construction Laboratory (CCLab) at the École Polytechnique Fédérale de Lausanne (EPFL) under the supervision of Prof. Dr. Thomas Keller and the Institute for Civil and Environmental Engineering (IBU) at HSR Rapperswil University of Applied Sciences under the supervision of Prof. Dr. Albin Kenel.

First of all, I would like to express my sincere gratitude to my thesis director, Prof. Keller, for giving me the opportunity to work on this research project, for his support, the constructive discussions, his ability to always ask precisely the right questions, and his valuable technical writing guidance. I also owe my deepest gratitude to my supervisor, Prof. Kenel, for the excellent collaboration during the last four years, the fruitful technical (and other) discussions, his tireless enthusiasm, advice and encouragement, and his inexhaustible supply of knowledge, ideas and food for thought, without ever losing sight of the aims.

I would like to thank the jury members for their time and commitment, and for their valuable suggestions: Prof. Dr. Eugen Brühwiler, Director of the Structural Maintenance and Safety Laboratory (MCS) at EPFL, Prof. Dr. Viktor Sigrist, Head of the Institute of Concrete Structures at Hamburg University of Technology (TUHH), and president of the jury Prof. Dr. Alain Nussbaumer of the Steel Structures Laboratory (ICOM) at EPFL.

I would like to acknowledge the funding of this research project provided by the Swiss Federal Commission for Technology and Innovation (CTI), Grant No. 11569.2 PFIW-IW. Industrial partner FJ. Aschwanden AG, Lyss, is also warmly thanked for their support and generous financing, and furthermore for the permission to use and publish certain experimental data.

A big thank you goes to all my former and current colleagues at IBU for the great time, the enjoyable memories and the friendships formed. Special thanks go to my office mates Kristine Hess and Christine Mosimann for the congenial work environment, for all the – not always work-related – discussions, and in general for the pleasant time I shared with you! Thanks to all my former and current collaborators at CCLab: for the friendly atmosphere you provided, the pleasant discussions, and for always making me feel welcome when I was in Lausanne.

I would also like to address my thanks to the lab technicians at IBU, in particular to Martin Egli and Markus Zemp, for their creativity, unfailing help and technical support during the smaller and larger projects in the laboratory. As representative for the entire lab crew at GIS-GE, EPFL, Sylvain Demierre is much appreciated for the support he provided.

Additionally I would like to thank Dr. Stefan Lips of FJ. Aschwanden AG, Lyss, for the technical discussions, his advice and the explanation of his iterative punching model, Margaret Howett

Acknowledgments

for her thorough English corrections, Dr. Patrick Strähl for the proofreading of the introductory and concluding chapters, and Dr. Vincent Diederich and Florian Emaury for the correction of the French abstract.

Many people unnamed here contributed in one way or another to the achievement of this work. To all of them I would like to express my deepest gratitude. Special thanks go also to Prof. Dr. Peter Marti for being the essential catalyst for getting me starting on a doctorate.

Finally, I would like to thank my family for their unconditional love and support throughout my education.

Abstract

Deformation-dependent punching shear resistance often constitutes the decisive design criterion for reinforced concrete slabs supported by columns. The increasing number of aging structures exhibiting insufficient punching resistance and detailing deficiencies, and undergoing changes of usage has resulted in a growing demand for strengthening against brittle punching failure. Hence, the research presented in this thesis aims at gaining a better understanding of the identified problems occurring especially in existing structures, such as pre-deformation. A further objective is the experimental and theoretical validation of the performance of a new strengthening concept. A detailed analysis is carried out of the structural behavior of centrally supported rotation-symmetric slabs subjected to punching.

In the first part of this research project a literature review is conducted to characterize the available punching models for new slabs and discuss to what extent they are able to consider the problems linked with existing slabs. Benefits and limitations of current strengthening solutions are illustrated, suggesting local prestressing as a promising concept.

In the second part such a concept is analyzed that has been developed to improve the system efficiency and punching resistance by immediately activating the post-installed shear reinforcement composed of carbon fiber-reinforced polymer (CFRP) composites, thus partially unloading the slab. An experimental campaign comprising sixteen slabs verifies that the installation of this strengthening concept leads to a more ductile system behavior and significant increase of punching resistance compared to a non-strengthened slab.

In the third part the load–deformation behavior of slabs is analyzed and a modification of an analytical model applied to a slab sector is developed, considering the influence of shear on flexural behavior. An overestimation of the flexural capacity and consequently of the punching resistance is thus avoided. The agreement of the modified sector model results with experimental results is confirmed for a large number of experiments from literature. The model is also capable of predicting the load–rotation responses and punching resistances of slabs strengthened with prestressed CFRP straps.

The fourth part of the research concerns the effect of pre-deformation, or load history, on the structural behavior of uniaxial members and biaxial slabs. Single unloading and reloading cycles, which reduce tension stiffening and result in additional deformations, leading to decreased concrete punching resistance, are investigated. In slabs prestressed CFRP straps can compensate the additional deformations caused by load history.

Keywords: reinforced concrete, CFRP, flat slabs, punching shear, load–deformation behavior, strengthening, prestressing, bonding, load history

Kurzfassung

Der verformungsabhängige Durchstanzwiderstand ist oftmals das massgebende Bemessungs- oder Überprüfungskriterium für punktförmig gestützte Stahlbetonflachdecken. Die zunehmende Anzahl alter Tragstrukturen mit unzureichendem Durchstanzwiderstand, infolge Nutzungsänderungen oder mangelhafter konstruktiver Durchbildung, führen zu einer wachsenden Nachfrage an Verstärkungslösungen. Mit der vorliegenden Arbeit soll ein Beitrag zum besseren Verständnis von insbesondere bei bestehenden Tragstrukturen auftretenden Fragestellungen, wie beispielsweise Vorverformungen, geleistet werden. Weiter soll das Potential eines neuen Verstärkungskonzepts experimentell und theoretisch bestätigt werden. Dazu wird das Tragverhalten zentrisch gestützter, rotationssymmetrischer Platten detailliert analysiert.

Der erste Teil dieser Arbeit charakterisiert bereits vorhandene Durchstanzmodelle für Neubauten und diskutiert, inwieweit sie bei bestehenden Bauten auftretende Problemstellungen berücksichtigen können. Vor- und Nachteile von vorhandenen Verstärkungslösungen werden aufgezeigt, mit dem Vorschlag einer lokalen Vorspannung als vielversprechendes Konzept.

Der zweite Teil analysiert ein solches Konzept, welches zur Erhöhung der Systemeffizienz und des -widerstands entwickelt wurde, mittels einer unmittelbaren Aktivierung der nachträglich eingebauten Schubbewehrung aus kohlenstofffaserverstärktem Kunststoff (CFK) und somit teilweisen Entlastung der Flachdecke. Eine Versuchskampagne mit sechzehn Versuchen bestätigt, dass der Einbau dieser Verstärkungslösung zu einem duktileren Tragverhalten und zur signifikanten Erhöhung des Durchstanzwiderstands gegenüber der unverstärkten Platte führt.

Im dritten Teil der Arbeit wird das Last-Verformungsverhalten von Flachdecken analysiert. Die daraus abgeleitete Modifikation eines analytischen Modells am Plattensektor berücksichtigt den Einfluss der Querkraft auf das Biegetragverhalten und verhindert somit eine rechnerische Überschätzung der Biegetraglast und des Durchstanzwiderstands. Eine Vielzahl von Versuchen aus der Literatur bestätigt die Übereinstimmung des modifizierten Sektormodells mit experimentellen Resultaten. Das vorgeschlagene Modell dient ebenfalls zur Bestimmung des Durchstanzwiderstands von mittels vorgespannten CFK-Strangschlaufen verstärkten Platten.

Der vierte Teil behandelt den Effekt von Vorverformungen, d.h. einer Belastungsgeschichte, auf das Tragverhalten von einachsigen Zuggliedern und von Platten. Entlastungs- und Wiederbelastungszyklen reduzieren die Zugversteifung und führen zu Zusatzverformungen, was bei Flachdecken den Durchstanzwiderstand des Betons reduziert. Die vorgespannten Strangschlaufen können diese Zusatzverformung aus der Belastungsgeschichte kompensieren.

Stichworte: Stahlbeton, CFK, Flachdecken, Durchstanzen, Last-Verformungsverhalten, Verstärkungen, Vorspannung, Verbund, Belastungsgeschichte

Résumé

La résistance au poinçonnement, dépendante de la déformation, est fréquemment un critère de rupture décisif pour des planchers-dalles en béton armé appuyés sur colonnes. Il existe un nombre croissant de structures âgées avec des résistances au poinçonnement insuffisantes. Liés à des changements d'utilisation ou à des défauts de construction, ces problèmes engendrent une demande grandissante pour le renforcement au poinçonnement des structures existantes. L'objectif des recherches présentées dans cette thèse est une meilleure compréhension des problèmes se développant en particulier dans des structures existantes, comme par exemple avec l'impact d'une déformation initiale. Le travail effectué durant cette thèse a aussi permis la validation expérimentale et théorique d'un nouveau concept de renforcement. Une analyse détaillée a été effectuée sur le comportement des dalles soumises à un poinçonnement symétrique.

Dans la première partie, des modèles existants sur les phénomènes de poinçonnement pour les nouvelles dalles sont caractérisés. Une discussion au sujet de leur utilité dans le cas des problèmes liés aux dalles existantes est présentée. Les avantages et désavantages des solutions existantes de renforcements sont évaluées, suggérant la précontrainte locale comme un concept prometteur.

Ce concept, qui est analysé dans la seconde partie, a été développé pour augmenter la performance et la résistance systémique en renforçant simplement la dalle existante par une armature d'effort tranchant basée sur un système en polymères renforcé de fibres de carbone (PRFC). Ce système, installé sur des dalles existantes, permet par conséquent de décharger en partie la dalle. L'investigation expérimentale de seize échantillons de planchers-dalles montre que l'installation de ce concept de renforcement crée un comportement plus ductile et une augmentation significative de la résistance au poinçonnement en comparaison avec une dalle non-renforcée.

Dans la troisième partie, le lien charge-déformation des dalles est analysé. Une modification du modèle analytique par secteur de dalle a été développé en considérant l'influence d'efforts tranchants sur le comportement à la flexion. Cela permet ainsi d'éviter la surestimation de la charge maximale en flexion et de la résistance au poinçonnement. La conformité de ce modèle aux résultats expérimentaux est validée par de nombreux essais dans la littérature. Ce modèle permet aussi de prédire la courbe charge-rotation et la résistance au poinçonnement des dalles renforcées avec des boucles en PRFC précontraintes.

La quatrième partie considère l'effet de la déformation initiale, ou de l'historique des sollicitations, sur le comportement des structures axiales et des dalles planaires. Des cycles de

décharge-recharge sont examinés, réduisant le tension stiffening et entraînant des déformations supplémentaires. Ceci mène à une réduction de la résistance du béton au poinçonnement. Dans le cas des plancher-dalles, les boucles en PRFC précontraintes peuvent cependant compenser ces déformations supplémentaires.

Mots-clés : béton armé, PRFC, planchers-dalles, poinçonnement, comportement à la charge-déformation, renforcements, précontrainte, adhérence, histoire des sollicitations

Table of contents

| | Page |
|--|------------|
| Preface | i |
| Acknowledgements | iii |
| Abstract / Kurzfassung / Résumé | v |
| Table of contents | xi |
| 1 Introduction | 1 |
| 1.1 General background | 1 |
| 1.2 Prestressed carbon shear reinforcement strengthening concept | 6 |
| 1.3 Objectives | 7 |
| 1.4 Methodology | 8 |
| 1.5 Thesis organization | 8 |
| 1.6 List of publications | 12 |
| 2 Overview punching shear models | 13 |
| 2.1 Introduction | 13 |
| 2.2 Strengthening against punching | 14 |
| 2.3 Punching shear models for new flat slabs | 20 |
| 2.4 Discussion | 23 |
| 2.5 Conclusions | 25 |
| 3 Experimental campaign | 27 |
| 3.1 First experimental series | 27 |
| 3.2 Second experimental series | 46 |
| 4 Effect of shear on load–deformation behavior | 67 |
| 4.1 Introduction | 67 |
| 4.2 Existing stiffness reduction approaches | 69 |
| 4.3 Consideration of shear in sector model | 74 |
| 4.4 Slab strengthening using prestressed CFRP straps | 80 |
| 4.5 Conclusions | 88 |
| | xi |

| | | |
|----------|---|----------------|
| 4.6 | Appendix A: Quadrilinear Sector Model | 89 |
| 4.7 | Appendix B: Modified Sector Model | 90 |
| 5 | Effect of load history on punching resistance | 91 |
| 5.1 | Load history of uniaxial tension chord | 91 |
| 5.2 | Load history of flat slabs | 112 |
| 6 | Conclusions and future research | 131 |
| 6.1 | Conclusions | 131 |
| 6.2 | Original contributions | 134 |
| 6.3 | Recommendations for future research | 134 |
| | Bibliography | 137 |
| | Notation | 153 |
| | Appendices | 161 |
| A | Strengthening system references | 163 |
| B | Summary experimental campaign | 165 |
| B.1 | Overview | 165 |
| B.2 | Summary of results | 168 |
| C | Flexural capacity of slabs | 171 |
| D | Reduction factor of flexural stiffness | 175 |
| E | Modified Sector Model: Validation | 177 |
| E.1 | Experiments from literature | 177 |
| E.2 | Experimental campaign | 192 |
| F | Effect of crack spacing on tension stiffening loss | 195 |

1 Introduction

1.1 General background

Buildings are often constructed using reinforced concrete (RC) flat slabs combined with punctual supports such as columns of varying cross section and slenderness. The advantages of this method are easier construction compared to joists, greater flexibility in the disposition of rooms that can be enclosed by easily removable non-structural walls, and therefore a high cost efficiency. The disadvantage, however, is the combination of locally high bending moments and shear forces around the columns (see illustrated internal forces of the slab strip in Figure 1.1), which increases the sensitivity of this zone to sudden brittle punching failure in cases without shear reinforcement, unlike a ductile flexural failure. In a typical punching failure, the exceeding of the shear-bearing concrete tensile strength leads to a collapse around a truncated cone above the column, as shown for example in Figure 1.2. This abrupt failure is followed by a drop in the load-bearing capacity of the slab, which may eventually lead to a progressive collapse of the entire structure. Thus the ultimate limit state has to be ensured by an adequate amount of longitudinal reinforcement providing flexural capacity, and also by sufficient punching resistance to bear the local concentration of shear loads in the vicinity of the column.

The flexural load-bearing capacity of reinforced concrete structures can be calculated using the plasticity theory by assuming rigid–perfectly plastic material properties and is therefore deformation-independent (Gvozdev 1938; Hill 1951, 1952; Drucker et al. 1951, 1952). In contrast the punching shear resistance of flat slabs depends on the slab rotation, ψ , among other parameters like the concrete compressive strength, f_c ; the effective depth, d , (representative for the slab thickness h); the geometrical ratio of the longitudinal reinforcement, ρ , and an increasing brittleness with increasing thickness, a so-called size effect (Talbot 1913; Kinnunen and Nylander 1960; Moe 1961; Bažant and Cao 1987; Muttoni and Schwartz 1991, see summaries by Sherif 1996; Birkle 2004; Häusler 2009). The complexity of this topic is reflected by a large number of punching models that have been established in the last fifty to sixty years. However, these models were primarily developed for new structures.

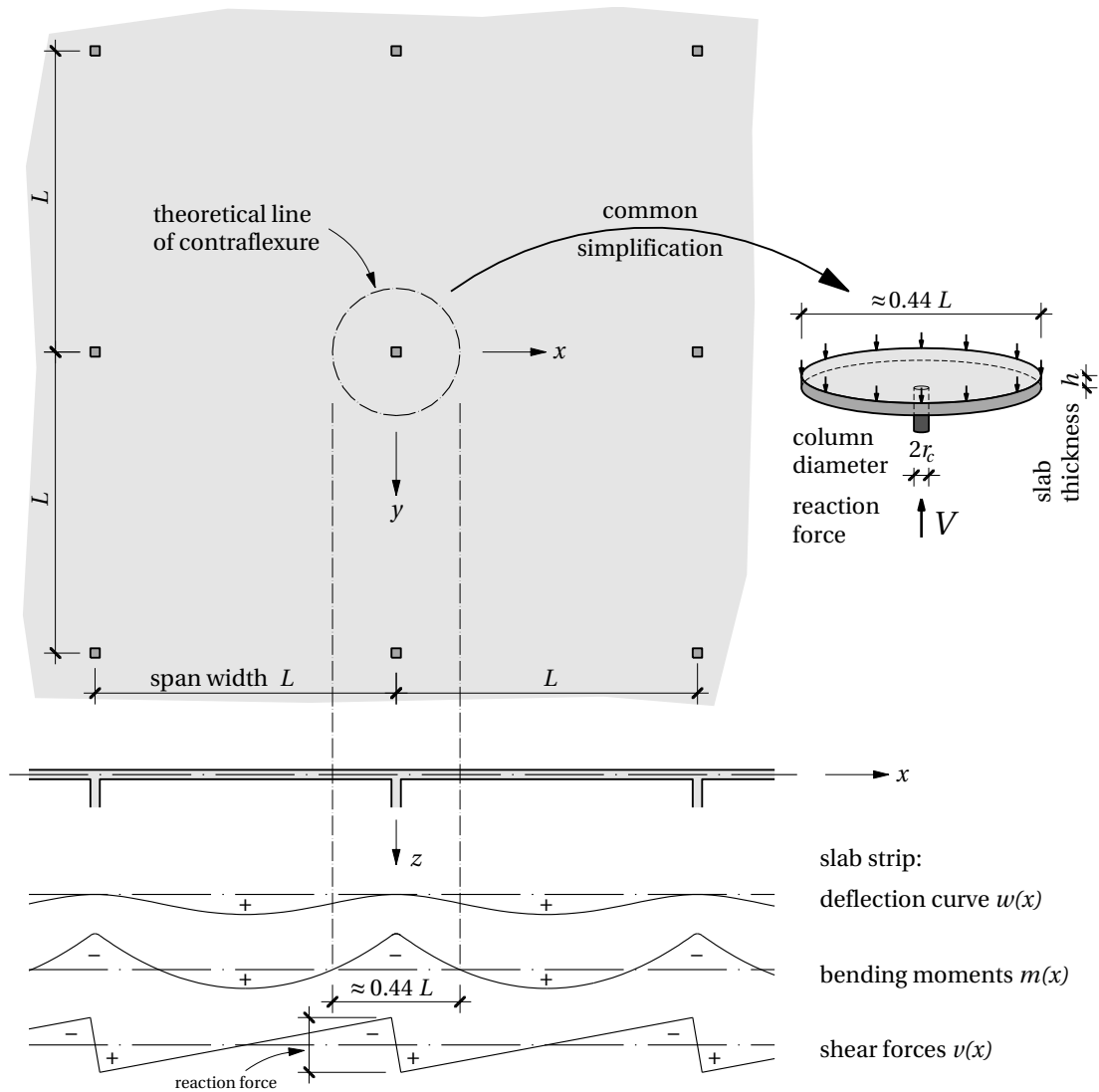


Figure 1.1: Plan view of typical flat slab, section of slab strip with internal forces, and common simplification by punching models considering a circular slab cutout with diameter $0.44L$ (adapted from Beutel 2003)

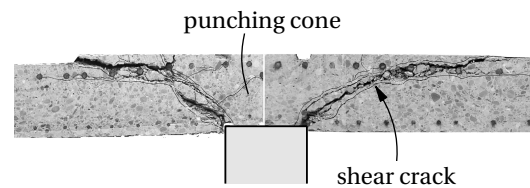
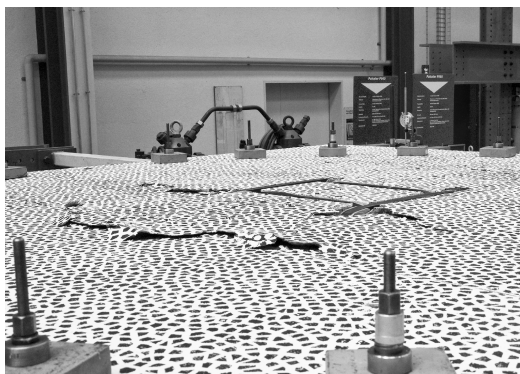


Figure 1.2: Visible punching cone on upper slab surface and in saw-cut (author's images)

An increasing number of existing flat slabs have required strengthening against punching shear failure in the recent past, for instance to compensate for insufficient properties with regard to durability and detailing deficiencies, or to increase the load-bearing capacity owing to changes of usage. Today around one third (BFS 2013) of building costs in Europe are related to the strengthening and upgrading of existing structures. To meet this new demand various post-installed systems exist for strengthening against punching, such as a widening of the slab support [Figure 1.3(a)], increase of bending resistance [Figure 1.3(b)], or a post-installation of additional shear reinforcement [Figure 1.3(c)]. The first two systems maintain the brittle behavior of the slab and still rely on the concrete tensile strength. In the third system, non-prestressed shear reinforcement first has to be activated by additional rotations and is therefore able to bear only additional loads. A low deformation capacity of the slab thus leads to a low utilization level i.e. efficiency of the strengthening system.

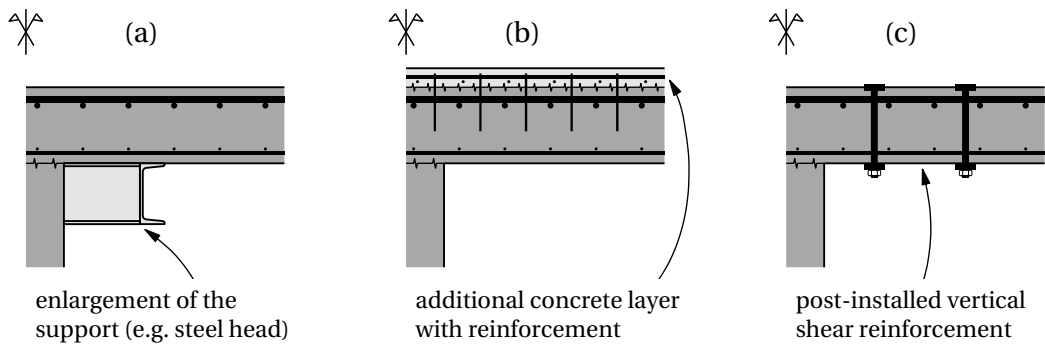


Figure 1.3: Existing flat slab strengthening systems: (a) increase of the support area, (b) increase of bending resistance, and (c) post-installed shear reinforcement

An efficient strengthening system is required that significantly increases punching resistance and enhances slab deformability. The installation of shear reinforcement around the column is a successful concept in new slabs, as shown by Lips (2012) for instance. Thanks to an optimization of the shear reinforcement's activation phase, its efficiency is also expected to be improved for existing slabs, resulting in the development of a strengthening concept (Keller 2010, 2013) which is presented in Section 1.2. This concept involves post-installed and prestressed shear reinforcement composed of carbon fiber-reinforced polymers (CFRP) and serves as a basis for the present thesis. On the one hand the performance of this system has to be verified experimentally, and on the other hand a calculation model is needed to provide reliable predictions of the punching resistance of slabs strengthened using this system.

Existing punching models for new slabs, as for instance models based on the rotation-dependent sector model by Kinnunen and Nylander (1960), serve as a starting point for the development of a new model – or modification of an existing model – for new and existing slabs. However, first an investigation is necessary to identify problems that may occur particularly in existing slabs, e.g. relating to reduced durability or caused by detailing deficiencies. Subsequently it has to be determined to what extent punching models, originally developed for new slabs, are capable of taking these problems into account.

During the investigation of slabs with high amounts of shear reinforcement Lips (2012) observed large shear deformations in the column vicinity. He concluded that the consideration of shear influencing the flexural behavior was necessary to avoid overestimating the flexural capacity, and consequently the punching resistance. Although this supports earlier findings by Pralong (1982) and Brändli (1985), slabs without shear reinforcement and only minimum longitudinal reinforcement did not exhibit any reduction of flexural capacity (Guandalini 2005). A detailed analysis of load–deformation behavior is therefore necessary for quantification of the shear effect on the punching resistance of new and existing slabs.

In addition to compliance with the ultimate limit state, an adequate slab design has to ensure the serviceability of a structure by defining admissible deformations, or crack width limitations for instance. Investigations of cracked structures have shown (Rehm and Martin 1968; Rostásy et al. 1976; Shima et al. 1987; Sigrist 1995; Alvarez 1998; Fürst 2001; Kenel 2002) that the contribution of concrete in tension – although its tensile strength, f_{ct} , is relatively low compared to its compressive strength, f_c , and exhibits considerable scatter – needs to be taken into account to achieve a good agreement between theoretical load–deformation behaviors and experimental observations. After cracking the contribution of the surrounding concrete between the cracks can be considered via bond stresses along the steel rebar surface, the so-called tension stiffening effect, as for instance discussed in the Tension Chord Model (TCM) by Marti et al. (1998). The behavior of concrete in the crack itself can also be taken into account : the concrete tensile stresses do not abruptly drop to zero after reaching their tensile strength, but still provide a fractional amount up to a critical crack width at which their contribution is exhausted. This was considered for example in the Fictitious Crack Model (FCM) by Hillerborg et al. (1976) and Hillerborg (1983), where a certain hindrance of crack growth by interlocking fibers growing out from the cement grains was analyzed, see Figure 1.4.

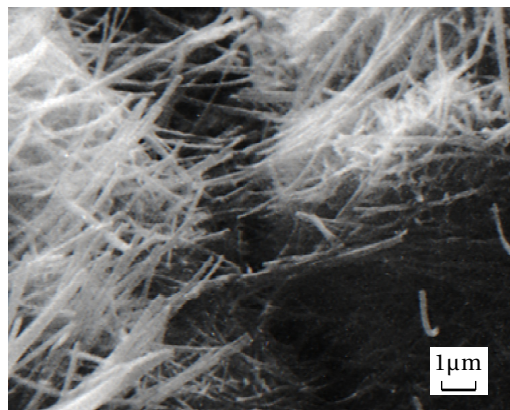


Figure 1.4: Scanning electron micrograph of hardened cement paste with interlocking cement fibers inside a crack (adapted from Higgins and Bailey 1976)

An adequate prediction of the load–deformation behavior of slabs is, however, not only important in the serviceability limit state, but also for the determination of punching resistance. Experiments on reinforcing bars embedded into concrete (Rehm 1961; Leonhardt 1978) and

on beams (Pfyl and Marti 2001; Kenel and Marti 2002) demonstrated higher deformations after the completion of unloading and reloading (URL) cycles. Thus, additional deformations caused by the load history may also be of importance for flat slabs, when a decrease of punching resistance with increasing rotation is assumed according to Muttoni (2003, 2008).

Such URL paths occur for instance when a slab has to be strengthened, see Figure 1.5. This figure illustrates a URL cycle of a (a) non-strengthened and (b) strengthened slab. Here, an increase of the support area is considered, which increases the flexural capacity, V_{flex} , and control perimeter, u_0 . The non-strengthened flat slab [Figure 1.5(a)] is loaded up to a service load, V_{ser} (point A). Before the strengthening system is installed, the slab is unloaded to improve the strengthening system efficiency. Even when the slab is completely unloaded, a residual slab rotation ψ_{res} remains (Marti et al. 1977; Pralong et al. 1979). If the slab remains non-strengthened and is reloaded back to V_{ser} – as observed for beams – the load path will pass point B instead of A, adding an irreversible rotation, $\Delta\psi_{URL}$, and resulting in a decrease of punching shear resistance from V_{R0} to $V_{R0,B}$. If on the other hand the slab is strengthened and then reloaded [Figure 1.5(b)], the punching shear resistance can be increased. However, it may also be affected by ψ_{res} : the intersection of the solid load path with the failure criterion at $V_{R1,B}$ is higher than V_{R0} , but lower than V_{R1} , which would be reached by a strengthened slab monotonically loaded from origin O (dashed curve).

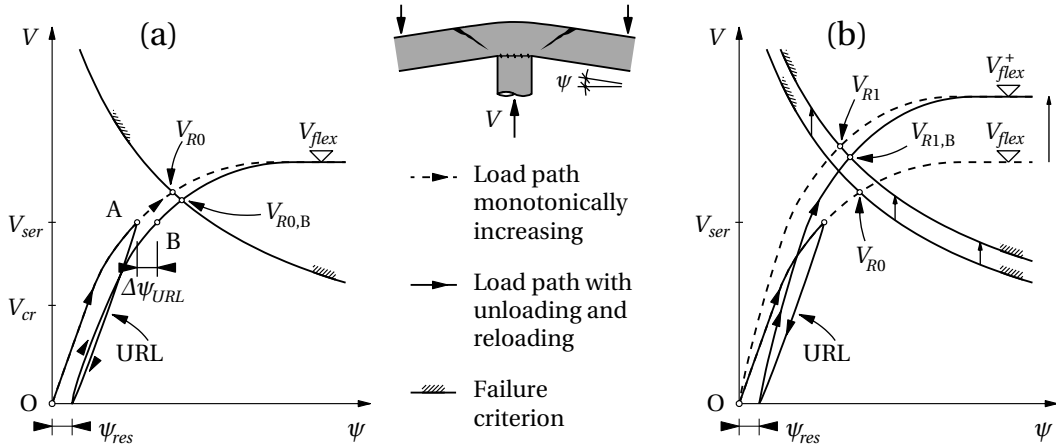


Figure 1.5: Effect of URL cycle on shear force–rotation (V – ψ) relationship: (a) non-strengthened, (b) strengthened by enlargement of support area

On the basis of the TCM the behavior of uniaxial members during unloading and reloading has only been analyzed for the limit cases of no bond damage (Alvarez 1998; Fürst 2001) and complete damage (Burns 2012) during unloading. A more detailed investigation of the degradation of bond attributed to the load history of elastic and also elasto-plastic tension members is required for the TCM to become applicable for URL cycles. An extension to flat slabs is necessary to allow the analysis of the effect of load history and pre-deformation on their load–rotation behavior and punching resistance.

1.2 Prestressed carbon shear reinforcement strengthening concept

The limited efficiency of existing strengthening systems against punching shear has resulted in the development of a system reflecting technological advances. This system presents a novel application for carbon fiber-reinforced polymer (CFRP) composites in structural engineering in the form of post-installed and prestressed shear reinforcements, see Figure 1.6. Prestressing significantly improves system efficiency due to a partial unloading of the slab. No additional live loads are necessary to activate the strengthening system. CFRP offers certain advantages compared to steel: reduced specific weight, high tensile strength to stiffness ratio, insensitivity to a corrosive environment and fatigue (Keller 2003b).

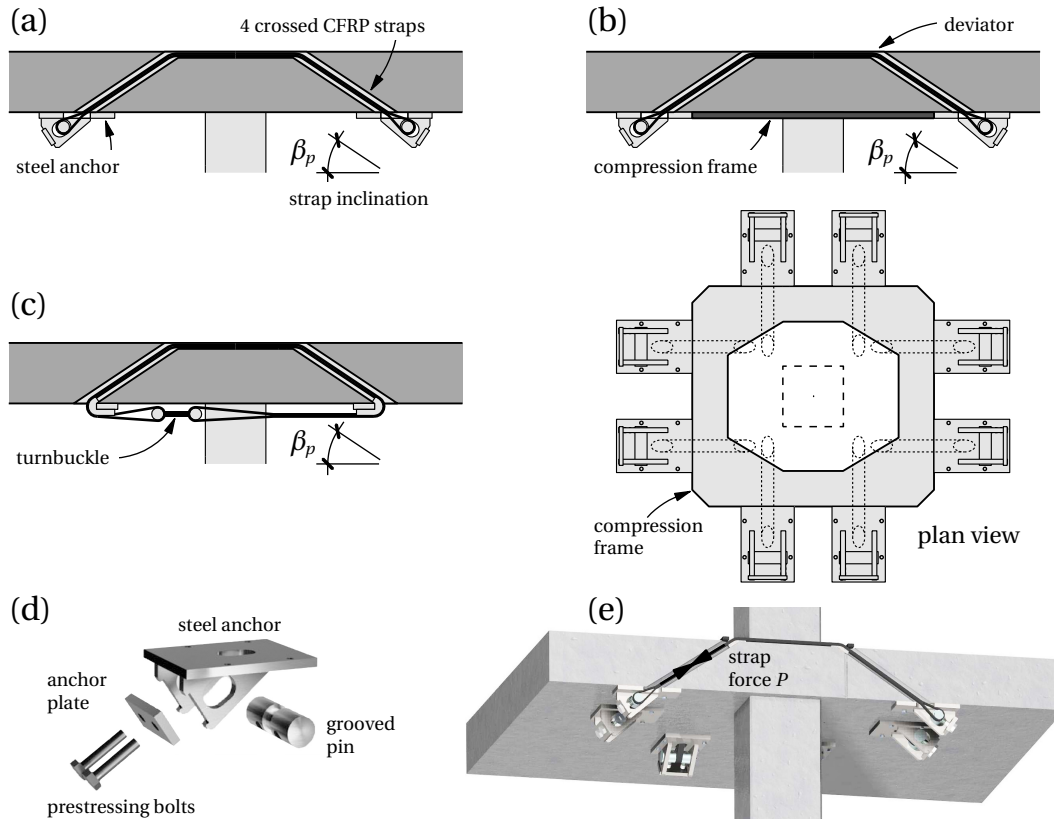


Figure 1.6: Strengthening concept: (a): open strap configuration with adhesively-bonded anchors, (b) with steel compression frame, (c) closed strap configuration, (d) anchor detail, (e) bottom view with adhesively-bonded anchors

The strengthening concept consists of non-laminated and prestressed CFRP straps (Meier and Winistörfer 1998; Winistörfer 1999; Lees and Winistörfer 2011) which are installed crosswise around the column in pre-drilled and pre-cut openings and can be anchored and prestressed from the lower side of the slab. Strap anchoring can be assured by three different systems: in an open strap configuration by steel anchors adhesively bonded to the concrete surface using an epoxy resin [Figure 1.6(a), Keller (2010)], or by fixing the anchors to a steel compression

frame mounted underneath the slab around the column [Figure 1.6(b)], and in a closed strap configuration by self-anchoring the straps using a turnbuckle [Figure 1.6(c), Keller (2013)]. The use of lightweight and flexible CFRP straps constitutes a considerable improvement for on-site installation, especially when only limited space is available. Minimum deviation radii are significantly lower than for heavy steel strands.

The designated prestressing force, P_0 , is either applied at the end-anchor or at the turnbuckle. Figure 1.6(d) illustrates the necessary components for the first case: the CFRP strap end is fitted into a grooved steel pin. The pin itself is placed into the slotted holes of the anchor flanges and connected to two steel bolts via threaded holes. By tightening the bolts using a torque wrench or a hydraulic jack, the pin is pulled back and the forced elongation prestresses the strap up to P_0 .

Each anchor transmits the compressive and shear components of the prestressing force to the concrete slab; the depth of the compression zone is increased in the case of the adhesively-bonded anchors. Due to the inclination angle, β_p , of about 35° to the horizontal, the strap forces act approximately perpendicularly to potential shear cracks. This is more efficient than a vertical arrangement where only a component of the bolt force acts against the opening of a shear crack. The CFRP straps [illustration in Figure 1.6(e)] are much longer than the short steel bolts of the vertical shear reinforcement [Figure 1.3(c)] and thus less sensitive to long-term losses of prestressing forces P .

1.3 Objectives

The aim of this research project is to gain a better understanding of the structural performance of flat slabs subjected to punching shear, with an emphasis on the problems occurring in existing structures. This comprises the following objectives:

- Identify specific problems that may occur in existing slabs, and discuss whether they can be simulated by available models
- Investigate the efficiency of available strengthening systems and of the above-presented prestressed system
- Analyze the effect of shear on the structural behavior and punching resistance of slabs, develop and validate a model to predict the increase of punching resistance resulting from this prestressed system
- Analyze the effect of load history on the structural behavior of uniaxial members and extend the results to slabs

This research project focuses on the investigation of the punching of flat slabs supported by interior columns. Therefore, based on the sector model by Kinnunen and Nylander (1960), a

rotation-symmetric slab layout according to Figure 1.1 is assumed for the calculation, obviating the need for finite element calculations. In the analysis of load history, time-dependent effects like the shrinkage or creep of concrete are excluded. Summaries of code provisions can be found elsewhere (*fib* 2001; Lips 2012).

1.4 Methodology

The objectives are achieved in the following way:

A literature review is conducted to characterize the analytical models available to predict the punching shear resistance of new slabs, and on which main parameters they depend. Problems that may occur in existing slabs, like detailing deficiencies or pre-deformation, are investigated. The frequent absence of their consideration in existing models is discussed. The performance and limits of available strengthening systems are investigated and compared to the prestressed concept presented in Section 1.2.

The successful applicability of this strengthening concept is proved with an experimental campaign in which the following parameters are investigated: CFRP strap size and prestressing level, benefits and deficiencies of the different strap anchoring systems, influence of slab thickness, concrete grade and pre-deformation before the slab is strengthened.

The sector model by Kinnunen and Nylander (1960) enables the load–deformation behavior of rotation-symmetric slabs to be calculated. The transformation of other slab, column, loading geometries and support conditions into a rotation-symmetric layout is analyzed. An investigation regarding shear, which affects the bending resistance in the column vicinity, is carried out. This serves as basis for the development of a simplified analytical model to improve the prediction of the load–rotation curves of slabs. The increased resistance of flat slabs strengthened by prestressed CFRP straps is implemented into the developed model for validation with the experimental results.

The load history resulting from a single unloading and reloading (URL) cycle of an existing slab is investigated. First a uniaxial tension chord is examined, considering a concrete contribution in tension on the basis of the TCM. The outcome is implemented in the developed analytical model for flat slabs. The effect of a URL cycle on the load–rotation behavior and punching resistance is analyzed using experimental curves and an analytical parametric study.

1.5 Thesis organization

This thesis comprises technical and research papers that have either been published or are currently under review. The structure is based on the layout in Figure 1.7, associated with the list of publications in Section 1.6 below.

Based on the question as to whether the punching models suggested for new slabs are able to consider problems occurring in existing slabs like detailing deficiencies and load history,

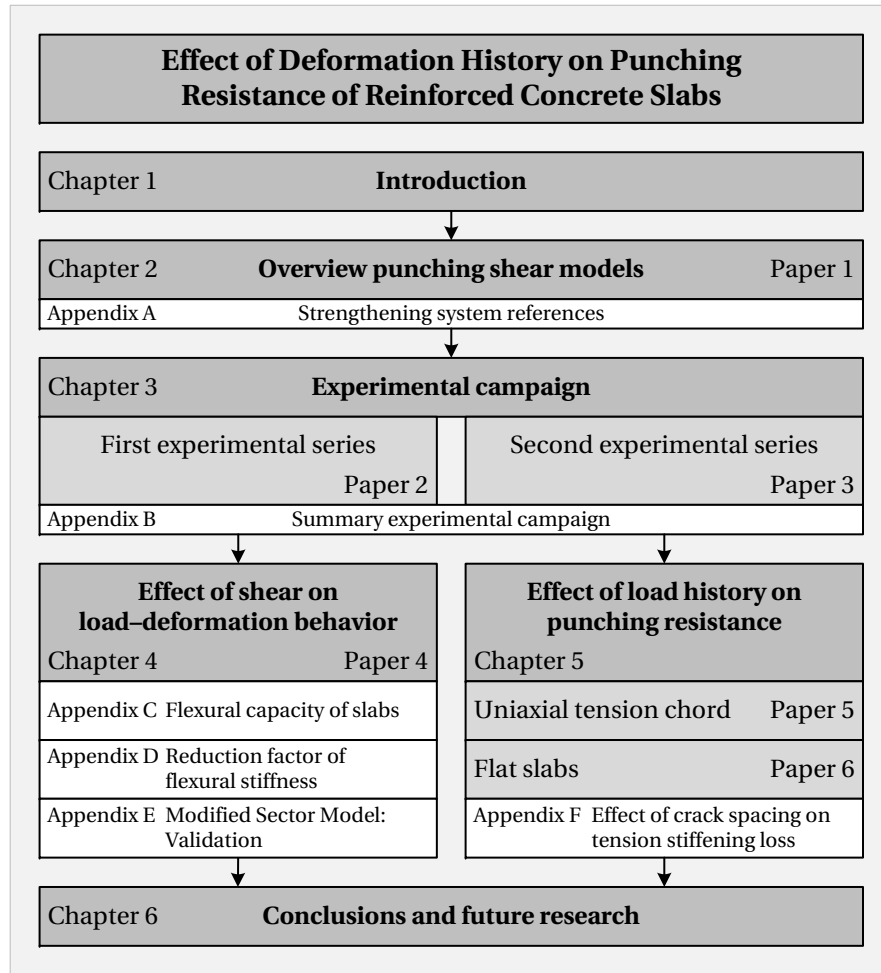


Figure 1.7: Thesis organization

Chapter 2 gives a short review of the research conducted on punching and presents a three-level classification of the wide range of calculation approaches. In addition to the discussion about the applicability of existing models for new slabs to specific aspects linked to existing slabs, the benefits and limitations of current strengthening solutions are evaluated, suggesting local prestressing as a promising concept. The performance of the latter has to be verified experimentally, which is done in Chapter 3. **Appendix A** tabulates the current strengthening solutions and classifies them in four categories.

Chapter 3 and **Appendix B** summarize the experimental campaign carried out within this research project. Sixteen full-scale concrete slabs of the same dimensions and longitudinal reinforcement ratios were tested. Figure 1.8 provides a graphical overview of the campaign. In Section 3.1 CFRP elements were installed to 1) reinforce new RC slabs with non-prestressed flexible plates as shear reinforcement (slabs P1–2), or 2) strengthen existing slabs against punching shear failure using non-laminated and prestressed straps. The straps were either anchored underneath the slab by adhesively-bonded steel anchors (So1–4), or self-anchored in a closed configuration using a turnbuckle (Sc1–2).

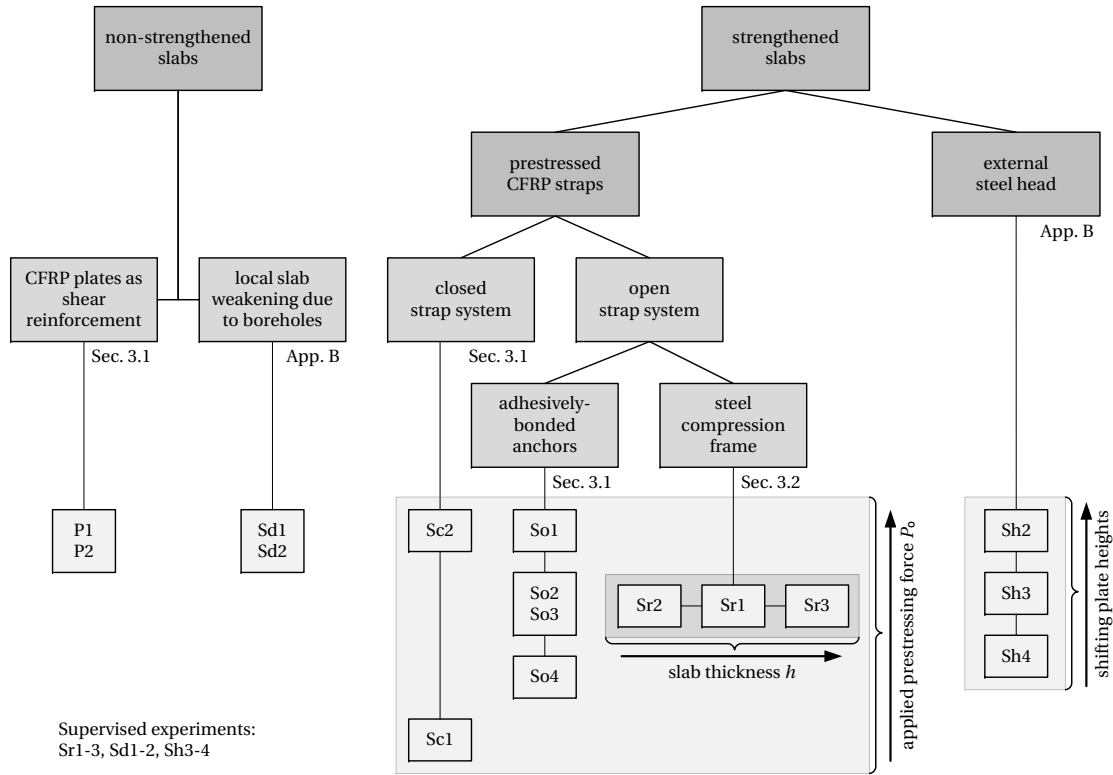


Figure 1.8: Overview of experimental campaign with varied parameters

Section 3.2 examines a second series of slabs with different thicknesses (Sr1–3) where an alternative strap anchoring system – a steel compression frame – was investigated. All three investigated strap anchoring systems resulted in similar punching resistances, which were significantly higher than in the non-strengthened case. Section B.1 briefly describes the additional experiments carried out. The main parameters of all sixteen specimens are summarized in Table B.1. In addition to the selected results presented in Chapter 3, Section B.2 recapitulates the punching resistances, load–rotation curves, and strap force activation of all experiments at a glance. These curves are necessary for the analysis in Chapter 4.

The load–rotation behavior of flat slabs is investigated in **Chapter 4** on the basis of the sector model by Kinnunen and Nylander (1960). A modification of that model – the Modified Sector Model (MSM) – is developed here which is capable of considering a shear influence on the flexural behavior of the slab. A strength reduction factor for the shear crack-crossing longitudinal reinforcement is introduced, which depends on the mechanical longitudinal reinforcement ratio, to take into account the fact that the longitudinal bending reinforcement also has to transmit forces resulting from shear. The developed model is validated by a series of flat slabs from literature and can also be applied to predict the load–rotation responses and punching shear resistances of flat slabs strengthened with prestressed CFRP straps.

The sector model requires a rotation-symmetric slab, column and loading geometry and assumes a yield-line mechanism (YLM) of a truncated cone when reaching flexural capacity.

Appendix C explains how other geometries can be transformed into an equivalent circular slab, and summarizes the common double-symmetric YLMs for square and circular columns. An orthogonal layout of the longitudinal reinforcement can be considered by flexural stiffness reduction factors that are analytically investigated in Chapter 4. In general, compression reinforcement is neglected in the analysis. The effect of an orthotropic compression reinforcement on the stiffness reduction is however shown in **Appendix D**. In **Appendix E** the developed analytical MSM is compared to seventy-two experimental slab responses from literature, and also validated by the experimental results conducted in Chapter 3.

Chapter 5 focuses on the effect of single unloading and reloading (URL) cycles on the bond properties and load–deformation behavior of RC members. Different topics such as high-cycle fatigue or reversed loading have been presented and summarized elsewhere (Kobarg 1986; Mainz 1993; Alvarez 1998; *fib* 2000). In Section 5.1 a uniaxial case is analyzed on basis of the TCM. Bond degradation caused by a URL cycle results in a reduction of tension stiffening. By irreversibly reducing the admissible bond shear stress in the bond stress–slip relationship, this effect can be considered here. The residual tension stiffening depends particularly on the stress level before and after unloading, and its dependence on different crack spacings is shown in **Appendix F**. In Section 5.2 the results obtained are extended to rotation-symmetric slabs. As well as the tensile contribution of concrete between the cracks (TCM), a contribution in the fracture process zone (FCM) is also taken into account by the use of a newly developed quintilinear instead of quadrilinear moment–curvature relationship. Finally, residual slab rotations after unloading and irreversible rotation increases after reloading of slabs are investigated. A parametric study is carried out to quantify punching resistance decreases caused by load history.

Chapter 6 summarizes the results obtained within this research project and is followed by recommendations for future research.

The references and notation are summarized at the end of this document.

1.6 List of publications

- **Paper 1:** Koppitz, R., Kenel, A., and Keller, T. (2013). Punching shear of RC flat slabs – Review of analytical models for new and strengthening of existing slabs. *Engineering Structures*, 52:123–130.
- **Paper 2:** Keller, T., Kenel, A., and Koppitz, R. (2013). Carbon Fiber-Reinforced Polymer Punching Reinforcement and Strengthening of Concrete Flat Slabs. *ACI Structural Journal*, 110(6):919–927.
- **Paper 3:** Koppitz, R., Kenel, A., and Keller, T. (2014). Punching shear strengthening of flat slabs using prestressed carbon fiber-reinforced polymer straps. *Engineering Structures*, 76:283–294.
- **Paper 4:** Koppitz, R., Kenel, A., and Keller, T. (2014). Effect of punching shear on load–deformation behavior of flat slabs. *Engineering Structures*, 80:444–457.
- **Paper 5:** Koppitz, R., Kenel, A., and Keller, T. (2014). Tension Chord Model Modification for Uniaxial Unloading and Reloading in Elastic and Plastic States. *ASCE Journal of Structural Engineering*, 140(10):04014077.
- **Paper 6:** Koppitz, R., Kenel, A., and Keller, T. Effect of load history on punching shear resistance of flat slabs. *Engineering Structures*, submitted in October 2014, revised in January 2015.

2 Overview punching shear models

Reference detail

Robert Koppitz, Albin Kenel and Thomas Keller. “Punching shear of RC flat slabs — Review of analytical models for new and strengthening of existing slabs”. *Engineering Structures*, 2013, Vol. 52, pp. 123–130. DOI: 10.1016/j.engstruct.2013.02.014

Abstract

The conversion of existing buildings, development of standards, material deterioration and detailing deficiencies have led to a need for strengthening an increasing number of concrete flat slabs against brittle punching shear failure. However, existing analytical and design models do not yet take into account the specific aspects of strengthening slabs against punching shear. More than 40 models exist for predicting the punching shear resistance of new slabs. A three-level classification is proposed to provide a consistent overview of the wide range of approaches adopted for resistance calculation. Based on this classification, models are evaluated with regard to their applicability for problems specific to the strengthening of existing slabs, such as pre-deformation of existing slabs, insufficient anchorage lengths of tensile reinforcement outside the punching zone, new openings in slabs within the punching zone, and the prestressing of post-installed shear reinforcement. The efficiency of current strengthening solutions is evaluated, suggesting local prestressing as a promising method.

2.1 Introduction

The structural concepts of buildings often comprise concrete flat slabs locally supported by columns. One advantage of this concept is easier construction compared to joist constructions. Additionally, it generates greater flexibility in the disposition of rooms that are simply enclosed by easily removable non-structural walls. The disadvantage, however, is the combination of locally high negative bending moments and shear forces around the columns, which increases

the sensitivity of this zone to brittle punching failure. In this failure mode, the slab collapses around a truncated cone above the column and this abrupt failure is followed by a drop in the load-bearing capacity of the slab which may eventually lead to a progressive collapse of the entire structure.

In the recent past, tragic examples of this hazardous failure mode have raised public awareness in this respect (Gardner et al. 2000; Wood 2003; Fernández Ruiz et al. 2010). Not only because of these failures but also generally due to the increasing number of aging structures, the need for the strengthening of existing concrete flat slabs against punching shear is significantly increasing. In Europe, already around one third (BFS 2013) of construction costs involve the strengthening and upgrading of existing structures. This includes the reorganization of buildings after a certain service life and a change in the purpose of the building often leads to higher permitted live loads. Poor detailing and pre-deformation in slabs, as well as durability problems like deterioration or rebar corrosion, are additional reasons for strengthening.

Although various systems to strengthen flat slabs exist (see Section 2.2.3), corresponding analytical and design models have not yet been developed which can take into account effects such as poor detailing or local prestressing as used in some strengthening solutions. The question arises whether the models developed for new slabs are also suitable for strengthening applications. This chapter reviews over 40 models concerning the punching shear of interior, edge and corner columns that have been published in the last decades and evaluates their applicability for the punching shear-strengthening of existing flat slabs. Suggestions are given for adjusting the available formulae accordingly.

2.2 Strengthening against punching

2.2.1 Detailing deficiencies of existing slabs

Based on the knowledge developed in recent years regarding the punching shear problem, numerous existing flat slabs no longer meet detailing requirements for sufficient punching shear resistance. Thin slabs are common and are often built without shear reinforcement around the columns. When shear reinforcement was installed, bent-up bars were often used, as shown in Figure 2.1(a), where the top longitudinal reinforcement in the support area continued as bottom reinforcement at midspan or was anchored at the lower side of the plate. This procedure minimized the amount of steel rebars necessary; at midspan the upper reinforcement was often omitted (discontinuous upper longitudinal reinforcement). One critical point is the location of the inclined part relative to the punching cone: if the latter is not crossed by the rebar [left case in Figure 2.1(a)], the rebar is ineffective as punching reinforcement. Figure 2.1(b) shows another typical problem: to effectively contribute to punching shear resistance, the top reinforcement has to be fully anchored outside the punching cone ($L_{bd,net}$ denotes the required length for full anchorage), which is often not the case. This problem either dates back to when the structure was built (too short rebars) or results from strengthening systems

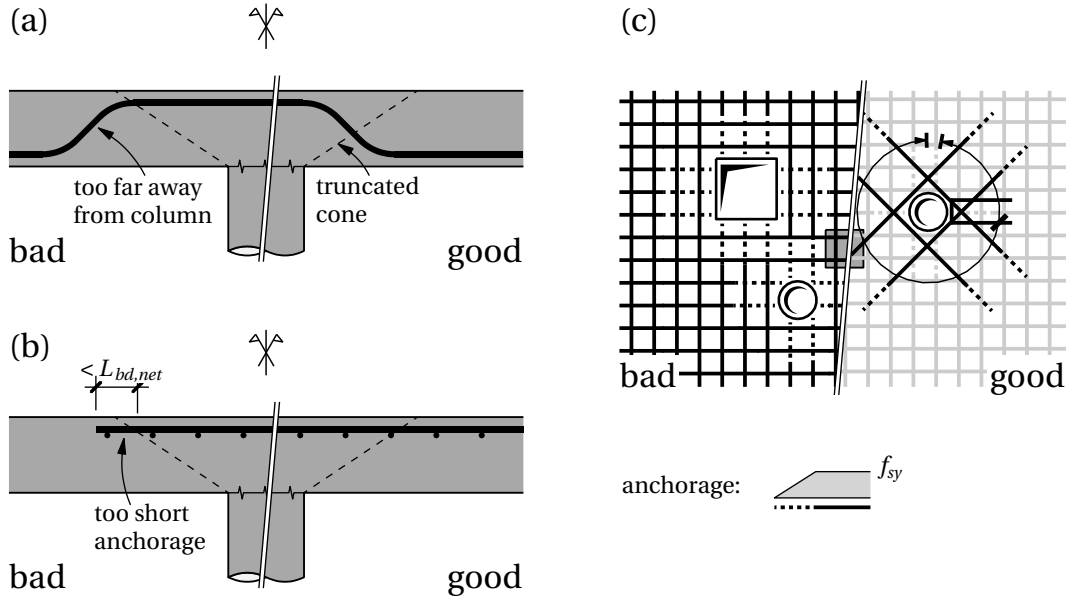


Figure 2.1: Detailing deficiencies: (a) shear reinforcement outside the truncated cone; (b) insufficient anchorage length of top reinforcement; (c) cut rebars for openings

that enlarge the punching cone (e.g. by widening of the column or adding mushrooms), as will be discussed in Section 2.2.3. The Pipers Row Car Park collapse is one example where deterioration of the concrete and rebar corrosion together with insufficient repair work resulted in an insufficient anchorage of the top reinforcement around the two columns where punching shear failure was probably initiated (Wood 2003). Note that sufficient anchorage is also needed for the bent-up bars on the right side of Figure 2.1(a). Large openings next to the column disturb the distribution of forces and therefore have a negative effect on punching resistance, especially when correct detailing around the holes is lacking, i.e. rebars are cut for subsequently drilled holes, as shown in Figure 2.1(c). The dashed lines denote the anchorage length of the rebars and f_{sy} denotes their yield strength.

2.2.2 Pre-deformation in existing slabs

Figure 2.2 illustrates how the shear force V increases with increasing slab rotation ψ (angle between deformed slab and horizontal axis, as shown in Figure 2.2), until (theoretically) reaching the ultimate (flexural) capacity, V_{flex} , of the slab. When a failure criterion according to Muttoni (2008) is assumed, where the punching shear resistance decreases with increasing slab rotation (also shown in Figure 2.2), the intersection between the curves denotes the (real) ultimate (punching) resistance, V_{R0} . The service loads, V_{ser} , of properly designed slabs are normally about 70% of V_{R0} , while the first cracks around the supported area already appear at around one third (Kinnunen and Nylander 1960; Moe 1961; Hassanzadeh 1996; Hassanzadeh and Sundquist 1998) of the ultimate load at V_{cr} (with considerable scatter).

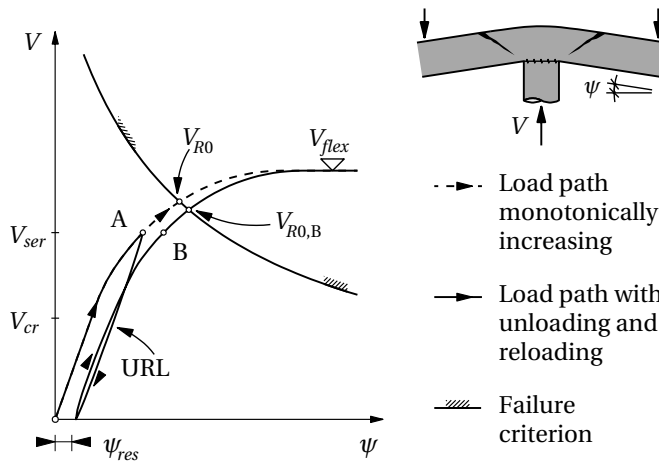


Figure 2.2: Shear force–rotation relationship during loading, unloading and reloading and rotation-dependent failure criterion according to Muttoni (2008)

When a flat slab is to be strengthened, pre-deformation of the slab due to cracking has to be assumed in most cases: during strengthening an unloading and reloading (URL) stress path is followed (see Figure 2.2): starting from point A, at load level V_{ser} , temporary supports such as bracings are normally installed which reduce the slab shear forces to zero. Due to the cracks that can no longer close, a residual rotation, ψ_{res} , of the slab remains. Without strengthening, the reloading path would either pass through point A or B. Case A assumes that the bond between concrete and reinforcing steel is not influenced by the URL path. Otherwise the path has to cross point B adding irreversible rotation and resulting in a decrease of punching shear resistance from V_{R0} to $V_{R0,B}$, see Figure 2.2. When partial plasticizing of the reinforcing steel bars has occurred (which is often the case), additional rotations are caused. The decreased resistance results from pre-deformation and has to be taken into account when designing the strengthening concept. Furthermore, many strengthening systems start by firstly damaging the structure, e.g. by drilling holes for additional shear reinforcement, which may reduce the critical section and cut some rebars.

2.2.3 Evaluation of existing post-installed strengthening systems

Punching shear resistance is calculated for a specific set of boundary conditions, such as reinforcement ratio or column size for example. The strengthening solutions discussed below either modify this set by enlarging the column for instance, or add shear resistance (e.g. via applied shear reinforcement), which is added to the initial resistance (Fernández Ruiz et al. 2010). In this regard, however, the upper limits of the concrete contribution to the shear resistance must be kept in mind, cf. ACI 318 (2011); EN 1992-1-1 (2004).

The available strengthening solutions can be summarized in four concepts according to Figure 2.3(a)–(d) [SIA Dokumentation D0226 (2008); FJ. Aschwanden AG (2014)]: first an en-

largement of the supported area by adding steel or concrete mushrooms or widening the whole column; second, a strengthening of the bending reinforcement by either casting an upper concrete layer or bonding externally reinforcement made of steel or carbon fiber-reinforced polymers (CFRP); third, post-installed shear reinforcement, either bonded or anchored (Fernández Ruiz et al. 2010; Menétrey and Brühwiler 1997); and fourth, prestressed solutions [F.J. Aschwanden AG (2014)].¹

The widening of the supported area primarily leads to an increase of the critical section, which is equivalent to a vertical shift of the failure criterion line, as indicated by the arrows in Figure 2.3(a) on the right. Additionally, the geometrical modification raises the flexural capacity, V_{flex} , of the slab. However, the behavior of the structure becomes much more brittle (i.e. exhibits smaller rotations at equal load stages), as confirmed by a comparison between the load–rotation behavior of Hassanzadeh’s (Hassanzadeh 1996; Hassanzadeh and Sundquist 1998) circular slab NS (non-strengthened) and slab series “k” (column enlargement with reinforced shotcrete) in Figure 2.4. This solution presumes a sufficient anchoring length of the top reinforcement outside of the widened punching cone, as discussed in Section 2.2.1 [see Figure 2.1(b)].

Strengthening of the bending reinforcement increases the effective depth, d , and the flexural capacity, V_{flex} , of the slab, as shown in Figure 2.3(b) on the right for externally-bonded reinforcement. The brittle behavior of the structure is amplified by this solution (reduced slab rotation at new ultimate load V_{R1}). Esfahani et al. (2009) confirmed the stiffer behavior of slabs strengthened with CFRP sheets, especially for low reinforcement ratios of the non-strengthened slabs, see Figure 2.5.

Post-installed shear reinforcement moves the failure criterion line up vertically, as indicated by the arrows in Figure 2.3(c). The shift corresponds to the shear resistance of the new shear reinforcement which is superposed to the concrete resistance. Shear reinforcement generally provides significant ductility increase, as shown by two of Hassanzadeh’s (Hassanzadeh 1996; Hassanzadeh and Sundquist 1998) slabs (Series “s”) with inclined post-installed anchors similar to those in Figure 2.3(c) on the left (curves are also plotted in Figure 2.4). However, non-prestressed shear reinforcement is activated by additional rotations only [see activation phase in Figure 2.3(c)] and is therefore only able to bear additional loads but not efficiently unload the slab. A low rotation capacity of the slab may lead to a low utilization level and therefore low efficiency of this strengthening system as the slab fails before the shear reinforcement is fully activated.

Prestressing solutions are much more efficient in this respect because the activation phase is skipped, as displayed in Figure 2.3(d), on the right. As shown in Figure 2.3(d), on the left, mushrooms may be prestressed or prestressed CFRP straps may be installed [F.J. Aschwanden AG (2014)]. Both systems efficiently unload the slab and also shift the failure criterion and loading lines upwards, thereby significantly increasing the new ultimate load V_{R1} .

¹A brief tabular overview of strengthening systems is given in Appendix A

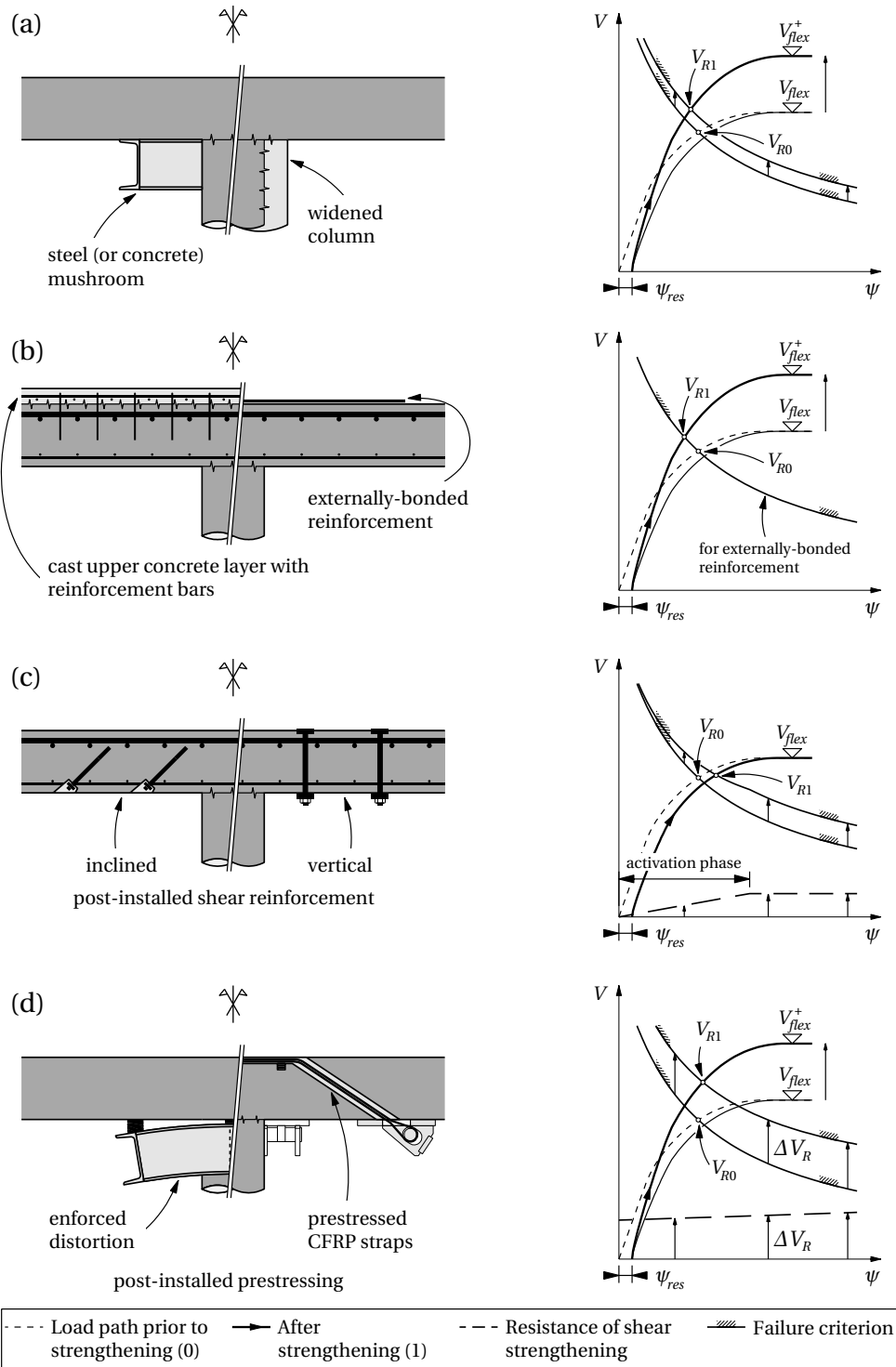


Figure 2.3: Existing post-installed strengthening systems and their effects on punching shear resistance: (a) enlargement of supported area; (b) additional bending resistance; (c) non-prestressed post-installed shear reinforcement; (d) prestressed solutions. Adapted from SIA Dokumentation D0226 (2008); F.J. Aschwanden AG (2014)

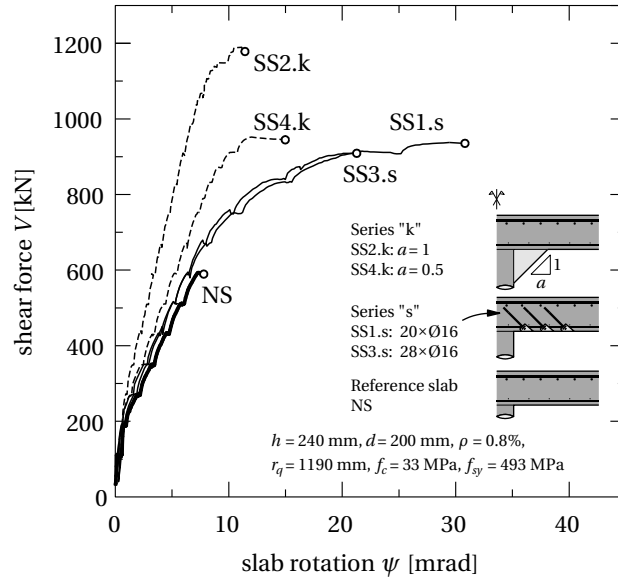


Figure 2.4: Tests by Hassanzadeh (1996) with column head reinforcement (series “k”) and with inclined post-installed shear reinforcement (series “s”) compared to control slab NS, r_q denotes radius from column center to load equipment

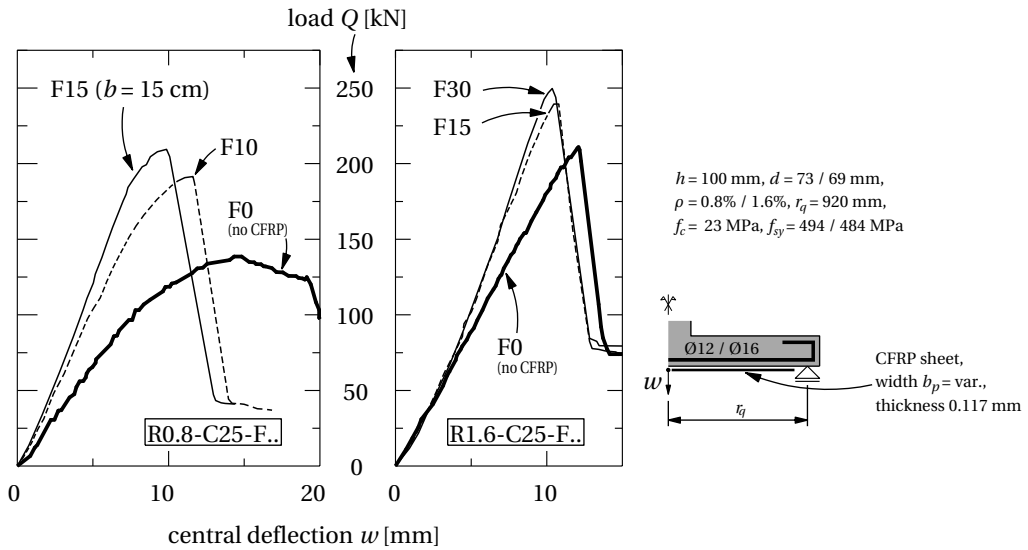


Figure 2.5: Load versus displacement relationship of quadratic test slabs with (F10, F15, F30) and without (F0) externally-bonded CFRP sheets for two different reinforcement ratios ρ ; F-numbers correspond to sheet width b_p in cm. Adapted from Esfahani et al. (2009)

2.3 Punching shear models for new flat slabs

2.3.1 Punching shear resistance parameters

Various parameters affect the punching shear resistance of flat slabs (Sherif 1996; Birkle 2004; Häusler 2009). One of the most important is the concrete compressive strength, f_c , considered either directly or indirectly when using the concrete tensile strength f_{ct} . The geometrical ratio of the longitudinal reinforcement, ρ , is in most cases considered by a similar square or cubic root assumption as for f_c . Higher reinforcement ratios, however, lead to a more brittle structural behavior. Hence ACI 318 (2011) neglects the influence of ρ on the punching resistance (Birkle 2004). A minimum reinforcement has to be provided in any case to ensure sufficiently small crack widths during service. A third major parameter is the effective depth d (used instead of the total slab thickness h): a higher depth not only increases the punching shear resistance but also the flexural capacity of the slab. The increase of the former, however, is limited by a size effect (Bažant and Cao 1987). Furthermore, modern structural codes define so-called critical sections at a predefined distance to the supported area, where the loads that have to be borne by the column are compared with the resistance of the slab. This concept, which was already introduced in 1913 by Talbot, has no physical meaning however.

The punching shear resistance of a slab is, however, not a constant value, but depends on the slab deformation, i.e. more specifically on the slab rotation, ψ , as already demonstrated by Kinnunen and Nylander in 1960. Additional rotations at the same load level decrease the punching shear resistance of the slab. In 2008, Muttoni proposed the Critical Shear Crack Theory (CSCT) for a rotation-symmetric case. He adopted the proportionality between the internal forces and the rotation angle ψ and replaced Kinnunen and Nylander's failure criterion by an empirical criterion validated by a large series of test results under the assumption of a relationship between the punching shear resistance and the width of a critical shear crack, described as proportional to $\psi \cdot d$ (Muttoni and Schwartz 1991). The CSCT was extended to non-symmetrical cases by Tassinari (2011), also using this failure criterion, and further refined by Lips (2012) to be applicable for high shear reinforcement ratios (again for a rotation-symmetric case).

2.3.2 Model classification

A review of existing models for predicting the punching shear resistance of new concrete flat slabs is carried out in the following in order to subsequently identify potential model categories, which either directly allow strengthening-specific aspects to be considered or may be revised to fulfill this purpose.

The first experimental investigation regarding punching shear was undertaken in the United States by Talbot (1913). He conducted load-bearing capacity tests on almost 200 footings of walls and columns of which about twenty failed in punching shear and proposed a simple formula to calculate the critical shear stress around a fictitious circumference. After an analysis

of mainly the flexural behavior of slabs (Graf 1938; Richart and Kluge 1939), extensive research concerning the punching resistance began during the 1950s with significant contributions from Elstner and Hognestad (1956) and Moe (1961) in the U.S. and Kinnunen and Nylander (1960) in Sweden. Since then various proposals have been published and several authors (e.g. Sherif 1996; Regan and Bræstrup 1985; Staller 2001; *fib* 2001) summarized and discussed the previously published models. Beutel (2003) discussed proposals concerning interior columns whereas Vocke (2002) analyzed mainly models concerning edge and corner columns and both proposed corresponding classifications or “model families”. In the following, these classifications will be merged, revised accordingly and updated with more recent models, as shown in Figure 2.6. The model families are unified, structured and categorized thematically. The solid and dashed lines illustrate the various connections between the models. The solid lines describe a general relationship while relationships which are considered by a few proposals only are indicated with dashed lines. Some models, like the one by Moe (1961), can be assigned to more than one category. Publications that just fit model parameters of existing models based on extensive statistical evaluations of real (from literature) or virtual punching tests (using numerical calculations) are not displayed.

All the models are essentially based either on the elasticity or plasticity theory (first level in Figure 2.6). In the former case, failure occurs for instance after the longitudinal reinforcement has reached its yield strength or the concrete tensile strength is exceeded. In the latter case, upper-bound and/or lower-bound solutions are used to predict the ultimate load. When an upper-bound solution is applied, a modified Mohr–Coulomb failure criterion for concrete is usually assumed.

On the second level, three categories are differentiated. Most models are developed using “plate analysis” to formulate equilibrium conditions. Corner and edge columns, in particular, are usually split into bending and torsion beams and summarized in the category “beam analogies”. A third approach is the formulation of spatial “strut-and-tie models” which allow the clear distribution of forces for rotation-symmetric cases. As an example for interior slabs without shear reinforcement, Andrä (1982) proposed a model with concrete compression and tension struts inclined at an angle of 45° which are overlaid with a compression fan at the column edge. An extension of this model to take headed shear studs as vertical shear reinforcement into account is widely used (in new constructions). Alexander and Simmonds (1992) used the “beam analogy” approach for their Bond Model, calculating the punching shear resistance for internal columns based on the bond stress between steel and concrete. The bond strength is reached when the splitting tensile strength of a so-called “V-notch” wedge around a single rebar up to the concrete surface is exceeded (spalling of the concrete cover).

The “plate analysis” category is split into eight sub-categories (third level). One major sub-category concerns “sector models” for internal columns based on Kinnunen and Nylander (1960). Assuming a rotation-symmetric case, rigid slab segments rotate around the edge of the column. The segments are delimited by the (critical) tangential shear crack and radial cracks. By formulating the equilibrium equation and assuming an ultimate tangential compressive

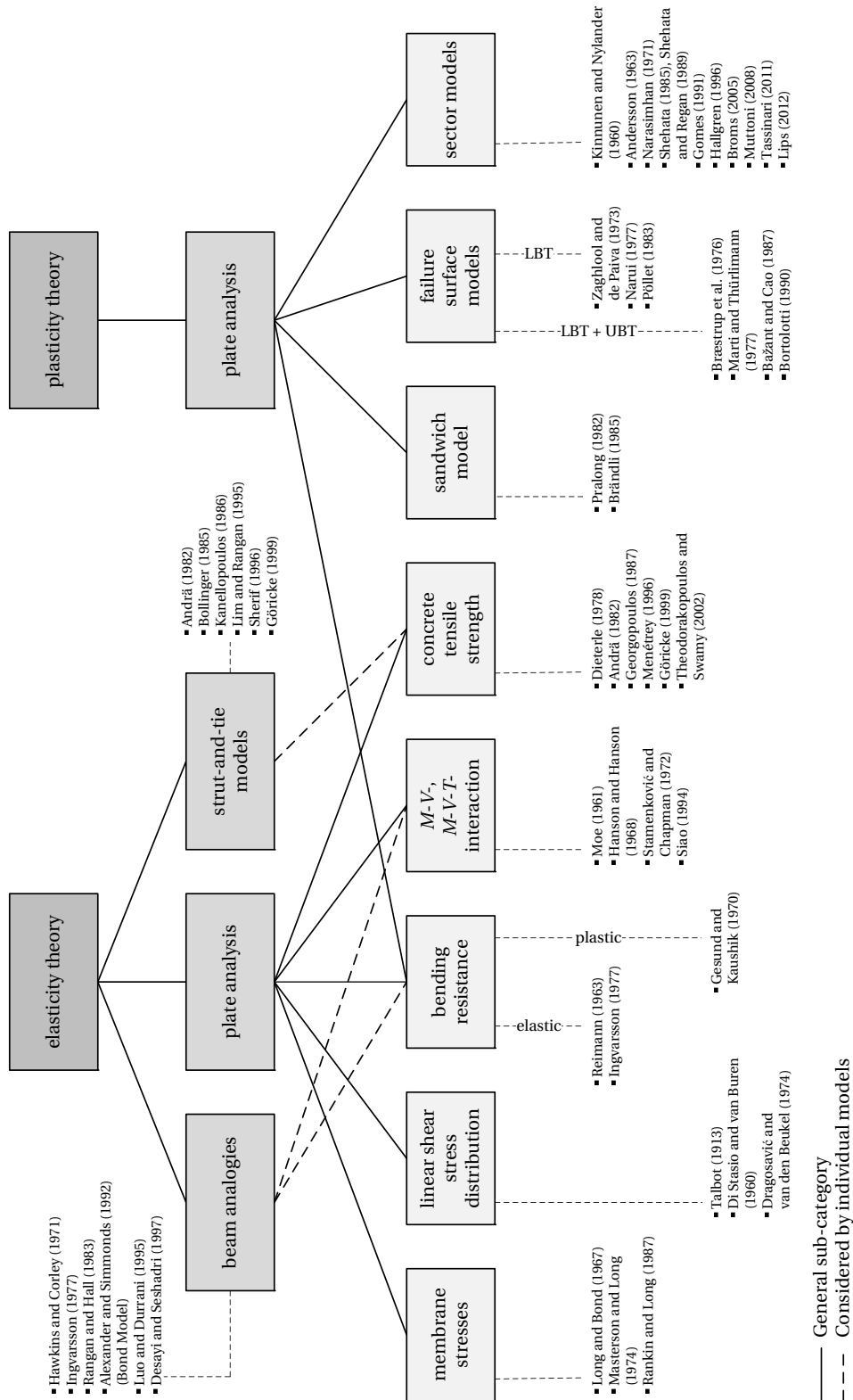


Figure 2.6: Proposed classification of existing punching shear models for new constructions (LBT: lower-bound theorem of plasticity; UBT: upper-bound theorem of plasticity)

strain of the concrete inside the compression ring around the column, an upper-bound solution can be derived iteratively. Bræstrup et al. (1976) proposed a “failure surface model” where they combined a straight line with a catenary curve and calculated an upper-bound solution, assuming a rigid ideal plastic behavior with a modified Mohr–Coulomb failure criterion for a rotation-symmetric case. Other models with alternative failure surfaces could not further optimize the upper and lower bound solutions of the ultimate load. In the sub-category “sandwich model” Pralong (1982) proposed the “rond-point” model which is based on modeling the flat slab like a sandwich: normal forces and the bending moments, replaced by couples, are assigned to the top and bottom covers while the core bears the shear forces. Brändli (1985) extended the model to edge and corner columns.

The remaining models can be attributed to the following sub-categories, some suggesting the “concrete tensile strength” instead of the compressive strength as determining parameter. For corner and edge columns, in particular, “moment–shear” ($M-V$) or “moment–shear–torsion interaction” ($M-V-T$) formulae are a common approach. Similarly, others consider the “bending resistance” of the slab for calculating the punching resistance. Again for edge and corner columns, some models and subsequently ACI 318 (2011) assume a “linear shear stress distribution” around the critical section. “Membrane action” of the slab can increase the ultimate punching resistance significantly. Empirical investigations showed an ultimate load increase of 30 to 50% (Rankin and Long 1987). However, the effective consideration in the models remains unclear, as the additional resistance is taken into account by a simple enlargement factor.

2.4 Discussion

2.4.1 Model evaluation

The following discussion evaluates to what extent the existing models developed for new constructions, according to the classification in Figure 2.6, are able to take into account the specific aspects linked to the strengthening of existing slabs. As discussed above, the effects of pre-deformation, insufficient anchorage length of the top reinforcement, supplementary cut openings and local prestressing on the punching shear resistance are specific to strengthening and it will be evaluated whether and how they can be considered by specific model families or if new models have to be developed.

2.4.2 Effect of pre-deformation

A potential residual rotation, ψ_{res} , can only be adequately taken into account by some of the models of the sub-category “sector models” like Kinnunen and Nylander (1960), Shehata and Regan (1989) or Muttoni (2008), which explicitly include the rotation parameter, ψ . The models dependent on the concrete compressive strength, f_c , (directly or indirectly via the tensile strength) could be modified using a reduction factor, k_c , to obtain an effective value of

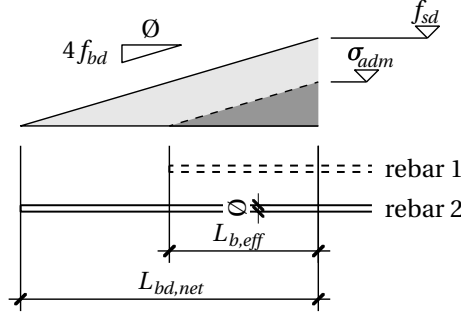


Figure 2.7: Reduction of admissible steel stresses to take into account insufficient anchorage length of top reinforcement

the compressive strength, $f_{c,eff}$, according to Eq. 2.1:

$$f_{c,eff} = k_c f_c \leq f_c \quad (2.1)$$

A reduction factor like this is dependent on the actual state of strains in the slab or on the crack width [cf. the Cracked Membrane Model by Kaufmann (1998) for shear walls]. However, the validation of this factor requires a significant amount of testing.

2.4.3 Effect of anchorage length

An insufficient anchorage length of the top reinforcement cannot directly be taken into account by the existing models. Alexander and Simmonds' (1992) Bond Model with (radial) spalling of the concrete cover around a reinforcement bar is not applicable for bond failure in the axial direction of the rebar. Indirectly, however, the effect can be taken into account in models based on the yield strength of the rebars. The design value, f_{sd} , of the yield strength, f_{sy} , could be reduced to an admissible stress, $\sigma_{adm} \leq f_{sd}$, depending on the effective anchorage length, $L_{b,eff} \leq L_{bd,net}$, according to Figure 2.7 and Eqs. 2.2 and 2.3:

$$L_{bd,net} = \frac{\phi f_{sd}}{4 f_{bd}} \quad (2.2)$$

$$\sigma_{adm} = \frac{L_{b,eff}}{L_{bd,net}} f_{sd} \leq f_{sd} \quad (2.3)$$

where ϕ denotes the rebar diameter, f_{bd} the design value of the bond stress and $L_{bd,net}$ the full anchorage length [see SIA 262 (2013)]. Eq. 2.2 assumes a linear increase of the stress limit per rebar length according to the Tension Chord Model (TCM) proposed by Marti et al. (1998). However, this approach also requires experimental validation.

2.4.4 Effect of openings

Openings near columns are normally taken into account by reducing the critical circumference [e.g. El-Salakawy et al. (1999); Teng et al. (2004)]. The effect of new openings in existing slabs on the punching shear resistance can basically be taken into account accordingly. However, the cutting of the top reinforcement reduces the contribution of this component of the punching shear resistance. The top reinforcement may no longer be sufficiently anchored outside of the punching cone, see Section 2.4.3. Special cases of openings are small boreholes for the post-installation of shear reinforcement.

2.4.5 Effect of prestressing

Local prestressing, as shown in Figure 2.3(d) on the left, has three positive effects:

1. the shear resistance is increased by the vertical component of the prestressing force,
2. the bending resistance of the slab is increased, and
3. crack widths and slab rotations are reduced.

Models of the sub-categories “sandwich model” (Pralong 1982; Brändli 1985), “membrane stresses” (Rankin and Long 1987) and “concrete tensile strength” (Menétrey 1996) allow the consideration of global prestressing forces, which generate a uniform stress state across the whole concrete cross section of the slab around the column. The bending resistance is increased by introducing a fictitious reinforcement ratio, ρ_{eff} , which includes the reinforcement ratio of the reinforcing steel, ρ_s , and the reinforcement ratio of the prestressing steel, ρ_p , weighted by the yield strength of the tendons (for bonded tendons). The vertical components of the prestressing forces are added to the punching shear resistance. The positive effect of the prestressing force on the crack width and slab rotation is disregarded.

Local prestressing, however, generates stress concentrations in the punching cone area, which are not uniformly distributed across the cross section. Fictitious reinforcement ratios for unbonded tendons are not suitable. Normally just the vertical component of the prestressing force is added. The significant advantages of local prestressing, as shown in Figure 2.3(d) on the right, cannot be sufficiently explored by the existing models and therefore the development of a new specific model is required.

2.5 Conclusions

Due to the conversion of existing buildings, development of standards and deficiencies in detailing the strengthening of existing concrete flat slabs against punching shear is becoming increasingly necessary. Critical aspects concerning strengthening against punching shear were identified and the following conclusions were drawn:

- More than 40 punching shear models for new slabs were classified and evaluated regarding their applicability for the strengthening of existing structures.
- Existing slabs may exhibit pre-deformation, expressed as an additional slab rotation. Models based on rotation-dependent punching shear resistance are able to take this effect into account in the design of the strengthening solution by adding this extra rotation.
- The top reinforcement is in many cases not sufficiently anchored outside the punching cone (the latter may have been enlarged by the strengthening procedure). The corresponding reduction of the punching shear resistance cannot be quantified by the existing models. Consequently, to remain on the safe side until adequate knowledge has been generated, the contribution of insufficiently anchored rebars has to be reduced by the ratio of the effective to the full anchorage length for calculating the bending resistance of the slab.
- Supplementary cut openings within the punching zone of existing slabs reduce the critical circumference and cut the top reinforcement. The first effect only can be taken into account with existing models. The partial contribution of the top reinforcement cut within the punching zone to the slab bending resistance cannot yet be reliably quantified and should therefore be neglected for calculation.
- Prestressing is an efficient and reliable way to activate post-installed strengthening components. Due to often limited slab rotation capacity, non-prestressed components may not be stiff enough to effectively increase the punching shear resistance. The performance of local prestressing around the punching cone, however, cannot yet be fully taken into account with existing models as compared to global prestressing. Adequate modeling of the effect of the non-uniform local stress fields needs further research.

3 Experimental campaign

3.1 First experimental series

Reference detail

Thomas Keller, Albin Kenel and Robert Koppitz. “Carbon Fiber-Reinforced Polymer Punching Reinforcement and Strengthening of Concrete Flat Slabs”. *ACI Structural Journal*, 2013, Vol. 110, No. 6, pp. 919–927. DOI: 10.14359/51686148

Abstract

Three different CFRP systems were used to reinforce new or strengthen existing concrete slabs against punching. Untensioned CFRP plates or only very low prestressed CFRP straps could not prevent brittle punching failure. Strap prestressing of at least 15% of the tensile strength led to a ductile two-peak slab response although the CFRP material systems were brittle. The ultimate load of the unreinforced slabs could be increased by 73–114% via a redistribution of forces from the concrete to the strap system. An empirical model was established, which is able to estimate the first peak load of all the applied CFRP systems. It takes into account the parameters CFRP plate or strap resistance, CFRP geometry and prestressing level, and punching load of the unreinforced slab. A cantilever strut-and-tie model was established to estimate the second peak load. Both models provide acceptable accuracy.

3.1.1 Introduction

Flat concrete slabs without shear reinforcement are susceptible to brittle punching failure (Kinnunen and Nylander 1960). Various punching shear reinforcement systems have therefore been developed to increase punching shear resistance and improve ductility (Fernández Ruiz and Muttoni 2009). Shear reinforcement systems consist mainly of studs, stirrups, or shear heads – all made of steel – and codes of practice are available for the designing of these reinforcements [ACI 318 (2011); SIA 262 (2013); EN 1992-1-1 (2004)].

In recent years, however, it has become evident that many flat slabs, particularly those built from the 1960s to the 1980s, have insufficient punching shear reinforcement and therefore require strengthening [SIA Dokumentation D0226 (2008)]. To fulfill this new demand, existing punching shear systems, originally conceived for new constructions, were modified to make them applicable for the strengthening of existing slabs.

Likewise in recent years, new materials have appeared on the construction market: fiber-reinforced polymer (FRP) composites (Keller 2003b). These are lightweight and high-strength and do not corrode as steel does. They are used in new constructions – in most cases hybrid applications (Schaumann et al. 2009) – and for the strengthening of existing structures (Lees et al. 2002; Keller 2003a; Lees and Winistörfer 2011). In the former case, glass fibers are mostly used, whereas in the latter case, due to stiffness requirements, carbon fibers are used (which are much more expensive than glass fibers). Until now, carbon fiber-reinforced polymer (CFRP) composites have been used as adhesively-bonded plates and laminated fabrics, mostly for bending-strengthening of concrete beams and slabs. Less frequent applications involve the shear-strengthening of beams and wrapping of columns to improve strength and ductility.

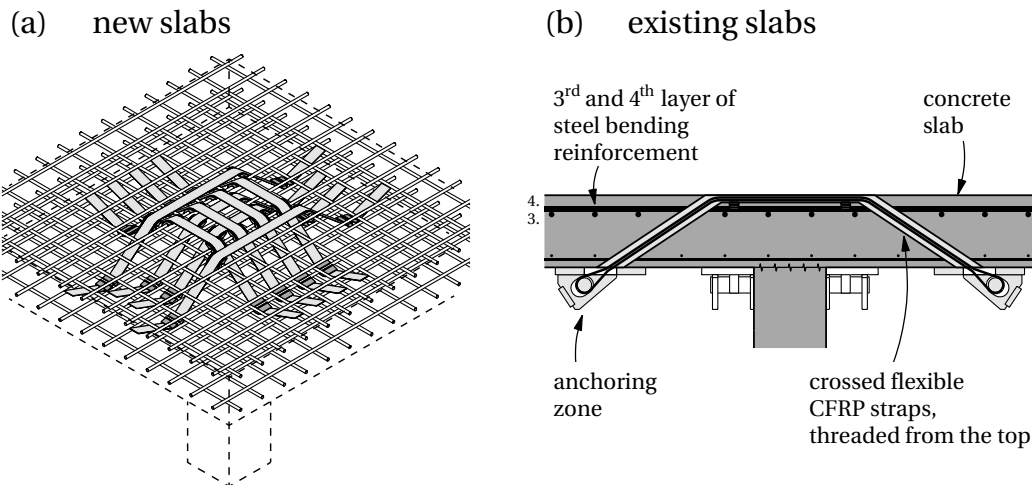


Figure 3.1: Arrangement of CFRP punching shear reinforcement: (a) in new slabs; (b) prestressed in existing slabs

In the following, a new application for CFRP composites is presented: their use as punching shear reinforcement for new concrete flat slabs and as a prestressed strengthening system for existing slabs. Linear and flexible lightweight CFRP plates and straps are used to crosswise shear reinforce or strengthen slabs in column or wall regions. In new constructions, thin, and therefore easily bendable, plates are threaded from the top into the already-completed four layers of steel bar reinforcement, as shown in Figure 3.1(a). The inclined plate segments cross the punching cone and thus suspend the shear load. The load introduction into the cone occurs at the upper deviation points and is therefore clearly defined and at the correct location. The plate ends, which are turned around the bottom steel bars, serve as anchoring zone. The thin plates can easily be inserted crosswise above the column within the concrete cover, just

above the third and fourth steel bar layers. To strengthen existing slabs, the system is slightly modified: in pre-drilled and pre-cut openings, unbonded CFRP straps are installed, which can easily be anchored and prestressed from the lower side; see Figure 3.1(b). Prestressing significantly improves the system efficiency due to the partial unloading of the slab. Described are the setup and results of full-scale punching shear experiments using a CFRP plate system as internal reinforcement and prestressed CFRP straps as a strengthening system.

3.1.2 Research significance

The strengthening of existing concrete flat slabs is becoming increasingly necessary. For this to be really efficient, prestressing of the strengthening system must be possible. The proposed CFRP punching shear reinforcing and strengthening system is an original and material-tailored application of innovative flexible CFRP materials. Compared to existing systems, three aspects, which not yet covered by existing design models, need research:

1. the effect of CFRP material brittleness on system ductility;
2. the effect of local prestressing (around the columns) on punching shear resistance; and
3. the effect of unbonded systems on punching shear resistance.

3.1.3 CFRP materials and devices

Pultruded CFRP plates were used as internal punching shear reinforcement. A pultruded CFRP laminate designed for strengthening concrete, timber, and masonry structures was selected to obtain maximum bending flexibility during installation. Plate dimensions (thickness t_p , width b_p , and cross-sectional area A_p) and mechanical properties (tensile strengths f_{pk} and f_{pu} , and Young's modulus E_p) are listed in Table 3.1. The plates were used in two ways: with sanded surfaces in the anchoring zone only or with completely sanded surface (over the entire length, as shown in Figure 3.2). In the first case, the plates were assumed to be almost unbonded in the inclined crossing segment of the punching cone, while they were assumed to be fully bonded in the second case and, therefore, more efficient than in the first case due to their ability to limit the shear crack width.

Table 3.1: CFRP plate and strap properties

| CFRP | t_p [mm] | b_p [mm] | A_p [mm ²] | f_{pk} / f_{pu} ^a [MPa] | E_p ^a [GPa] |
|------------------------------|--------------------|---------------|-----------------------------|---|-----------------------------|
| Plate | 1.2 | 50 | 60 | 3000 / 3100 | 162 / 165 |
| Strap (tape) | 0.125 | 30 | 3.75 | 2100 / 2460 | 132 / 132 |
| Strap (system ^b) | 6.25 / 8.25 / 12.5 | 30 | 188 / 248 / 375 | 1660 / 1820 | 132 / 132 |

^a 5% fractile values / mean values

^b 2 × 25 / 33 / 50 loops

Non-laminated CFRP straps (Keller 2010; Lees and Winistörfer 2011) were used for the pre-stressed strengthening application. The dimensions and mechanical properties of one tape layer (consisting of unidirectional carbon fibers and a thermoplastic polyamide matrix) and of the multi-layer strap system are summarized in Table 3.1. Three strap configurations were used: straps of 25, 33, and 50 loops, the latter presenting the maximum available size. The resistance of the plates and straps, P_u , as well as the prestressing levels, α , and applied prestressing forces, P_0 , of the straps are summarized in Table 3.2.

The CFRP straps were arranged and anchored in two different ways: in an open configuration, as shown in Figure 3.3, using two steel end-anchors, or in a closed configuration, as shown in Figure 3.4, using steel end-pins and a turnbuckle to prestress the strap. Both systems exhibit advantages and disadvantages: the open system requires a precise strap length while the closed systems allow for compensation in the turnbuckle. In the latter case, however, the system is less stiff due to the longer strap length. Steel deviators were used on the top in the open configuration, and on the top and bottom in the closed configuration. In the latter case, therefore, adhesive bonding of anchoring devices was not necessary. The diameter of all steel pins and deviators was between 22.5 and 40 mm. Table 3.2 summarizes the parameter combinations of the CFRP plates and straps.

Table 3.2: Overview of denominations and experimental matrix

| Slab | CFRP | Anchors | A_p [mm ²] | P_u^a [kN] | α [%] | P_0 [kN] | β_p [°] | f_c [MPa] | V_{R0}^b [kN] |
|------|--------|--------------|-----------------------------|-----------------|-----------------|---------------|------------------|----------------|--------------------|
| P1 | plates | end-sanded | 60 | 186 | – | – | 34 | 30.3 | 827 |
| P2 | plates | fully-sanded | 60 | 186 | – | – | 31 | 31.3 | 865 |
| So1 | straps | open | 375 | 683 | 47 | 318 | 30 | 39.9 | 908 |
| So2 | straps | open | 248 | 450 | 49 | 220 | 30 | 40.7 | 946 |
| So3 | straps | open | 188 | 341 | 66 | 225 | 30 | 40.3 | 974 |
| So4 | straps | open | 375 | 683 | 15 | 102 | 30 | 40.9 | 947 |
| Sc1 | straps | closed | 375 | 683 | 5 | 32 | 34 | 51.5 | 1063 |
| Sc2 | straps | closed | 375 | 683 | 41 | 278 | 34 | 56.6 | 1061 |

^a nominal^b see Section 3.1.6

3.1.4 Experimental set-up

Specimen description and installation

Eight square full-scale flat slabs with dimensions of $3.2 \times 3.2 \text{ m}^2$ and a thickness $h = 0.26 \text{ m}$ were fabricated (Figure 3.5). These dimensions were selected to exclude any scale effects and to not affect the punching region by the loading system. Two slabs (P1 and P2) were internally reinforced (before pouring the concrete) with two non-prestressed CFRP plates in each direction, as shown in Figure 3.2. Four slabs (So1 to So4) were poured with eight inclined tubes previously inserted into the steel reinforcement, in which the open strap system

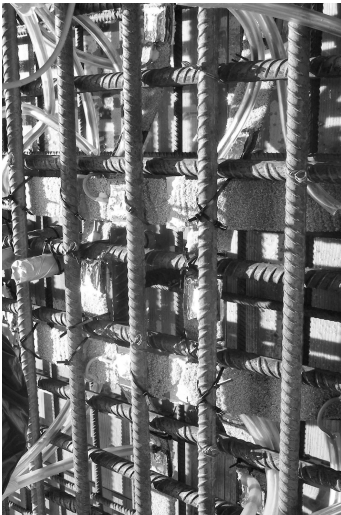
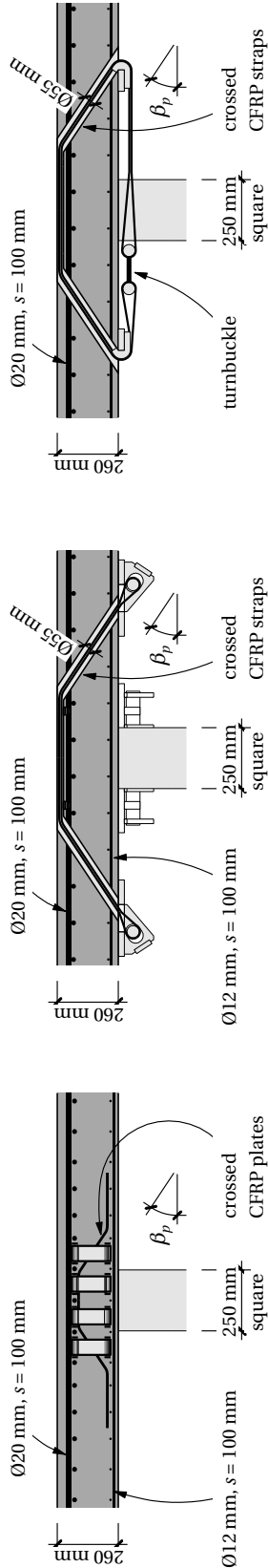


Figure 3.2: Crossed fully-sanded CFRP plates for new slabs

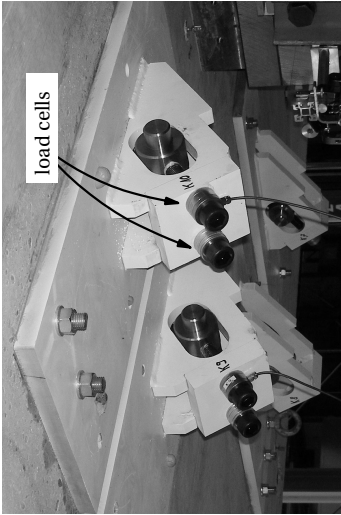


Figure 3.3: Crossed open CFRP straps for strengthening of existing slabs



Figure 3.4: Crossed closed CFRP straps for strengthening of existing slabs

was installed and subsequently prestressed (again, two CFRP elements in each direction, see Figure 3.3). In the last two slabs (Sc1 and Sc2), prepared for the closed system (Figure 3.4), the inclined openings for the straps were drilled from the upper side. The angle of the inclined CFRP segments, β_p , was planned to be 34° . In Slabs So1 to So4, however, β_p was reduced to 30° due to the weight of the concrete on the tubes during pouring, which was why the openings were drilled in the last two slabs (which also corresponds to the actual application procedure).

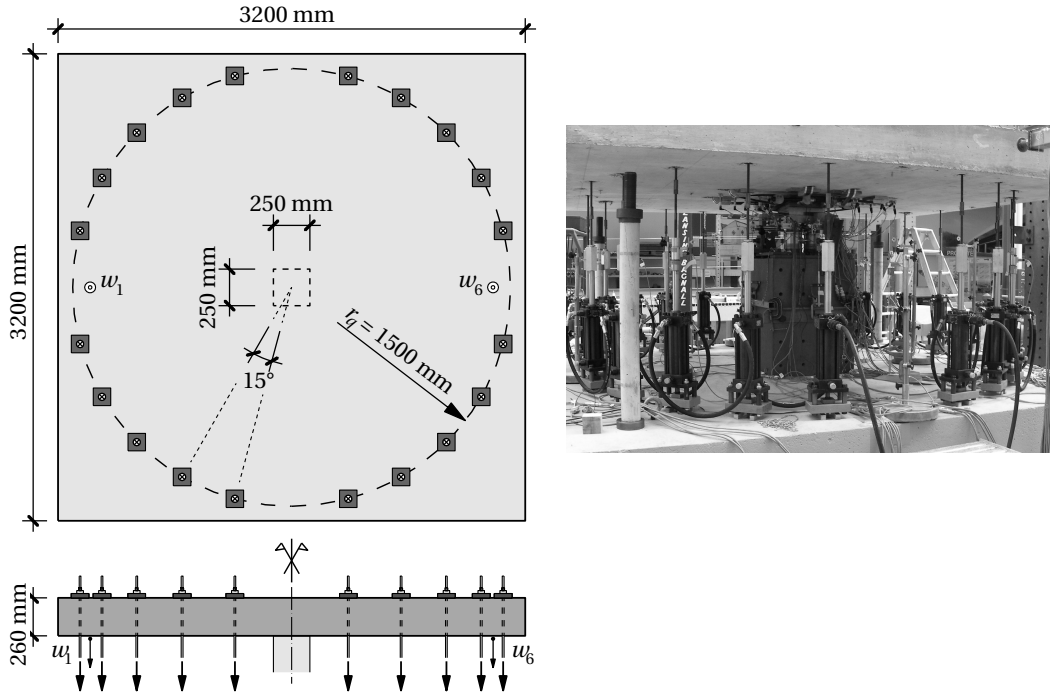


Figure 3.5: Experimental set-up

Slabs P1–2, So1–4, and Sc1–2 were each poured together (three series); the resulting compressive cylinder strengths f_c are listed in Table 3.2 (average of six cylinders per slab, diameter 150 mm, height 300 mm, and maximum aggregate size $d_g = 32$ mm). A lower-strength concrete was selected for the CFRP reinforcement slabs, whereas higher-strength concrete was used in the strengthening cases to simulate new and old concrete. An identical steel-bar reinforcement was used for all slabs and arranged in four layers: diameter $\varnothing = 20$ mm at $s = 100$ mm spacing, crosswise top and $\varnothing = 12$ mm at $s = 100$ mm crosswise bottom reinforcement (nominal¹ yield tensile strength $f_{sy} = 500$ MPa, Young's modulus $E_s = 205$ GPa, and concrete cover: 35 mm top, 20 mm bottom).

The geometry of the CFRP elements in the stronger slab direction (parallel to the first and fourth steel bar layers; axis A) is shown in Figs. 3.2, 3.3 and 3.4. To exclude anchoring failure, the CFRP plate end segments (which were sanded in both slabs) were horizontally extended up to the slab edges. The plates were not threaded from the top in this case to avoid damaging the strain gages (see next section, p. 33), but inserted from the sides and then lifted and fixed at

¹measured average yield strengths for $\varnothing 20$: $f_{sy} = 514$ MPa and for $\varnothing 12$: $f_{sy} = 535$ MPa; refer to Table B.1

the upper steel bars (thus wasting 12 to 20 mm of effective depth). In the strengthening slabs, before installation of the straps, horizontal grooves and openings for the steel deviators were cut into the top concrete cover in such a way that the straps were inserted flush to the top edge of the concrete; refer to Figure 3.6. For the closed system, openings for the bottom deviators were also cut. The anchors of the open system and all the deviators were then adhesively bonded into the openings, using a filled epoxy adhesive.

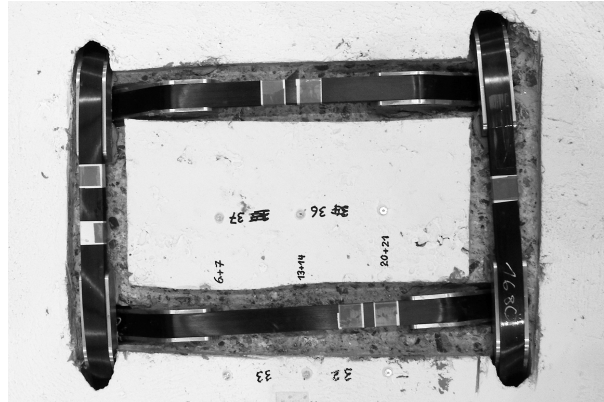


Figure 3.6: Top view of installed straps

The slabs were placed on a center column, on a steel supporting plate of $0.25 \times 0.25 \text{ m}^2$. The loading system was installed, which consisted of 20 hydraulic cylinders of 150 kN capacity each, arranged in a circle of 3.00 m diameter around the slab center; refer to Figure 3.5. All cylinders were connected to the same hydraulic circuit to provide uniform and symmetric loading. The strap systems were then installed and prestressed to levels of 5 to 66% of the strap resistance (applied prestressing forces P_0 , prestressing level $\alpha = P_0/P_u$, see Table 3.2) – that is, from very low prestressing to almost maximum allowable prestressing of the strap system (70% according to the manufacturer). Prestressing of the open system was applied stepwise from both strap sides to eliminate friction losses. The measurements of the strap forces (see next section), however, showed that friction losses were small (6% on average over the two upper deviators, which corresponds to a friction coefficient of approximately 6%).

Instrumentation

Load cells were placed below the steel supporting plate and integrated into four of the 20 loading cylinders. Furthermore, small load cells were placed below the anchor nuts to measure the strap forces; see Figure 3.3. Strain gages were applied on the CFRP plates at the beginning of the anchorage zones, in the middle of the inclined segments, and in the middle of the top horizontal segments; see Figure 3.7.

Deflections (marked by circles in Figure 3.7) were measured along the weak axis **B** at 180- / 780- / 1380-mm distances on both sides from the center point and along the strong axis **A** at a 180- / 1380-mm distance on both sides from the center point. On the bottom side, on one side

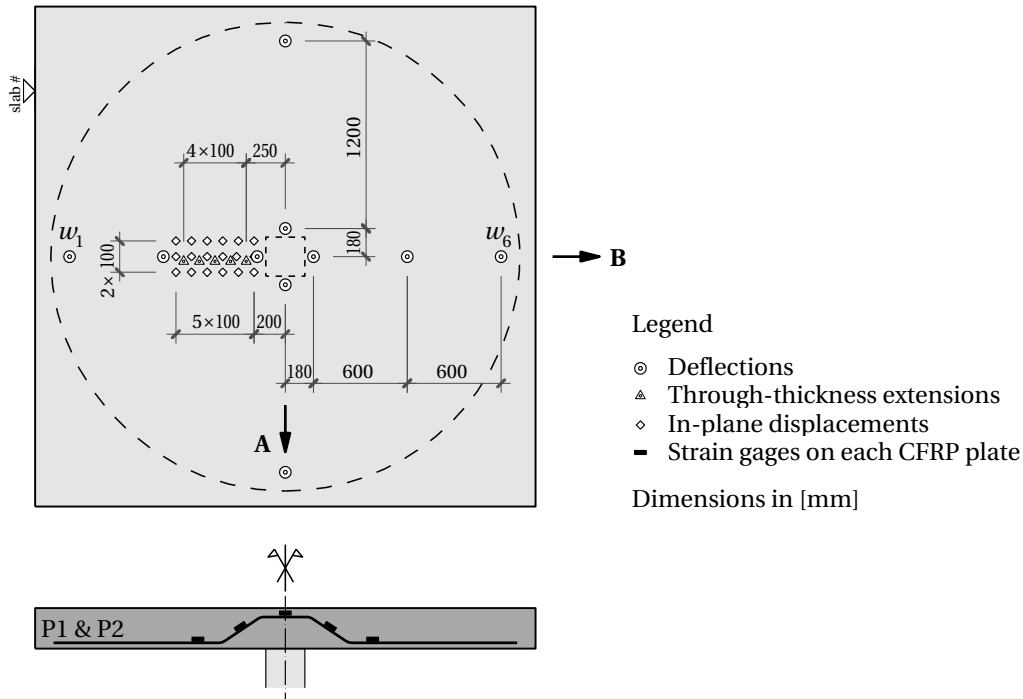


Figure 3.7: Principal elements of instrumentation of slabs P, So and Sc

along the weak axis, axial and tangential in-plane displacements were measured across 100- and 200-mm gage lengths, respectively, at 100-mm distances, starting at a 200-mm distance from the slab center point (marked by diamonds). Similarly, on the corresponding top side, along the weak axis again, axial and tangential displacements were measured across 100-mm gage lengths at 100-mm distances, starting at the center point. Furthermore, along the weak axis on the same side as the in-plane displacements, the through-thickness extension of the slab was measured at 100-mm distances (by transducers installed in small tubes through the slab thickness, marked by triangles), starting at 250 mm from the center point. On the top surface, a number of cracks were selected and their width was monitored.

Experimental program

Reference measurements were made before and after prestressing. Prestressing forces were adjusted based on the load cell measurements below the anchoring nuts. Loading was then manually applied at 100-kN intervals in load-control mode at a rate of approximately 50 kN/min. A spring manometer allowed the simulation of displacement control and enabled the post-peak response to be captured. A full set of measurements was executed after each loading interval. The intervals were shortened when approaching the peak load and during the post-peak phase. One slab, So2, which exhibited a clear peak plateau, was unloaded from this plateau and a second load cycle was applied to investigate the system ductility (see Figure 3.8). After demounting, the plates were cut along the strong and weak axes to analyze the failure modes.

3.1.5 Experimental results and discussion

Load–deflection responses and failure modes

The typical load–deflection responses of one slab of each configuration – P2, So1, and Sc1 – are shown in Figure 3.8, together with the two-cycle response of So2. The weaker axis average deflections of both sides of the center point, w_B , at 1380-mm distances, are shown (average of deflections w_1 and w_6 in Figure 3.5). The deflections of the stronger axis were 85% at the first and 87% at the second peak load (on average) of those of the weaker axis.

The nonlinear responses up to approximately 800 kN depended on the prestressing force. The higher the prestressing force, the later concrete cracking and corresponding stiffness loss were observed. Subsequent to cracking, the slope of all slabs developed similarly. Without any warning, sudden punching failure occurred in Slab P2 at 1017 kN; the load dropped and could no longer be increased. Slab P1 behaved similarly to P2, the ultimate load being slightly lower. A similar unannounced punching failure occurred in Slab Sc1 at 1180 kN. Subsequent to a significant drop of the load of approximately 20%, however, the slab could be slowly reloaded up to a second, slightly higher peak of 1200 kN. Slabs So1 and So2 behaved differently. Failure did not occur suddenly, a plateau was approached, and a ductile failure through concrete crushing and yielding of the upper steel reinforcement developed slowly up to the ultimate load of 1990 kN in the case of So1. So2 was unloaded from the plateau at 1801 kN, exhibiting a residual deflection of 13 mm, and was then reloaded. Again a plateau was reached; however, the resulting ultimate load of 1573 kN, when the load dropped definitively, was only 87% of the first cycle maximum load. The remaining slabs – So3, So4, and Sc2 – behaved similarly. So1 and Sc2, in particular, which were strengthened with the same straps and prestressing levels, showed similar results, although the open system was applied in the former case and the closed system in the latter case. From the structural point of view, the closed system therefore did not show any beneficial effect. However, as previously mentioned, relying on adhesively-bonded anchorage plates is not necessary, which is preferred from case to case.

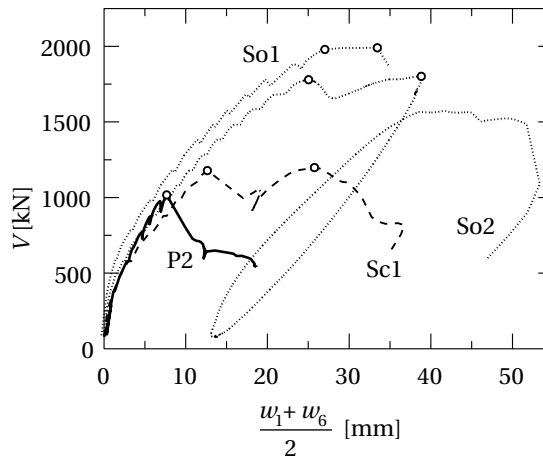


Figure 3.8: Load–deflection response of slabs P2, So1, So2, Sc1

All ultimate loads, $V_{R,exp}$, are given in Table 3.3; two values are shown in the plateau cases, the first and second peak values (whereby the second peak in So3 was 11% below the first peak). The first peak loads mainly depended on the applied prestressing force P_0 : the highest ultimate load was obtained for Slab So1, which had the highest prestressing force, while the lowest values were obtained for Slabs P1–2 and Sc1 without any or the lowest prestressing forces.

Details of the failure modes are shown in Figure 3.9. In Slabs P1 and P2, where classic punching occurred, a comparatively shallow punching cone formed through cracks at angles of approximately 20° (measured from the horizontal bottom line). The concrete thereby debonded in the lower curvature part from the lower side of the CFRP plate, at the CFRP sanding / concrete interface (in P2), or CFRP / concrete interface (in P1). The debonding did not stop behind the lower plate deviation but propagated into the anchorage zone.

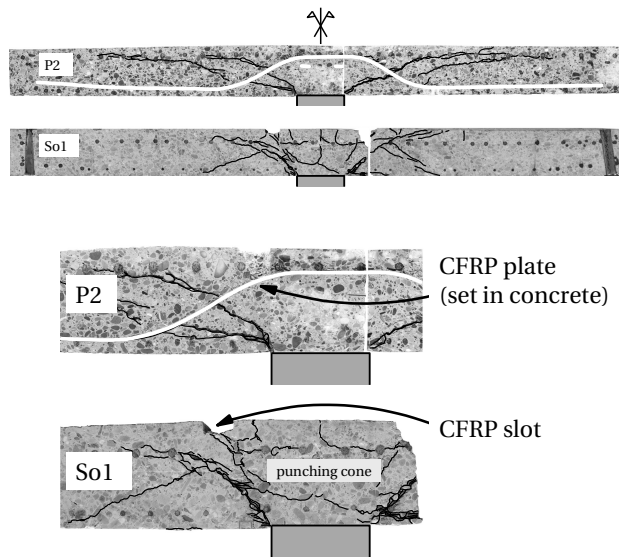


Figure 3.9: Failure modes of slabs P2 and So1 (top: overall view, bottom: detail above column)

Table 3.3: Experimental results

| Slab | $P_{V_{R,exp,1/2}}$ [kN] | $\Delta P_{V_{R,exp,1/2}}$ [kN] | $\frac{\Delta P_{V_{R,exp,1/2}}}{P_u}$ [%] | $V_{R,exp,1/2}$ [kN] | $V_{C,V_{R,exp,1/2}}$ [%] | $\varepsilon_{c,inf,tang,1/2}$ [‰] | FM ^a | $\frac{V_{R,exp,1}}{V_{R0}}$ [-] | $V_{R,pred,1}$ [kN] | Δ [%] |
|------|-----------------------------|------------------------------------|---|-------------------------|------------------------------|---------------------------------------|-----------------|-------------------------------------|------------------------|-----------------|
| P1 | 18 / - | 18 / - | 10 / - | 896 / - | 91 / - | -2.1 / - | A | 1.08 | 828 | -8 |
| P2 | 33 / - | 33 / - | 18 / - | 1017 / - | 87 / - | -2.2 / - | A | 1.18 | 845 | -17 |
| So1 | 422 / 459 | 104 / 141 | 15 / 21 | 1939 / 1990 | 13 / 8 | -3.1 / -2.9 | B | 2.14 | 2091 | 8 |
| So2 | 324 / 471 | 104 / 251 | 23 / 56 | 1779 / 1801 | 27 / 0 | -3.1 / -3.8 | B | 1.88 | 1520 | -15 |
| So3 | 299 / 364 | 74 / 139 | 22 / 41 | 1778 / 1575 | 33 / 8 | -3.3 / -3.1 | B | 1.83 | 1303 | -27 |
| So4 | 253 / 343 | 151 / 241 | 22 / 35 | 1771 / 1742 | 43 / 21 | -3.2 / -3.0 | B | 1.87 | 1540 | -13 |
| Sc1 | 43 / 156 | 11 / 124 | 2 / 18 | 1180 / 1200 | 84 / 42 | -1.4 / -1.6 | A | 1.11 | 1519 | 29 |
| Sc2 | 403 / - | 125 / - | 18 ^b / - | 1839 / - | 2 / - | -2.5 / - | B | 1.73 | 2238 | 22 |

^a Failure Mode A is brittle punching; B is ductile concrete crushing during steel yielding

^b assumed value

Table 3.4: Maximum normalized CFRP vertical component, $V_p, V_{R,exp,1/2}/V_{pu}$, vs. maximum normalized concrete shear force, $V_c, V_{R,exp,1/2}/V_{R0}$

| | P1 | P2 | So1 | So2 | So3 | So4 | Sc1 | Sc2 | Sr1 | Sr2 | Sr3 |
|--|----------|----------|-------------|-------------|-------------|-------------|-------------|----------|-------------|-------------|----------|
| $V_p, V_{R,exp,1/2}$ [kN] | 85 / - | 134 / - | 1688 / 1837 | 1297 / 1883 | 1197 / 1455 | 1011 / 1373 | 192 / 698 | 1803 / - | 1398 / 1414 | 1372 / 1299 | 1263 / - |
| V_{pu} [kN] | 835 | 755 | 2730 | 1802 | 1365 | 2730 | 3053 | 3053 | 3053 | 3053 | 3053 |
| $\frac{V_p, V_{R,exp,1/2}}{V_{pu}}$ [-] | 0.10 / - | 0.18 / - | 0.62 / 0.67 | 0.72 / 1.05 | 0.88 / 1.07 | 0.37 / 0.50 | 0.06 / 0.23 | 0.59 / - | 0.46 / 0.46 | 0.45 / 0.43 | 0.41 / - |
| $V_c, V_{R,exp,1/2}$ [kN] | 811 / - | 883 / - | 252 / 154 | 482 / -82 | 581 / 120 | 760 / 369 | 988 / 502 | 35 / - | 582 / 564 | -299 / -514 | 1252 / - |
| $\frac{V_c, V_{R,exp,1/2}}{V_{R0}}$ [-] | 0.98 / - | 1.02 / - | 0.28 / 0.17 | 0.51 / 0 | 0.60 / 0.12 | 0.80 / 0.39 | 0.93 / 0.47 | 0.03 / - | 0.58 / 0.56 | 0 / 0 | 0.83 / - |

In slabs showing ductile failure, cracks delimiting the punching cone were much steeper. One series of cracks always went from the top slot of the CFRP strap down to the support edge (at angles of around 60°) and a second series of cracks developed at $30\text{--}48^\circ$, almost perpendicular to the CFRP strap that crossed the crack. Concrete crushing during the ductile failure was always observed on the bottom side around the support; refer to Figure 3.10. In one slab only – So3 – failure of the two straps of the stronger axis occurred at the second, slightly lower, peak; refer to Figure 3.11.



Figure 3.10: Bottom side concrete crushing around support steel plate (So2)

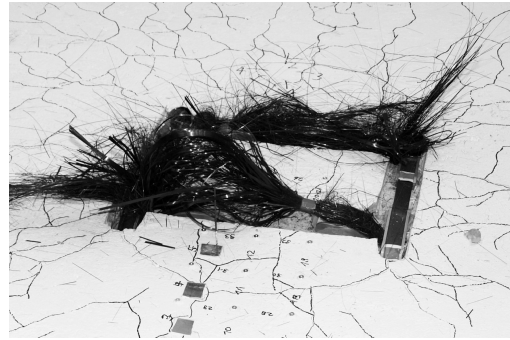


Figure 3.11: Strap failure in So3 at second (lower) peak (top view)

Load–displacement and load–strain responses

The normalized through-thickness extensions, $\Delta h/h$, of Slabs P2, So1, So2, and Sc1 on the weaker axis at 250 mm from the center point (125 mm from the support edge) are shown in Figure 3.12. These elongations resulted from the formation of the inclined cracks. The curves followed the trends of the deflection curves shown in Figure 3.8. The values remained small – less than 2.5 mm (9.6‰) before the first peak load – but then strongly increased during propagating on the plateau, up to 11.7 mm (45‰) in Slab So2 at the second peak load.

The bottom radial and tangential in-plane concrete compressive strains, the former in the weak and the latter in the strong axis direction, of Slab So3 at ultimate load (first peak) are shown in Figure 3.13. The axial strains were small, while the tangential strains $\varepsilon_{c,inf,tang}$, also given in Table 3.3 at a 200-mm distance from the center point, were in the order of the concrete

ultimate strain (negative signs mark compressive strains). All open strap slabs showed similar results, while the tangential strains of the plate and closed strap slabs were significantly smaller.

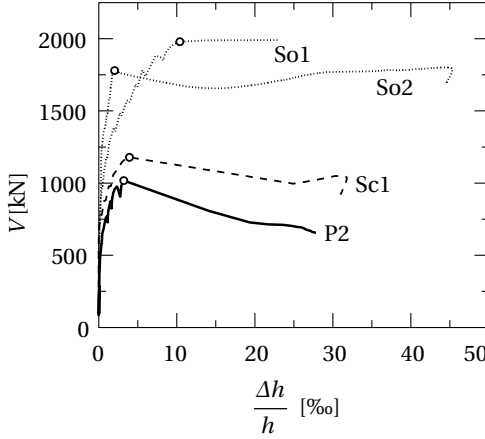


Figure 3.12: Through-thickness elongation $\Delta h/h$ of slabs P2, So1, So2, Sc1

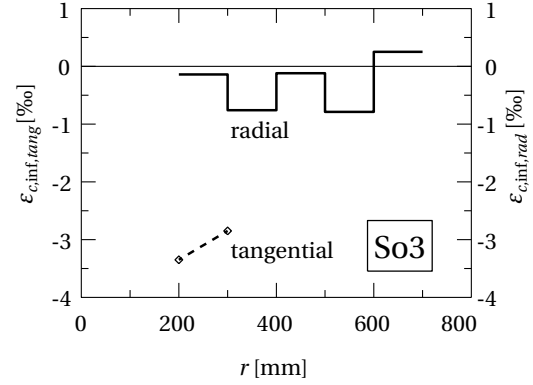


Figure 3.13: Bottom radial and tangential concrete compressive strains of slab So3 at ultimate load

CFRP plate and strap forces

The increase of the CFRP forces, ΔP , of the same slabs as above (P2, So1, So2, Sc1) is shown in Figure 3.14. The values are averages of all four CFRP plates or straps of each slab and normalized by the CFRP strap resistances, P_u . The corresponding values and CFRP forces at the peak loads, $P_{V_{R,exp}}$, are given in Table 3.3 (again for both Peaks 1 and 2, if applicable).

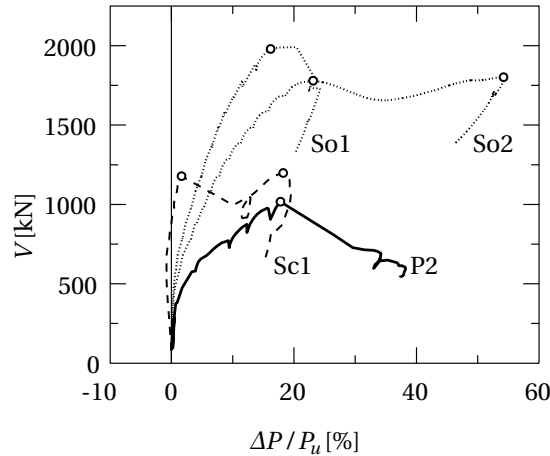


Figure 3.14: Increase of average normalized CFRP force $\Delta P/P_u$ of slabs P2, So1, So2, Sc1

Subsequent to concrete cracking, normalized CFRP forces increased at different slopes: for a certain load increment, the largest increase occurred in the CFRP plate slabs, while the

smallest was seen in the closed strap slabs; the slope of the open strap slabs was situated in between. This more “efficient” behavior of the plate system could be attributed to the bond between plates and concrete, whereby the sanded plate P2 slab exhibited slightly higher plate forces and ultimate loads than the unsanded plate P1 slab, as shown in Table 3.3. The closed strap system of Slab Sc1, which had the longest unbonded length and was almost not prestressed, was significantly activated after the first peak punching only. Table 3.3 shows that the first peak load was reached in all cases at a similar normalized CFRP force increase of 18% on average (varying from 10 to 23%), with the exception of Sc1, where this value was reached at the second peak only due to the aforementioned late strap activation. This 18% value was increased by propagating on the plateau to the second peak up to 54% maximum in the case of Slab So2 (refer to Table 3.3). The CFRP strap forces of the stronger axis were 18% higher on average at the first peak and 38% at the second peak than those of the weaker axis. During propagation on the plateau, a redistribution of forces from the weaker to the stronger axis therefore occurred.

Slab Sc2, which reached almost the same high ultimate load as Slab So1, did not exhibit any increase of the strap forces (during loading subsequent to prestressing) in the lower segment where the forces were measured (at the turnbuckle). This result could be explained by significant friction forces, which occurred at the lower deviators, where the straps were deviated at an angle of 146° (in contrast to the upper deviations of $30^\circ / 34^\circ$). Based on the previous experiences (So1 in particular), a CFRP force increase in the inclined segment of $\Delta P = 0.18P_u$ was assumed in the following calculations (average of all other slabs, refer to paragraph above and Table 3.3).

Shear transmission in concrete

The shear forces transmitted in the concrete to the support, V_c , can be estimated as follows

$$V_c = V - V_p = V - 8P \sin \beta_p \quad (3.1)$$

where V_p is the vertical component of the CFRP force, P , which is taken as the average force of the four CFRP elements; and β_p is the inclination angle of the CFRP elements. Dowel effects from the bending reinforcement thereby were neglected as yielding occurred. The corresponding curves for Slabs P2, So1, So2 and Sc1 are shown in Figure 3.15, while the values at the two peak loads, $V_c, V_{R,exp,1/2}$, of all slabs are given in Table 3.3. The negative V_c -values on the abscissa of Figure 3.15 represent the prestressing forces, which turned to positive values with increasing load. Maximum concrete shear force values were reached at the first peak load and then decreased during propagation on the plateau toward the second peak (except in the P1–2 cases without second peak). Table 3.3 also shows this force redistribution between the two peaks, particularly for the open strap system: at the first peak, 13 to 43% of the load was transferred via the concrete while these values decreased to 0 to 23% at the second peak. The remaining forces were transferred by the CFRP suspension.

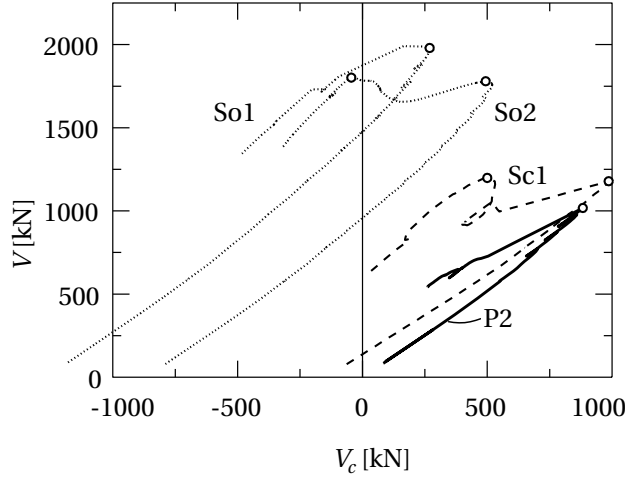


Figure 3.15: Shear force V_c transferred by concrete of slabs P2, So1, So2, Sc1

3.1.6 Modeling and discussion

Empirical relationship to predict first peak load

As deduced previously, the concrete shear loading was reduced with increasing CFRP forces. Based on these results, at the peak load, $V_{R,exp}$, the CFRP vertical component, $V_{p,V_{R,exp}}$, was compared to the concrete shear force, $V_{c,V_{R,exp}}$, in Figure 3.16 (corresponding values are given in Table 3.4). To correctly compare the different parameter combinations, the former values were normalized by V_{pu} (sum of vertical components of strap resistances, P_u) and the latter by V_{R0} [theoretical punching resistance of unreinforced concrete slab, calculated using the simplified design method according to Muttoni (2008) as the intersection between the load-rotation curve – approximated with his Eq. 8² taking the flexural capacity of the slab, V_{flex} , into account – and the failure criterion calculated according to his Eq. 5³]. The estimated values are given in Table 3.2.

Figure 3.16 shows that the resulting values are distributed around a straight line:

$$\frac{V_{p,V_{R,exp}}}{V_{pu}} = 1 - \frac{V_{c,V_{R,exp}}}{V_{R0}} \quad (3.2)$$

Taking furthermore the first peak relationship into account

$$P_{V_{R,exp}} = P_0 + 0.18P_u = (\alpha + 0.18)P_u \quad (3.3)$$

²power function $\psi = 1.5 \frac{r_s}{d} \frac{f_{sy}}{E_s} \left(\frac{V}{V_{flex}} \right)^{1.5}$

³see Eq. 4.3

and

$$V_{R,exp} = V_{c,V_{R,exp}} + V_{p,V_{R,exp}} \quad (3.4)$$

results in an empirical relationship to predict the first peak load $V_{R,exp,1}$ as follows

$$V_{R,pred,1} = V_{R0} + (V_{pu} - V_{R0}) (\alpha + 0.18) \quad (3.5)$$

or

$$V_{R,pred,1} = V_{R0} + (8P_u \sin \beta_p - V_{R0}) (\alpha + 0.18) \quad (3.6)$$

The resulting predicted first peak loads $V_{R,pred,1}$ are compared to the experimental values, $V_{R,exp,1}$, in Table 3.3 and the deviations Δ (in percent) are shown. Considering the three different CFRP systems and the multitude of other parameters, the agreement is fair (average deviation of 17%). The effects of the main parameters (CFRP resistance, prestressing level, and concrete shear resistance contribution) on the ultimate load and their interaction are combined into a coherent formulation and the resulting trends are appropriately simulated. Additional experimental results, however, are required to improve the relationships and reduce the scatter.

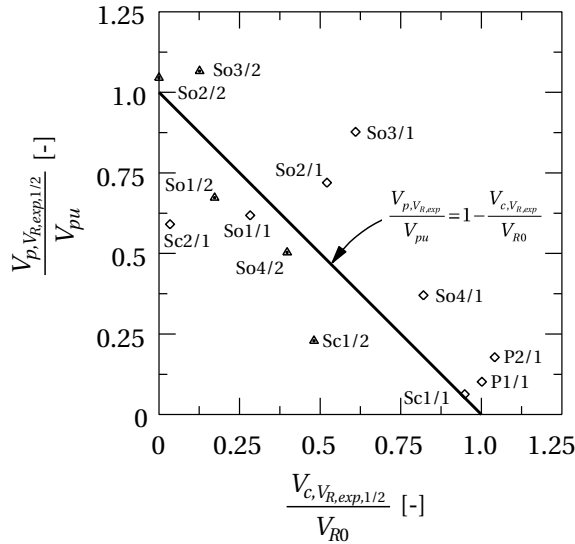


Figure 3.16: Maximum normalized CFRP vertical component, $V_{p,V_{R,exp,1/2}}/V_{pu}$, vs. max. normalized concrete shear force, $V_{c,V_{R,exp,1/2}}/V_{R0}$ ('/1': first peak, '/2': second peak)

Cantilever model to predict second peak load

The aforementioned analysis has shown that slabs clearly exhibiting ductile failure mode (So1 to So4, and Sc2) transferred, at the second peak, almost the entire ultimate load via the CFRP straps, only 0 to 23% being transferred by the concrete (see Table 3.3). Failure occurred though

concrete crushing at the lower edge during yielding of the upper tensile steel reinforcement. From these observations, the formation of a cantilever mechanism at the second peak could be derived, as shown in Figure 3.17. The majority of the load (77 to 100%) was transferred via a compression strut, at an angle of approximately 16° , to the anchoring point of the CFRP strap. Only the small concrete contribution was directly transferred, across the crack of the punching cone, at an angle of approximately 8° , toward the column. The upper steel reinforcement bore the necessary deviation force. At the lower anchoring point the compression strut was hung up by the strap. This deviation produced a compressive force parallel to the lower slab edge. From the high tangential compressive strains around the column and the low axial strains it could further be derived that this compressive force was not directly supported by the column but that a compression ring formed around the column.

The model is conceived as a cantilever beam, which is loaded by one-fourth of the total load at a 1.3-m distance from the center point (which represents the distance of the center of gravity of a 90° circle segment). The strut-and-tie model is isostatic and the member forces can be calculated from the geometry shown in Figure 3.17, the second peak load, $V_{R,exp,2}/4$, and the shear fractions transferred by the CFRP system and concrete. The application of this model to predict the ultimate load is preferable because it is based on clear equilibrium conditions and not only on fitting of the experimental results (as the first-peak model does).

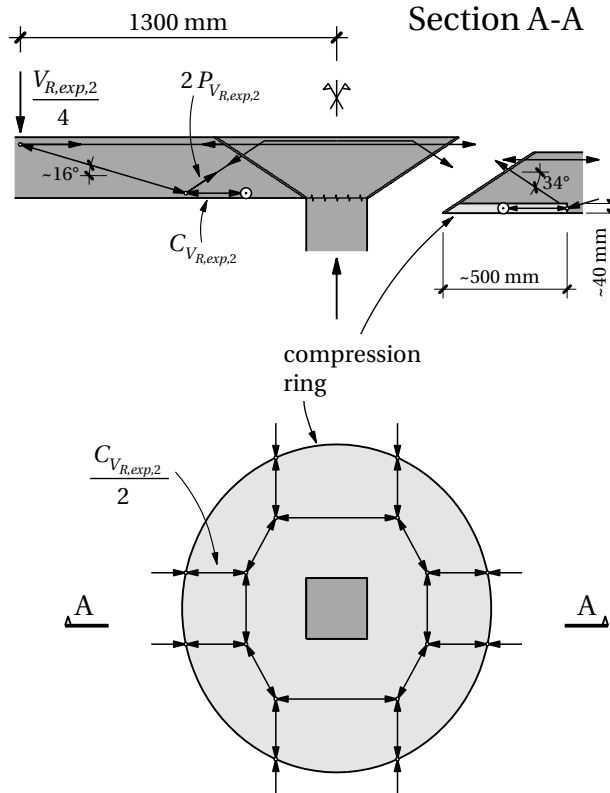


Figure 3.17: Cantilever model at second peak

The resulting compressive forces in the bottom compression ring, $C_{V_{R,exp,2}}$, are given in Table 3.5. Assuming a width of the compression ring of 2×500 mm (the distance from the anchoring point to the column edge on each column side) and taking into account moment equilibrium results in a thickness of the compression ring of 40 mm, which seems reasonable. Calculating further the stress in the compression ring, $f_{c,V_{R,exp,2}} = C_{V_{R,exp,2}} / (2 \times 500 \times 40 \text{ mm}^2)$, led to the values for the open system given in Table 3.5, which represent 1.1 to 1.5 times the uniaxial concrete strength (values $f_{c,V_{R,exp,2}} / f_c$). This result also is reasonable – a compressive strength of 1.2 to 1.4 times the uniaxial strength can be assumed at the lower edge due to a multiaxial stress state according to SIA 262 (2013). A similar analysis showed that the compression diagonal from the strap deviation point to the support was not critical.

Table 3.5: Cantilever model at second peak

| | | So1 | So2 | So3 | So4 | Sc1 |
|---------------------------------|-------|------|------|------|------|-----|
| $\frac{V_{R,exp,2}}{4}$ | [kN] | 498 | 450 | 394 | 435 | 300 |
| $C_{V_{R,exp,2}}$ | [kN] | 2397 | 2386 | 1898 | 1792 | 867 |
| $f_{c,V_{R,exp,2}}$ | [MPa] | 60 | 60 | 47 | 45 | 22 |
| $\frac{f_{c,V_{R,exp,2}}}{f_c}$ | [-] | 1.5 | 1.5 | 1.2 | 1.1 | 0.4 |

3.1.7 Conclusions

Three different CFRP systems were used to reinforce new or strengthen existing concrete slabs against punching. CFRP plates were applied as partially or fully bonded internal slab reinforcement while CFRP straps were used in an open and closed configuration for strengthening. The plates were untensioned whereas the straps were prestressed to different levels. The following conclusions were drawn:

- Untensioned plates or only very low prestressed straps (<5% of their resistance) could not prevent a brittle punching failure. Strap prestressing of at least 15% and more led to a ductile behavior exhibiting a first peak load, a subsequent plateau, and a second peak load, although the CFRP material systems were brittle. The punching resistance of the unreinforced slabs could be increased by 8 to 18% only in the brittle cases, whereas increases of 73 to 114% could be achieved in the ductile cases via a redistribution of forces from the concrete to the strap systems.
- Sanding of the plate systems could not prevent debonding in the lower curved part of the plates, which prevented a significant stress increase in the cracks of the punching cone. Strengthening of the bond between concrete and sanded surface may improve the behavior. In the strap cases, prestressing of at least 15% of the strap resistance prevented negative effects of the unbonded system (which became evident at lower prestressing levels).

- An empirical model was established that is able to estimate the first peak load and is applicable to all three CFRP systems (internal plates, open or closed strap system). It takes the following parameters into account: CFRP plate or strap resistance, CFRP angle, CFRP prestressing level, and punching load of the unreinforced slab. Considering the large parameter ranges and the limited number of tests, the model provides acceptable accuracy. It demonstrates and takes into account the interaction of the different parameters in a coherent way and can be refined further.
- A cantilever strut-and-tie model was established to estimate the second peak load of the ductile cases (which exhibit sufficient prestressing). The model provides acceptable accuracy.

Further research is required, in particular, to take the following additional parameters into account: plate thickness (which may change the 18% constant of CFRP force increase) and pre-deformation (cracked state) of existing slabs. Furthermore, the experimental database needs to be extended to further refine the models.

3.2 Second experimental series

Reference detail

Robert Koppitz, Albin Kenel and Thomas Keller. “Punching shear strengthening of flat slabs using prestressed carbon fiber-reinforced polymer straps”. *Engineering Structures*, 2014, Vol. 76, pp. 283–294. DOI: 10.1016/j.engstruct.2014.07.017

Abstract

An experimental study of full-scale reinforced concrete flat slabs crosswise strengthened with prestressed carbon fiber-reinforced polymer (CFRP) straps against punching shear was performed. The effects of two strap anchoring systems and of slab thickness on punching behavior were compared. In one system the anchors were adhesively bonded to the concrete surface, while an external steel frame balanced the horizontal strap force components in the second system. Strap activation and thus strap force increments were higher in cases with either lower prestressing or higher strap stiffness. The deformability of the steel frame allowed a balancing of the strap forces. In the cases with steel frame, the friction bond between the steel anchors and the concrete surface reduced the concrete compression zone. The system stiffness was thus increased and the rotation capacity reduced compared to the cases with bonded anchors. The thickest slab exhibited a reduced rotation capacity and thus strap activation. The slab therefore failed at the lowest load increase, which however was still 67% above the theoretical resistance of the non-strengthened slab.

3.2.1 Introduction

In the recent past an increasing number of load-bearing structures in the structural engineering field have required increased maintenance or even strengthening for reasons such as insufficient durability or structural resistance due to, for instance, changes of usage, see Chapter 2. Many building structures comprise reinforced concrete (RC) flat slabs supported by columns. In this case, one design criterion concerns the sudden and brittle punching failure that causes a significant loss of load-bearing capacity and may eventually lead to progressive collapse resulting from a limited redistribution capacity of internal forces inside the slab. By providing sufficient shear reinforcement around the column, the punching resistance as well as the deformation capacity of the slab can be enhanced (Lips et al. 2012). The punching resistance is not a constant value but depends on the slab rotation ψ and decreases with increasing rotation (Muttoni and Schwartz 1991).

However, many existing flat slabs were constructed without any or only insufficient shear reinforcement in the column zone and need to be strengthened against punching shear failure. Several concepts⁴ exist for the strengthening of flat slabs against punching shear

⁴see also Section 2.2.3 and tabular summary in Appendix A

such as a widening of the slab support with concrete mushrooms or steel heads (Martinez-Cruzado et al. 1994; Hassanzadeh 1996). In addition, the bending resistance of the slab can be increased with an external reinforcement made of steel or new materials like fiber-reinforced polymer (FRP) composites (Harajli and Soudki 2003; Ebead and Marzouk 2004; Chen and Li 2005; Esfahani et al. 2009; El-Enein et al. 2014). For both concepts the behavior of the slab remains brittle however. A third possibility is the installation of additional shear reinforcement, which normally increases ductility; examples are shear studs (Menétrey and Brühwiler 1997; El-Salakawy et al. 2003; Adetifa and Polak 2005; Fernández Ruiz et al. 2010; El-Shafiey and Atta 2011; Feix et al. 2012; Polak and Bu 2013), drop panels (Martinez-Cruzado et al. 1994; Ebead and Marzouk 2002), FRP shear bolts (Lawler and Polak 2011; Meisami et al. 2013) or stirrup solutions with FRP laminates (Binici and Bayrak 2005a; Sissakis and Sheikh 2007). In some cases, the elements are prestressed for immediate unloading of the slab (Menétrey and Brühwiler 1997; El-Shafiey and Atta 2011). However, in the case of prestressed bolts, due to their short length, even small deformations caused by creep for example can substantially decrease the designated prestressing force. Faria et al. (2009, 2011) strengthened square concrete slabs with a side length of 2.3 m and 100- or 120-mm thickness with prestressed steel strands. These were placed above the column on the upper concrete surface and anchored on both sides in the bottom part of the slab, in holes drilled at an inclination of ca. 11° , using an epoxy adhesive. The punching resistance was increased by 34–48% for slabs with two strands in one direction only and by 61% for one slab with strands in both directions. The prestressing method also improved the serviceability limit state and the post-collapse behavior where a second peak load at 78% of the first peak load was reached on average (Faria et al. 2012).

A similar solution for improving punching shear resistance was presented in Section 3.1. In this case, four non-laminated prestressed CFRP straps (Meier and Winistörfer 1998; Lees and Winistörfer 2011) were installed crosswise around the column (Keller 2010); see Figure 3.18(a)–(b). The thin, flexible straps allowed small radii of curvature and thus an optimum strap inclination of between 30° and 60° (perpendicular to the shear crack), avoiding a glancing intersection between the borehole (diameter 55 mm) and the upper concrete surface. Furthermore, the straps were anchored below the slab using steel anchors adhesively bonded to the concrete surface. Laboratory experiments on eight full-scale flat slabs showed that, although CFRP is a brittle material, a strap prestressing of at least 15% assured a ductile system behavior with a first peak load, a subsequent plateau with redistribution of forces from the concrete to the strap system and a second peak load at 89 to 103% of the first peak load. A punching shear resistance increase of up to 114% was observed in the ductile case.

The prestressed CFRP strap strengthening system presented in Section 3.1 was further developed. The adhesively-bonded anchors, which allow direct transmission of the horizontal component of the strap forces to the concrete, also present some drawbacks. The limited shear transfer capacity of the adhesive leads to relatively large contact plates and thus heavy constructions, and the adhesive joint, which is sensitive to elevated temperatures, has to be thermally insulated. A purely mechanical (unbonded) anchor system was thus developed and again examined in full-scale punching shear experiments.

In the following the effects of the modified anchoring system on the overall system behavior are analyzed. The effect of different slab thicknesses on punching behavior is investigated, which was not done in Section 3.1. Furthermore, preloading up to the serviceability load was applied before strengthening to simulate the effect of concrete cracking during the preceding service life, which may lead to residual slab rotations and thus lowered punching shear resistance.

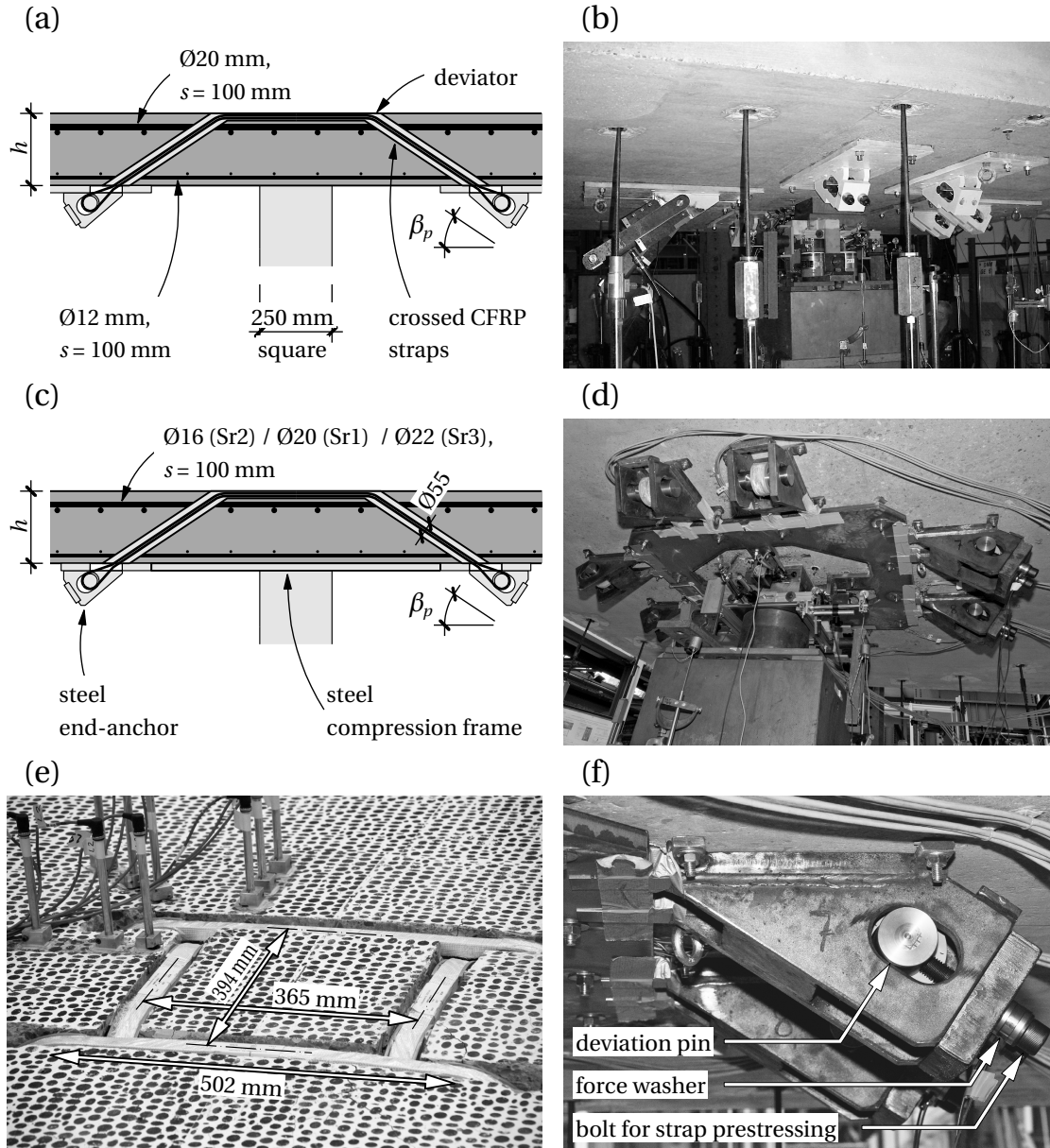


Figure 3.18: Adhesively-bonded anchors: (a) sectional and (b) bottom view (So1). Anchors connected by steel frame: (c) sectional and (d) bottom view (Sr1), (e) top view with crossed CFRP straps above central column (Sr2), and (f) detail view of end-anchor with force washer between anchor plate and bolt head (Sr1)

3.2.2 New mechanical anchoring system

The new anchoring solution includes a steel frame, which is mounted underneath the slab around the column and serves as support for the CFRP strap anchors, see Figure 3.18(c)–(f). The presence of the steel compression frame alters the flow of forces. The horizontal components of the strap forces no longer have to be transmitted to the concrete by shear stresses but can be directly carried by the steel frame, which unloads the concrete compression zone. Three full-scale slabs, Sr1 to Sr3, of nominal heights of 260, 180, and 320 mm were experimentally investigated using the new anchoring system. The results were compared to those obtained for the four slabs So1 to So4, all of 260-mm height and comprising the adhesively-bonded anchors. The dimensions of the compression steel frame had to be adapted to the slab thickness and thus varied slightly, see Figure 3.19(a)–(b). The frame was fixed to the slab by vertical bolts with sufficient bolt clearance to assure buckling stability but not influence the horizontal flow of forces.

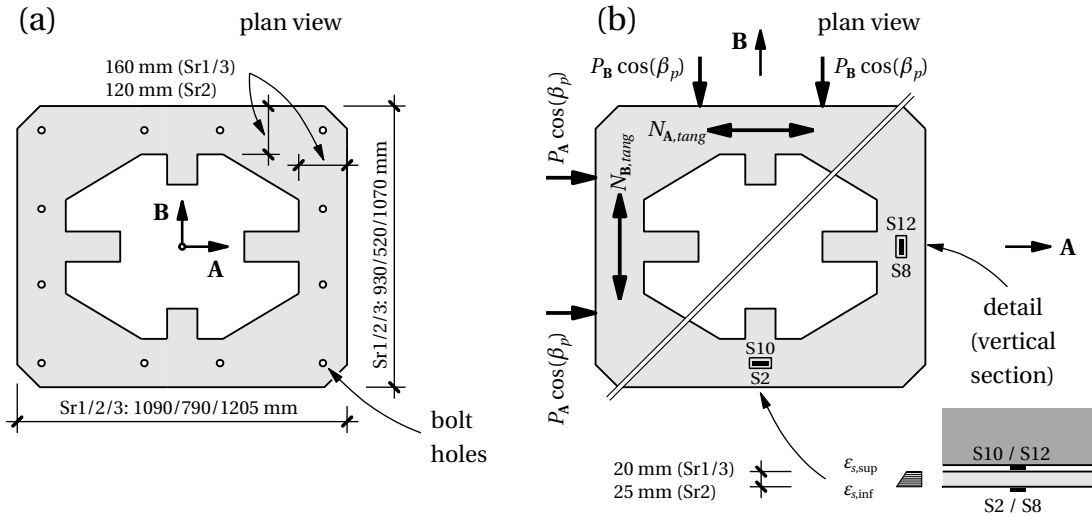


Figure 3.19: Plan view of steel frame with (a) dimensions and bolt holes, (b) frame thickness, applied strain gages on upper (S10 / S12) and lower (S2 / S8) steel surfaces, and acting forces

3.2.3 Experimental set-up

Specimen description and installation

The dimensions of the three investigated slabs were $3.2 \times 3.2 \text{ m}^2$. Effective slab thicknesses, h , and average effective depths (distance from the bottom slab edge to the average level of the centroids of the two upper reinforcement layers), d_m , are listed in Table 3.6. Also listed are the corresponding values of the previous slabs So1 to So4 with adhesively-bonded anchors. All slabs were supported by a center column, represented by a square steel plate of $0.25 \times 0.25 \text{ m}^2$. Strap installation was identical for all slabs. Subsequent to the drilling of the required eight

holes at angles of $\beta_p = 34^\circ$, the steel frame and the anchors were fixed below the slab. The CFRP straps were then pushed through the holes and steel pins were fitted into the strap ends in order to apply the prestressing forces by pulling the pins back, see Figure 3.18(f).

Slabs Sr1 and Sr2 were uniformly loaded by 20 hydraulic cylinders of a capacity of 150 kN each, which were arranged around the slab center in a circle with a radius of 1.50 m, see Figure 3.20. For slab Sr3 of 325-mm thickness, four additional cylinders along the principal axes **A** and **B** were installed.

Table 3.6: Specimen overview with relevant parameters and results

| Slab | h [mm] | d_m [mm] | β_p [°] | f_c [MPa] | E_c [GPa] | A_p [mm ²] | P_u [kN] | P_0 [kN] | α [%] | V_{R0} [kN] | $V_{R,exp}$ [kN] |
|------|-------------|---------------|------------------|----------------|----------------|-----------------------------|---------------|---------------|-----------------|------------------|---------------------|
| So1 | 260 | 194 | 30 | 39.9 | 33.9 | 375 | 683 | 318 | 47 | 908 | 1939 ^a |
| So2 | 260 | 199 | 30 | 40.7 | 33.7 | 248 | 450 | 220 | 49 | 946 | 1779 ^a |
| So3 | 260 | 204 | 30 | 40.3 | 33.0 | 188 | 341 | 225 | 66 | 974 | 1778 ^a |
| So4 | 260 | 199 | 30 | 40.9 | 34.9 | 375 | 683 | 102 | 15 | 947 | 1771 ^a |
| Sr1 | 257 | 200 | 34 | 48.1 | 41.0 | 375 | 683 | 203 | 30 | 1010 | 1981 |
| Sr2 | 187 | 138 | 34 | 43.1 | 35.8 | 375 | 683 | 199 | 29 | 524 | 1073 |
| Sr3 | 325 | 264 | 34 | 44.2 | 35.1 | 375 | 683 | 208 | 31 | 1510 | 2515 |

^a First peak load. In Sr1–3 no reloading to second peak carried out

Material properties

To simulate a 30- to 40-year-old RC slab, concrete with compressive cylinder strengths, f_c , of between 40 and 50 MPa was used (maximum aggregate size $d_g = 32$ mm). Table 3.6 lists the cylinder strengths for all slabs at the time of slab testing. These values were determined from six standard cylinders (diameter 150 mm, height 300 mm) per slab, which were tested both at the time of slab testing and at other ages. The values were adjusted according to the strength-in-time-relationship in the *fib* Model Code 2010 (2013). The Young's modulus, E_c , was derived from two standard cylinders at the time of slab testing.

All slabs were reinforced with an identical reinforcement layout. The spacing of all layers was $s = 100$ mm and the bottom reinforcement always consisted of rebars $\varnothing = 12$ mm, arranged crosswise. The diameter of the top reinforcement was altered from $\varnothing = 16$ mm to 20 mm and 22 mm according to slab thicknesses to keep the average geometrical reinforcement ratio, ρ_m , constant at approximately 1.5%. Axes **A** and **B** refer to the 1st / 4th layer (strong axis) and 2nd / 3rd layer (weak axis) of the reinforcement. For every rebar diameter five tensile tests were carried out on 1-m pieces. Average yield strength, f_{sy} , for the top reinforcement was 521, 515 and 525 MPa ($\varnothing 16$, $\varnothing 20$ and $\varnothing 22$), and 534 MPa for the bottom reinforcement ($\varnothing 12$), respectively; the Young's modulus was $E_s = 205$ GPa. The steel compression frame and anchors were made of steel grade S355 [EN 1993-1-1 (2005)]. The pins were composed of a high-strength 42CrMo4 [EN 10083-3 (2006)].

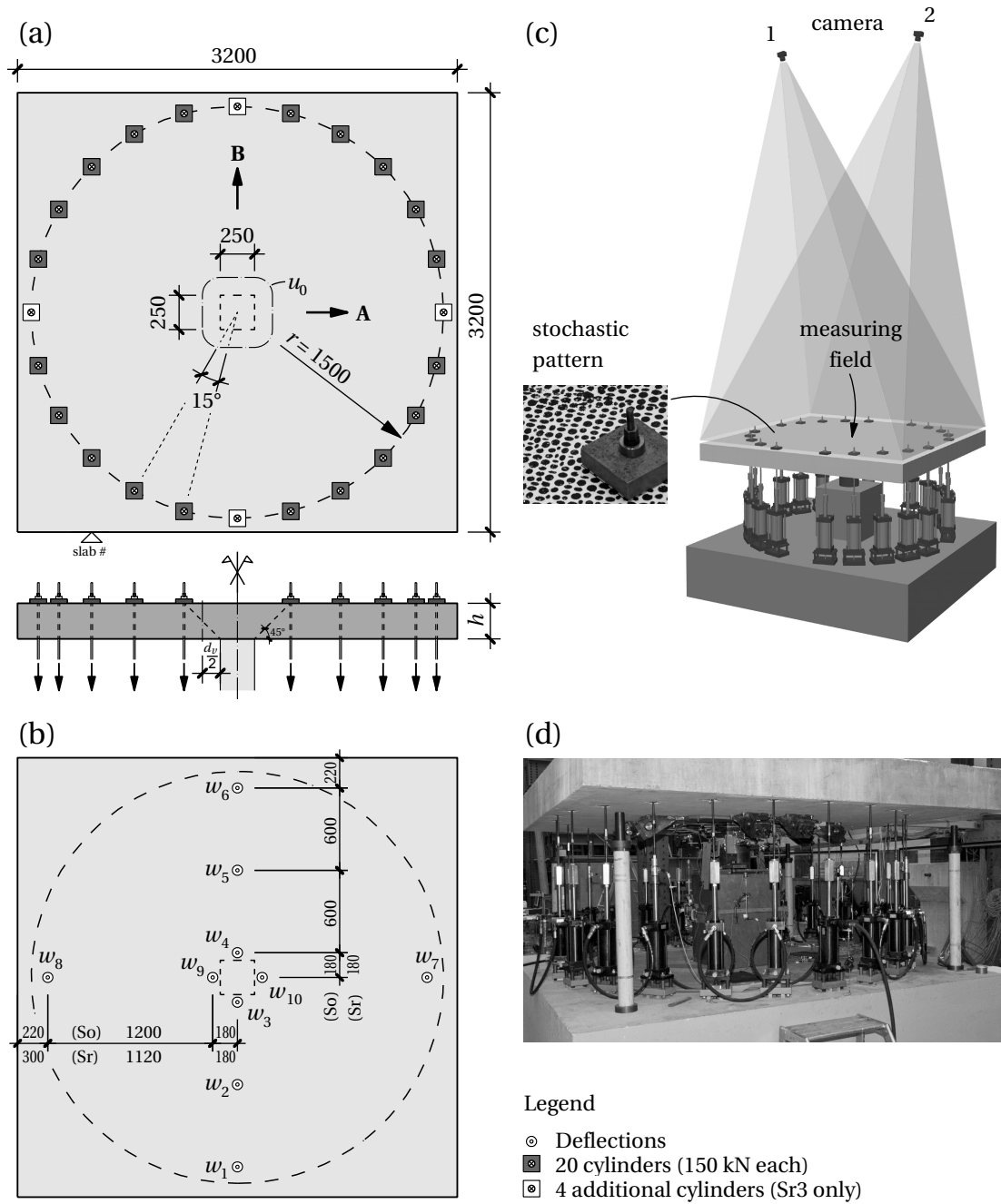


Figure 3.20: Experimental set-up and slab orientation, (b) location of deflection measurements by LVDTs, (c) working principle of applied Image Correlation System (ICS), (d) side view of Sr3. All dimensions in [mm]

The non-laminated CFRP straps were produced by Carbo-Link AG, Fehraltorf, Switzerland. The straps of Sr1–3 consisted of thermoplastic PES (polyethersulfone) tapes containing unidirectional Toray T700SC fibers with a fiber content of 55%. The matrix was thus different from the thermoplastic Nylon PA12 matrix used in slabs So1–4 and the fiber content was slightly lower (60% in So1–4). The tape layers were continuously wrapped around two circular steel pins during fabrication. The two outer layers were fusion-bonded along a length of about 100 mm; the inner end was anchored by a friction bond (Lees and Winistörfer 2011). The 30-mm-wide straps were protected with a glass braided sleeve and a plastic foil [Figure 3.18(e)]. The dimensions (thickness, t_p , cross sectional area, A_p) and mechanical properties (mean and 5% fractile tensile strength, f_{pu} and f_{pk} , Young's modulus, E_p) of one tape layer and of the multilayer strap system are summarized in Table 3.7. The strap resistance, P_u , was identical for slabs Sr1–3. The applied prestressing force of each strap, P_0 , thus the prestressing level $\alpha = P_0/P_u$, was kept constant at around 30%. The values and those obtained for slabs So1–4 are summarized in Table 3.6. The prestressing force P is always the average of the four straps.

Table 3.7: CFRP tape and strap properties (width $b_p = 30$ mm)

| CFRP | Matrix | Loops | t_p [mm] | A_p [mm ²] | f_{pu} [MPa] | f_{pk} [MPa] | E_p [GPa] |
|----------------|--------|-------|---------------|-----------------------------|-------------------|-------------------|----------------|
| Tape (1 Layer) | PA12 | – | 0.125 | 3.75 | 2460 | 2100 | 132 |
| | PES | – | 0.125 | 3.75 | 2460 | 2100 | 120 |
| Strap system | PA12 | 2×25 | 6.25 | 188 | 1820 | 1660 | 132 |
| | PA12 | 2×33 | 8.25 | 248 | 1820 | 1660 | 132 |
| | PA12 | 2×50 | 12.5 | 375 | 1820 | 1660 | 132 |
| | PES | 2×50 | 12.5 | 375 | 1820 | 1660 | 120 |

Instrumentation

Four of the hydraulic cylinders were equipped with load cells. The dead loads of the slabs (including the equipment) of $G = 60 / 80 / 98$ kN had to be added to the applied cylinder loads for nominal slab thicknesses of $h = 180 / 260 / 320$ mm. The forces in the CFRP straps were monitored by small force washers, which were placed below the anchor nuts at the deviation pins, see Figure 3.18(f).

An Image Correlation System (ICS), refer to Herwig and Motavalli (2012), was used for measuring the full field displacements of the entire upper slab surface of slabs Sr1–3, see Figure 3.20(c). The surface was prepared with white paint on which a stochastic pattern of black dots at ca. 18- to 20-mm intervals was applied. Two digital 4-megapixel cameras were installed at a fixed position 4.9 m above the measuring field. At every load stage, the cameras simultaneously photographed the whole patterned slab surface. Numerical analysis of the photographs allowed the deflections of a predefined measuring grid (with 15-mm spacing, i.e. from around 45 000 measuring points) to be obtained in all three directions relative to a reference measurement at zero loads. However, coarser meshes were interpolated for analysis of the slab deflections

(mesh grid size of 100 mm) and crack patterns (25 mm grid size). To validate the ICS deflection data, the deflections, w , were also measured by 5 LVDT sensors at four points next to the column [$w_{3,4,9,10}$ in Figure 3.20(b)] and at one slab edge (w_8) on the strong axis **A**. In slabs So1–4, the deflections were only measured by 10 LVDT sensors (w_1 – w_6 along the weak, w_7 – w_{10} along the strong axis), see Figure 3.20(b). For all the main experiments, the average slab rotation about the two axes **A** and **B**, ψ_m , was obtained, derived by using the LVDTs near the slab edge and next to the column or by equivalent points in ICS. In the preloading experiments the slab rotation was derived as $\psi_A = (w_8 - w_9) / 1120$ mm, as the ICS data was not recorded.

Tangential in-plane displacements were obtained from nine strain gages, B1–B9 (gage length 150 mm), on the bottom slab surface along axes **A** and **B** and one diagonal [Figure 3.21(a)]. In slabs So1–4, two LVDTs, U5–U6, with 200-mm gage lengths measured displacements perpendicular to the weak axis **B**, starting at a distance of 200 mm from the slab center [Figure 3.21(b)]. Additional strain gages S2 / S10 and S8 / S12 (gage length 6 mm) were applied on the top and bottom surfaces of the steel frame, to determine the compressive frame forces [Figure 3.19(b)].

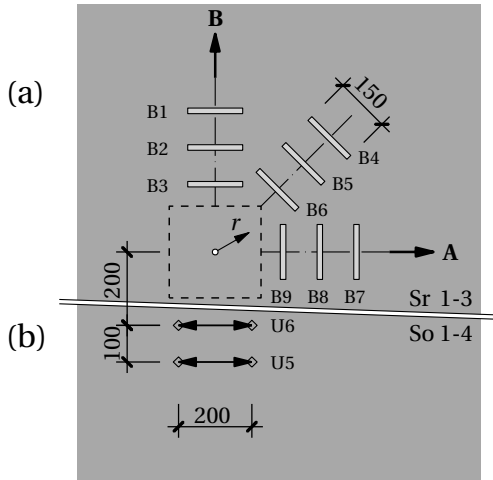


Figure 3.21: (a) Top view of applied strain gages on bottom surface of Sr1–3. Detailed gage positions see Figure 3.28; (b) tangential in-plane deformation measurements of So1–4. All dimensions in [mm]

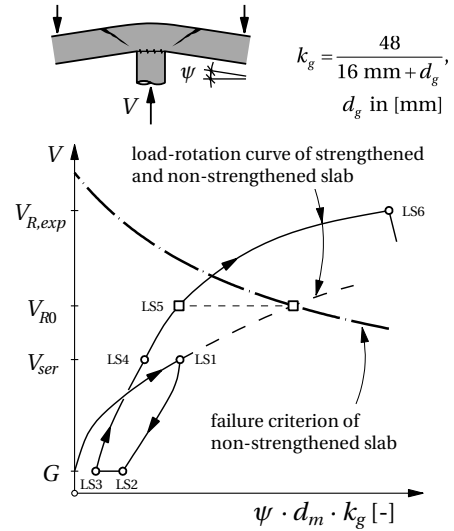


Figure 3.22: Definition of load stages LS1 to LS6

Experimental program

Six load stages (LS) were defined, see Figure 3.22. LS1 denotes the maximum load during preloading (before final installation and prestressing of the CFRP straps) and is equal to a service load, V_{ser} , of the non-strengthened slab, assumed as being ca. 65% of its theoretical (punching) failure load, V_{R0} . LS2 and LS3 mark the no-load stage prior and subsequent to prestressing up to the strap force P_0 . LS4 is at the same applied load as LS1, but after preloading

and prestressing, while LS5 and LS6 denote the failure loads of the non-strengthened slab, V_{R0} , and strengthened slab, $V_{R,exp}$, respectively. On the abscissa, the product of slab rotation, ψ , average effective depth, d_m , and a factor, k_g , which takes into account the aggregate size, is shown according to Muttoni (2003). Muttoni and Schwartz (1991) assumed the product ψd_m to be proportional to the width of the critical shear crack. V_{R0} was calculated according to Muttoni (2008) using the simplified method (see Section 3.1.6, p. 41); the results are given in Table 3.6.

Reference measurements were taken before preloading and prior to and after prestressing of the CFRP straps. The further loading program for slabs Sr1–3 was similar to that for slabs So1–4, see Section 3.1.4, p. 34. Loading intervals, initially 100 kN, were shortened when approaching the failure load. After each interval a full set of measurements was recorded. During experiment Sr3, a sudden fracture of one of the 24 tension rods occurred at $V \approx 1750$ kN. The slab was completely unloaded and reloaded at this stage (not shown in the following diagrams) and further loaded up to failure.

3.2.4 Experimental results and discussion

Preloading

Slabs Sr1–3 were preloaded to LS1 before the CFRP straps were installed and prestressed. To take into account different concrete compressive strengths, f_c , and the slab geometry, the load–rotation curves, shown in Figure 3.23, were normalized according to Muttoni (2008): on the ordinate an equivalent shear stress, $V / (u_0 \cdot d_v)$, along a control section, u_0 , located at $d_v/2$ (here: shear-resisting effective depth d_v = effective depth d_m) from the supported area [see Figure 3.20(a)], was calculated and divided by $\sqrt{f_c}$, which is assumed as being proportional to the concrete shear strength. The influence of the slab thickness was not fully eliminated because the plate stiffness is proportional to the third power of the effective depth; see also Guandalini (2005). On the abscissa the same product as described above (in Figure 3.22) was applied.

All curves in Figure 3.23 exhibited a steep slope at the beginning until cracking of the concrete occurred and stiffness losses were observed for additional loading. The incomplete normalization of the slab thickness is illustrated by the steeper slope of Sr3 (thick) compared to Sr2 (thin) in the cracked elastic state. A residual crack width (or slab rotation) after the complete unloading to LS2 was observed for all slabs. By subsequent prestressing of the CFRP straps up to P_0 (LS2→LS3) the residual cracks were fully overpressured, which led to a stiffer system behavior during reloading that continued parallel to the initial slope of the uncracked slab.

Load–deflection responses and strap activation

The vertical deflections obtained from ICS are shown in Figure 3.24 at the three load stages LS4–6. At LS6 (failure load), the location of the measuring points w_1 and w_6 are indicated;

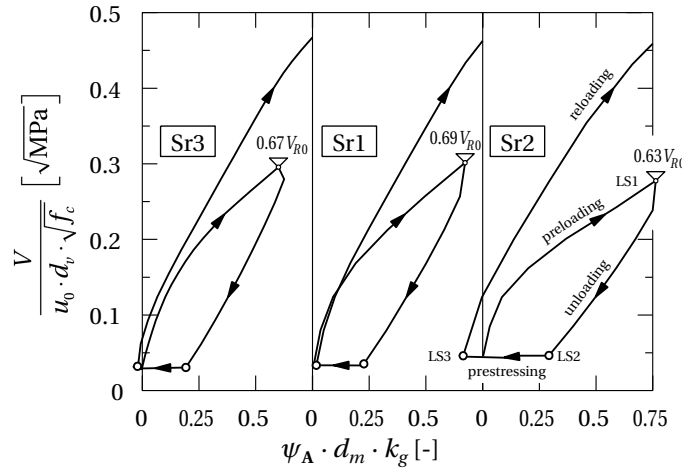


Figure 3.23: Normalized preloading and unloading curves of slabs Sr3, Sr1 and Sr2, followed by strap prestressing and reloading

their average deflection is denominated as w_B . The influence of slab thickness on deformation behavior is clearly shown: the thinnest slab, Sr2, exhibited the highest deflections and failed at 1073 kN at $w_B = 37.0$ mm. In contrast, the thickest slab, Sr3, failed at 2515 kN but exhibited very stiff behavior ($w_B = 11.6$ mm). Slab Sr1 lay in between, exhibiting a punching resistance of 1981 kN at 19.8 mm deflection. The shape of the contour lines is always elliptic due to the different effective depths of the 3rd and 4th reinforcement layers. This effect of the orthotropy is accentuated for the thin slab due to the largest difference in the effective depths of the two main axes compared to d_m . Between LS4 and LS5 the slab deflections approximately doubled and subsequently significantly increased up to failure. Note that parts of the contour lines are masked because of interference caused by measuring devices on the slab surface.

The normalized load–rotation and normalized strap force increase–rotation of all slabs are shown in Figure 3.25. The CFRP strap force increments, ΔP , were normalized by the ultimate strap resistance of the largest strap, $P_{u,\max} = 683$ kN. The applied prestressing force P_0 influenced the load–rotation behavior and strap activation, which is demonstrated by comparing slabs So1 and So4 with the same strap size. So1 with $P_0 = 318$ kN behaved stiffer than So4 ($P_0 = 102$ kN), which may be attributed to the fact that the vertical components of the higher strap forces unloaded the slab and further compressed it via their horizontal components. On the other hand slab So4 was less unloaded and reached the cracked elastic state earlier. To fulfill the equilibrium conditions, its straps thus had to bear additional loads already at a lower external load, resulting in the steeper slope of the strap–force activation curve of So4 compared to So1. Contrary to P_0 , the influence of the axial strap stiffness $E_p A_p$ on the load–rotation behavior was small, as the curves of So2 and So3 (with the same P_0) were almost identical despite the different strap sizes with cross sections of 248 and 188 mm² (see Table 3.6). However, the axial stiffness directly influenced the strap force activation. Slab So3 exhibited a significantly smaller slope than So2 and was thus less activated. Although a higher P_0 is generally preferred to permanently unload the concrete slab, it is possible — at least to some

extent — to compensate a lower initial prestressing force (limited by the dead load, G , of the slab for example) with a steeper strap activation gradient by installing a larger strap. Thus the interplay of P_0 , ΔP and $E_p A_p$ can be optimized from case to case, depending also on the ratio of live to dead loads.

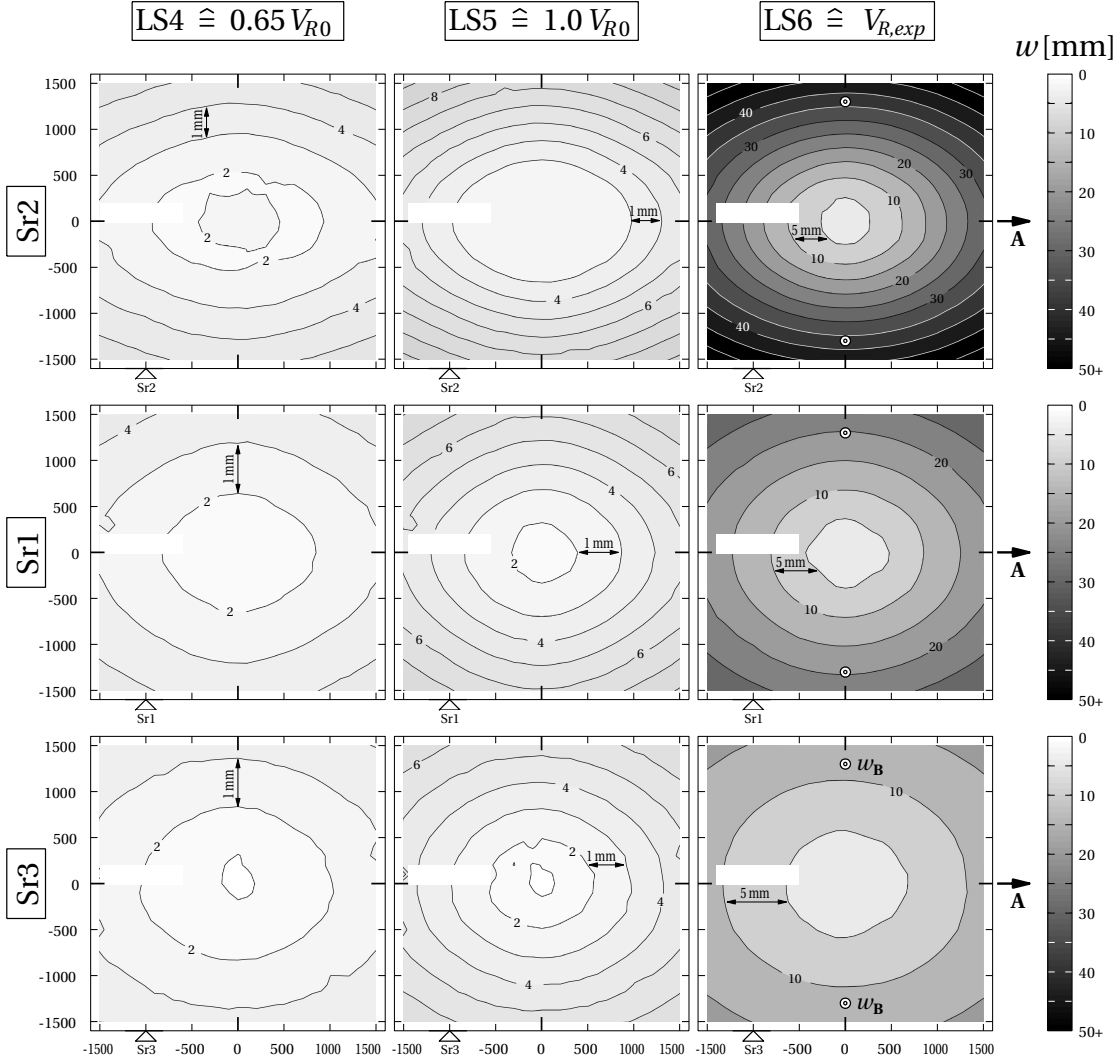


Figure 3.24: ICS slab deflections of Sr2 (top row), Sr1 (middle row) and Sr3 (bottom row) for load stages LS4, LS5 and LS6. All dimensions in [mm]

Slab Sr1 was initially prestressed to $P_0 = 203 \text{ kN}$, approximately equal to So2–3 and had the same strap cross sections as So1 and So4 (375 mm^2). The smaller gradient of Sr1 compared to So1–4 in the load–rotation response, at the beginning up to around $0.25\sqrt{\text{MPa}}$, resulted from preceding concrete cracking during preloading (Figure 3.23). The load–rotation curve of Sr1 lay in between those of So1 and So4, corresponding to the order of P_0 (203, 318, 102 kN). However, although the P_0 of Sr1 was about the same as that of So2–3, the slab eventually behaved stiffer

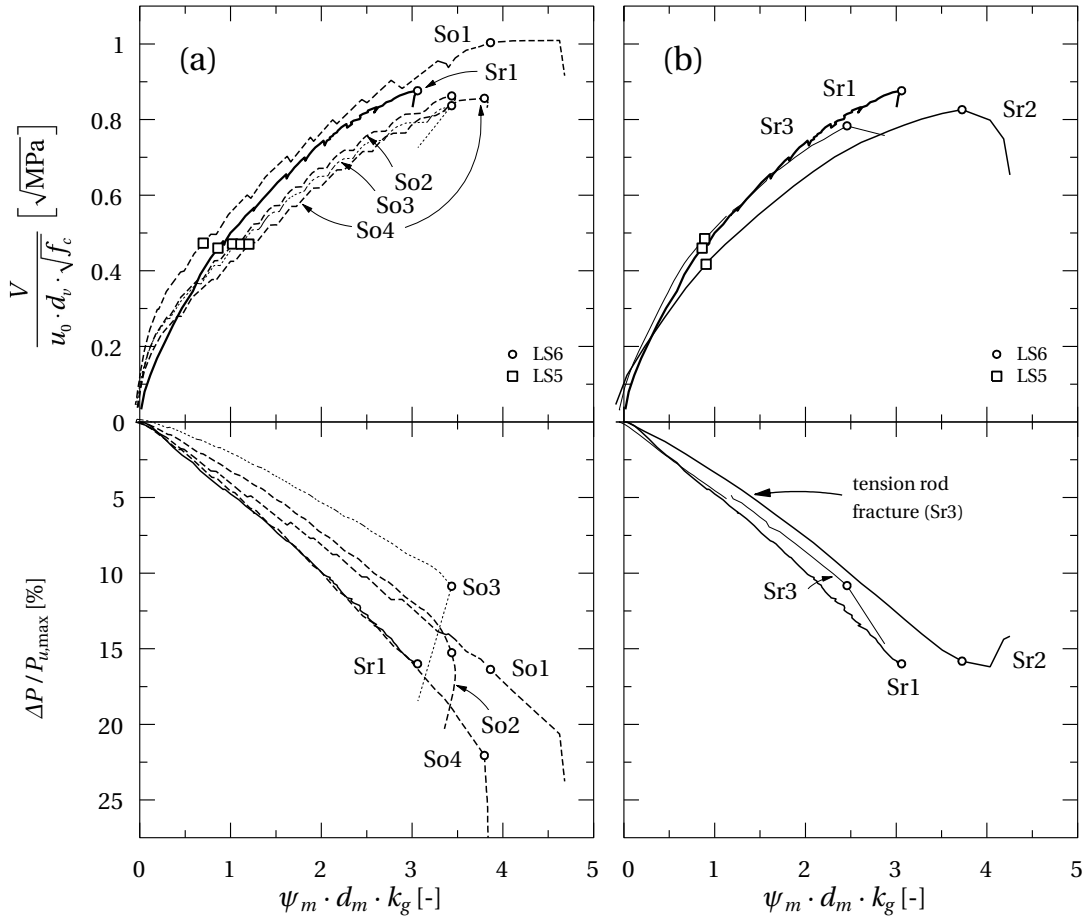


Figure 3.25: Normalized load and strap force increase vs. rotation curves for (a) So1–4 and Sr1, and (b) Sr1–3

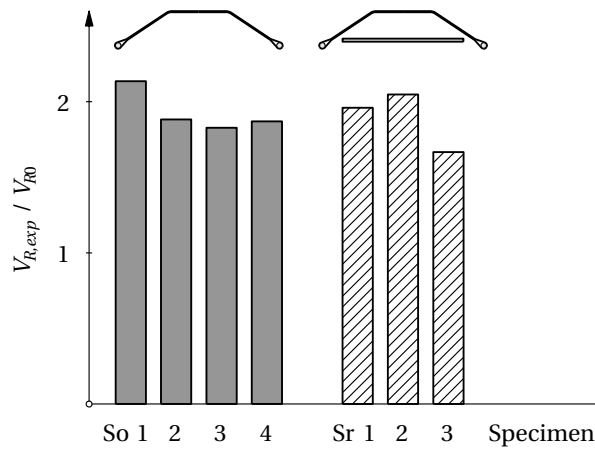


Figure 3.26: Summary of experimental failure loads $V_{R,exp}$, normalized by corresponding theoretical punching resistance of non-strengthened slab V_{R0}

and approached the curve of So1. This can be attributed to the steel frame, which caused a deformation reduction due to its additional stiffness and bearing of the compressive forces (see next section, pp. 58–61). The strap activation curves of Sr1, So2 and So3 were directly related to the axial stiffness, and the steepest slope of Sr1 corresponded to the largest strap size. The slabs Sr1, So1 and So4 had the same strap size, and despite the different P_0 the curve slopes of Sr1 and So4 were almost identical. Because of the steel frame the straps in Sr1 were more strongly activated than they would have been without it (also discussed in the next section).

Slabs Sr1–3 had the same initial prestressing force and strap size. Sr1 and Sr3 exhibited almost identical load–rotation and strap activation–rotation responses and behaved stiffer than Sr2 although the latter was more strongly prestressed relating to its smaller slab thickness. For the thin slab the increased orthotropy disproportionately influenced the slab stiffness leading to a softer response in both diagrams in Figure 3.25(b).

Slabs So2–4 failed at normalized loads of ca. $0.85\sqrt{\text{MPa}}$; the punching resistance of slab So1 was $0.98\sqrt{\text{MPa}}$ at approximately the same rotation as the other three slabs with adhesively-bonded anchors. The normalized punching shear resistance of the three slabs with a steel frame was also similar, ranging between 0.78 and $0.88\sqrt{\text{MPa}}$, the lowest value was observed for the thick slab Sr3. A summary of the experimental results is shown in Figure 3.26, where the ultimate loads are normalized by the punching shear resistance of the non-strengthened slabs [calculated using the simplified method of Muttoni (2008); values in Table 3.6]. Both end-anchor fixation systems significantly strengthened the slabs and raised the resistance by 67–114% compared to the theoretical value V_{R0} . The high initial prestressing force of 318 kN in So1 caused an above-average increase, with the thickest slab Sr3 exhibiting the lowest punching resistance increase of 67%.

Interaction between steel frame and concrete slab

In addition to the above-described effects of the steel frame on the load–rotation responses and strap activation, a balance of the strap forces was observed during the stepwise prestressing and subsequent loading up to failure due to the crosswise arrangement of the straps around the rectangular steel frame, as shown in Figure 3.27(a), which shows the development of the horizontal components of the strap forces, $P \cos \beta_p$. The final prestressing forces were the same along both axes. Subsequently, both strap forces increased almost linearly and only started to diverge slightly in the last phase. The prestressing of two parallel straps compressed the frame in one direction but pushed it apart in the perpendicular direction, which led to an activation of the straps in that direction and thus a balance of the forces. The slabs with the rigidly supported (bonded) anchors did not exhibit any noticeable interaction between the CFRP straps during prestressing and the final prestressing forces along the two axes were thus different, see Figure 3.27(b). During further loading, the straps along the strong axis were more strongly activated than those in the weak direction.

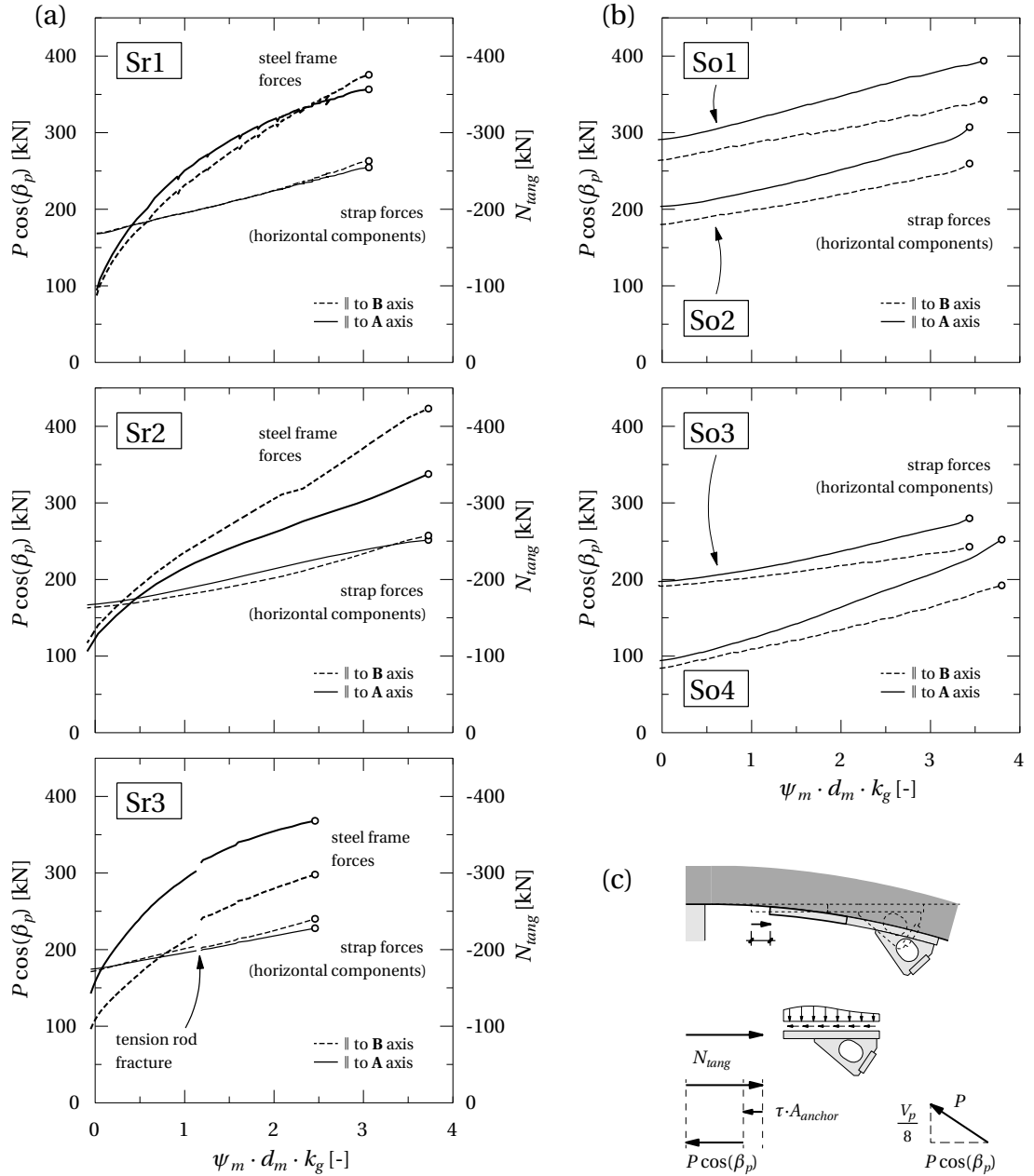


Figure 3.27: (a) Horizontal strap force components, $P \cos \beta_p$, and tangential steel frame forces N_{tang} of Sr1–3 vs. slab rotation, (b) horizontal strap force components vs. slab rotation of So1–4, (c) friction bond between anchor and slab

The horizontal strap force components of Sr1–3 were further compared to the tangential forces in the steel frame, N_{tang} , which were derived from the strain gage measurements on the steel surface. The ratio of the tangential forces in the steel frame along the two axes depended on the aspect ratio of the steel frame and thus its different stiffness in the two directions. The tangential forces in the steel frame were different from the horizontal components of the strap forces; close to failure N_{tang} in the steel frame was 40–50% higher than $P \cos \beta_p$. This difference resulted from slipping friction between the steel anchors and concrete surface caused by the frame, which hindered the movement of the anchors towards the column, see Figure 3.27(c). The compression zone of the slab was thus unloaded by a friction-induced force acting on the bottom surface of the slab.

The development of the bottom tangential in-plane concrete strains, $\varepsilon_{c,inf,tang}$, in the direction of axis **A** is shown in Figure 3.28(a) for the load stages LS1–6 (where applicable) of slabs So1, So2 and Sr1. At LS3 the strains were almost zero or minor tensile strains of max. 0.2‰ were measured, and they increased up to LS6 proportionally to the load–rotation response. The beneficial effect of the strengthening measure is shown for Sr1, where the tangential strains of LS5 were almost identical as for LS1 but at a 44% higher applied load (980 vs. 681 kN). As the ultimate load was approached (LS6) the strains progressively increased and slabs So1–4 reached an almost identical peak compressive strain value of 3.2‰ at a 200-mm distance from the column center (Table 3.3). A smaller strain peak of –2.5‰ was however measured for slab Sr1, confirming a reduction of the slabs’ concrete compressive forces by the steel frame contribution. The corresponding tangential in-plane concrete strains for slabs Sr1–3, but in all directions and at ultimate loads, are shown in Figure 3.28(b). In the direction of the weak axis **B** higher compressive strains than along the strong axis **A** were measured, the difference between them being reduced with increasing slab thickness (affine to the vertical deflection measurements). At 45° only low values were recorded.

The installed steel frame caused an unloading of the concrete slab and thus led to the gain in slab stiffness, shown in Figure 3.25. Furthermore, the rigid frame support and associated slipping friction between anchors and concrete caused an additional elongation of the carbon straps, which resulted in the observed stronger strap activation.

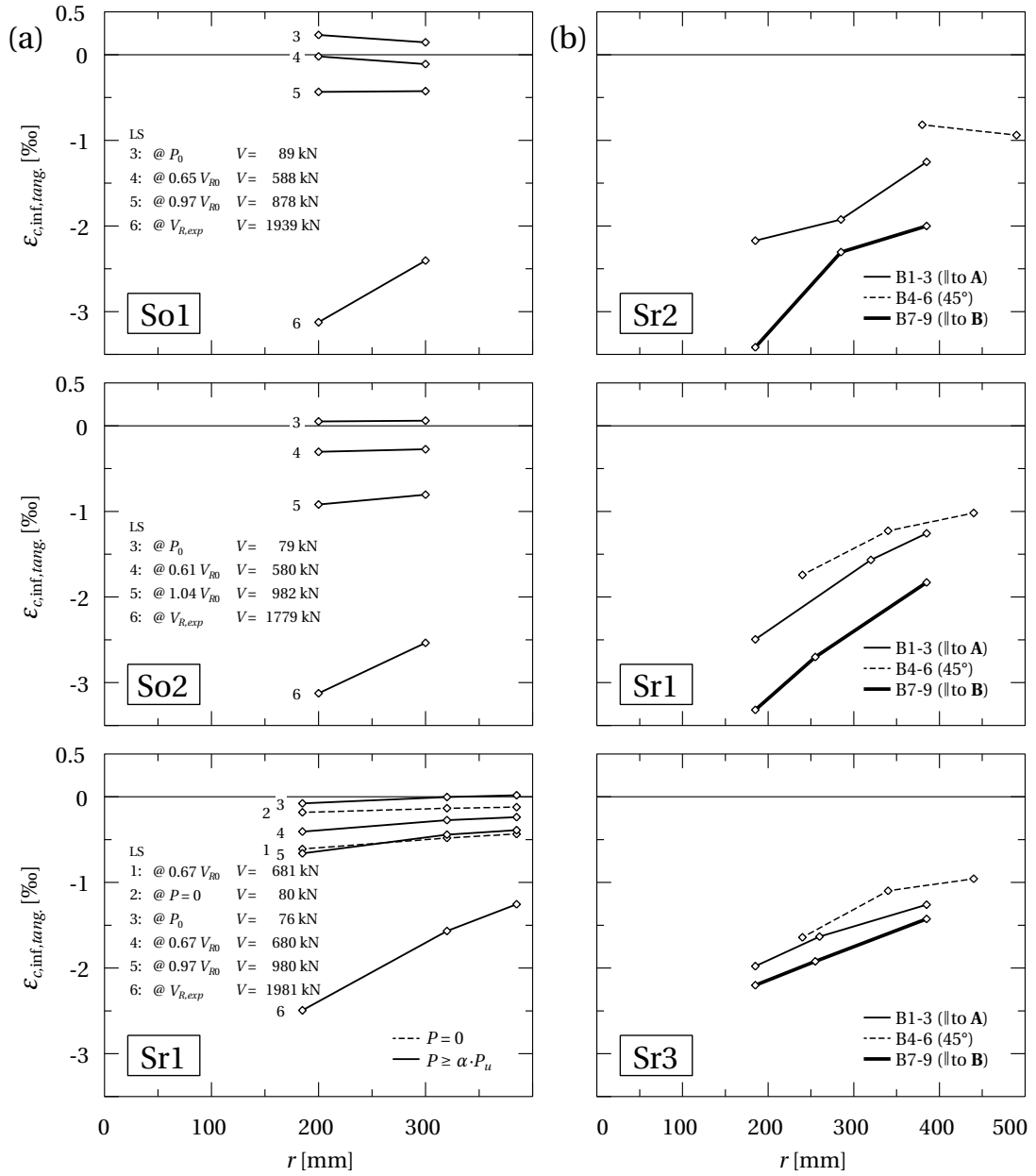


Figure 3.28: Tangential strains at bottom surface next to columns of: (a) So1, So2 and Sr1 at selected load stages (in axis A direction); and (b) Sr2, Sr1 and Sr3 at ultimate load $V_{R,exp}$ (in all three directions)

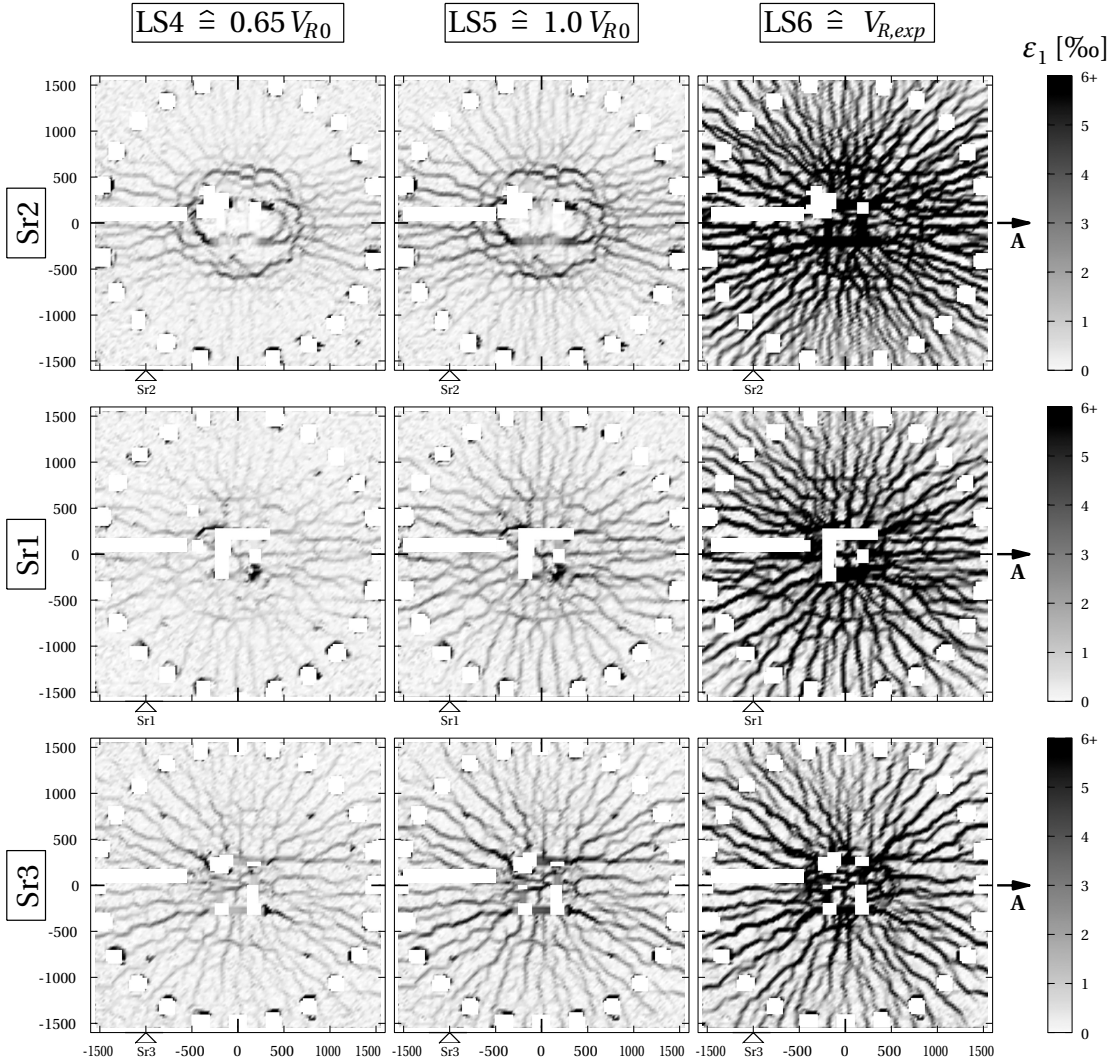


Figure 3.29: Maximum principal strains ε_1 of Sr2 (top row), Sr1 (central row) and Sr3 (bottom row) for three load stages LS4, LS5 and LS6. All dimensions in [mm]

Crack pattern in tensile zone

Since ICS allows the monitoring of the displacements of the upper concrete surface in all three directions it was possible to calculate principal strains ε_1 in the horizontal plane by applying Mohr's circle for the axial strains in **A**- and **B**-direction, as shown in Figure 3.29 for load stages LS4 to LS6 of slabs Sr1–3. The ICS images represent crack patterns as large strains represent the propagation of a crack between two grid points. Large tangential strains representing radial cracks were measured in all slabs, while large radial strains indicating clear crack rings around the column appeared only in Sr1 and Sr2. Again for the thin slab Sr2 the largest strain peaks were reached (due to the large rotation), whereas for the thick slab Sr3 they were significantly lower. Despite the presence of only two CFRP straps in each of the two main axes, a uniform crack pattern was observed for all three slabs, which was influenced only by the orthotropy.

The crack pattern of slab Sr2 at LS5 is shown in Figure 3.30, together with two saw-cuts running along the weak axis **B** and through the strap boreholes parallel to axis **A**; also shown are the ICS deflections along these sections at LS5 and LS6. The ring of radial strain peaks was more or less located above the strap anchoring points where the strap forces acted on the concrete surface. With a weaker strap activation, i.e. at LS5, these points acted as almost rigid supports for the slab and the outer part of the slab was thus fully fixed along this ring of maximum radial stress peaks. This is confirmed by the maximum curvatures (and horizontal tangents) in the deflection curves at these locations (see LS5). At the same load, the truncated punching cone started developing whose edge, on the level of the upper longitudinal reinforcement, almost corresponded to the location of the ring of radial strain peaks. The location of the strap anchoring points thus seemed to define the edge location and thus the angle of the punching cone. With a stronger strap activation, i.e. LS6, the supports at the anchoring points started lowering and the points of maximum curvature moved towards the column.

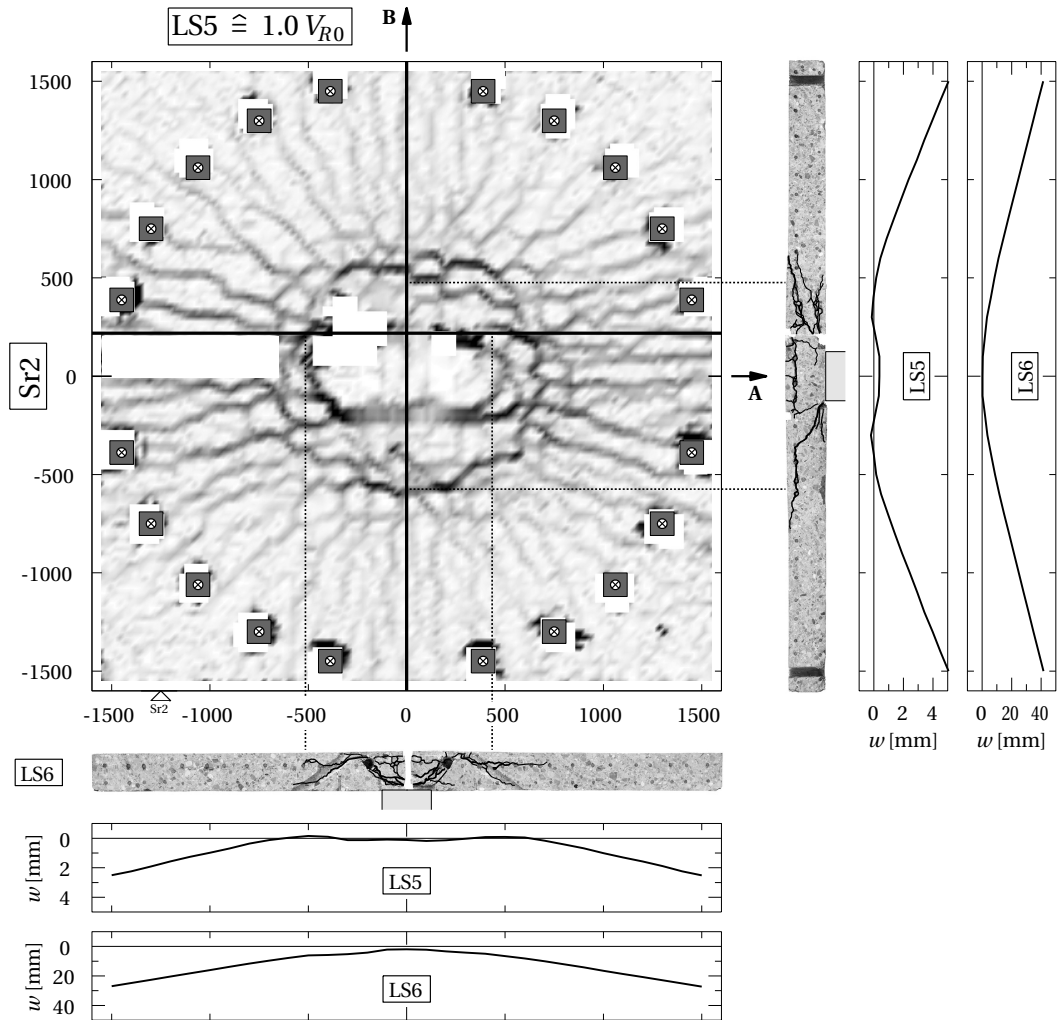


Figure 3.30: Crack pattern of Sr2 at LS5, saw-cuts after failure, and corresponding ICS deflections at LS5 and LS6. All dimensions in [mm]

Influence of slab thickness

The interaction between the presented punching shear-strengthening system and the concrete slab was investigated for three different slab thicknesses in a range of 187 to 325 mm. The summary of the failure loads in Figure 3.26 confirms a significant increase of punching resistance for all slabs. Nevertheless an influence of the slab thickness is visible, as the increase was lowest for the thickest slab Sr3 and highest for the thinnest slab Sr2. Thicker slabs tend toward a relatively earlier punching failure due to a reduced deformability with increasing slab thickness, which limits the possibility of increasing the strap forces during loading since they require slab deformations to become further activated before failure. At LS6, the strap forces of Sr1 and Sr2 increased by 16%, while those of the thick slab Sr3 increased by only 11%, as indicated by the black circles plotted in Figure 3.25. Another effect influencing resistance is the variation of strap prestressing relative to slab thickness; the thin slab Sr2 had a higher strengthening level in relation to slab thickness than the thick slab Sr3 for identical initial prestressing forces of ca. 200 kN.

The square symbols in Figure 3.25 denote the theoretical punching resistance of the non-strengthened slabs. Different slab thicknesses were not fully compensated by the normalization of the ordinate, contrary to the concrete cylinder strength and the equivalent shear stress for the slabs with 260-mm thickness. The squares were thus not located at the same ordinate value because of the disproportionate influence of the effective depth on plate stiffness and bending resistance.

3.2.5 Conclusions

An experimental study of full-scale reinforced concrete slabs strengthened against punching shear with non-laminated prestressed carbon fiber-reinforced polymer (CFRP) straps was carried out. The adhesive connections of the earlier system were replaced by an external steel compression frame between the strap anchors underneath the slab. The effects of different slab thicknesses, preloading of the non-strengthened slabs, varying prestressing forces and strap sizes on the punching shear behavior were investigated. The following conclusions were drawn:

- Preloading of the non-strengthened slabs caused residual slab rotations after full unloading which reduced the punching shear resistance. The prestressing eliminated the residual slab rotations however and closed the residual cracks and thus increased the punching shear resistance compared to the preloaded slab.
- The applied prestressing force influenced the load–rotation behavior and strap activation. The strap force increments were lower in the cases with higher slab prestressing.
- The effect of axial strap stiffness on the load–rotation behavior of the slabs was marginal. However, the strap force increments were higher in cases with higher strap stiffness. The

strap activation was further increased by the steel frame, which hindered the movement of the anchors towards the column.

- The deformability of the steel frame allowed a balancing of the strap forces in both directions compared to the system with adhesively-bonded anchors.
- The friction bond between the steel anchors and the concrete surface unloaded the concrete compression zone but additionally loaded the steel frame in compression. The system stiffness was thus increased and the rotation capacity was reduced compared to the case with bonded anchors and without steel frame.
- The thickest slab exhibited a reduced rotation capacity, and thus strap activation. Therefore the slab failed at the lowest load, which however was still 67% above the theoretical resistance of the non-strengthened slab.
- The location of the strap anchoring points seemed to determine the angle of the punching shear cone.
- The punching shear resistance of both strengthening systems – the former with adhesively-bonded anchors and the new system with steel frame – was similar.

4 Effect of shear on load–deformation behavior

Reference detail

Robert Koppitz, Albin Kenel and Thomas Keller. “Effect of punching shear on load–deformation behavior of flat slabs”. *Engineering Structures*, 2014, Vol. 80, pp. 444–457. DOI: 10.1016/j.engstruct.2014.09.023

Abstract

Punching shear resistance usually constitutes the decisive design criterion for reinforced concrete flat slabs supported by columns. Modeling approaches based on Kinnunen and Nylander’s rotation-symmetric sector model, such as the Quadrilinear Sector Model (QSM), allow the prediction of the slab’s load–rotation behavior. To take into account an orthogonal reinforcement layout, the steel Young’s Modulus is usually reduced. A mechanically better justified flexural stiffness reduction factor is derived here which depends on the longitudinal reinforcement and modular ratio. The QSM also neglects shear deformations, which may reduce the flexural capacity. A Modified Sector Model (MSM) is derived which considers the influence of shear on the flexural behavior. A strength reduction factor for the shear crack-crossing longitudinal reinforcement is introduced which depends on the mechanical longitudinal reinforcement ratio. The factor takes into account that the longitudinal reinforcement also has to transmit forces resulting from shear. The MSM can also be applied to predict the load–rotation responses and punching shear resistances of flat slabs strengthened with prestressed carbon fiber-reinforced polymer (CFRP) straps.

4.1 Introduction

Reinforced concrete (RC) flat slabs supported by columns are widely used in structural engineering as they are easy to build, therefore cost-efficient, and provide greater architectonic flexibility compared to joist constructions. Effective slab design has to ensure flexural capacity

by providing adequate longitudinal reinforcement and sufficient punching resistance to bear the local concentration of shear loads in the column vicinity, e.g. via the placing of shear reinforcement. Additionally, the serviceability has to be ensured by e.g. limiting deformations or crack widths. In many cases the punching resistance is the decisive design criterion, in particular for elevated bending reinforcement ratios. However, mutual interaction between both failure mechanisms has been observed. The punching shear resistance is therefore described as a function of the bending resistance (Reimann 1963; Gesund and Kaushik 1970; Ingvarsson 1977; Nölting 1984) or as a moment–shear interaction relationship (Moe 1961; Hanson and Hanson 1968; Stamenković and Chapman 1972; Siao 1994).

The sector model, first introduced by Kinnunen and Nylander (1960) and later adopted e.g. by Shehata (Shehata 1985, 1990; Shehata and Regan 1989), Gomes (Gomes 1991; Gomes and Regan 1999a,b), or Muttoni (2008) [when deriving his Critical Shear Crack Theory, CSCT], applies the plasticity theory to rotation-symmetric rigid slab segments rotating around the edge of a central column, see Figure 4.1(a). The model assumes rotation-symmetric reinforcement and establishes moment equilibrium on the slab segment. In the case of orthogonal reinforcement, the flexural stiffness is reduced since the directions of the principal moments may deviate from the rebar directions and a reduction of the torsional to the flexural stiffness ratio of the slab occurs due to concrete cracking (Muttoni 2008; Lips 2012). This stiffness reduction is taken into account by limiting the reinforcing steel's Young's modulus, E_s , by a reduction factor, β_E , for which numerous values are suggested (Muttoni 2003, 2008; Guandalini 2005; Villiger 2009; Lips 2012).

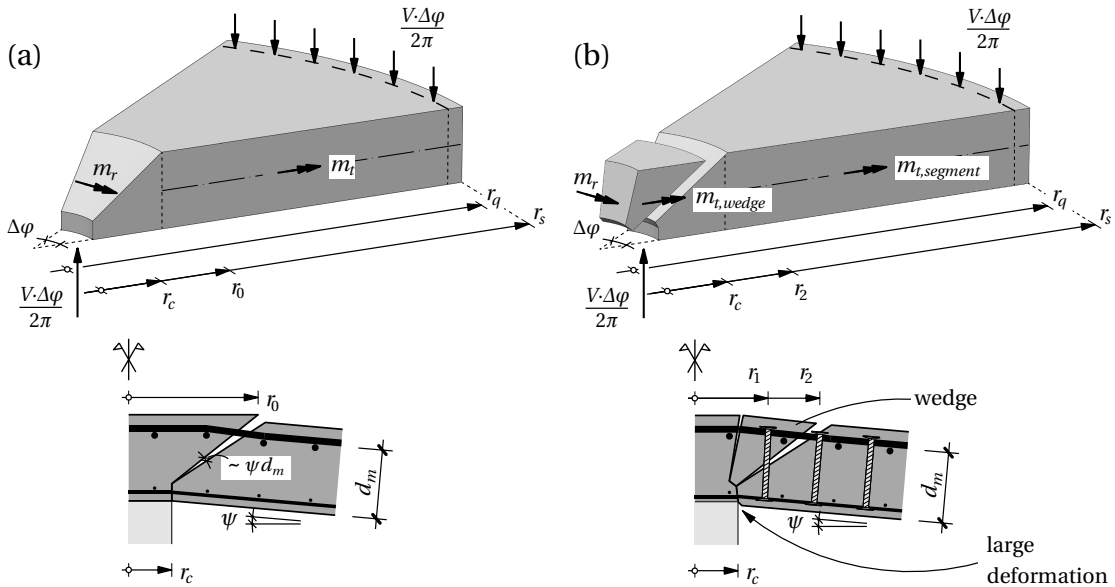


Figure 4.1: (a): Sector model with rigid outer slab segment and acting forces (Muttoni 2008), (b) with additional wedge in shear-critical region (Lips 2012)

Recently, Lips' (2012) experiments on square slabs with high shear reinforcement ratios showed a less stiff slab behavior and reduced flexural capacity compared to predictions by the CSCT.

On the other hand, Guandalini's (2005) slabs, without shear reinforcement, did not exhibit any reduction of flexural capacity for cases with minimum longitudinal reinforcement. Slabs with higher longitudinal reinforcement ratios, however, failed in punching at loads and deformations much lower than at flexural failure. According to Lips (2012), the reduced flexural stiffness and capacity were a consequence of large shear deformations in the column vicinity. Since the influence of shear forces on deformation behavior is neglected in the original sector model, he proposed an iterative model for slabs with shear reinforcement considering a shear-critical region next to the column by adding a wedge [Figure 4.1(b)] and limiting the radial curvatures inside the latter. The reducing effect of shear on the flexural capacity, however, had already been recognized before (Pralong 1982; Brändli 1985). Based on the plasticity theory, a limitation of the bending moments was suggested to take the effect into account, but information on the deformation behavior was not provided since elastic deformations were neglected.

In the following, the rotation-symmetric Quadrilinear Sector Model (Muttoni 2008) is firstly summarized and both effects are discussed: orthogonal reinforcement leading to reduced slab stiffness, and shear effect causing reduced flexural capacity. To take into account the first effect, a reduction factor of the flexural stiffness, β_{EI} , is then derived (instead of a reduction factor of the reinforcement's Young's Modulus as by Muttoni 2008) based on the Linear Compression Field Theory (LCFT) developed by Kupfer (1964). A Modified Sector Model (MSM) is subsequently proposed, in which a strength reduction factor, κ_V , for the longitudinal reinforcement, which crosses the shear crack, is introduced. This factor takes the shear effect into account and depends on the mechanical reinforcement ratio of the longitudinal reinforcement, ω . The MSM is validated using a set of experiments from literature, which was selected to cover an adequate variation of slab geometry, reinforcement ratio and material properties. The new model can also be applied to existing flat slabs that are strengthened against punching failure.

4.2 Existing stiffness reduction approaches

4.2.1 The sector model

In Kinnunen and Nylander's (1960) sector model, the rigid slab segments rotate around the column edges with a rotation angle, ψ . The segments are formed by one tangential shear crack and radial cracks. The assumption of a conical slab shape of the segment outside the shear crack geometrically defines the tangential curvature, thus $\chi_t = \psi/r$ (r = radius from slab center). Subsequently equilibrium conditions can be applied to the segment, depending on the constitutive relationship. Kinnunen and Nylander (1960) assumed a bilinear moment-curvature ($m-\chi$) relationship, as shown in Figure 4.2. According to their sector model, punching failure occurs when the tangential compressive strain of the concrete inside the compression ring around the column reaches an empirically derived ultimate value. The depth of the concrete compression zone at the column edge specifies the root of the tangential shear crack propagating up to the upper slab surface, defining the radius r_0 , see Figure 4.1(a), for which an empirical formula exists for orthogonal reinforcement.

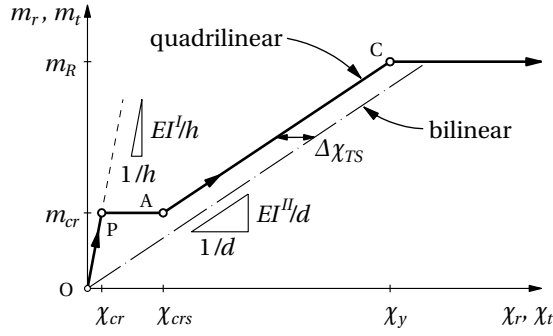


Figure 4.2: Quadrilinear and bilinear moment–curvature relationship (see Section 4.6 and Muttoni 2008)

Muttoni (2008) adopted Kinnunen and Nylander’s sector model and developed the Critical Shear Crack Theory (CSCT) for slabs without shear reinforcement. He assumed a steeper inclination of the critical tangential shear crack by proposing $r_0 = r_c + d_m$, see Figure 4.1(a) (d_m = average effective depth). By further assuming a quadrilinear moment–curvature relationship for the RC section, see Figure 4.2, he derived Eq. 4.1 for the RC slab (operator $\langle x \rangle$ is x for $x \geq 0$ and 0 for $x < 0$).

$$V_{skt}(\psi) = \frac{2\pi}{r_q - r_c} \cdot \left[m_r(\psi) \cdot r_0 + m_R \langle r_y - r_0 \rangle + EI^I \psi \langle \ln(r_{crs}) - \ln(r_y) \rangle + \right. \\ \left. + EI^I \Delta\chi_{TS} \langle r_{crs} - r_y \rangle + m_{cr} \langle r_{cr} - r_{crs} \rangle + EI^I \psi \langle \ln(r_s) - \ln(r_{cr}) \rangle \right] \quad (4.1)$$

where $V_{skt}(\psi)$ = shear force as a function of the slab rotation, m_R = bending resistance, EI^I and EI^I = uncracked and cracked flexural stiffness, $\Delta\chi_{TS}$ = tension stiffening curvature offset, m_{cr} = cracking moment, refer to Figure 4.2. The first term in the square bracket defines the contribution of the radial moment m_r at $r = r_0$ in Figure 4.1(a) with the quadrilinear moment–curvature relationship where the radial curvature is given by $\chi_r = \psi / r_0$. The remaining terms result from the integration of the tangential moments, m_t , along the slab segment using the same moment–curvature relationship. Eq. 4.1 contains three rotation-dependent radii: the radius of the cracked zone, r_{cr} , of the zone in which cracking is stabilized, r_{crs} , and of the yielded zone, r_y . They indicate where points P, A and C in Figure 4.2 are reached, see Section 4.6. When r_y equals the slab radius, r_s , the flexural capacity, V_{flex} , and corresponding bending resistance, m_R , of the total radial and tangential reinforcement are reached:

$$V_{flex} = \frac{2\pi \cdot [m_R r_0 + m_R (r_s - r_0)]}{r_q - r_c} = \frac{2\pi \cdot m_R r_s}{r_q - r_c} \quad (4.2)$$

Muttoni (2003) replaced Kinnunen and Nylander’s failure criterion by one where the punching resistance depends on the width of the critical shear crack, which is proportional to $\psi \cdot d_m$ (Muttoni and Schwartz 1991):

$$V_{Rc}(\psi) = \frac{0.3u_0 d_v \sqrt{f_c}}{0.4 + 0.125\psi d_m k_g} \quad (4.3)$$

where u_0 = control perimeter at $d_v/2$ distance to the support area, d_v = shear-resisting effective depth¹, and $k_g = 48/(d_g + 16 \text{ mm})$ with d_g = maximum aggregate size. The effective punching resistance of the flat slab is defined as the intersection of the load–rotation curve, Eq. 4.1, with the failure criterion of the concrete, Eq. 4.3, and is denoted V_{R0} . Basically, slab rotations of the weak axis have to be considered (Tassinari 2011) to calculate the intersection. Although the rotation-symmetric Quadrilinear Sector Model is based on the average geometrical properties of the two axes, it agrees satisfactorily with experimental results (Fernández Ruiz and Muttoni 2009). For slabs with low reinforcement ratios, the flexural capacity of the slab, according to Eq. 4.2, may be lower than the punching resistance, V_{R0} .

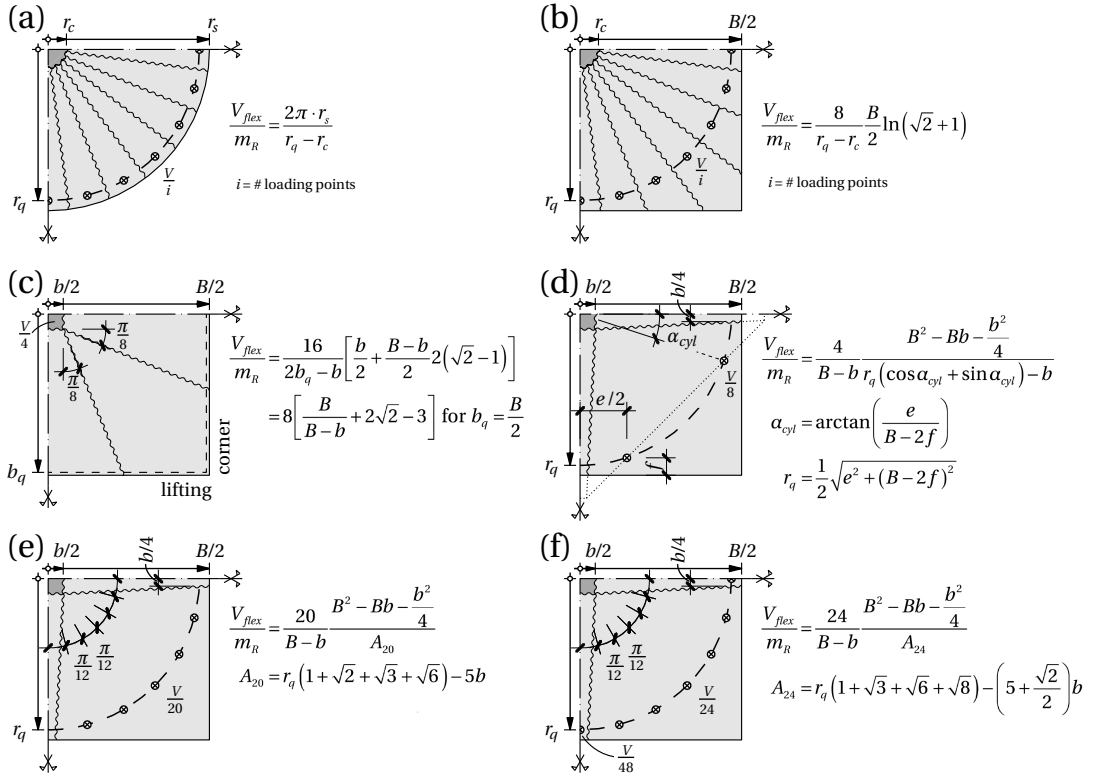


Figure 4.3: Yield-line mechanisms: (a) truncated cone; (b) fan mechanism for round column; (c) centrally loaded edge-supported square column with lifting corners; four-point star mechanisms for (d) eight, (e) 20, (f) 24 load points

The flexural capacity is usually calculated based on the yield-line theory (YLT) developed by Johansen (1943, 1962). According to the upper-bound theorem of plasticity (Gvozdev 1938; Hill 1951, 1952; Drucker et al. 1951, 1952) the yield-line mechanism (YLM) with the smallest applied load has to be found. The YLMs for the different slab, column and loading geometries used in the following sections are summarized in Figure 4.3² and assigned to the slabs in

¹taking into account a possible penetration of the supported area in the slab, see SIA 262 (2013); for the laboratory experiments: $d_v = d_m$

²further yield-line mechanisms are summarized in Appendix C

Tables 4.1 and 4.2, respectively [mechanism Figure 4.3(a) see Guandalini (2005) and earlier Nielsen (1999) for $r_q = r_s$, (b) see Sawczuk and Jaeger (1963) for a single load instead of a column with radius r_c , (c) see Elstner and Hognestad (1956) for the special case $b_q = B/2$, (d) see Guidotti (2010), Figure 4.3(e)–(f) are based on (d) and consider different numbers of loading points].

The resistance of slabs with shear reinforcement is determined either by flexural failure or punching failure. The latter can occur either within the shear-reinforced zone, by crushing of the concrete strut near the column, or outside the shear-reinforced area (Beutel 2003; Fernández Ruiz and Muttoni 2009; Lips 2012). The punching resistance within the shear-reinforced zone, $V_{R,in}$, is obtained by superposing the contribution of the concrete and of the shear reinforcement, which are both rotation-dependent (Fernández Ruiz and Muttoni 2009). The crushing resistance of the concrete strut near the column, $V_{R,crush}$, can be estimated as follows (Fernández Ruiz and Muttoni 2009):

$$V_{R,crush}(\psi) = k_{sys} V_{Rc}(\psi) \quad (4.4)$$

where V_{Rc} from Eq. 4.3 is multiplied by an empirical system factor, k_{sys} (Fernández Ruiz and Muttoni 2009). By default k_{sys} is equal to 2.0 (SIA 262 2013; *fib* 2013) and is increased to 2.5 for stirrups or shear links (Lips 2012), and to 3.0 (Fernández Ruiz and Muttoni 2009) for double-headed studs. Punching failure outside the shear-reinforced area, $V_{R,out}$, is obtained in the same way as for slabs without shear reinforcement, but with the outermost perimeter of shear reinforcement, instead of the column cross section, as support area.

4.2.2 Stiffness reduction by orthogonal reinforcement layout

A difference between orthogonally placed reinforcement and a radial and tangential layout in terms of the flexural stiffness had been experimentally observed by Kinnunen and Nylander (1960). Kinnunen (1963) thus limited the flexural stiffness in his model by introducing a reduction coefficient for the tangential reinforcement. In the Quadrilinear Sector Model β_E reduces the steel Young's modulus and therefore also the flexural stiffness in the cracked elastic state. Muttoni (2003) proposed an empirical value of $\beta_E = 0.4$, and increased it to 0.6 in 2008. Guandalini (Guandalini 2005; Guidotti 2010) developed an analytical formula based on the axial stiffness of a beam with reinforcement placed parallel or at an angle of 45° to the applied axial tensile force and obtained β_E as being approximately 0.7.

Villiger (2009) used an alternate approach to quantify β_E by investigating an RC panel of unit length that was axially loaded in tension by $\sigma_1 = 1$ in the principal direction 1 only, see Figure 4.4(a). For this purpose he applied the linear compression field theory (LCFT) developed by Kupfer (1964) (see also summary by Kaufmann 1998). Villiger calculated the principal strain, ε_1 , using the virtual work principle by applying the equilibrium conditions and Baumann's (1972) solution for the compatibility condition that connects the crack inclination, θ_r (= direction of compression field), with the principal direction 1. The result was Eq. 4.5

which denotes the directional axial stiffness reduction factor, $\beta_{E\varphi}$, depending on the direction of the applied force, φ :

$$\beta_{E\varphi} = \frac{\sigma_1}{\rho E_s \varepsilon_1} = \left[\sqrt[3]{\cos^4 \varphi} + \sqrt[3]{\frac{\rho_x}{\rho_y} \sin^4 \varphi} \right]^{-3} \quad (4.5)$$

where ρ_x, ρ_y = geometrical reinforcement ratios in x -, y -direction. Eq. 4.5 is plotted in Figure 4.4(b) for different reinforcement ratios. In the perpendicular direction ($\varphi = \pi/2$) a reduction factor of ρ_y/ρ_x results, in between the stiffness decreases. The reduction factor β_E is defined as the average of the directional axial reduction factor, $\beta_{E\varphi}$, integrated over φ between $0 \leq \varphi \leq \pi/2$. For isotropic reinforcement ($\rho_x = \rho_y$) β_E is equal to 0.66.

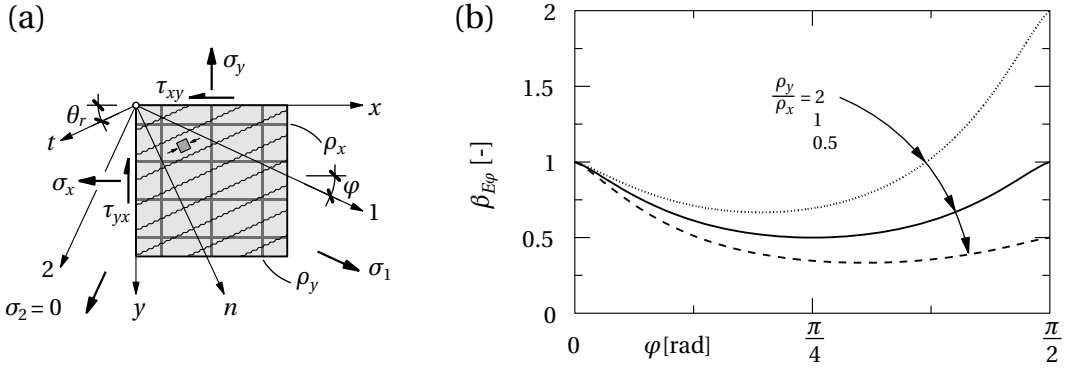


Figure 4.4: (a) Notation of uniaxially loaded panel according to Kupfer (1964), (b) directional axial reduction factor $\beta_{E\varphi}$ for different reinforcement ratios (adapted from Villiger 2009)

Lips (2012) adjusted β_E to the results of numerical calculations regarding flexural stiffness. He investigated square and circular slabs with orthogonal reinforcement using a nonlinear finite element analysis (NLFEA) and stated that the stiffness distribution in the slab depends mainly on the type of YLM. The comparisons between the Quadrilinear Sector Model and the NLFEA resulted in a fitted value of $\beta_E = 0.75$ for the square slabs and 0.65 for the circular case. The latter value corresponds well to that given by Villiger (2009).

4.2.3 Effect of shear on flexural capacity

Lips (Lips 2012; Lips et al. 2012) investigated RC flat slabs with double-headed shear studs or vertical stirrups around the column. He experimentally observed a less stiff slab behavior and reduced flexural capacity compared to the theoretical calculations using the Quadrilinear Sector Model, Eq. 4.1. He attributed the observations to large shear deformations in the column vicinity which he determined from measured vertical displacements at the bottom side of the slab next to the column face. Thus, he concluded that calculation models neglecting the influence of the shear forces on the flexural behavior inevitably produce predictions that may overestimate the slab stiffness and flexural capacity. In the back calculation with a NLFEA

he reduced the longitudinal reinforcement ratio by the measured ultimate load divided by the calculated flexural capacity and obtained good agreement with the test results. In order to develop an analytical model, Lips readopted the former suggestion by Shehata (Shehata 1985, 1990; Shehata and Regan 1989) and Gomes (Gomes 1991; Gomes and Regan 1999a,b) of inserting a wedge between the existing column and the outer segment, separated by a circumferential crack at the column edge and by the inclined shear crack, see Figure 4.1(b). Inside the wedge the transverse force of the shear reinforcement at r_1 required a radially decreasing moment to fulfill equilibrium. Thus, he limited the admissible radial curvature at r_2 , to prevent an exceeding of the yielding curvature at r_1 for the same applied load. With his analytical model he obtained a similar reduction of stiffness and flexural capacity as that obtained from the NLFEA back calculation.

Another investigation of the shear-induced reduction of the flexural capacity resulted in the proposal of the “rond-point” model by Pralong (1982) for interior columns [Figure 4.5(a)], and its extension by Brändli (1985) for edge and corner columns. Normal forces and tangential bending moments, replaced by a force couple, are assigned to top and bottom plates acting in tension (steel) and compression (concrete). A group of radially arranged and equally distributed beams (shear wall elements, see also Marti 1990) bear the radial bending moments and the shear forces which are assigned to a uniform diagonal compression field in the core, Figure 4.5(b). In the estimation of the punching resistance the radial bending resistance is restricted, since the radial forces resulting from shear have to be borne by the same reinforcement. Between r_c and $r_0 = r_c + z \cot \theta_r$ a full plasticization of the tangential reinforcement is assumed. The crack inclination θ_r depends on the quotient of the longitudinal and transversal reinforcement ratio. A straightforward solution for the punching resistance including a limitation of the flexural capacity due to shear was thus found.

4.3 Consideration of shear in sector model

4.3.1 Flexural stiffness reduction factor

Based on Villiger’s (2009) approach, a reduction factor for the flexural stiffness, β_{EI} , is directly determined. With the assumption that $\rho_m = \rho_x = \rho_y$ and $d = d_x = d_y$, the parameters ρ_m , d , n , and $\beta_{E\varphi}$ from Eq. 4.5 can be inserted in Eqs. 4.22 and 4.23, resulting in a flexural stiffness $EI^I = f(\varphi)$. By expressing the ratio of the flexural stiffness in principal direction 1 to that in x -direction, a directional flexural stiffness reduction factor, $\beta_{EI\varphi}$, results which is plotted in Figure 4.6(a). Unlike $\beta_{E\varphi}$ in Figure 4.4(b), $\beta_{EI\varphi}$ depends on the reinforcement and the modular ratio. For isotropic reinforcement with identical effective depths the solid and dotted curves exhibit a lower stiffness reduction for higher reinforcement ratios ($\rho_m = 1.5\%$ vs. 0.25%), as well as for higher modular ratios ($n = 18$ vs. 6), which is even more pronounced for higher ρ .

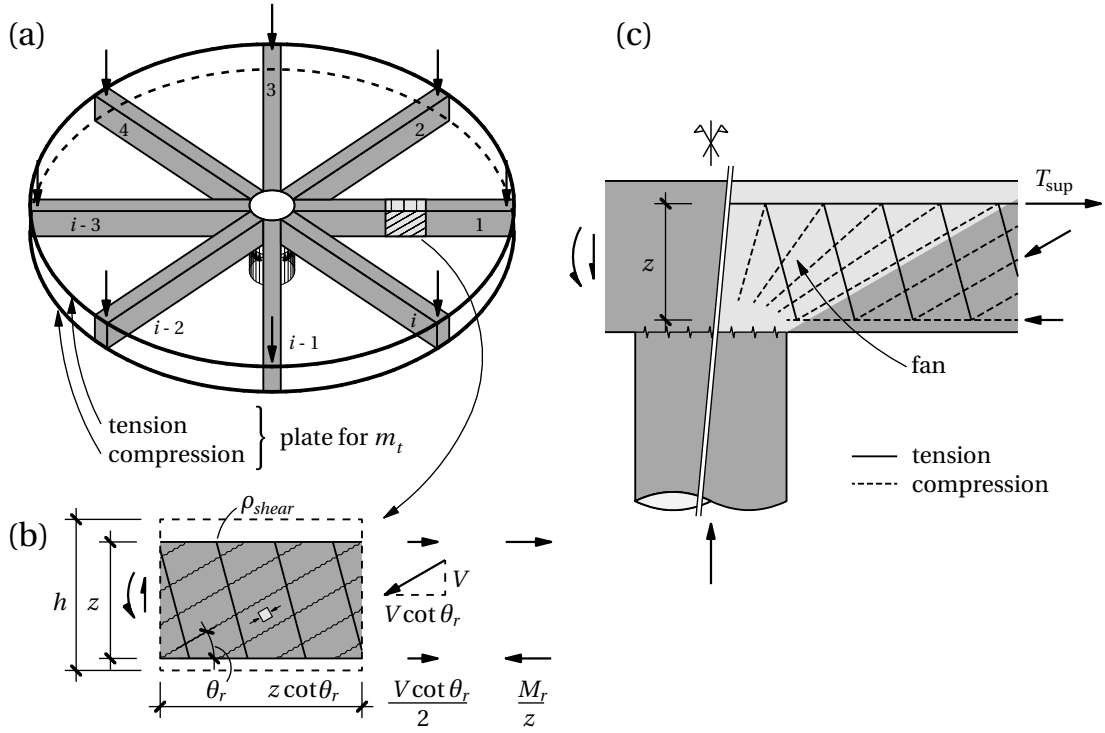


Figure 4.5: (a) "Rond-point" model by Pralong (1982), (b) parallel compression field for beam, (c) fan at column (adapted from Marti 1990)

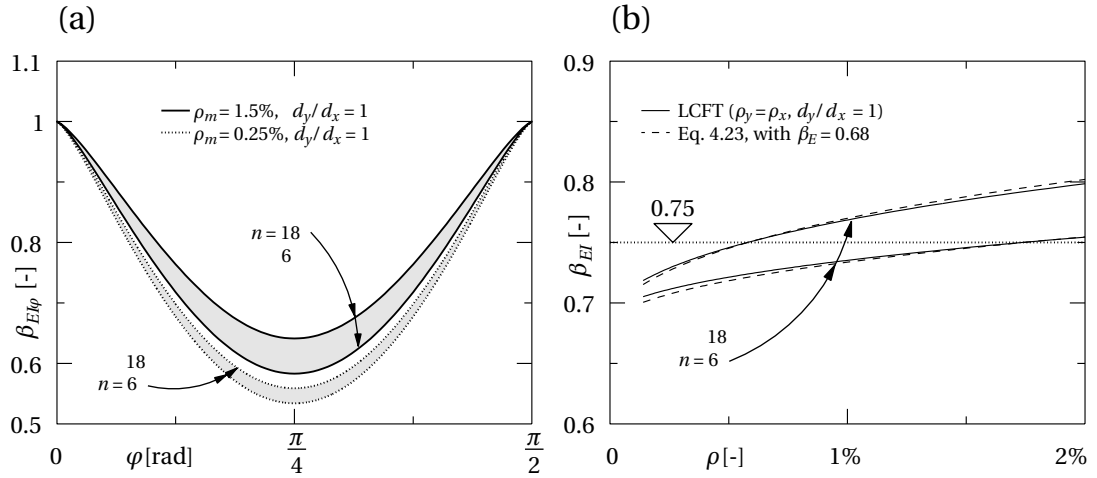


Figure 4.6: (a) Directional flexural stiffness reduction factor $\beta_{EI\varphi}$ for different reinforcement and modular ratios, (b) comparison of reduction factors β_{EI} derived according to LCFT (Kupfer 1964) (solid curves) and for orientation independency with $\beta_E = 0.68$ (dashed curves)

Likewise for β_E an average value of the flexural stiffness reduction factor, β_{EI} , is calculated via integration over φ and shown in Figure 4.6(b)³ for isotropic reinforcement. The curves increase slightly for increasing ρ and n . For ordinary reinforcement ratios around columns of flat slabs, $\rho = 0.5\% - 2\%$, the factor can be approximated to $\beta_{EI} = 0.75$ (horizontal line). The two β_{EI} -curves according to the LCFT are compared to curves with rotation-independent properties based on Eqs. 4.22–4.23 and plotting $\beta_{EI} = EI^I(\beta_E) / EI^I(\beta_E = 1)$. By selecting $\beta_E = 0.68$ almost identical curves result. Thus, a β_E -factor of approximately 0.7 (as suggested by Guandalini 2005 for instance) corresponds to a β_{EI} -factor of ca. 0.75. The direct determination of the reduction factor β_{EI} on the basis of the LCFT provides a mechanical justification of the approach used in the sector model. Hitherto factor β_E has been – except by Guandalini – calibrated to experimental or numerical results to indirectly reduce the cracked flexural stiffness, EI^I , by limiting E_s . However, for other slab and load geometries both values β_E and β_{EI} may differ and have to be verified again using the experimental load–rotation curves, see Lips (2012).

4.3.2 Modified Sector Model

The load transfer in Pralong’s (1982) “rond-point” model assumes a plastic redistribution of the stresses without restricting deformations. With regard to punching the deformation capacity of the slab is limited however. The punching resistance of concrete slabs decreases with increasing deformations, which is not taken into account in Pralong’s model. The sector model concentrates the rotation in one tangential shear crack in the column vicinity and allows prediction of load–deformation behavior from zero up to the ultimate resistance. Lips’ (2012) extension of the sector model with the consideration of the shear influence by adding a wedge and limiting radial curvatures at the crack radius resulted in a rather complex calculation method which included several geometrically fixed factors and fitting coefficients.

An alternative approach – a Modified Sector Model (MSM) – is proposed here which implements the core element of the “rond-point” model into the Quadrilinear Sector Model (QSM), i.e. the fact that the longitudinal reinforcement also has to bear the radial forces resulting from shear.

According to the truss model approach for beams (refer to Pralong 1982; Brändli 1985; Marti 1990), the tensile force of the radial longitudinal reinforcement, T_{sup} , is composed of the upper component of the bending couple, m_r/z , and the shear induced tensile force of $v_r \cot \theta_r / 2$, which is half of the horizontal component of the diagonal concrete compression force, see Figure 4.5(b). T_{sup} is limited by the tensile resistance of the reinforcement (per unit width):

$$T_{\text{sup}}(\psi) = \frac{m_r(\psi)}{z} + \frac{v_r(\psi) \cdot \cot \theta_r}{2} \leq f_{sy} \rho d \quad (4.6)$$

where z = lever arm of internal forces, f_{sy} = yield strength of reinforcing steel.

³Appendix D provides an additional diagram displaying β_{EI} evaluated considering compressive reinforcement

The normalized bending resistance has thus to be reduced by the shear component, e.g. as proposed in Eq. 4.7, in which this reduction comprises a strength reduction factor, κ_V , and a linear function proportional to the ratio of the applied load to the flexural capacity, as follows:

$$\frac{m_r(\psi)/z}{f_{sy}\rho d} = 1 - \kappa_V \frac{V(\psi)}{V_{flex}} \quad (4.7)$$

The strength reduction factor, κ_V , depends on the inclination of the compression field (or shear crack) in the slab core: e.g. a steeper inclination reduces the horizontal component of the shear force that has to be borne by the reinforcement and the concrete. However, the load is transferred from the slab to the column by developing a fan in the column region, which makes it difficult to determine one specific inclination angle, θ_r , see Figure 4.5(c). A trend of decreased crack inclination with increasing reinforcement ratio was observed by Guandalini et al. (2009). Georgopoulos (1987) proposed a hyperbolical formula for $\tan \theta_r$ depending on the mechanical reinforcement ratio, ω . However, in comparing measured crack inclinations, as e.g. reported by Lips (2012); Guandalini (2005); Guidotti (2010), with Georgopoulos' prediction a considerable scatter is observed. The read-out of the crack inclination from saw-cuts provides a margin of discretion and the punching cone varies along the entire column perimeter.

As the determination and verification of crack inclinations remain uncertain, a direct dependence of κ_V on ω is therefore assumed as follows:

$$0 \leq \kappa_V = \frac{\omega - \omega_{\min}}{\omega_{\max}} \leq 1 \quad (4.8)$$

The minimum reinforcement ratio, ω_{\min} , is derived from the bending resistance, Eq. 4.25, which is set equal to the cracking moment, Eq. 4.21 and thus results in

$$\omega_{\min} = 1 - \sqrt{1 - \left(\frac{h}{d_m}\right)^2 \cdot \frac{f_{ct}}{3f_c}} \quad (4.9)$$

Typical values vary from 0.015 to 0.03, e.g. $\omega_{\min} = 0.02$ results for $d_m/h = 0.9$ and $f_{ct}/f_c = 0.1$. The second boundary for κ_V , the maximum value, ω_{\max} , is obtained at the maximum bending resistance, according Eq. 4.10, which results from Eq. 4.25 by assuming a rectangular stress block for concrete with a depth $x_c = \omega d_m = 0.85x$ according to SIA 262 (2013), where x is the depth of the compression zone which is exactly half of the effective depth at the maximum bending resistance.

$$\omega_{\max} = \frac{0.85 \cdot 0.5 d_m}{d_m} = 0.425 \quad (4.10)$$

The right-hand side of Eq. 4.7 can be applied to the radial moment acting at $r = r_0$ and after a

few transformations (refer to Section 4.7) Eq. 4.20 is modified to Eq. 4.11:

$$V_{mod}(\psi) = \frac{1}{1 + \kappa_V \frac{m_r(\psi)}{m_R} \frac{r_0}{r_s}} \cdot V_{skt}(\psi) \quad (4.11)$$

The MSM shear force, V_{mod} , is thus equal to V_{skt} (according to Eq. 4.1) multiplied by a rotation-dependent reduction factor (which includes the κ_V reduction factor, with m_r calculated at $r = r_0$), which is valid for any moment–curvature relationship, such as a quadrilinear or bilinear one (see Figure 4.2).

4.3.3 Experimental validation

The Modified Sector Model, Eq. 4.11, was validated through comparisons with experimentally obtained load–rotation curves from literature. In the selection, an adequate variation of slab geometry, reinforcement ratio and material properties was considered; the properties of eight selected specimens are summarized in Table 4.1⁴. To verify the dependence of the strength reduction factor, κ_V , on the mechanical longitudinal reinforcement ratio, ω , the ratio was varied from 0.07 (minimum reinforcement) to 0.29 (high ratio). Figure 4.7 compares the experimental load–rotation responses (solid curves) with the Quadrilinear Sector Model (QSM, dotted curves), Eq. 4.1, and the Modified Sector Model (MSM) using Eq. 4.11 (dashed curve). The curves were normalized according to Muttoni (2008). On the ordinate the equivalent shear stress, $V/(u_0 d_v)$, was divided by $\sqrt{f_c}$, which was assumed as being proportional to the concrete shear strength. On the abscissa, the product $\psi d_m k_g$ was plotted. The transition points where plasticizing of the slab segment begins ($r_y = r_0$) are marked by triangles. Solid circles denote the rotation at which the flexural capacity is reached ($r_y = r_s$). Guandalini (curves PG7 and PG10, refer to Guandalini 2005; Guandalini et al. 2009) and Lips (curves PL3, PL7 and PF4, refer to Lips 2012; Lips et al. 2012) measured the slab rotation of the weak axis directly using inclinometers, which were installed near the applied load and these values were directly used. The slab rotation in the specimen of Heinzmann et al. (2012) (curve SP2, refer also to Etter et al. 2009) was obtained by calculating the secant rotation from four (near the weak axis) deflection measuring points, located at 1.7 m from the slab center, and from another two inductive transducers measuring the support deformation. In Elstner and Hognestad (1956) (curves A7b and B12) the deflections were recorded at the square column that centrally loaded the edge-supported slabs. Hence, a secant rotation was also calculated by assuming zero deflection of the edges.

For all specimens a better agreement between the MSM and the experimental results is obtained than between the QSM and the experiments. In the uncracked state both model curves are identical, immediately after cracking of the slab the rotations are slightly overestimated by the models. Only in PG7 was the behavior in the uncracked state already much softer than calculated. The MSM curve slope in the cracked elastic state is steeper than the measurements,

⁴in Appendix E, Section E.1, further experimental results (total 72) are compared to the MSM prediction

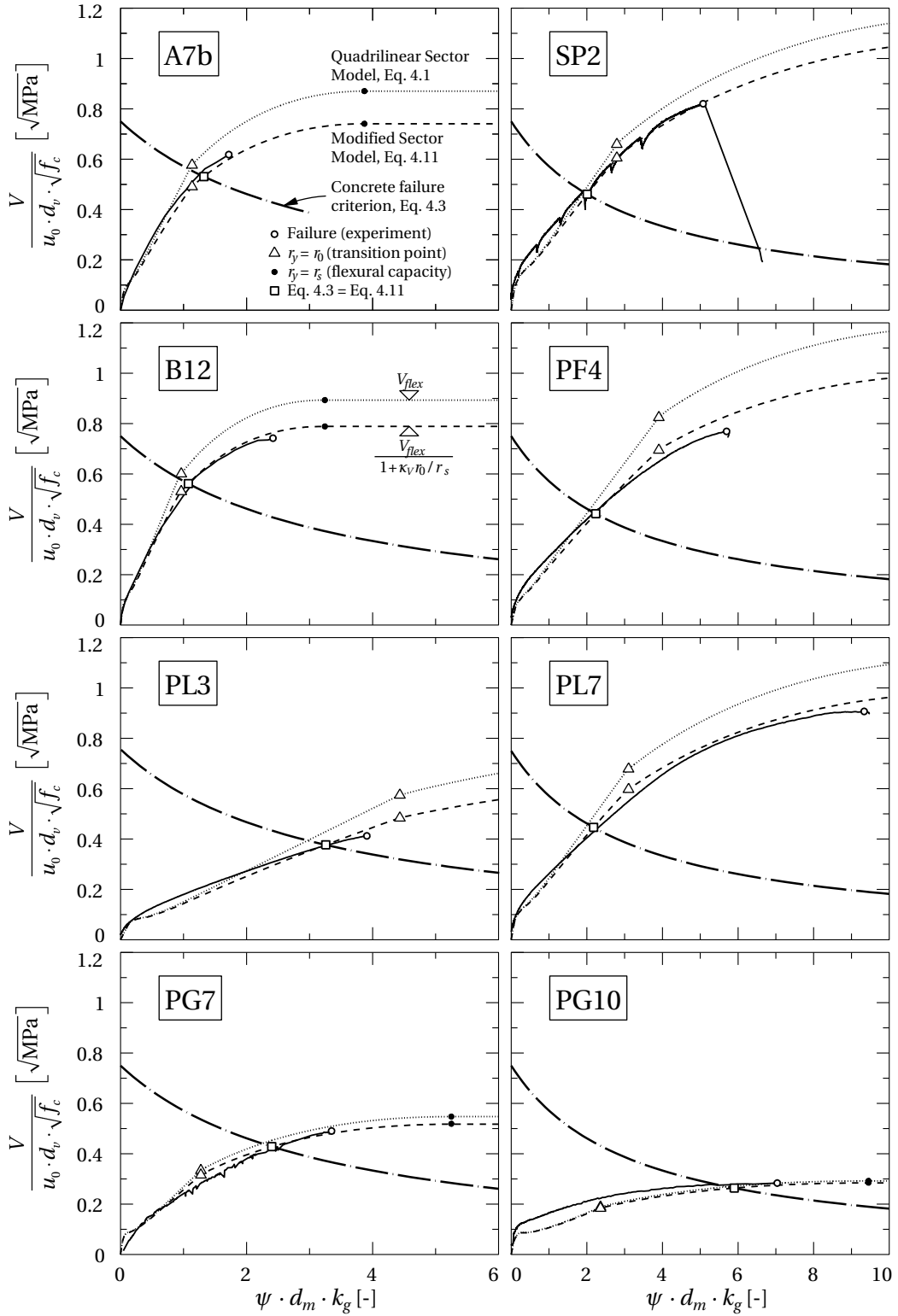


Figure 4.7: Comparison of model and experimental load–rotation curves for eight specimens (properties in Table 4.1) with concrete failure criterion according to Eq. 4.3. Slabs SP2, B12, PF4 and PL7 contain shear reinforcement

except for A7b where it is approximately the same because the crack inclination is fixed to one specific value of ca. 45° (Muttoni 2008) by the radius of the critical shear crack, which is generally steeper than actual values from slabs without shear reinforcement (Kinnunen and Nylander 1960; Hallgren 1996; Guandalini et al. 2009). A higher r_0 results in a softer slab response below the transition point where plasticizing begins. The QSM overestimates the flexural capacity of the slab and the curves are too stiff compared to the experiments, except for PG7 and PG10 where they reproduce the load–rotation behavior well. In fact, these two specimens have low mechanical reinforcement ratios and thus small reduction factors, κ_V , see Table 4.1. The rotation-dependent reduction factor in Eq. 4.11 reaches its maximum as soon as the radial moment at r_0 equals the bending resistance, m_R (triangles in Figure 4.7). From that point onwards, applying the reduction factor shifts the QSM curves vertically down to the MSM curves, and thus the rotation at which the flexural capacity is reached is identical. Consequently the stiffness overestimation of the QSM curves is a result of the overestimation of the flexural capacity. The concrete failure criterion of Eq. 4.3 is also drawn in Figure 4.7 and its intersection with the MSM (squares) denotes the theoretical punching resistance of the four slabs A7b, PL3, PG7 and PG10. All squares are close to the experimental values (circles). The other four slabs contain shear reinforcement whose additional resistance is not shown. A further validation of the MSM in cases of strengthening of existing flat slabs is presented in the next section.

4.4 Slab strengthening using prestressed CFRP straps

4.4.1 Strengthening concept

A strengthening method for existing flat slabs consisting of non-laminated and prestressed carbon fiber-reinforced polymer (CFRP) straps (Meier and Winistörfer 1998; Lees and Winistörfer 2011) installed crosswise around the column was presented in Chapter 3. The four straps are installed in pre-drilled and pre-cut openings and are anchored and prestressed from the bottom side of the slab. Two different anchor systems are available: the first system (slabs So1–4) consists of eight steel anchors adhesively bonded to the concrete surface using an epoxy resin [Figure 4.8(a)], while in the second system (slabs Sr1–3) the anchors are fixed to a steel compression frame mounted underneath the slab around the column, thus unloading the concrete compression zone, see Figure 4.8(b) and (c). The method was experimentally validated in Chapter 3, the experimental set-up is given in Figure 4.8(d), and the slab and strap properties are summarized in Table 4.2 and Table 4.3, respectively. The prestressing forces were measured using small force washers placed below the anchor nuts at the deviation pins located at the strap ends [as displayed in Figure 3.18(f)].

4.4.2 Application of Modified Sector Model

The prestressed straps increase the bending resistance, m_R^+ , and thus also the flexural capacity, V_{flex}^+ , of the strengthened slab. As the YLMs in Figure 4.3(e) and (f) for 20 and 24 loading

Table 4.1: Properties of specimens from literature with decisive YLMs and reduction factor κ_V from Eq. 4.8

| Reference | Slab | B | b | h | d_m | ρ_m | r_q | d_g | f_c | f_{ct} | E_c | f_{sy} | E_s | YLM | $\frac{V_{flex}}{m_R}$ | ω_m | κ_V |
|------------------------------|------|------|------------------|------|-------|----------|------------------|-------|-------|------------------|-------------------|----------|-------|----------|------------------------|------------|------------|
| | | [mm] | [mm] | [mm] | [mm] | [%] | [mm] | [mm] | [MPa] | [MPa] | [GPa] | [MPa] | [GPa] | Fig. 4.3 | [-] | [-] | [-] |
| Elstner and Hognestad (1956) | A7b | 1829 | 254 | 152 | 114 | 2.48 | 890 ^a | 25 | 27.9 | 2.8 ^b | 30.3 ^b | 321 | 200 | (c) | 8.17 | 0.29 | 0.60 |
| | B12 | 1829 | 254 | 152 | 114 | 3.02 | 890 ^a | 38 | 45.8 | 3.8 ^b | 35.8 ^b | 332 | 200 | (c) | 8.17 | 0.22 | 0.45 |
| Guandalini (2005) | PG7 | 1500 | 130 | 125 | 100 | 0.75 | 752 | 16 | 34.7 | 2.4 ^c | 33.7 | 550 | 205 | (d) | 6.96 | 0.12 | 0.22 |
| | PG10 | 3000 | 260 | 255 | 210 | 0.33 | 1505 | 16 | 28.5 | 2.2 ^c | 29.5 | 577 | 205 | (d) | 6.96 | 0.07 | 0.10 |
| Heinzmann et al. (2012) | SP2 | 4100 | 200 ^a | 350 | 294 | 1.21 | 1962 | 32 | 34.5 | 3.3 ^d | 35.2 | 577 | 209 | (b) | 8.20 | 0.20 | 0.42 |
| Lips (2012) | PL3 | 3000 | 520 | 250 | 197 | 1.60 | 1505 | 16 | 36.5 | 3.3 ^b | 33.2 ^b | 583 | 200 | (d) | 8.14 | 0.25 | 0.54 |
| | PL7 | 3000 | 260 | 250 | 197 | 1.60 | 1505 | 16 | 35.8 | 3.3 ^b | 33.0 ^b | 583 | 200 | (d) | 6.96 | 0.26 | 0.55 |
| | PF4 | 3000 | 340 | 320 | 274 | 1.54 | 1505 | 16 | 32.5 | 3.1 ^b | 31.9 ^b | 562 | 200 | (d) | 7.29 | 0.27 | 0.58 |

^a b_q instead of r_q (A7b, B12); r_c instead of b (SP2)^b values calculated using relationships acc. to SIA 262 (2013): $E_c = 10000 \text{ MPa}^{2/3} \cdot \sqrt[3]{f_c}$, $f_{ct} = 0.3 \text{ MPa}^{1/3} \cdot f_c^{2/3}$ (both in MPa)^c values from direct tension tests on cylinders ($h = 320 \text{ mm}$, $\phi = 160 \text{ mm}$)^d values from double-punch tests on cylinders ($h = \phi = 150 \text{ mm}$) acc. to Chen (1970); Marti (1989)Table 4.2: Properties of own specimens ($r_q = 1500 \text{ mm}$, $d_g = 32 \text{ mm}$,) with decisive YLMs and κ_V from Eq. 4.8

| Reference | Slab | B | b | h | d_m | ρ_m | f_c | f_{ct}^a | E_c | f_{sy} | E_s | YLM | $\frac{V_{flex}}{m_R}$ | ω_m | κ_V |
|-------------|------|------|------|------|-------|----------|-------|------------|-------|----------|-------|----------|------------------------|------------|------------|
| | | [mm] | [mm] | [mm] | [mm] | [%] | [MPa] | [MPa] | [GPa] | [MPa] | [GPa] | Fig. 4.3 | [-] | [-] | [-] |
| Section 3.1 | So1 | 3200 | 250 | 260 | 194 | 1.62 | 39.9 | 3.3 | 33.9 | 514 | 205 | (e) | 7.39 | 0.21 | 0.43 |
| | So2 | 3200 | 250 | 260 | 199 | 1.58 | 40.7 | 3.2 | 33.7 | 514 | 205 | (e) | 7.39 | 0.20 | 0.42 |
| | So3 | 3200 | 250 | 260 | 204 | 1.54 | 40.3 | 3.4 | 33.0 | 514 | 205 | (e) | 7.39 | 0.20 | 0.41 |
| | So4 | 3200 | 250 | 260 | 199 | 1.58 | 40.9 | 3.6 | 34.9 | 514 | 205 | (e) | 7.39 | 0.20 | 0.41 |
| Section 3.2 | Sr1 | 3200 | 250 | 257 | 200 | 1.57 | 48.1 | 3.6 | 41.0 | 517 | 205 | (e) | 7.39 | 0.17 | 0.35 |
| | Sr2 | 3200 | 250 | 187 | 138 | 1.46 | 43.1 | 3.4 | 35.8 | 521 | 205 | (e) | 7.39 | 0.18 | 0.36 |
| | Sr3 | 3200 | 250 | 325 | 264 | 1.44 | 44.2 | 3.4 | 35.1 | 525 | 205 | (f) | 7.24 | 0.17 | 0.36 |

^a values from double-punch tests on cylinders ($h = \phi = 150 \text{ mm}$) and cubes (side length 150 mm) acc. to Chen (1970); Marti (1989)

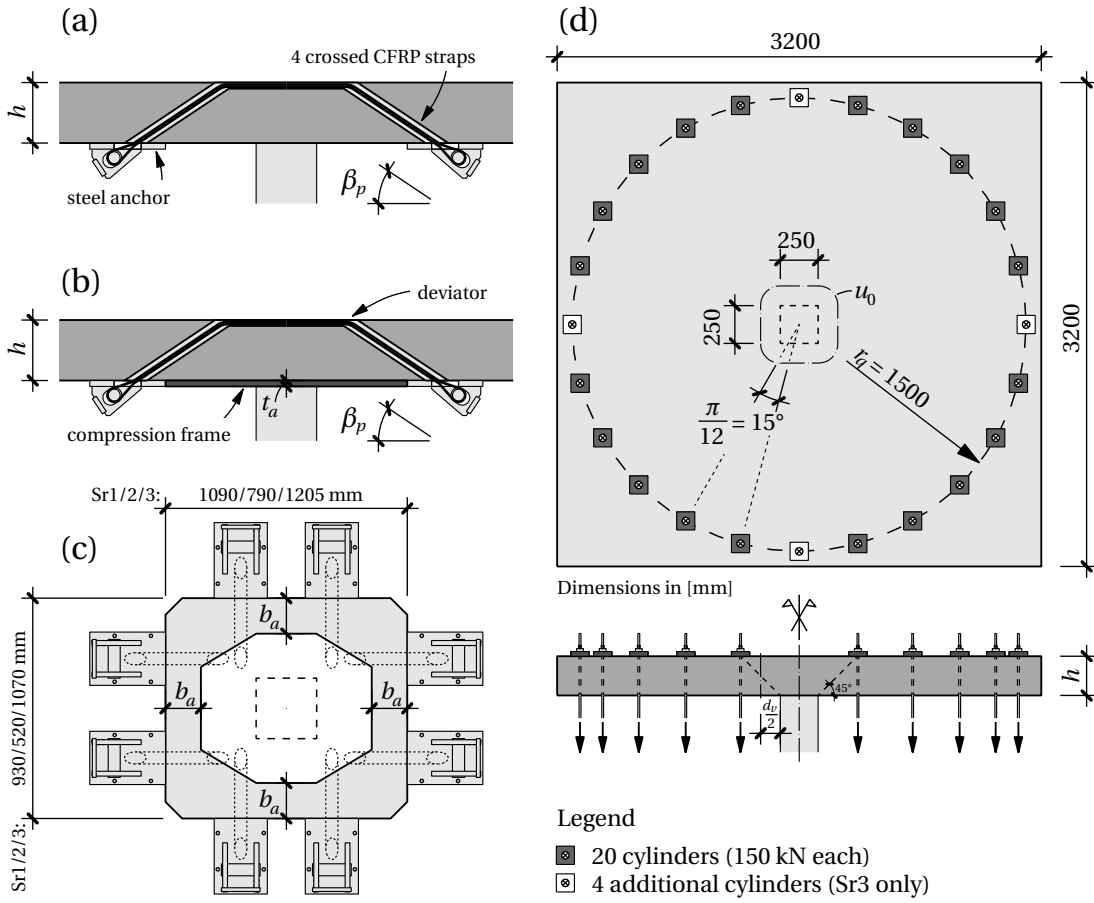


Figure 4.8: Sections of strengthening system: (a) adhesively bonded on bottom surface, (b) attached to steel compression frame, (c) Plan view of strengthening system with steel frame, (d) experimental set-up

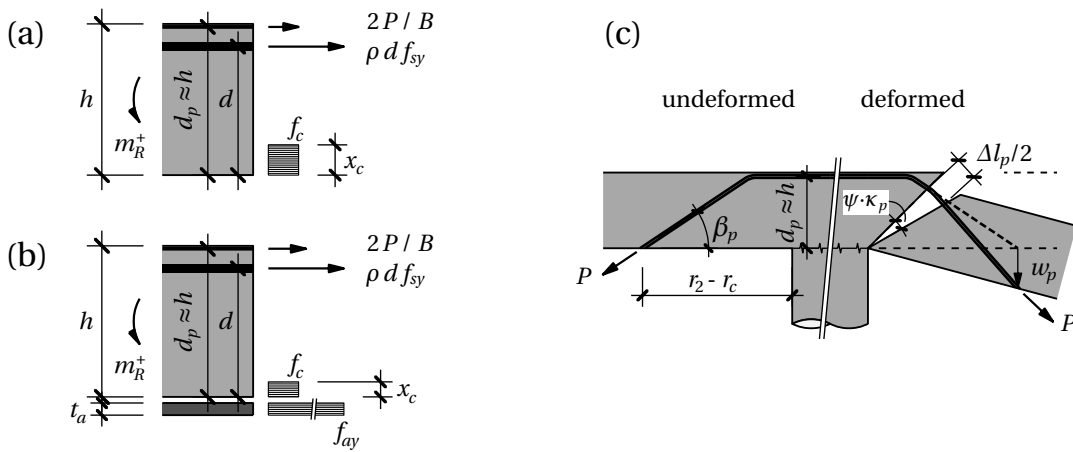


Figure 4.9: Free-body diagrams of strengthened RC slabs for (a) adhesively-bonded anchors and (b) steel frames; (c) concept of strap elongation due to slab deformation

Table 4.3: Properties of CFRP straps, steel frame (steel grade S355)

| Reference | Slab | E_p [GPa] | A_p [mm ²] | l_p [mm] | β_p [°] | P_0 [kN] | P_u [kN] | b_a [mm] | t_a [mm] |
|-------------|------|----------------|-----------------------------|---------------|------------------|---------------|---------------|---------------|---------------|
| Section 3.1 | So1 | 132 | 375 | 1756 | 30 | 318 | 683 | – | – |
| | So2 | 132 | 248 | 1881 | 30 | 220 | 451 | – | – |
| | So3 | 132 | 188 | 1862 | 30 | 225 | 342 | – | – |
| | So4 | 132 | 375 | 1888 | 30 | 102 | 683 | – | – |
| Section 3.2 | Sr1 | 120 | 375 | 1971 | 34 | 203 | 683 | 160 | 20 |
| | Sr2 | 120 | 375 | 1656 | 34 | 199 | 683 | 120 | 25 |
| | Sr3 | 120 | 375 | 2191 | 34 | 208 | 683 | 160 | 20 |

cylinders, respectively, lead to the lowest flexural capacity, yield-lines along the main axes propagate and intersect with the installed four straps at the upper slab surface. The bending resistance of the slab's plastic hinges is provided by the longitudinal reinforcement with a tensile force per unit width, T_s , and the two strap forces per direction. The deviations across the deviators in Figure 4.8(a) are assumed as being frictionless, since friction losses were small, less than 6% (see Section 3.1.4, p. 33). Plasticity theory allows the effect of the strap forces to be smeared over the entire slab width, B , thus the strap force per unit width, T_p , is given by $2P/B$, see Figure 4.9(a)–(b). For the slabs without steel frame the two tensile forces are balanced by concrete compressive stresses, assumed as an equivalent rectangular stress block with compressive strength, f_c . The steel frame is taken into account by assuming full plasticizing when developing the YLM. Thus the compression zone of the concrete is considerably reduced because only the remaining compressive force has to be borne by the concrete. Hence, the lever arm of the internal forces, z , is increased. The resistance of the steel frame [twice the width b_a ; thickness t_a , see Figure 4.8(c)] is also smeared over the entire slab width, B .

The slab rotation leads to an elongation of the strap, Δl_p , which activates it further by a value ΔP , superposing the applied prestressing load P_0 . As the behavior of the strap is linear elastic up to its failure the strap force is

$$P(\psi) = P_0 + \Delta P(\psi) = P_0 + \frac{E_p A_p \Delta l_p(\psi)}{l_p / \xi_p} \leq P_u \quad (4.12)$$

where $E_p A_p$ = axial strap stiffness, l_p = strap length, ξ_p takes into account the compliance of the applied parts (e.g. the steel anchors and pins, prestressing bolts, mortar bed below the deviation points, etc.) and is estimated as 0.9 by comparative calculations using elastic springs. Supposing that the entire strap elongation concentrated in a single crack on the left and right column sides, a consideration of similar triangles [see Figure 4.9(c): deformed slab part with single crack right to the column] leads to the following relationship:

$$\frac{w_p(\psi)}{r_2 - r_c} \approx \frac{\Delta l_p(\psi)}{2h} \approx \psi \cdot \kappa_p \quad (4.13)$$

An empirical reduction factor, κ_p , is introduced to take several effects into account. One effect is the depth of the concrete compression zone that was neglected in Eq. 4.13 and is e.g. $x = h/5$ for $\omega = 0.2$, $d/h = 0.85$ and $x_c/x = 0.85$. The main effect however is that the yield-line mechanism is not fully developed for applied loading below the flexural capacity. Combining Eqs. 4.12 and 4.13 results in a linear dependence of the strap force on the slab rotation:

$$P(\psi) = P_0 + \frac{E_p A_p}{l_p / \xi_p} 2h \kappa_p \psi \leq P_u \quad (4.14)$$

The contribution of the strap to the bending resistance is calculated for the slab rotation at which the reduced flexural capacity of the non-strengthened slab is reached (cf. solid circles in Figure 4.7 where $r_y = r_s$). This particular point in the load–rotation curve is determined by r_s multiplied by χ_y from Figure 4.2, giving Eq. 4.15 for a quadrilinear moment–curvature relationship:

$$\psi_{flex} = r_s \cdot \chi_y = \frac{V_{flex}}{m_R} \frac{r_q - r_c}{2\pi} \left(\frac{m_R}{EI^H(\beta_E)} - \Delta\chi_{TS} \right) \quad (4.15)$$

The resulting modification of the load–rotation curve is shown in Figure 4.10. The marginal increase of flexural stiffness resulting from the CFRP straps is neglected as their benefit is mainly based on the higher ultimate strength compared to steel by a factor of ca. 3.5 and their Young's modulus is only ca. 60% of the steel modulus (Table 3.7). Therefore both the non-strengthened and strengthened curve slopes are modeled as being identical up to the applied load at which the former reaches plasticization of the slab segment. Because of the strap activation, the bending resistance is increased, which likewise increases the flexural capacity from V_{flex} to V_{flex}^+ , thus shifting the load–rotation curve upwards. The increased bending resistance, m_R^+ , is determined according to Eq. 4.16, incorporating a value P_{flex} , which is calculated using Eq. 4.14 in which ψ_{flex} from Eq. 4.15 is inserted.

$$m_R^+ = \underbrace{\rho d f_{sy}}_{T_s} \left(d - \frac{x_c}{2} \right) + \underbrace{\frac{2P_{flex}}{B}}_{T_p} \left(d_p - \frac{x_c}{2} \right) + \underbrace{\frac{2b_a t_a f_{ay}}{B}}_{C_a} \left(\frac{t_a + x_c}{2} \right) \quad (4.16)$$

where $x_c = (T_s + T_p - C_a) / f_c$ and $d_p \approx h$. For slabs without steel compression frame (So1–4) $C_a \equiv 0$. The rotation-dependent shear force of the strengthened slab can be derived by inserting the increased bending resistance, m_R^+ , instead of m_R into Eq. 4.1 and multiplying it by a reduction factor similar to that in Eq. 4.11, finally resulting in the following expression:

$$V_{mod}^+(\psi) = \frac{1}{1 + \kappa_V \frac{m_r(\psi) r_0}{m_R^+ r_s}} \cdot V_{skt}(\psi, m_R^+) \quad (4.17)$$

where the CFRP straps are not considered in the reinforcement ratio since their percentage of the cross-sectional area is negligible compared to the longitudinal reinforcement. Therefore all other factors (ω , κ_V , r_s) remain exactly as in the non-strengthened case.

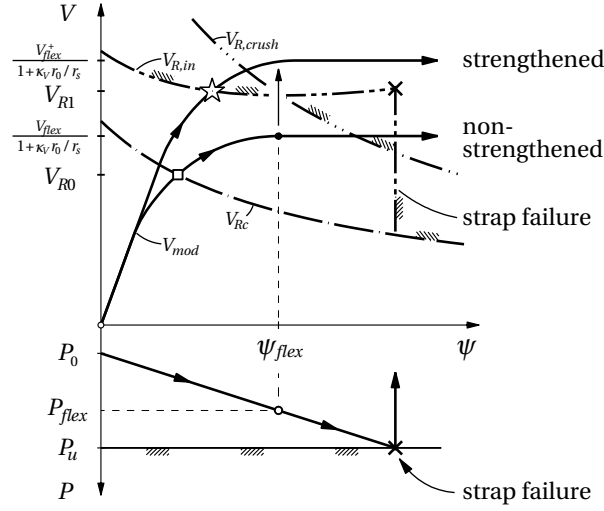


Figure 4.10: Effect of strap activation on flexural capacity and punching resistance

4.4.3 Punching shear resistance

The four CFRP straps shift the failure criterion, Eq. 4.3, upwards by their vertical strap force component $V_{Rp}(\psi) = 8P(\psi) \sin \beta_p$. The failure criterion for punching within the shear-reinforced area, $V_{R,in}$, is thus

$$V_{R,in}(\psi) = V_{Rc}(\psi) + 8P(\psi) \sin \beta_p \quad (4.18)$$

The criterion for the crushing of the compression strut, $V_{R,crush}$, was obtained by adjusting Eq. 4.4 to the experimental punching resistances, from which a system factor of $k_{sys} = 2.5$ was derived. The intersection point of the load–rotation curve, Eq. 4.17, with the lower of the failure criterions, Eqs. 4.4 or 4.18, denotes the punching shear resistance of the strengthened slab, V_{R1} , see Figure 4.10, whereby strap failure would cause an immediate drop of $V_{R,in}$ down to V_{Rc} . Failure outside the shear-reinforced area was not observed in the experimental campaign.

4.4.4 Comparison with experiments

The analytical modeling and experimental load–rotation curves (of the specimens according to Tables 4.2 and 4.3) are compared in Figure 4.11⁵. Also shown are the strap forces (on the lower ordinates), normalized by the ultimate resistance of the largest strap ($P_{u,max} = 683 \text{ kN}$). Generally the linear increase of strap force with increasing slab rotation reproduces the measured results well by selecting $\kappa_p = 0.6$. Slabs So1 and Sr2 had the highest prestressing levels with regard to the slab thickness. Therefore the strap activation was smaller than predicted until the slab exceeded decompression. The agreement could be improved by splitting κ_p into sub-factors in order to take into account more precisely the effects described

⁵in Appendix E, Section E.2, all slabs of the experimental campaign are compared to the MSM

above and, in this case, the dependence on the decompression moment. Nevertheless one constant value for κ_p was maintained since the load–rotation curves of these two and the other slabs still fit well to the experimental results, see below.

The normalized load–rotation curves are drawn on the upper ordinates. The solid experimental curves (maximum rotation of weak axis) are compared to the MSM (dashed curves) with increased average bending resistance, m_R^+ , and to the QSM, also with m_R^+ but without considering the effect of shear on the resistance (dotted curves acc. to Eq. 4.1). The increase of bending resistance (m_R^+/m_R) is also summarized in Table 4.4. Both modeling curves predict a softer behavior for small and medium loads (uncracked and cracked-elastic state up to ca. $0.3\sqrt{\text{MPa}}$ on the y-axis), since no stiffness increase caused by the strengthening system was considered. For instance, local prestressing of the slab around the column was neglected in the analysis. For higher loads, approaching failure, the MSM model and experimental curves correspond well in contrast to the QSM curves, which overestimate the loads significantly (with the exception of slab Sr1).

Figure 4.11 also shows the failure criteria (Eqs. 4.3, 4.4 and 4.18) and the intersection points with the MSM curves (Eq. 4.17), which denote the punching shear resistance predictions, V_{R1} (five-point star symbols). In slabs So1 and Sr2, $V_{R,in}$ is above the diagram frame, its minimum value on the abscissa is 1.28 and $1.40\sqrt{\text{MPa}}$, respectively. In slabs with high strap contribution to $V_{R,in}$ (So1–3, Sr1–2), crushing of the strut near the column limited the punching shear resistance. In slabs So4 and Sr3 with lower prestressing and thus lower strap forces, however, punching shear failure occurred through failure in the shear-reinforced zone.

Table 4.4: Experimental punching resistances and slab rotations at failure, increase of bending resistance and comparison of predicted and experimental results

| Reference | Slab | $\frac{V_{R,exp}}{u_0 d_v \sqrt{f_c}}$ [$\sqrt{\text{MPa}}$] | $\psi d_m k_g$ [–] | $\frac{m_R^+}{m_R}$ [–] | $\frac{V_{R1}}{V_{R,exp}}$ [–] | $\frac{\psi_{R1}}{\psi_{R,exp}}$ [–] |
|-------------|------|---|-----------------------|----------------------------|-----------------------------------|---|
| Section 3.1 | So1 | 0.98 | 4.10 | 1.31 | 0.91 | 0.85 |
| | So2 | 0.86 | 4.01 | 1.20 | 1.01 | 0.92 |
| | So3 | 0.84 | 3.99 | 1.16 | 1.03 | 0.94 |
| | So4 | 0.86 | 4.27 | 1.19 | 0.94 | 0.73 |
| Section 3.2 | Sr1 | 0.88 | 3.45 | 1.31 | 0.99 | 1.07 |
| | Sr2 | 0.83 | 4.94 | 1.57 | 0.97 | 0.87 |
| | Sr3 | 0.78 | 2.57 | 1.23 | 1.02 | 1.04 |
| Average | | | | | 0.98 | 0.92 |
| COV | | | | | 0.05 | 0.13 |

Table 4.4 compares the predicted punching resistances, V_{R1} , and slab rotations at failure, ψ_{R1} , to the experimental results. On average, the punching resistance was underestimated by only 2% with a coefficient of variation (COV) of 5%. The underestimation of the slab rotations was

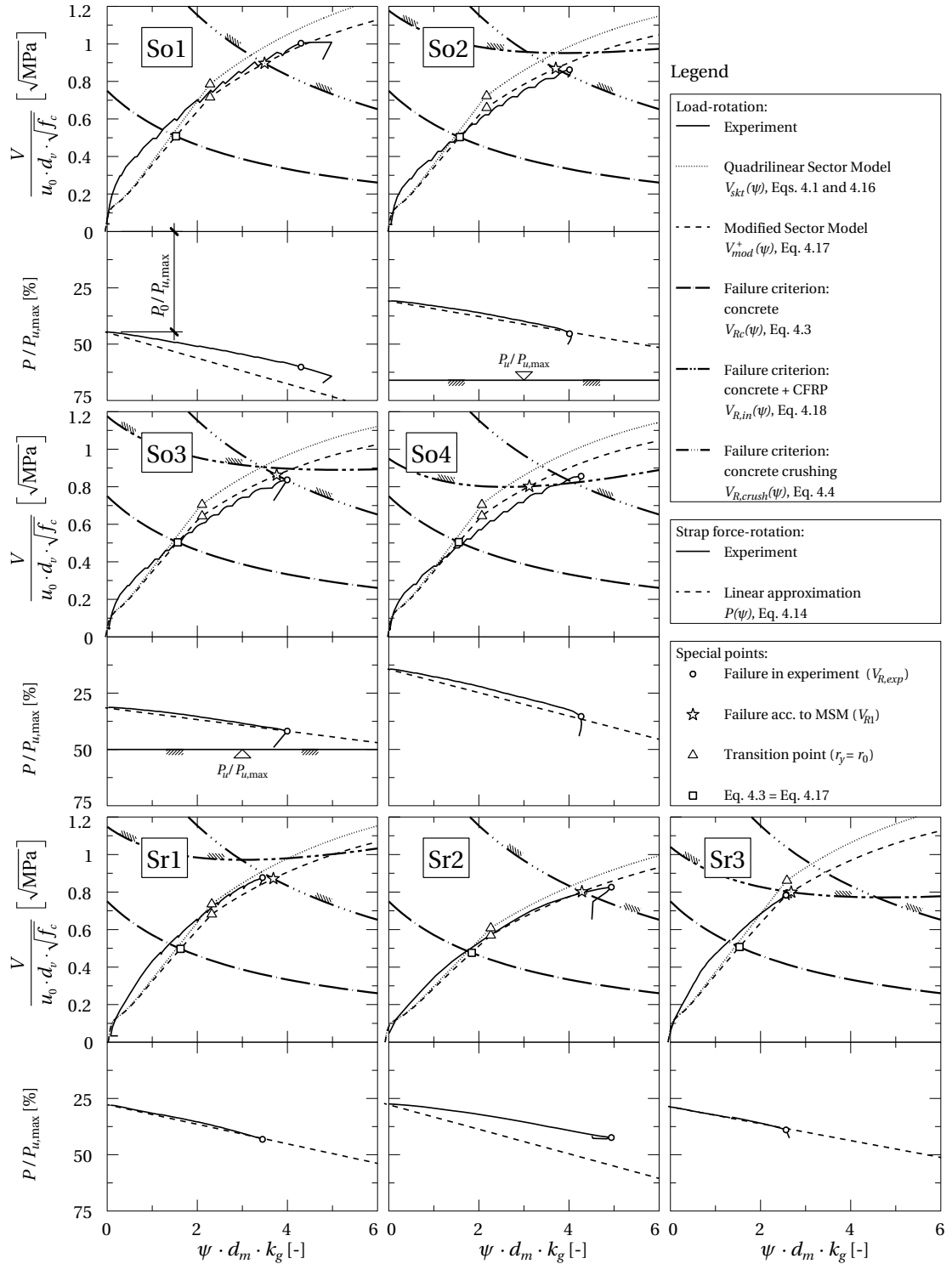


Figure 4.11: Comparison of own experiments with model curves (properties in Tables 4.2–4.3, results in Table 4.4)

slightly higher ($8 \pm 13\%$). The strengthening systems were able to significantly increase the punching resistances and the slab rotations at failure, i.e. the intersection points of Eqs. 4.3 and 4.17, square symbols in Figure 4.11, are at much lower loads and rotations than at failure of the strengthened slabs (circle symbols).

4.5 Conclusions

The Quadrilinear Sector Model (QSM) allows the modeling of the load–rotation responses of reinforced concrete flat slabs. To take into account an orthogonal reinforcement layout and the associated increased slab deformations, the steel Young’s Modulus is normally reduced by a factor, β_E . The QSM also neglects shear deformations, which may reduce the flexural capacity. The work presented here introduces the following improvements of the QSM:

- Instead of the mechanically not well-justified Young’s Modulus reduction factor, β_E , a flexural stiffness reduction factor, β_{EI} , is derived based on the linear compression field theory (LCFT). β_{EI} depends on the longitudinal reinforcement and modular ratio and provides equivalent slab stiffness reduction to the current β_E -factor.
- A Modified Sector Model (MSM) is derived which considers the influence of shear on the flexural behavior. A strength reduction factor, κ_V , for the longitudinal reinforcement that crosses the shear crack is introduced. This factor depends on the mechanical longitudinal reinforcement ratio and takes into account the fact that the longitudinal reinforcement also has to transmit forces resulting from shear and that the flexural capacity of the slab is thus reduced. Based on experimental results the increased accuracy of the MSM compared to the QSM was demonstrated, particularly for cases with higher longitudinal reinforcement ratios.
- Furthermore, it was demonstrated that the MSM could also be applied to predict the load–rotation responses of flat slabs strengthened with prestressed CFRP straps.
- For these slabs very good agreement between the predicted punching shear resistances and rotations and the experimental data was obtained. The strengthening systems increased the punching shear resistance by 74% on average.

4.6 Appendix A: Quadrilinear Sector Model

This appendix summarizes the equations of the Quadrilinear Sector Model by Muttoni (2008) used in this Chapter. Eq. 4.19 describes the equilibrium of moments between the inner and outer forces acting on the slab segment in Figure 4.1(a).

$$V \frac{\Delta\varphi}{2\pi} (r_q - r_c) = m_r r_0 \Delta\varphi + \int_{r_o}^{r_s} m_t dr \cdot \Delta\varphi \quad (4.19)$$

The tangential moments are integrated along the segment with opening angle $\Delta\varphi$ and m_r is the moment in the radial direction at $r = r_0$. Transforming Eq. 4.19 results in the load–rotation relationship of the sector model as follows:

$$V_{skt}(\psi) = \frac{2\pi}{r_q - r_c} \cdot \left[m_r(\psi) \cdot r_0 + \int_{r_o}^{r_s} m_t(\psi) dr \right] \quad (4.20)$$

The linear elastic uncracked segment in the quadrilinear m – χ –relationship of Figure 4.2 has a flexural stiffness $EI^I = E_c h^3 / 12$ per unit width up to the cracking moment, m_{cr} , at which the tensile strength of the concrete, f_{ct} , is reached (h = slab thickness):

$$m_{cr} = \frac{f_{ct} h^2}{6} \quad (4.21)$$

By assuming a linear elastic behavior of both concrete in compression and reinforcement in tension after cracking, a constant depth of the compression zone is derived as:

$$x^{II} = \rho \beta_E n d \left(\sqrt{1 + \frac{2}{\rho \beta_E n}} - 1 \right) \quad (4.22)$$

where ρ = geometrical longitudinal reinforcement ratio, modular ratio $n = E_s / E_c$, d = effective depth. The cracked flexural stiffness is given by

$$EI^{II} = \rho d^3 \beta_E E_s \left(1 - \frac{x^{II}}{d} \right) \left(1 - \frac{x^{II}}{3d} \right) \quad (4.23)$$

The reduction factor β_E is discussed in Section 4.2.2. The contribution of the concrete in tension between the cracks, known as tension stiffening effect, is considered by a shift of the curvature by the load-independent value of

$$\Delta\chi_{TS} = \frac{f_{ct}}{6\rho h \beta_E E_s} \quad (4.24)$$

Eq. 4.24 is based on the Tension Chord Model (Marti et al. 1998) and was suggested by Muttoni (2008), adapting Marti's (1999) proposal for beams⁶. The tension stiffening effect depends on the crack spacing. Maximum crack spacing is assumed in Eq. 4.24, which seems reasonable for the calculation of the punching resistance of slabs with elevated reinforcement ratios.

Assuming a perfectly plastic behavior of the reinforcement after yielding and an equivalent rectangular stress block for concrete in the compression zone, the bending resistance of the section is given by:

$$m_R = \rho d^2 f_{sy} \left(1 - \frac{\rho f_{sy}}{2 f_c} \right) = \omega d^2 f_c \left(1 - \frac{\omega}{2} \right) \quad (4.25)$$

By applying the quadrilinear moment–curvature relationship of Figure 4.2 to the equilibrium of moments, Eq. 4.19, Eq. 4.1 is obtained. The radii r_{cr} , r_{crs} , r_y , corresponding to the tangential curvatures χ_{cr} , χ_{crs} , χ_y in Figure 4.2 (points P, A, C), are given by $r = \psi / \chi_t \leq r_s$.

4.7 Appendix B: Modified Sector Model

The derivation of Eq. 4.11 is shown in this appendix. The rotation-dependent shear force according to the sector model, Eq. 4.20, is modified to the following equation by applying the right-hand side of Eq. 4.7 to the radial moment acting at $r = r_0$:

$$V_{mod}(\psi) = \frac{2\pi}{r_q - r_c} \cdot \left[m_r(\psi) \cdot r_0 \cdot \left(1 - \kappa_V \frac{V_{mod}(\psi)}{V_{flex}} \right) + \int_{r_o}^{r_s} m_t(\psi) dr \right] \quad (4.26)$$

which is transformed to:

$$V_{mod}(\psi) \cdot \left(1 + \frac{2\pi r_0 \cdot m_r(\psi)}{r_q - r_c} \frac{\kappa_V}{V_{flex}} \right) = \frac{2\pi}{r_q - r_c} \cdot \left(m_r(\psi) \cdot r_0 + \int_{r_o}^{r_s} m_t(\psi) dr \right) \quad (4.27)$$

The right-hand side is equal to Eq. 4.20 and inserting Eq. 4.2 results in

$$V_{mod}(\psi) \cdot \left(1 + \kappa_V \frac{m_r(\psi) \cdot r_0}{m_R \cdot r_s} \right) = V_{skt}(\psi) \quad (4.28)$$

from which Eq. 4.11 is deduced.

⁶see Section 5.2.2, p. 115

5 Effect of load history on punching resistance

5.1 Load history of uniaxial tension chord

Reference detail

Robert Koppitz, Albin Kenel and Thomas Keller. “Tension Chord Model Modification for Uniaxial Unloading and Reloading in Elastic and Plastic States”. *ASCE Journal of Structural Engineering*, 2014, Vol. 140, No. 10, 04014077. DOI: 10.1061/(ASCE)ST.1943-541X.0000999

Abstract

The bond properties between concrete and steel reinforcement influence structural stiffness and deformation behavior due to tension stiffening. In specific cases, the load-bearing capacity of engineering structures depends on the deformation behavior and may be affected by load history due to unloading and reloading (URL) cycles. The bond stress–slip relationship of the original Tension Chord Model (TCM) was modified to make it applicable for general URL cycles in the elastic and plastic states of the reinforcing steel by reducing the admissible bond shear stress, thus taking into account the progressive and irreversible damage to the concrete around the ribbed bar not only due to yielding but also due to the load history. The residual tension stiffening in the elastic state is influenced by the degree of slip reversal for which an analytical function was found that is dependent on the stress level prior to and after unloading, crack spacing and bond stress. The proposed analytical model was successfully validated with experimental results.

5.1.1 Introduction

The load-bearing capacity of engineering structures may depend, in specific cases, on the deformation behavior. A typical example is the punching shear resistance of flat concrete slabs, which depends on the slab rotation (Muttoni 2008). For cases in which post-installed strengthening of such structures is required, they often have to be unloaded before the strengthening

measures can be applied and the structure is reloaded. However, unloading and reloading (URL) cycles may influence the deformation behavior, particularly the tension stiffening effect.

In contrast to “naked” reinforcing steel, embedded rebars exhibit smaller elongations for the same tensile load because of the contribution of the encasing concrete between the cracks, an effect that is known as tension stiffening. Although the tensile strength of concrete represents a small, fractional amount of its compressive strength, it is necessary for a load transfer from steel to concrete via bond stresses along the rebar surface.

The bond between concrete and reinforcement and the progressive and irreversible damage of the concrete around the ribbed rebar attributable to cyclic loading or plasticization of the reinforcing steel has been intensively investigated during the last decades (Marti et al. 1998; Alvarez 1998; *fib* 2000; Borosnyói and Balázs 2005; Shima et al. 2011). For uniaxial stress states, bond stress–slip relationships have been proposed on the basis of Rehm’s (1961) differential equation of slipping bond. One of these approaches is the tension chord model (TCM) presented by Marti et al. (1998). The TCM assumes Sigrist’s (1995) stepped rigid–perfectly plastic bond shear stress–slip relationship for monotonic loading, shown in Figure 5.1(a). Alvarez (1998) extended the model for cracked untensioned and prestressed concrete tension members until (plastic) failure for determining the necessary minimal reinforcement ratios. The applications and developments of the TCM have been proposed for, among others, plane stress problems [cracked membrane model by Kaufmann (1998)], loading cycles and fatigue of prestressed tension ties (Fürost 2001), fracture mechanics based investigations for bending (Kenel 2002), and bending members under sustained loads (Burns 2012). The applicability of the model using Sigrist’s bond stress–slip relationship was confirmed by these studies.

Rehm’s (1961) equation can be solved analytically for linear or power functions. To take other bond stress–slip relationships into account, iterative numerical calculations are necessary. Thus, for investigations into high-cycle fatigue, slip versus number of load cycle (S – N) curves have been proposed to reduce the computational efforts (Balázs 1991; Zanuy et al. 2010). In these cases, the steel reinforcement remains in the elastic state, whereas for problems in earthquake engineering, plasticizing of the reinforcement may occur, but under a reversed cyclic loading. For reinforcement in the elasto-plastic state that is unloaded and reloaded without alternating the sign of the load, no experimental results have been found. For the analytical TCM, contrary to monotonic loading, the behavior of tension members during unloading and reloading has not yet been successfully reproduced: Alvarez (1998) investigated the load–deformation curve for one specific loading cycle, assuming full bond for unloading and reloading and linear elastic behavior for reinforcing steel and concrete. Fürost (2001) adopted these assumptions for calculating general URL cycles of elastic prestressed ties. On the other hand, Burns (2012) investigated a neglect of bond stresses between concrete and steel for the unloading of an elastic tension chord. Both approaches defined limit cases of no damage and full bond damage during unloading. The former assumption led to the conclusion that loading cycles would not affect the deformation behavior and the ultimate load of the tension member; the latter eliminated the hysteretic behavior of the chord’s load–

deformation path during unloading and reloading. By contrast, experimental beams exhibited hysteresis loops and higher deformations after the completion of loading cycles (Pfyl and Marti 2001; Kenel and Marti 2002), thus confirming earlier findings and results of tensile tests on reinforcing bars embedded into concrete (Rehm 1961; Leonhardt 1978). However, the original TCM was not applied for URL cycles in the case of elasto-plastic reinforcement.

Thus, a detailed investigation is necessary to quantify the degradation of bond attributable to the load history for elastic and elasto-plastic tension members, to eventually adapt the TCM for URL cycles. This study is intended to provide an easily understandable and straightforward, yet accurate, analytical solution to discuss this influence on the deformation behavior of a tension chord; additionally, it is validated by experimental results. The investigation is restricted to the following assumptions: symmetrical short-term tensile loading of non-prestressed members with bar-shaped steel reinforcement; no reversed cyclic loading (alternating sign); damage of the chord considered by reducing bond stress between steel and concrete; no long-term effects or fatigue.

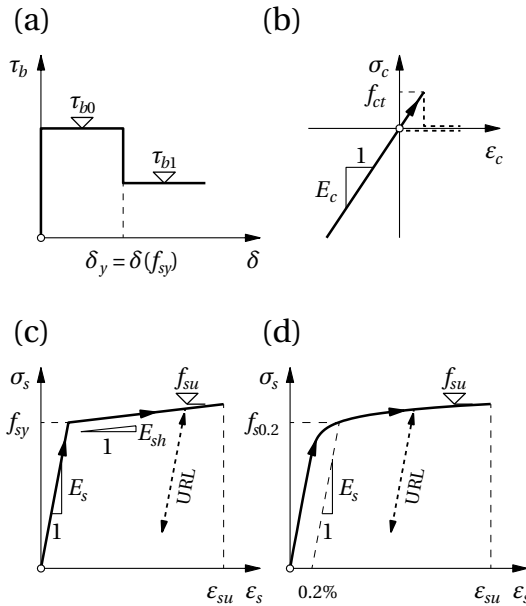


Figure 5.1: (a) Stepped rigid-perfectly plastic bond shear stress-slip relationship for monotonic loading proposed by Sigrist (1995), (b) stress-strain relationship for linear elastic concrete, (c) for bilinear reinforcing steel, (d) for cold-formed reinforcing steel

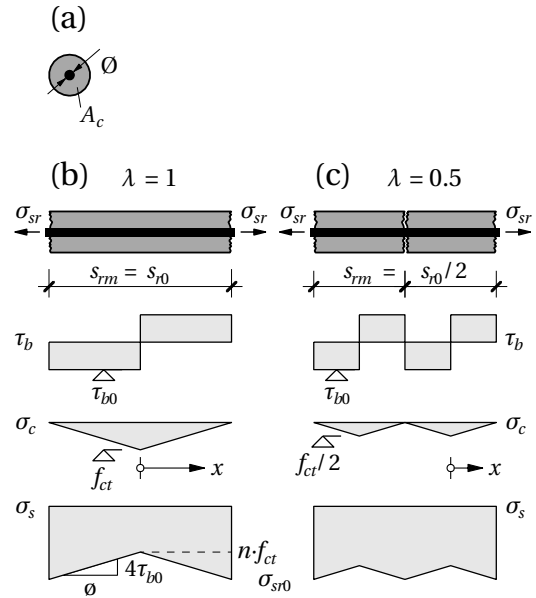


Figure 5.2: (a) Tension chord with stress distributions at crack stress $\sigma_{sr} = \sigma_{sr0}$ for (b) maximum and (c) minimum crack spacing (adapted from Marti et al. 1998)

5.1.2 Tension Chord Model

Properties of the tension chord element

According to Marti et al. (1998), a linear elastic behavior is assumed for concrete [Figure 5.1(b)]; once tensile strength, f_{ct} , is reached, it irreversibly drops to zero. Unless stated otherwise, the stress–strain relationship for reinforcing steel is assumed to be bilinear, with yield strength, f_{sy} , and hardening modulus, $E_{sh} > 0$ [Figure 5.1(c)]. The quotient of the Young's modulus of the materials is defined as modular ratio $n = E_s/E_c$. Figure 5.1(d) shows a cold-formed steel response: because cold-formed rebars do not exhibit pronounced yield strength, steel stress $f_{s0.2}$ with residual 0.2% strain is adopted for f_{sy} .

The tension chord in Figure 5.2(a) with gross cross-sectional area, A_c , is loaded by a constant axial force, N . It is reinforced by a single steel rebar with diameter \emptyset (thus $A_s = \frac{\pi}{4}\emptyset^2$), which corresponds to a geometrical reinforcement ratio $\rho = A_s/A_c$ and a remaining net cross-sectional area of $(1 - \rho)A_c$ for the surrounding concrete.

The upper bond shear stress, $\tau_{b0} = 2f_{ct}$, of the assumed bond stress–slip relationship in Figure 5.1(a) is valid for slips, δ (relative displacement between steel and concrete), smaller than δ_y , where the rebar has reached f_{sy} . For higher steel stresses, the bond is $\tau_{b1} = f_{ct}$ to account for the irreversible bond reduction after yielding. These values were suggested by Sigrist (1995) for ordinary ribbed steel rebars, after having studied the experiments by Shima et al. (1987). Although the relationship is a considerable simplification of the complex bond behavior, it provides reasonably accurate results for monotonic loading (Marti et al. 1998).

Monotonic loading for chord element between two cracks

Load is applied on the initially stress-free tension chord in Figure 5.2 (Marti et al. 1998; Alvarez 1998). A linear elastic uncracked behavior under rigid bond is observed (State 1) until the concrete's tensile deformation capacity, f_{ct}/E_c , is reached and cracks open: at the crack edge, rebar stresses have to increase abruptly from nf_{ct} to crack stress σ_{sr0} to take over the tensile contribution of the concrete, to fulfill the equilibrium of forces. This crack stress is calculated according to Eq. 5.1 and its limitation by the yield strength leads to a minimum required reinforcement ratio, ρ_{\min} , to prevent a sudden collapse at cracking (assuming $f_{ct} = 3 \text{ N/mm}^2$, $n = 6$, $f_{sy} = 500 \text{ N/mm}^2$ gives $\rho_{\min} \approx 0.6\%$).

$$\sigma_{sr0} = \frac{f_{ct}}{\rho} [1 + \rho(n - 1)] \leq f_{sy} \quad (5.1)$$

Because stresses are load induced, a fully developed crack pattern is reached immediately: all cracks open with a constant average crack spacing, s_{rm} , according to Eqs. 5.2 and 5.3:

$$s_{rm} = \lambda s_{r0} = \lambda \frac{\emptyset f_{ct}(1 - \rho)}{2\tau_{b0}\rho} = \lambda \frac{\emptyset}{4} \frac{1 - \rho}{\rho} \quad (5.2)$$

and

$$0.5 \leq \lambda \leq 1.0 \quad (5.3)$$

where s_{r0} = maximum crack spacing. The constant λ can theoretically freely vary between the two boundaries 0.5 and 1.0. In fact, λ is often determined by the spacing of the transverse reinforcement, which disturbs the tension zone. On the other hand, if stresses are induced by restraints (e.g. imposed deformation or shrinkage), cracks open one after another, producing a saw-toothed curve until the crack formation phase is completed (Alvarez 1998).

Figure 5.2(b) and (c) display the two boundary crack elements after they reach σ_{sr0} : Figure 5.2(b) illustrates an element with maximum crack spacing ($\lambda = 1$). Steel stress, σ_{sr0} , at each crack edge is linearly reduced as a result of integrated constant bond shear stresses, τ_{b0} , along the rebar surface. Accordingly, concrete stresses increase linearly until f_{ct} is reached at the center (zero point of slip) of the element, which allows the s_{r0} of Eq. 5.2 to be calculated. However, another crack may open at this location, constituting the lower bound of crack spacing ($\lambda = 0.5$), as shown by the element in Figure 5.2(c).

The entire global stress–strain path is illustrated in Figure 5.3(a) for monotonic loading: on the abscissa, steel strains, ε_{sm} , are displayed, which are averaged over the crack element, whereas maximum steel stresses at the crack edge, σ_{sr} , are plotted on the ordinate. At crack stress σ_{sr0} , these ε_{sm} are reduced by a constant factor $\Delta\varepsilon_0$, as shown in Eqs. 5.4 and 5.5, compared to naked steel.

$$\Delta\varepsilon = \frac{1}{4} \left(\frac{\sigma_{sr0}}{E_s} - \frac{f_{ct}}{E_c} \right) = \frac{f_{ct}}{4E_s} \frac{1-\rho}{\rho} \quad (5.4)$$

$$\Delta\varepsilon_0 = 2\lambda \cdot \Delta\varepsilon \quad (5.5)$$

During further load increases, the stress path follows a parallel line to the steel characteristic at distance $\Delta\varepsilon_0$ (State 2) until it arrives at yield strength f_{sy} . In State 3, parts of the crack element are in the elasto-plastic phase. Because of the lower tangent stiffness, E_{sh} , and the reduction of bond shear stresses to τ_{b1} along the yielded portions, steel strains are concentrated in the area near the crack. Eventually, the whole crack element is fully plasticized (State 4) and follows the steel characteristic again until ultimate strength, f_{su} , at the crack location eventually causes the rupture of the rebar. For the assumed properties, the rebar of the crack element with $\lambda = 1$ in the right-hand diagram of Figure 5.3(a) fails before achieving State 4. The typical steel stress and strain distributions inside the crack element are shown in Figure 5.3(b) for all four states.

Because of the tension stiffening effect, which is present until rupture, the full plastic deformation capacity of the reinforcing bar cannot be utilized for the tension member. The decrease depends on the bond shear stress, the diameter of the rebar (bond radius), the effective rein-

forcement ratio of the tension chord, the hardening branch of the steel stress–strain curve, the reinforcement ductility characteristics, and particularly, the size of crack spacing (Alvarez 1998; Kenel 2002).

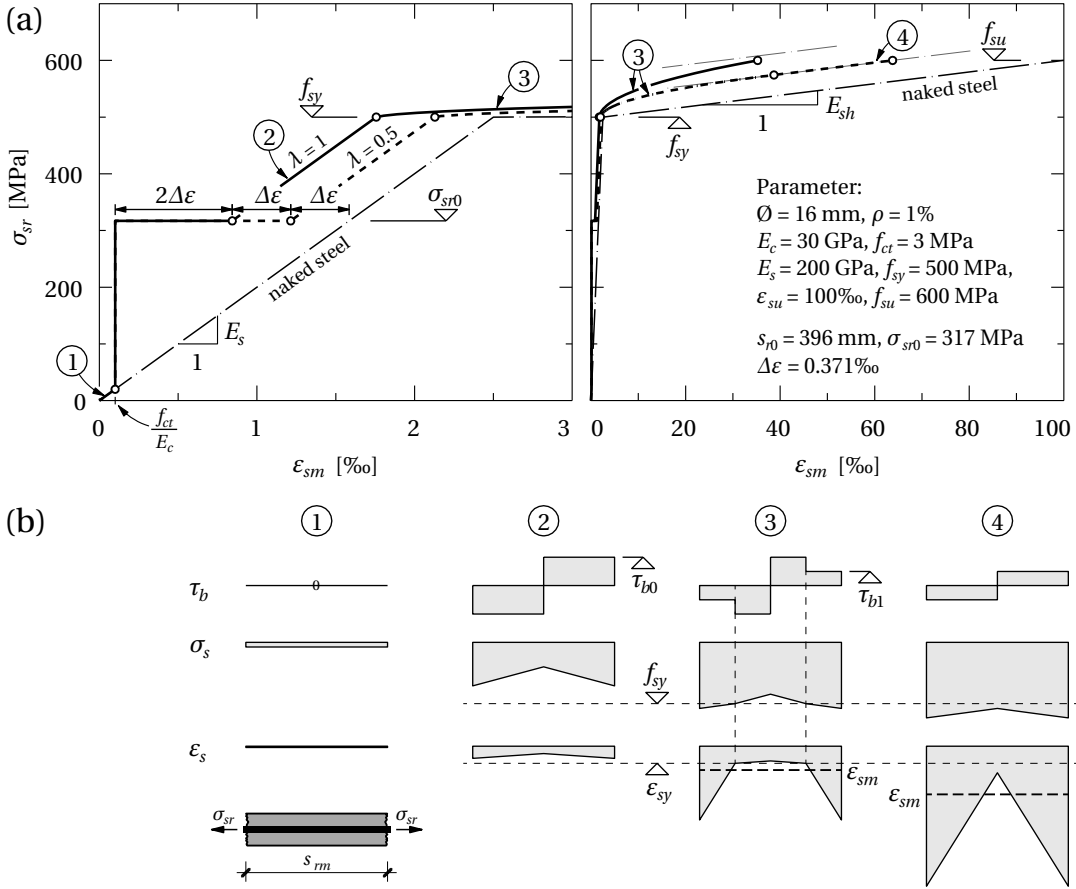


Figure 5.3: Monotonic loading of tension chord: (a) crack edge stress vs. average steel strain relationship, (b) stress distributions inside crack element for states 1 to 4 (adapted from Alvarez 1998)

5.1.3 Unloading and reloading of uniaxially stressed elements

Bond–slip relationship for unloading and reloading

Sigrist's bond shear–slip relationship forms the basis for Figure 5.4. Bond stress path OABCDEF is followed for monotonic loading, according to Figure 5.3: Path OAB corresponds to reaching crack stress σ_{sr0} . After loading is continued within State 2 (BC), bond shear stress immediately drops to half its value when yield strength at the crack is reached (CD). DEF is followed for stresses above f_{sy} .

For both unloading and reloading, a bond shear stress proportional to f_{ct} is given in Eq. 5.6, introducing bond stress factor, k_τ , as a proportionality constant. It is presumed in this work

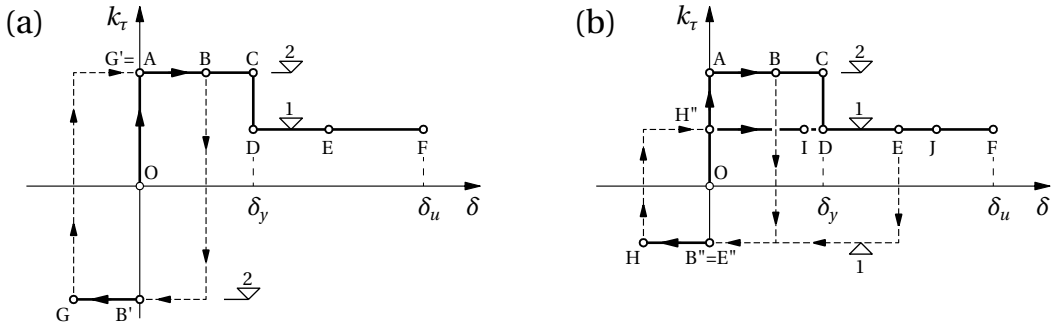


Figure 5.4: Bond-slip relationship for URL cycles with (a) $k_\tau = 2$ and (b) $k_\tau = 1$

that bond shear stress is identical for unloading and reloading:

$$\tau_{bU} = \tau_{bR} = k_\tau f_{ct} \leq \tau_{b0} \quad (5.6)$$

Alvarez' elastic URL cycle for $k_\tau = 2$ (full bond) is amended in Figure 5.4(a): when Point B is reached, unloading causes a slip reversal, immediately jumping from Point B to B'. Unloading takes place between Points B' and G, reloading is accomplished by G'B, arriving at the same point as before unloading. For a small load reduction, this is reasonable. However, when the chord element is significantly unloaded, the strength may decrease: relative displacements during initial loading constitute secondary cracks attributable to spalling, which damages the concrete microstructure around the bar [Goto (1971) provided a schematic diagram of concrete deformations around the rebar after the formation of internal cracks], causing an irreversible loss of bond strength. It is hypothesized that the bond shear stress, once reduced, cannot be increased again. Thus, the bond stress for reloading cannot exceed the value for unloading and the same load level is resumed at additional deformations. On the other hand, assuming no bond for unloading ($k_\tau = 0$) leads to safe upper bounds of deformations, but overestimates deformation capacity and neglects the development of a hysteresis curve during unloading and reloading. Kenel evaluated the unloading path of a four-point bending experiment, assuming $k_\tau = 1$, and obtained very good agreement with measurements obtained by using Bragg grating sensors (Kenel and Marti 2002; Kenel 2002). Thus, Kenel's k_τ , as an average value between the two boundary cases, is adopted in the following and a corresponding elastic URL stress path is displayed in Figure 5.4(b): unloading starts by jumping from B to B'', finally arriving at H, and reloading represents Path H'I. Damaged sections of the tension chord directly follow Path IDEF for higher loads. When the chord is unloaded after yielding has occurred for some of its parts, stress path EE''HH''JF is followed, which will be discussed in the section after the next, pp. 101–102.

Unloading and reloading in the elastic state

The stress distributions inside the crack element for both assumptions $k_\tau = 2$ and $k_\tau = 1$ are compared in Figure 5.5(a)–(d). Again, initial loading up to σ_{sr0} and full unloading are

investigated [the stress diagrams for $k_\tau = 2$ were represented by Alvarez (1998)]. Initial loading is identical for both k_τ -values. At cracking, the steel stresses jump abruptly from 1 to A. Unloading follows BG or BH, where at Points G and H, a positive average strain remains [indicated by the light gray areas, A_{res} , in the central stress diagrams of Figure 5.5(c)–(d) and causing a residual crack opening], although stresses are zero at the crack edge. For $\lambda = 1$, slip reversal has taken place up to a distance $x_{sU} < s_{rm}/2$ from the crack edge, whereas for $\lambda = 0.5$, a full slip reversal for the whole element has occurred ($x_{sU} = s_{rm}/2$). Further inside the element, the rigid bond leads to a reduction of transformed section stresses for compatibility reasons (analogous to State 1 in Figure 5.3). Along GB or HI, the tension chord is reloaded. The slope of the slip reversal zone remains $4\tau_{bR}/\phi$, even if stresses are higher than they were before (irreversible damage). The zone with transformed section properties ($s_{rm} - 2x_s$) was not effectively unloaded; therefore, the initial value of $4\tau_{b0}/\phi$ is still valid, and thus, the length of slip reversal is limited to x_{sU} . For $k_\tau = 1$, the stress distribution changes after reloading to I: an additional area, A_{add} [dark gray in the bottom diagrams of Figure 5.5(d)] causes higher average steel strains. Therefore, Point I is located to the right of the initial Point B, as shown in Figure 5.4(b), and the distance to the naked steel characteristic is reduced. In the following, the tension chord under consideration and its load history are parameterized to quantify the tension stiffening losses under general load cycles for any bond shear factor. A parameter study was conducted to discuss the influence of the individual factors.

Several k -factors are defined in Figure 5.6(a). They describe the whole stress–strain path in the elastic state: the crack element is loaded from O to Point B, which lies between crack stress at Point A and yield strength, and its stress at the crack edge is defined in relation to σ_{sr0} by a maximum stress factor, k_σ , according to Eq. 5.7. This factor denotes the ratio between the applied load and the cracking load. The element is unloaded to Point H, introducing a minimum stress factor, k_U , in Eq. 5.8, specified by the ratio of crack edge steel stresses at B to the same value at H. Full unloading is equivalent to $k_U = 0$.

$$1 \leq k_\sigma = \frac{\sigma_{sr}^{(B)}}{\sigma_{sr0}} \leq k_{\sigma,adm} = \frac{f_{sy}}{\sigma_{sr0}} \quad (5.7)$$

$$0 \leq k_U = \frac{\sigma_{sr}^{(H)}}{\sigma_{sr}^{(B)}} \leq 1 \quad (5.8)$$

As soon as full slip reversal is reached along stress path BH, the curve runs parallel to the naked steel characteristic (and to stress path AB). Because of the bond stress modification from τ_{b0} to τ_{bU} , the distance of the parallels is altered to $(\tau_{bU}/\tau_{b0}) \cdot \Delta\varepsilon_0 = (k_\tau/2) \cdot \Delta\varepsilon_0$. Thus, the maximum horizontal distance between the parallels to the naked steel curve through Points B and H [= $\Delta\varepsilon_{BH}$ in Figure 5.6(b)] is

$$\Delta\varepsilon_0 \left(1 + \frac{\tau_{bU}}{\tau_{b0}} \right) = \Delta\varepsilon_0 \left(1 + \frac{k_\tau}{2} \right) \quad (5.9)$$

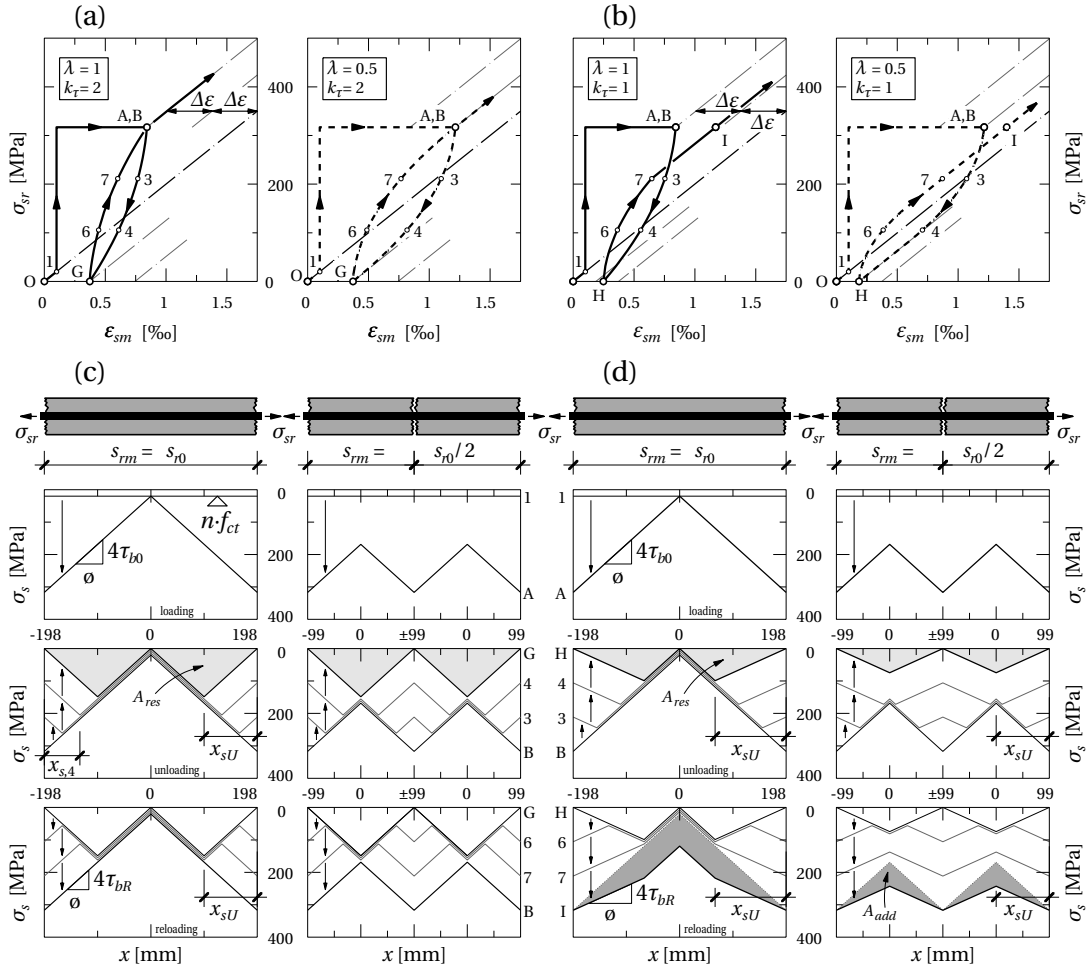


Figure 5.5: Crack edge stress-average steel strain relationship for elastic URL cycle: (a) $k_\tau = 2$, (b) $k_\tau = 1$. Corresponding steel stresses inside boundary crack elements for (top to bottom) loading, unloading, reloading: (c) $k_\tau = 2$, (d) $k_\tau = 1$. All parameters are identical to those in Figure 5.3. See Figure 5.14 for details of steel stress distribution

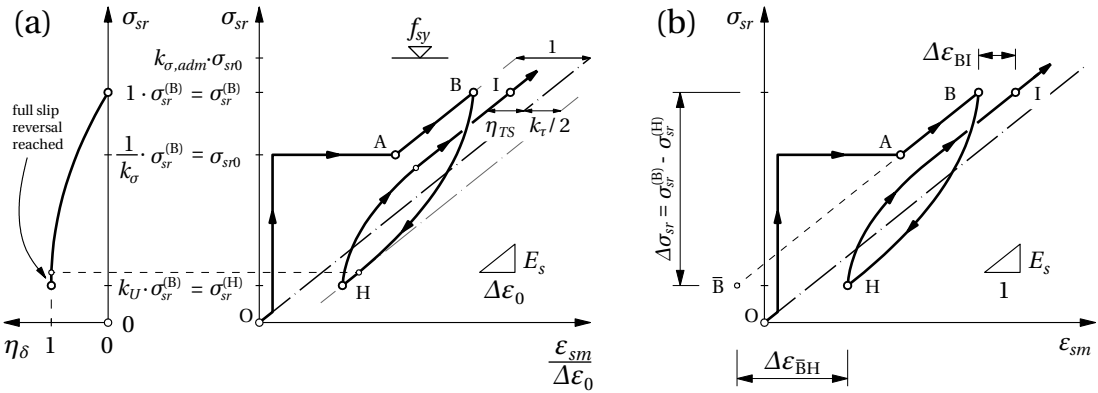


Figure 5.6: (a) General elastic URL stress path with introduced variables, (b) auxiliary numbers for calculation of degree of slip reversal and residual tension stiffening factor

and corresponds to $\eta_\delta = 1$, where η_δ is introduced to represent the degree of slip reversal:

$$\eta_\delta = \frac{\Delta \varepsilon_{\overline{BH}}}{\Delta \varepsilon_0 \left(1 + \frac{k_\tau}{2}\right)} \quad (5.10)$$

Full slip reversal means that all shear stresses along the steel bar have reversed their direction as a result of the unloading. This factor is calculated according to Section 5.1.6, resulting in the following simple quadratic function

$$0 \leq \eta_\delta = 2\xi - \xi^2 \leq 1 \quad (5.11)$$

where

$$0 \leq \xi = \frac{(1 - k_U)k_\sigma}{\lambda} \frac{2}{2 + k_\tau} \leq 1 \quad (5.12)$$

For three different $k_\tau (= 2, 1, \text{ and } 0.5)$, a set of curves for several k_U -values is plotted in Figure 5.7(a)–(c)¹ [η_δ on the ordinate, k_σ on the abscissa]. Curves for the same k_U are located at higher η_δ -levels for lower bond factors k_τ : full slip reversal is reached earlier, therefore, tension stiffening loss is higher, which is caused by the assumption of a low bond factor. As soon as it equals one, η_δ remains constant. The influence of the reinforcement ratio, ρ , is restricted to crack stress σ_{sr0} and to $k_{\sigma,adm}$ (the vertical boundary lines where σ_{sr0} is equal to f_{sy}). The results do not depend on the rebar diameter \emptyset .

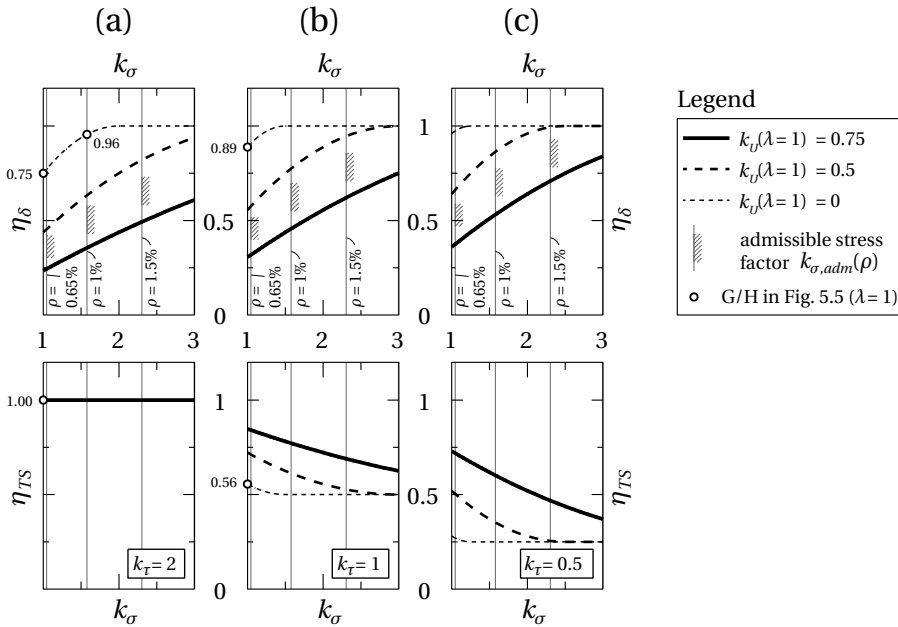


Figure 5.7: Parameter study of degree of slip reversal η_δ and residual tension stiffening factor η_{TS} for different bond stress factors: (a) $k_\tau = 2$, (b) $k_\tau = 1$ and (c) $k_\tau = 0.5$

¹Figure 5.7 is illustrated for $\lambda = 1$. Appendix F presents a transformation for $\lambda = 0.5$ to $\lambda = 1$

The initial strain reduction, $\Delta\varepsilon_0$, is multiplied by a residual tension stiffening factor, $\eta_{TS} \leq 1$, and results in a residual tension stiffening $\eta_{TS} \cdot \Delta\varepsilon_0$ after unloading and reloading because of progressive damage in the interface along the ribbed bar, caused by slip reversal (Goto 1971). The value of η_{TS} can be calculated analogously to η_δ by determining the (normalized) distance between Points I and B [Figure 5.6(b) and Section 5.1.6] and is linearly dependent on the degree of slip reversal of Eq. 5.11:

$$1 \geq \eta_{TS} = 1 - \eta_\delta \left(1 - \frac{k_\tau}{2}\right) \geq \frac{k_\tau}{2} \quad (5.13)$$

Full slip reversal causes a maximum tension stiffening loss that linearly depends on the bond factor, k_τ , as shown in the bottom diagrams in Figure 5.7. Assuming full bond leads to $\eta_{TS} = 1$ (no tension stiffening loss), regardless of which degree of slip reversal is obtained. For $k_\tau = 1$, there is a residual tension stiffening of 50%; for $k_\tau = 0.5$, the lower boundary is 25%. Corresponding values of the example in Figure 5.5 (with parameters: $k_\sigma = 1$, $k_U = 0$, $\rho = 1\%$) are plotted in Figure 5.7(a) and (b) for $k_\tau = 2$ and $k_\tau = 1$. For maximum crack spacing, $\eta_\delta = 0.75$ and 0.89 , respectively, are derived (circles in Figure 5.7). For $k_\tau = 2$, full slip reversal is impossible to achieve because the intersection between the curve and the vertical line at $k_{\sigma,adm} = 1.58$ ($\rho = 1\%$) is at $\eta_\delta = 0.96$. The remaining tension stiffening lies between 0.56 and 0.50 for $k_\tau = 1$, depending on the effective average crack spacing. The nomograms in Figure 5.7, based on Eqs. 5.11–5.13, clearly demonstrate the influence of individual factors on tension stiffening losses, and particular mention must be made of the minimum stress factor, k_U . Rapid graphical estimates of tension stiffening losses attributable to any URL cycle can be derived; conservative lower bounds of the remaining tension stiffness always directly depend on the assumed bond shear stress factor, k_τ .

Unloading and reloading in the elasto-plastic state

Another tension chord (using the parameters in Figure 5.3 and $k_\tau = 1$) is monotonically loaded up to 525 MPa (OE) at the crack edge and afterward unloaded to $f_{sy}/2 = 250$ MPa before being reloaded, as shown in Figure 5.8(a). Therefore, the total stress path in Figure 5.4(b) is OABCDEE"HH"JF. For the elastic case, the stress distribution inside the crack element is plotted in Figure 5.8(b). After steel stresses have reached f_{sy} , the slope is divided by two because of bond reduction at yielding (τ_{b1} instead of τ_{b0}).

During unloading (EH), slip reversal occurs up to a distance of x_{sU} , which remains the upper limit for the length of slip reversal during reloading (HJ). As soon as x_{sU} exceeds the length of the plasticized zone between σ_{sr} and f_{sy} , an irreversible bond shear stress reduction attributable to the URL cycle causes higher average steel strains after reloading [additional dark gray area, A_{add} , in Figure 5.8(b)] when parts of the crack element are still elastic; thus, Point J is located to the right of Point E. Particularly for maximum crack spacing, the distance between J and E is significant.

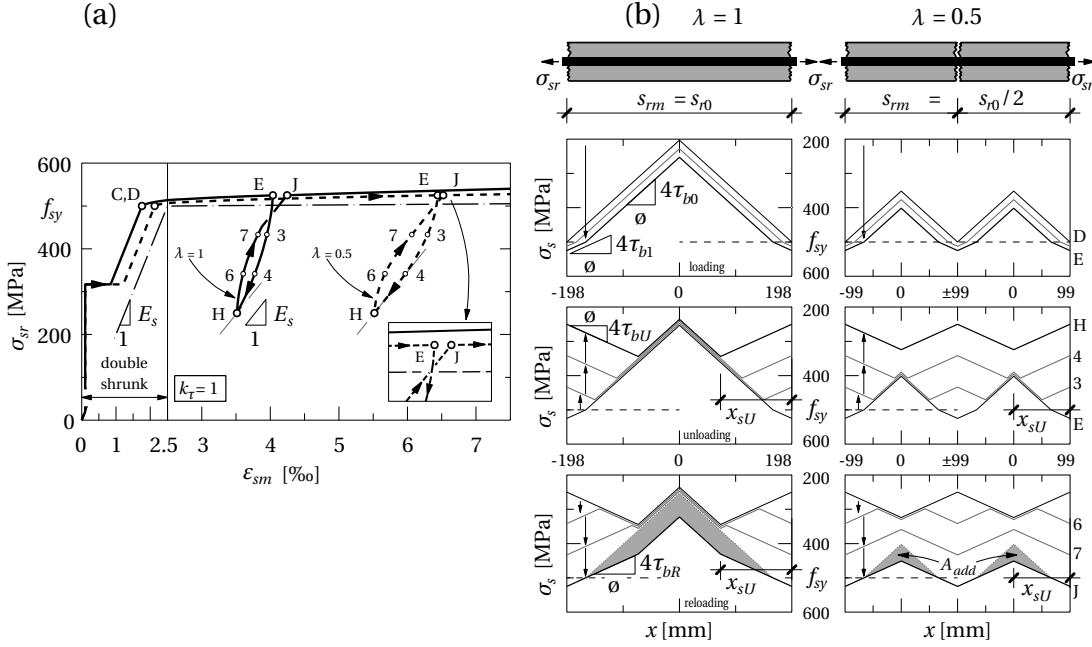


Figure 5.8: (a) Crack edge stress–average steel strain relationship for elasto-plastic URL, $k_t = 1$, (b) corresponding steel stresses inside boundary crack elements. All parameters are identical to those in Figure 5.3

5.1.4 Validation of proposed model

Based on the assumption of half the initial bond stress for unloading and reloading ($k_t = 1$), analytical curves are compared to experimental results derived from flexural and tensile tests on full-scale RC members. First, local stress and strain distributions inside crack elements of a beam under flexural loads are investigated. Subsequently, global elongation measurements of a tension member are compared to the modified TCM.

Bending experiments by Kenel

Kenel performed five four-point bending tests on 4-m-long RC beams (Kenel and Marti 2002; Kenel et al. 2005); the longitudinal and cross sections of Specimen B3 are shown in Figure 5.9(a). Beam B3 was reinforced with eight cold-formed bars of $\varnothing 10$ mm in the longitudinal direction, providing an overall reinforcement ratio $\rho = 0.31\%$. The material properties are summarized in Figure 5.9. An idealized stress–strain relationship according to Figure 5.1(d) was assumed for the reinforcing steel (with corresponding coefficients $c_s = 22.9$, $\kappa_s = 721$ MPa for Eq. 5.14 based on Ramberg and Osgood 1943):

$$\varepsilon_s = \frac{\sigma_s}{E_s} + \left(\frac{\sigma_s}{\kappa_s} \right)^{c_s} \quad (5.14)$$

Although it is not possible to directly measure bond shear stresses, they can be back-calculated from steel strain measurements along the reinforcing bar: between two load stages, strain differences at every measured location, x , are calculated and transformed to stress differences via a constitutive law, e.g., based on Eq. 5.14. Stress differences along the x -axis refer to bond stresses between concrete and steel (for constant bending moments). To obtain these steel strains, one of the eight longitudinal bars was equipped with 146 5-mm-long Bragg grating sensors (spaced at 10.4 mm) in an optical fiber that was epoxy glued into a $1.0 \times 1.0 \text{ mm}^2$ planed groove [Figure 5.9(b)]. Local reinforcing steel strains were analyzed in the undisturbed region of (approximately) constant bending moments between $x = 1.8 \text{ m}$ (midspan between the supports) and $x = 2.4 \text{ m}$ (right support). Figure 5.9(c) illustrates the measured strains for Load Stage (LS) 5 and LS10.

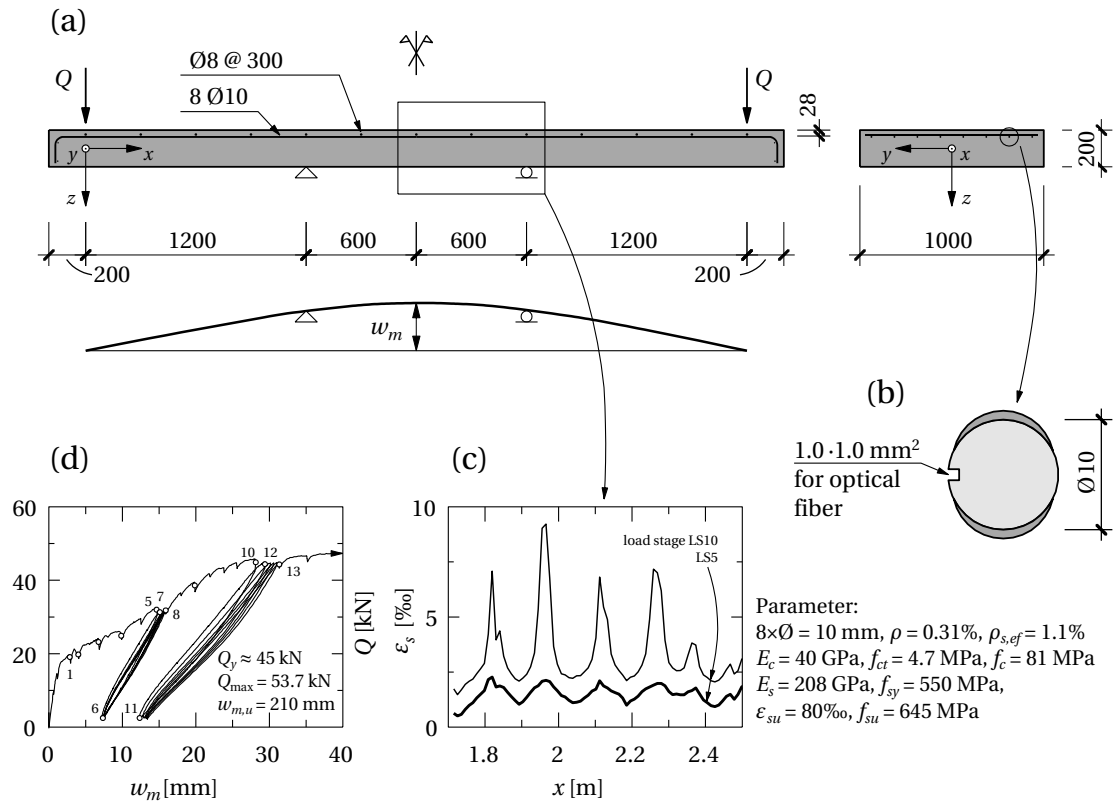


Figure 5.9: (a) Longitudinal and cross section of Kenel's beam B3 (dimensions in mm), (b) planed groove for optical fiber, (c) Bragg grating sensor results at LS5 and LS10, (d) load-mid-span deflection curve (adapted from Kenel and Marti 2002)

Beam B3 was loaded under displacement control by two hydraulic jacks at each end of the specimen (distance 3.6 m); load-deflection response within Load Stages 1–13 is shown in Figure 5.9(d). At LS1, the first bending cracks formed between the two supports. The crack pattern was fully developed at LS10, where the yield strength of the rebars was exceeded ($Q_y \approx 45 \text{ kN}$). Average crack spacing was observed between 140 and 150 mm, which is equal to half of the rebar spacing of the transverse reinforcement [$\text{Ø}8$ rebars at 300-mm spacing, as

shown in Figure 5.9(a)]. A maximum load of $Q_{\max} = 53.7 \text{ kN}$ could be applied, and at failure, a midspan deflection was measured relative to the beam ends of $w_{m,u} = 210 \text{ mm}$. Collapse was induced by failure of the concrete compression zone next to the left support.

Specimen B3 was loaded to $Q = 32 \text{ kN}$ at LS5. Bragg grating measurements are shown by solid lines in Figure 5.10(a). Five clear peak strains developed, each at a distance of 146 mm (equal to the distance between 15 Bragg grating sensors); each peak represents a flexural crack. Based on the resulting steel stress at each crack edge, a modeling curve (dashed line) was calculated for each crack element [parameters: $\varnothing = 10 \text{ mm}$, $\rho_{s,ef} = 1.1\%$, according to *fib* Model Code 2010 (2013), $n = 5.2$, $\tau_{b0} = 2f_{ct} = 9.4 \text{ MPa}$, $s_{rm} = 146 \text{ mm}$, thus $\lambda = 0.65$]. Experimental and modeling slopes correspond well, especially for the two left crack elements between $x = 1.8$ and 2.1 m ; experimental minimum steel stresses were slightly higher than predicted.

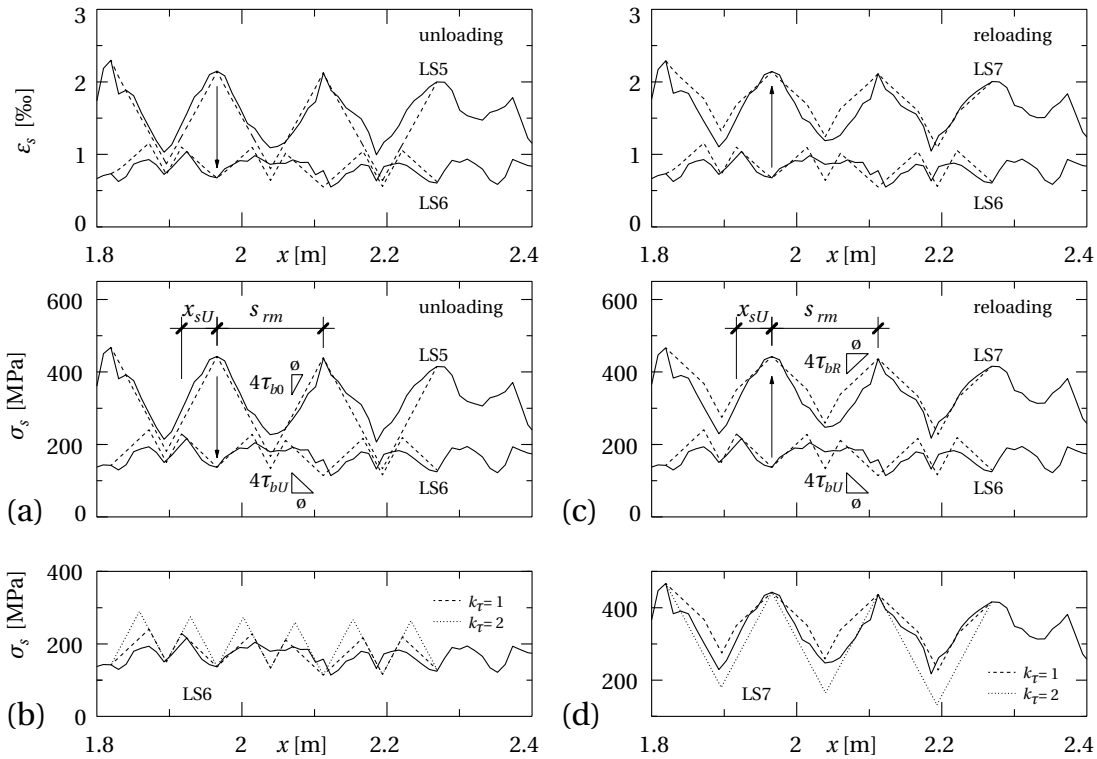


Figure 5.10: Experimental (solid) and modeled (dashed and dotted) steel stress and strain distribution for (a) unloading LS5 to LS6, (b) comparison of different bond stress factors after unloading, (c) reloading LS6 to LS7, (d) comparison of different bond stress factors after reloading

Subsequently, the beam was unloaded to $Q = 3 \text{ kN}$ [solid line in Figure 5.10(a), LS6]. Analogue to LS5, modified TCM steel stresses were calculated by subtracting stress increments between LS5 and LS6. Slip reversal occurred along length $x_{sU} \approx 50 \text{ mm}$; full slip reversal was not achieved. The area under the steel strain curve (neglecting concrete deformation) is equal to the crack width. The residual crack width at LS6 is overestimated by 5% if applying the modified TCM (dashed line, $k_\tau = 1$), which is much less than the 20% overestimation resulting from the

original model, whose stress curve (dotted line, $k_\tau = 2$) is compared to the measurements and modified TCM in Figure 5.10(b). The gradient of the steel stresses of the original TCM is too steep with regard to the measurements; the bond stresses of concrete to steel are overestimated. The agreement of the modified TCM to the experimental results is much better. To quantify this agreement, a coefficient of variation (COV) of the differences between experimental and calculated strains of each sensor was derived because strains and not stresses were measured. The COV of the modified TCM is 13%, which is 90% lower than for the original model.

LS7 denotes the load stage after reloading to $Q = 31$ kN [Figure 5.10(c)]. Along x_{sU} , only τ_{bR} could be activated, as suggested by the hypothesis of irreversible bond stress reduction. Again, original and modified TCMs are compared [Figure 5.10(d)]. The dotted line in Figure 5.10(d) is equal for LS5 and LS7 because a URL cycle did not affect the curve distribution. The modified TCM overestimates the crack width at LS7 by only 7%; on the contrary, the original TCM underestimates it by 11%. Again, the modified model corresponds better to the measurements than the original TCM. In particular, a good agreement is achieved for the stress minimums at the center of the three crack elements and for the stress distribution in the right element. The COV of the modified model is equal to 9.7% and 77% lower than that of the latter. The modified TCM confirms the measured increase of deformation (or crack width) after reloading.

Between LS7 and LS8, additional unloading and reloading cycles were conducted. It was assumed that x_{sU} remained constant during these load cycles. Subsequently, the beam was further loaded to $Q = 44$ kN (LS10). Figure 5.11(a) illustrates partial yielding of the steel reinforcement near to the crack edges (horizontal lines at f_{sy} and ε_{sy}). Within x_{sU} (from LS6), the gradient of the stress curve remained reduced, although plasticizing had not yet occurred. Both the strain and stress distribution according to the modified TCM (dashed line) correspond very well to the Bragg grating sensor results. The modified TCM underestimates the crack width at LS10 by 5%, in contrast to a 17% underestimation resulting from the original TCM. The steel stress curves of both models are shown in Figure 5.11(b). The stress gradients of the former model correspond well to the measurements, whereas the original TCM overestimates the bond stresses of concrete to steel, as shown by overly steep gradients near the stress maximums. COVs of 17% for the modified and 27% for the original model, respectively, confirm this observation. However, the scatter of the strain differences between the two TCMs and the measurements is affected by the results of two Bragg sensors in the left crack element at $x \approx 1.96$ m, as shown by the solid strain curve in Figure 5.11(a). It is probable that a crack may have opened exactly between the two grating sensors. Thus, the measurements do not correspond to the actual (higher) maximum values at the crack. By excluding these two data points, the COVs are reduced to 10% for the modified TCM and 23% for the original TCM.

Unloading to LS11 ($Q = 3$ kN) caused an elastic reduction of strains and stresses. Almost the whole crack element experienced a slip reversal [the already damaged zone along x_{sU} (LS6) was extended to $x_{sU} \approx 68$ mm; $s_{rm}/2 = 73$ mm]. Again, the shape of predicted and measured values is very similar. Figure 5.11(c) shows the predicted and measured curves after reloading to LS12, $Q = 44$ kN. For the comparison in Figure 5.11(d), it must be considered that the

original TCM was not intended to be applicable for URL cycles in the elasto-plastic state. The dotted curve depicted in the diagram shows the distribution for a monotonic loading between LS10 and LS12. The previous observation in Figure 5.11(b) is confirmed. The modified TCM reproduces the experimental curve much better; the crack widths (thus, beam deformations) of both the modified TCM and the experiment are approximately 4% higher than for LS10.

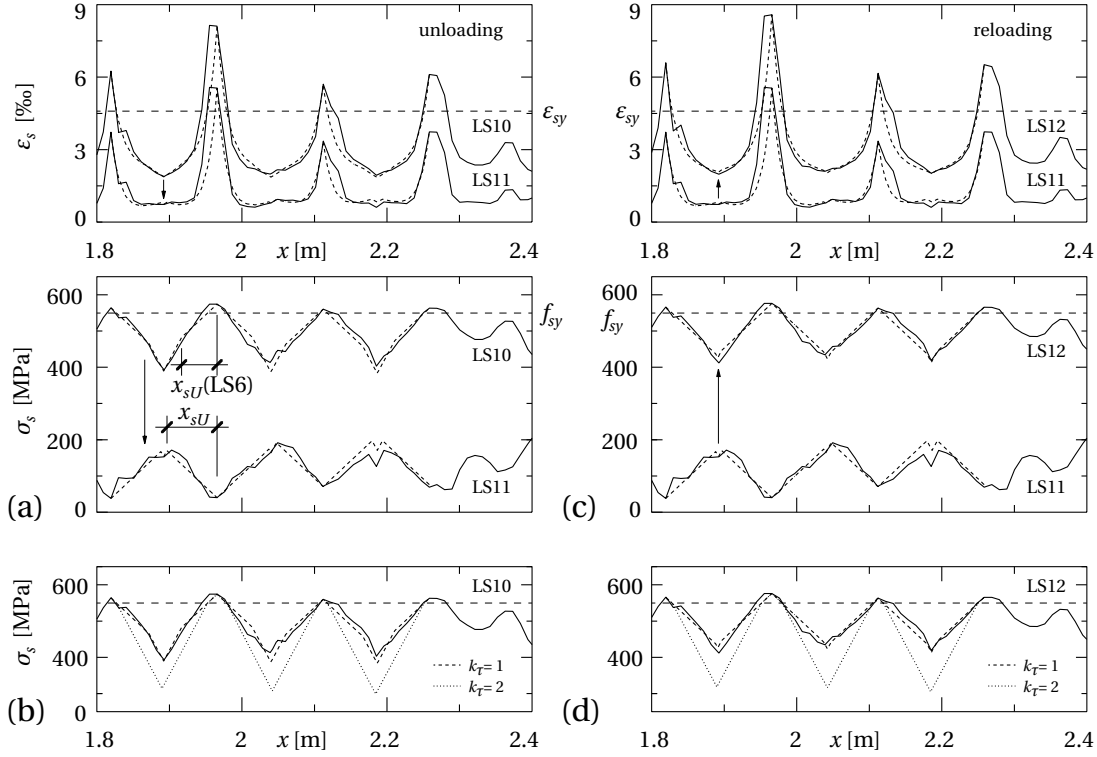


Figure 5.11: Experimental (solid) and modeled (dashed and dotted) steel stress and strain distribution for (a) unloading LS10 to LS11, (b) comparison of different bond stress factors before unloading, (c) reloading LS11 to LS12, (d) comparison of different bond stress factors after reloading to LS12

Tensile experiments by Pfyl

Pfyl conducted experimental and theoretical investigations concerning the application of steel fibers in reinforced and prestressed concrete structures with low reinforcement ratios (Pfyl and Marti 2001; Pfyl 2003). Tensile and flexural beams with varying reinforcement ratio and fiber contents and a reference beam without any fibers were investigated. Specimen T100.0 [longitudinal and cross sections in Figure 5.12(a) and (b)] was reinforced with four Ø8 mm bars in the longitudinal direction [$\rho = A_s / A_c = 0.67\%$, corresponding to the minimum reinforcement requirements according to SIA 262 (2013)]. Their ends were welded to steel anchor plates. Two additional Ø8 mm bars and stirrups in the transverse direction were placed in the anchoring zone. At the beam center, two Ø4 mm cross-rods fixed the target position of the longitudinal reinforcement and served to induce the crack position. Relevant material

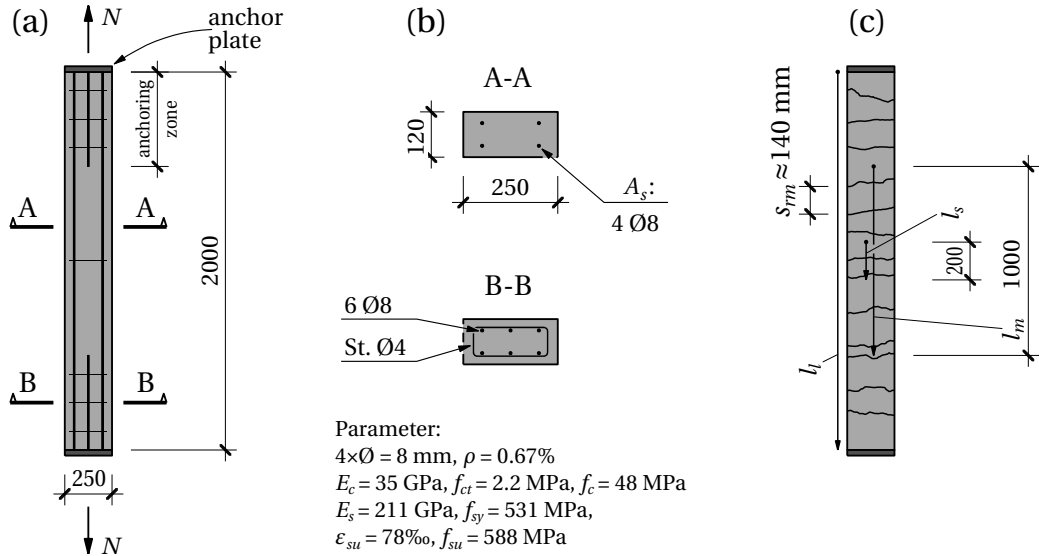


Figure 5.12: (a) Longitudinal section of Pfyl's beam T100.0 with placed reinforcement (dimensions in mm), (b) cross sections A–A and B–B, (c) crack pattern and installed LVDT sensors (adapted from Pfyl and Marti 2001)

properties are summarized in Figure 5.12; a bilinear stress–strain relationship according to Figure 5.1(c) was assumed for reinforcing steel.

Elongation of the beam was measured by seven inductive LVDTs, labeled l_1 , l_m , and l_s in Figure 5.12(c). Three displacement transducers measured the overall extension of the beam between the anchor plates (2 m base length; l_{l1} , l_{l2} , l_{l3}), two LVDTs were installed to measure the elongation between the load application zones (1 m base length; l_{m1} , l_{m2}), and two further transducers had a base length of 200 mm (l_{s1} , l_{s2}).

The load was applied under displacement control at each beam end. Specimen T100.0 cracked at $N = 68 \text{ kN}$ at midspan (location of the two Ø4 cross-rods). A tensile strength for the structural member of $f_{ct} = 2.2 \text{ MPa}$ was derived, according to the TCM (considering net cross sections, $n = 6.1$ and $\rho = 0.67\%$). At LS8 [Figure 5.13(a)], the crack pattern was fully developed with seven primary cracks. The average crack spacing, s_{rm} , was 140 mm, approximately corresponding to the lower limit value of $\lambda = 0.5$. Because of the low effective concrete tensile strength, crack stress, σ_{sr0} , was only 340 MPa. Maximum load was $N = 123 \text{ kN}$; the beam failed as a result of rupture of two of the four longitudinal rebars at $N = 119 \text{ kN}$ and the average elongation measured between the load application zones at failure was 34 mm.

Figure 5.13(a) and (b) show stress–elongation diagrams: on the abscissa in Figure 5.13(a), Δl_m was obtained from the average of the two medium LVDTs l_{m1} and l_{m2} ; the average values, Δl_s , of the two short LVDTs l_{s1} and l_{s2} are shown in Figure 5.13(b). At cracking, cracks formed progressively, as illustrated by the saw-toothed curves. In Figure 5.13(a), the trace is quite regular (results from the long base length), because almost all cracks formed between the two sensors, and is located between the two analytical limit curves for $\lambda = 0.5$ and 1.0

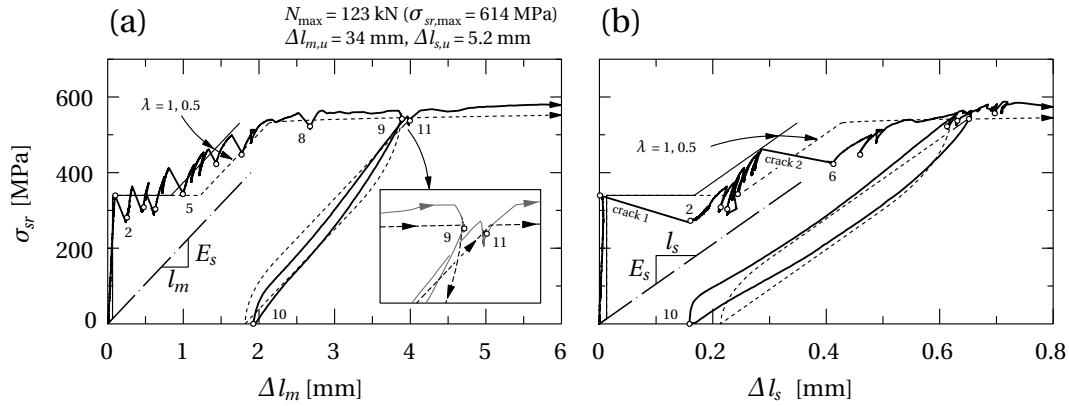


Figure 5.13: (a) Crack edge stress–elongation relationship for (a) LVDTs with base length 1000 mm, (b) short LVDTs with base length 200 mm

according to the TCM. The short base length of the transducers in Figure 5.13(b) shows the large deformation increase at each of the two cracks formed within this length.

After initially loading the beam up to the elasto-plastic state, a complete URL cycle was performed between LS9 and LS11. A comparison of the measurements in Figure 5.13(a) with the predicted curve (for $\lambda = 0.5$) shows that:

1. the loading cycle causes additional extensions after LS11,
2. almost the same residual deformation results as at LS10, but
3. the hysteresis is overestimated by the modified TCM and the slope of the measurements (proportional to the Young's modulus, E_s) is higher.

This apparently higher Young's modulus is most likely attributable to the additional rebars of the anchoring zone, which, by ending close to the measuring section of the LVDTs [Figure 5.12(a) and (c)], influence the flow of forces and decrease the hysteretic response. Also, not all cracks occur between the two transducers. In Figure 5.13(b), the agreement between the unloading and reloading predictions and the measurements is much better with respect to the corresponding hysteresis and slope (stiffness).

5.1.5 Conclusions

The bond of concrete to steel reinforcement is essential for the appropriate functioning of RC members. The bond properties determine crack widths and spacing and influence structural stiffness and deformation behavior as a result of the concrete contribution in tension (tension stiffening). In this contribution, the original TCM is modified to make it applicable for general URL cycles in the elastic and plastic states of the reinforcing steel. The conclusions described in the following can be drawn:

- Unloading and reloading reduces tension stiffening, which results in additional deformations. Thus, the admissible bond shear stresses in bond stress–slip relationships have to be irreversibly reduced, not only because of yielding of the reinforcement, but also before this, because of load cycles in the cracked elastic state.
- For a low number of URL stress cycles, an irreversible reduction of bond stress to 50% of its initial value ($k_\tau = 1$) is proposed. A significant increase of cycles may lead to further irreversible reductions.
- The residual tension stiffening effect is influenced by the degree of slip reversal, η_δ . A simple quadratic function for η_δ was found, in which the latter depends on the stress level before and after unloading, crack spacing, bond stress, and reinforcement ratio (via the crack stress, σ_{sr0}). A parameter study shows a strong influence of the ratio of unloading stress level to initial loading stress on the residual tension stiffening. This effect is intensified for low bond stresses.
- For members with reinforcement in the elasto-plastic state, additional deformations after unloading and full reloading were observed, as for the load cycles in the elastic state.
- The modified TCM allows the sufficiently accurate description of the local bond stress development between steel and concrete in the case of two RC beams, which were unloaded and reloaded with the reinforcement in the elastic and elasto-plastic states.
- Load history can significantly influence the deformation behavior and has to be considered, especially for cases with deformation-dependent load-bearing capacities.

5.1.6 Appendix: Degree of slip reversal

This section provides detailed calculation steps for deriving the degree of slip reversal, η_δ , and the residual tension stiffening factor, η_{TS} . Average steel strains are calculated by integrating steel strains (via the stress–strain relationship) along the tension chord. To take unloading and reloading into account, the stress path has to be split into segments: for each segment, $\Delta\epsilon_{sm}$ has to be calculated, and finally, all segmental results are superposed. In Figure 5.6, η_δ is derived by segmentally calculating the average steel strains for Point H:

$$\epsilon_{sm} [\sigma_{sr}^{(H)}] = \Delta\epsilon_{sm} (\sigma_{sr}^{(B)} - 0) + \Delta\epsilon_{sm} (\sigma_{sr}^{(H)} - \sigma_{sr}^{(B)}) \quad (5.15)$$

then subtracting the average steel strains for B (previously shifted parallel to the naked steel characteristic down to the stress level of H), giving the distance \bar{BH} according to Figure 5.6(b):

$$\Delta\epsilon_{\bar{BH}} = \epsilon_{sm} (\sigma_{sr}^{(H)}) - \left[\epsilon_{sm} (\sigma_{sr}^{(B)}) - \frac{\sigma_{sr}^{(B)} - \sigma_{sr}^{(H)}}{E_s} \right] \quad (5.16)$$

and normalizing by the right side of Eq. 5.9, giving the following term identical to Eq. 5.10

$$\eta_\delta = \frac{\Delta\epsilon_{\bar{BH}}}{\Delta\epsilon_0 \left(1 + \frac{k_\tau}{2} \right)} \quad (5.17)$$

The steel stress difference at the crack edge between B and H is denoted as $\Delta\sigma_{sr}$. For a bilinear steel stress–strain relationship according to Figure 5.1(c), the average steel strain difference, $\Delta\epsilon_{sm}$ (as function of $\Delta\sigma_{sr}$), is given by

$$\Delta\epsilon_{sm} (\Delta\sigma_{sr}) = \frac{\Delta\sigma_{sr}}{E_s} - \frac{4\tau_b}{\emptyset} \frac{x_s (s_{rm} - x_s)}{E_s s_{rm}} \quad (5.18)$$

with

$$x_s (\Delta\sigma_{sr}) = \frac{\emptyset}{4\tau_b} \frac{1 - \rho}{1 + \rho (n - 1)} \Delta\sigma_{sr} \quad (5.19)$$

where τ_b = sum of the initial and unloading bond shear stress and x_s = length along which slip reversal has already occurred for a certain stress difference (Figure 5.14). The value corresponding to the stress path arrival at Point H is denoted x_{sU} (also shown in Figure 5.5), and subsequently, specifies the upper limit of x_s during crack element reloading (stress path HI). Substituting Eqs. 5.18 and 5.19 into 5.17, together with Eqs. 5.1–5.8, η_δ can be rewritten as Eq. 5.11 by introducing the coefficient ξ [Eq. 5.12].

The calculation steps for the residual tension stiffening factor, η_{TS} , are analogous to the previous procedure. Here, the (normalized) horizontal distance between Points I and B is calculated instead [Figure 5.6(a) and (b)]:

$$\eta_{TS} = 1 - \frac{\Delta\epsilon_{BI}}{\Delta\epsilon_0} \quad (5.20)$$

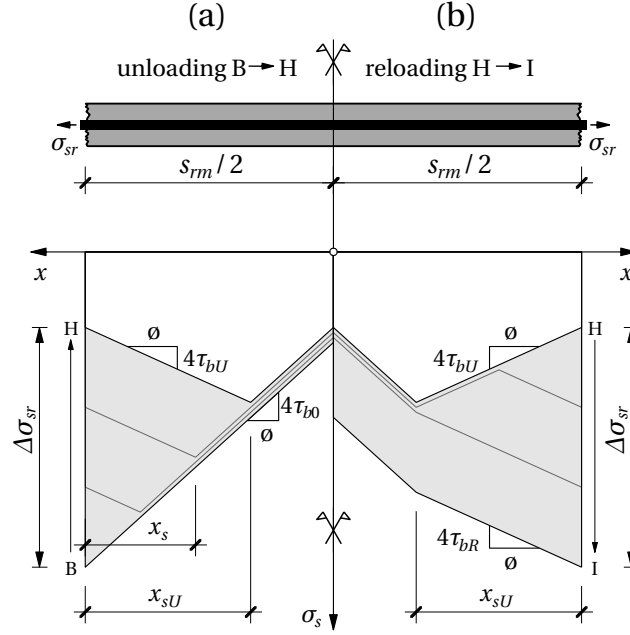


Figure 5.14: Steel stress distribution along crack element for (a) unloading and (b) reloading

When segmenting stress path OABHI, the absolute value, $\Delta\sigma_{sr}$, for HI is equal to BH, but not the average steel strain difference. Eq. 5.18 has to be derived by inserting x_{sU} as upper limit for x_s (Figure 5.14). For the same $\Delta\sigma_{sr}$, Eq. 5.19 would exceed x_{sU} because $\tau_b = \tau_{bU} + \tau_{bR} \leq \tau_{b0} + \tau_{bU}$. Eq. 5.20 is finally rewritten as Eq. 5.13, which is linearly dependent on η_δ [Eq. 5.11].

5.2 Load history of flat slabs

Reference detail

Robert Koppitz, Albin Kenel and Thomas Keller. “Effect of load history on punching shear resistance of flat slabs”. *Engineering Structures*, submitted in October 2014, revised in January 2015.

Abstract

The unloading of reinforced concrete slabs results in residual slab rotations and reloading to the same load results in irreversible rotation increases. Unloading and reloading (URL) cycles applied to non-strengthened and strengthened flat slabs may thus affect the punching resistance, which is rotation-dependent. A quintilinear moment–curvature relationship, which takes concrete softening and tension stiffening into account, combined with URL cycles, modeled as bilinear envelopes, is developed to predict residual slab rotations and irreversible rotation increases. A parametric study shows that the effect of URL cycles on the punching resistance of concrete is normally small, however, it may be significant if the slab is strengthened after unloading, particularly for thin and low-reinforced slabs, which exhibited plastic slab rotations before unloading. Prestressing of the strengthening system may reduce the residual slab rotations and thus limit or compensate the loss of punching resistance.

5.2.1 Introduction

In contrast to the bending resistance, the punching shear resistance of flat slabs depends on the slab rotation (Kinnunen and Nylander 1960). For slabs with interior columns, the punching resistance can be estimated with analytical formulas, which are based on the assumption of a rotation-symmetric slab cutout. Load–rotation curves can be derived for different, e.g. bilinear or quadrilinear, moment–curvature relationships (Muttoni 2008). Based on the Tension Chord Model (TCM) by Marti et al. (1998), the quadrilinear relationship takes a contribution of the concrete tensile stresses between the cracks into account. This leads to a decrease of the average steel stresses in the cracked zone and thus to the so-called “tension stiffening effect”, which may influence the punching resistance of slabs with low reinforcement ratios of the longitudinal reinforcement (Muttoni 2008).

In addition to the consideration of concrete tensile stresses between cracks, the behavior of concrete in the crack itself was also investigated. Studies on cement pastes (Higgins and Bailey 1976; Grudemo 1979) showed that their crystalline structure can hinder or even arrest the growth of micro-cracks by means of interlocking fibers growing out from the cement grains. Thus the concrete tensile stresses do not abruptly drop to zero after tensile strength is reached, but still provide a fractional contribution up to a critical (fictitious) crack width, w_{cr} . This behavior is considered by the Fictitious Crack Model (FCM) by Hillerborg et al. (1976) and Hillerborg (1983) for instance, where one sharp crack of zero initial length is assumed, or by the blunt Crack Band Model (CBM) by Bažant and Oh (1983) and Bažant et al. (1994), which smears the crack over a fracture process zone of a certain width.

A Modified Sector Model (MSM) has been proposed in Chapter 4, which takes into account the fact that the punching resistance also depends on the level of transverse shear loading. This model considers a quadrilinear moment–curvature relationship including the tension stiffening effect. Comparisons with experimental results indicated that slab rotations generally agree very well, but are slightly overestimated immediately after the cracking of the slab, see Figure 4.7. This overestimation was attributed to the tensile contribution in the fracture process zone, which had not been taken into account.

The unloading and reloading of slabs may further influence the deformation behavior and thus the punching resistance. Prior unloading of slabs may be required (e.g. by bracings) if existing slabs have to be strengthened against punching shear in order to activate the post-installed strengthening systems. For the uniaxial tension chord it was shown in Section 5.1 that unloading and reloading (URL) cycles influence the deformation behavior by affecting the bond properties between the reinforcing steel and surrounding concrete. A residual slab rotation, ψ_{res} , was noticed after unloading of the slab, see Figure 3.23. After reloading up to the same load as previously applied, an irreversible increase of rotation, $\Delta\psi_{URL}$, was observed by Marti et al. (1977) and Pralong et al. (1979). Some experiments even failed in punching before reaching the same load as previously applied (Pralong et al. 1979). Additional deformations resulting from such load histories may thus reduce the punching resistance and their accurate modeling or prediction is important.

In the following, the modeling of the effects of URL cycles on the deformation behavior of the uniaxial tension chord is therefore extended to bidirectional slabs, focusing on single URL cycles required for slab strengthening. On the basis of the MSM, the residual slab rotations after unloading and irreversible rotation increases after reloading of slabs are described. Furthermore, the tensile contribution of the fracture process zone is taken into account by a softening branch in the concrete stress–strain relationship in order to eliminate the above-mentioned overestimation of deformations during cracking. A parametric study is carried out to quantify the effects of these parameters on the punching shear resistance of non-strengthened and strengthened flat slabs.

5.2.2 Concrete contribution in tension

Tension Chord Model

The contribution of the concrete between the cracks in tension can be considered using the TCM (Marti et al. 1998), which assumes Sigrist's (1995) stepped rigid–perfectly plastic bond shear stress–slip relationship for monotonic loading, see Figure 5.1(a). As long as the rebar stress is below the yield strength, f_{sy} , an upper bond shear stress of $\tau_{b0} = 2f_{ct}$ is assumed. After yielding, the bond shear stress is reduced to a lower value of $\tau_{b1} = f_{ct}$ to take an irreversible bond reduction into account. A linear elastic behavior is assumed for concrete up to the tensile strength, f_{ct} ; no softening behavior is subsequently considered [Figure 5.1(b)].

In a tension chord with applied axial force, N , bond stresses between the cracks reduce the average steel stresses and thus the average steel strains, ε_{sm} , inside the crack element with constant average crack spacing s_{rm} , compared to the case where f_{ct} is neglected (equal to naked steel characteristic). Applying the TCM results in a horizontal shift of the average steel strains by a constant factor $\Delta\varepsilon_0$, see Figure 5.15(a) and Eq. 5.21:

$$\Delta\varepsilon_0 = \frac{\lambda f_{ct}}{2E_s} \frac{1-\rho}{\rho} \quad (5.21)$$

where $\rho = A_s/A_c$ with $A_s = \pi\varnothing^2/4$ (centrally arranged rebar with diameter \varnothing), A_c = gross cross-sectional area of tension chord; and $0.5 \leq \lambda \leq 1.0$. The two boundaries of λ represent minimum and maximum values for crack spacing. The actual value is determined by the spacing of the transverse reinforcement.

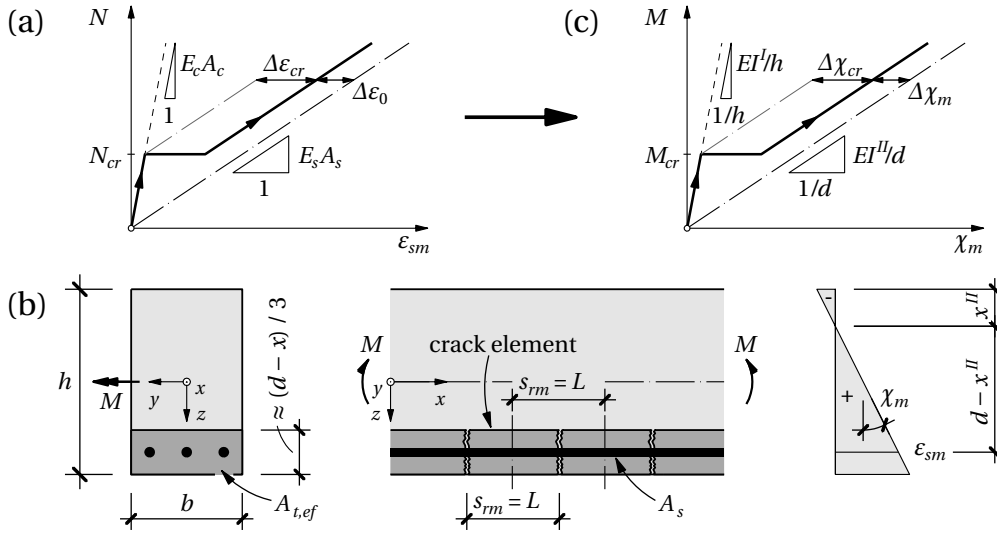


Figure 5.15: (a) Tension chord with applied load–average steel strain diagram in uncracked and cracked elastic state, (b) denomination of beam and (c) transformation to applied moment–average curvature diagram in uncracked and cracked elastic state according to Marti (1999)

The behavior of the uniaxial tension chord was investigated for URL cycles in Section 5.1. Based on Kenel (Kenel and Marti 2002; Kenel et al. 2005), an irreversible reduction of bond shear stress $\tau_b = k_\tau f_{ct}$ between rebar and surrounding concrete from the initial value of $k_\tau = 2$ to $k_\tau = 1$ was suggested for unloading and reloading cycles (see Section 5.1.3, p. 97). The bond stress–slip path is therefore altered during the URL cycle, see Figure 5.16(a), resulting in the load–average steel strain curve of Figure 5.16(b) (abscissa normalized by $\Delta\varepsilon_0$). The path is represented by BHI, whereby the deformation at I is higher than at B due to the irreversibly reduced bond properties. Small circles between B and H, and H and I, respectively, denote full slip reversal in the tension chord, where all shear stresses along the rebar have reversed their direction. Further unloading (or reloading) results in a slope equal to the steel axial stiffness at a distance of $k_\tau/2 \cdot \Delta\varepsilon_0$ to the curve where f_{ct} is neglected.

In beams subjected to bending moments, M , the contribution of concrete in tension can be assumed as being analogous to the uniaxial case in Section 5.1. The zone around the rebars in Figure 5.15(b) is considered as tension chord with crack spacing s_{rm} and effective reinforcement ratio $\rho_{s,ef} = A_s/A_{t,ef}$. Marti (1999) approximated the effective tension area, $A_{t,ef}$, as one third of the area below the neutral axis according to Martin et al. (1980) and Schießl (1989), and for beams he derived a constant curvature offset, $\Delta\chi_m$, due to tension stiffening, see Eq. 5.22 and Figure 5.15(c).

$$\Delta\chi_m = \frac{\Delta\varepsilon_0}{d - x^II} \approx \frac{\lambda f_{ct}}{6a_s E_s} \quad (5.22)$$

where x^II = depth of concrete compression zone in cracked elastic state, a_s = cross-sectional area of tensile reinforcement per unit width. Burns (2012) proposed a solution for $\Delta\chi_m$ using an effective reinforcement ratio compatible with the Bernoulli bending theory. To take into account a loss of bond stress due to creep under sustained loads she reduced $\Delta\chi_m$. As a limit case she investigated an unloading of a tension chord for a complete loss of bond stress (equivalent to setting $k_\tau = 0$); a reloading case, however, was not investigated.

In the rotation-symmetric Quadrilinear Sector Model (QSM) for slabs Muttoni (2008) further revised Eq. 5.22 by setting $\lambda = 1$, $\rho \approx a_s/h$, and reducing E_s by a factor β_E to take an orthogonal instead of radial and tangential reinforcement layout into account, see Section 4.2.2:

$$\Delta\chi_{TS} = \frac{f_{ct}}{6\rho h \beta_E E_s} \quad (5.23)$$

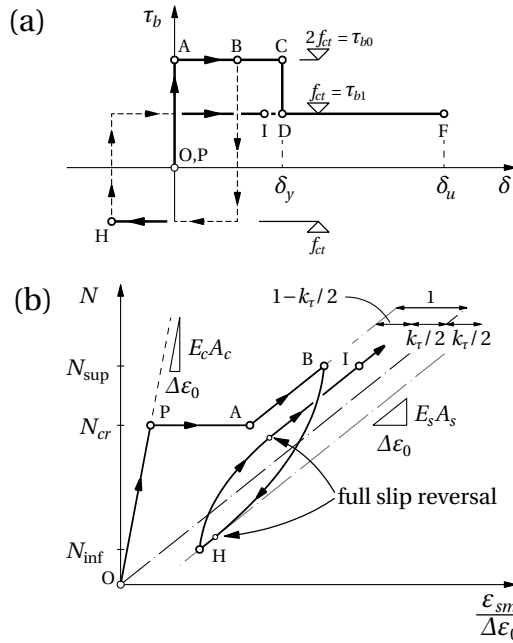


Figure 5.16: (a) Rigid-perfectly plastic bond-slip relationship for URL cycles, (b) elastic URL load path for tension chord [refer to Figs. 5.4 and 5.6]

Fictitious Crack Model

In displacement-controlled tensile tests on short concrete specimens a softening behavior instead of a sudden brittle failure was observed after tensile strength was reached at the weakest point inside the specimen (Weibull 1939; Hughes and Chapman 1966; Evans and Marathe 1968; Heilmann et al. 1969). The softening at this point accompanied deformation localization in a single fracture process zone because of progressive micro-cracking between the cement matrix and aggregates (Sigrist 1995; Kaufmann 1998; Kenel 2002).

The Fictitious Crack Model (FCM) was proposed by Hillerborg (Hillerborg et al. 1976; Hillerborg 1983) in which the total elongation of a concrete beam [with initial length L , see Figure 5.17(a)] after cracking, ΔL , is composed of the elastic unloading deformation of the intact beam part [Figure 5.17(b)] and a local deformation due to the softening inside the fracture process zone. A corresponding stress–crack opening relationship [Figure 5.17(c)] assumes that the fracture process zone has an initial length of zero, i.e. is a fictitious crack. The tensile strength decreases with increasing crack opening, w , until it drops to zero at a critical value, w_{cr} , and the fictitious crack becomes a real crack.

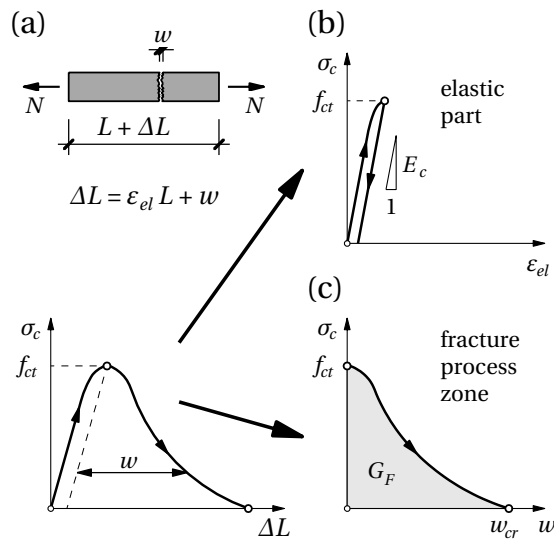


Figure 5.17: Fictitious Crack Model by Hillerborg (1983): (a) behavior of concrete beam loaded in tension; (b) stress–strain relationship of elastic beam parts; (c) stress–crack opening relationship inside fracture process zone (adapted from Sigrist 1995)

The softening behavior of concrete in the fracture process zone was described by various analytical functions. Common relationships are either constant (Dugdale 1960) or linear (Hillerborg 1983; Zhu 1991), bilinear (Petersson 1981), power functions (Foote et al. 1987), or e.g. balances of elastic and plastic energy (Barenblatt 1962); see summary by Kenel (2002). The area below the stress–crack opening curve represents the specific fracture energy in tension, G_F , which is dissipated per unit area of the fracture process zone until complete separation of the two specimen parts occurs. Wittmann et al. (1988), Hordijk (1992) and Trunk (1999) experimentally confirmed a primary dependence of G_F on the concrete tensile strength and

the aggregate size. Following CEB-FIP Model Code 90 (CEB 1993), Marti (Marti 1999; Marti et al. 1999) proposed an empirical formula for the specific fracture energy, depending on concrete tensile strength, f_{ct} (in MPa), and maximum aggregate size, d_g (in mm):

$$G_F = \frac{f_{ct} \sqrt[4]{d_g}}{80 \text{ mm}^{-3/4}} \quad (\text{in N/mm}) \quad (5.24)$$

5.2.3 Modified Sector Model

In the rotation-symmetric sector model based on Kinnunen and Nylander (1960) isolated rigid slab segments are considered, which rotate around the edge of a central column with a rotation angle, ψ , see Figure 5.18. Equilibrium of moments results in a shear force as a function of the slab rotation, $V_{skt}(\psi)$, according to Muttoni (2008):

$$V_{skt}(\psi) = \frac{2\pi}{r_q - r_c} \cdot \left[m_r(\psi) \cdot r_0 + \int_{r_o}^{r_s} m_t(\psi) dr \right] \quad (5.25)$$

A quadrilinear moment–curvature relationship is suggested and the radial curvature χ_r of the radial moment m_r at $r = r_0$ is assumed as $\chi_r = \psi/r_0$ and the tangential curvature as $\chi_t = \psi/r$ along the segment. The maximum slab resistance is limited by the flexural capacity, V_{flex} (Eq. 4.2), which is reached as soon as the bending resistance, m_R , of the entire radial and tangential reinforcement is fully activated.

In Chapter 4 the Modified Sector Model (MSM) introduces a strength reduction factor, κ_V (Eq. 4.8), for the shear crack-crossing longitudinal reinforcement, thus taking the influence of shear on the flexural behavior into account. κ_V depends on the mechanical longitudinal reinforcement ratio, $\omega = \rho f_{sy}/f_c$, see Eqs. 4.9–4.10. Eq. 5.26 follows from Eq. 5.25, multiplied by a reduction factor with m_r calculated at $r = r_0$ and corresponds to Eq. 4.11.

$$V_{mod}(\psi) = \frac{1}{1 + \kappa_V \frac{m_r(\psi) r_0}{m_R r_s}} \cdot V_{skt}(\psi) \quad (5.26)$$

In the Critical Shear Crack Theory (CSCT) Muttoni (2008) proposed a concrete failure criterion as function of ψ , $V_{Rc}(\psi)$, as follows:

$$V_{Rc}(\psi) = \frac{0.3 u_0 d_v \sqrt{f_c}}{0.4 + 0.125 \psi d_m k_g} \quad (5.27)$$

where u_0 = control perimeter at $d_v/2$ distance to support area, d_v = shear-resisting effective depth, d_m = average effective depth, $k_g = 48/(d_g + 16 \text{ mm})$, d_g = maximum aggregate size, and f_c = cylinder compressive strength of concrete. For slabs without shear reinforcement the intersection of Eqs. 5.26 and 5.27 determines the (theoretical) punching resistance of the slab, V_{R0} , see also Section 4.2.1, p. 71.

The punching resistance of slabs with shear reinforcement cannot exceed the crushing resistance of the concrete strut near the column (Beutel 2003), $V_{R,crush}$, which can be estimated as follows (Fernández Ruiz and Muttoni 2009):

$$V_{R,crush}(\psi) = k_{sys} V_{Rc}(\psi) \quad (5.28)$$

where $V_{Rc}(\psi)$ from Eq. 5.27 is multiplied by an empirical system factor, k_{sys} .

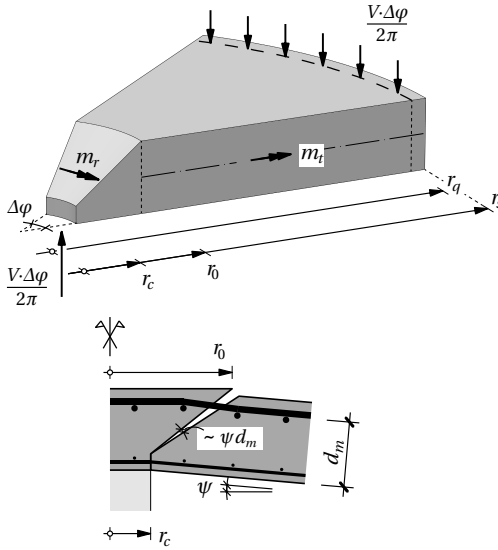


Figure 5.18: Sector model with rigid outer slab segment and acting forces (Muttoni 2008)

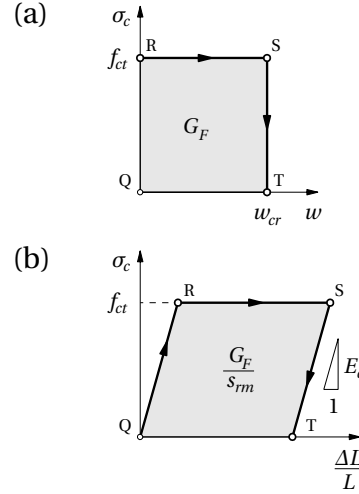


Figure 5.19: (a) Stress–softening diagram acc. to Dugdale (1960), (b) smeared crack approach

5.2.4 Effect of URL cycles on slab behavior

Extension of Modified Sector Model by concrete softening

The consideration of the softening behavior of concrete after cracking, which was neglected in the MSM in Chapter 4, results in a further deformation reduction, in addition to the tension stiffening effect. The Dugdale model (Dugdale 1960) provides the simplest approach to take the effect of interlocking cement fibers into account, as the tensile strength is maintained constant until it drops to zero at w_{cr} [Figure 5.19(a)] where all fibers are pulled out. This model has the advantage of omitting a crack-opening dependence of the transferrable stress in the fracture zone below w_{cr} . Here, the fracture zone developing in each crack element is smeared along its length s_{rm} . Upper and lower boundaries for s_{rm} are given according to the TCM, see Eq. 5.2. In fact s_{rm} is often determined by the spacing of the transverse reinforcement. The area QRST below the stress–strain curve in Figure 5.19(b) thus represents the specific fracture energy G_F divided by s_{rm} . Accordingly, the load–average strain and moment–curvature diagrams in Figure 5.20(a) and (b) are modified by this additional area QRST, which is now $G_F A_{t,ef} / s_{rm}$. After the cracking load N_{cr} (or the cracking moment per unit width m_{cr}) is reached, the curves

ascend reflecting the cracked axial (flexural) stiffness until the critical crack opening is reached. Subsequently, the curves are horizontally shifted back to the original quadrilinear curve by $\Delta\epsilon_{cr}$ ($\Delta\chi_{cr}$, respectively), as already shown in Figure 5.15.

Applying Eq. 5.26 using the quintilinear moment–curvature relationship of Figure 5.20(b) (OQRSCDF) results in:

$$V_{mod}(\psi) = \frac{1}{1 + \kappa_V \frac{m_r(\psi)}{m_R} \frac{r_0}{r_s}} \cdot \frac{2\pi}{r_q - r_c} \cdot \left[\begin{aligned} &m_r(\psi) \cdot r_0 + m_R \langle r_y - r_0 \rangle + \\ &+ EI^I \psi \left\langle \ln \frac{\tilde{r}_{crs}}{r_y} \right\rangle + EI^I \Delta\chi_{TS} \langle \tilde{r}_{crs} - r_y \rangle + \\ &+ (m_{cr} + \Delta m_{cr}) \langle \tilde{r}_{cr} - \tilde{r}_{crs} \rangle + EI^I \psi \left\langle \ln \frac{r_s}{r_{cr}} \right\rangle + \\ &+ EI^I \psi \left\langle \ln \frac{r_{cr}}{\tilde{r}_{cr}} \right\rangle + EI^I (\Delta\chi_{TS} + \Delta\chi_{cr}) \langle r_{cr} - \tilde{r}_{cr} \rangle \end{aligned} \right] \quad (5.29)$$

where m_{cr} = cracking moment, m_R = bending resistance [Δm_{cr} and $\Delta\chi_{cr}$ according to Figure 5.20(b)], EI^I and EI^I = uncracked and cracked flexural stiffness ($\Delta\chi_{TS}$ according to Eq. 5.23), $r_0 \leq r_i = \psi/\chi_i \leq r_s$ with subscript $i = cr, crs$ or y . Tilde symbols denote curvatures and corresponding radii at points R, S instead of P, A (e.g. $\tilde{\chi}_{cr} = \chi_{cr} + \Delta m_{cr}/EI^I$, $\tilde{r}_{cr} = \psi/\tilde{\chi}_{cr}$). Operator $\langle x \rangle$ is x for $x \geq 0$ and 0 for $x < 0$.

Omitting G_F [corresponding to the quadrilinear relationship in Figure 5.20(b), path OPTCDF] results in Δm_{cr} and $\Delta\chi_{cr}$ equal to zero, and \tilde{r}_{cr} and \tilde{r}_{crs} are identical to r_{cr} and r_{crs} . The last line of Eq. 5.29 is dropped and the remaining terms in the squared brackets are equivalent to Eq. 6 in Muttoni (2008). Additionally neglecting f_{ct} [= bilinear relationship in Figure 5.20(b)] leads to $\Delta\chi_{TS} = 0$. Only the first three terms in the squared brackets of Eq. 5.29 remain, where r_{cr} and r_{crs} derive to r_s . For $\kappa_V = 0$ Eq. 5.29 corresponds to Eq. 7 in Muttoni (2008).

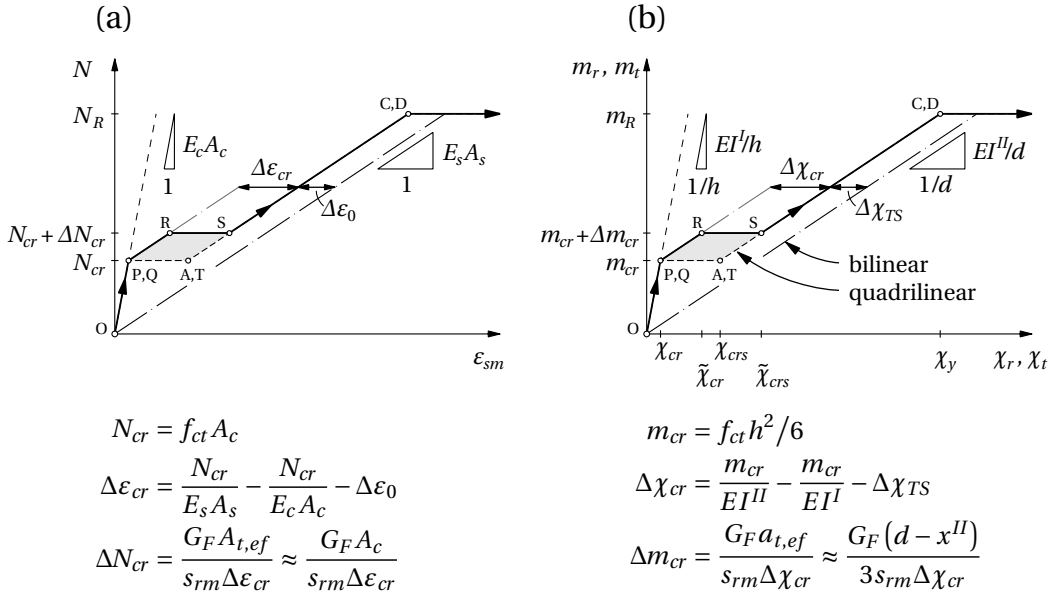


Figure 5.20: Extension of (a) load–average elongation and (b) moment–curvature diagram with stress–softening behavior of concrete after cracking

Unloading and reloading of slabs

Every point in the slab segment is unloaded and reloaded from a different stress level, because the slab moments are radius-dependent, see Figure 5.21(a). To avoid having different URL paths for every slab point, a simplification is made which is explained for the elastic uniaxial tension chord in Figure 5.21(b). By assuming that full slip reversal is always reached, i.e. a sufficiently large load difference $N_{\text{sup}} - N_{\text{inf}}$ is ensured, the curve progression can be approached by a rigid–fully cracked envelope. Unloading from B to H is modeled by an immediate load drop to the parallel line at $k_{\tau}/2 \cdot \Delta\epsilon_0$ distance to the naked steel characteristic (BY), and a further curve progression along that parallel line down to N_{inf} (= YH). Reloading is modeled likewise by path HZI.

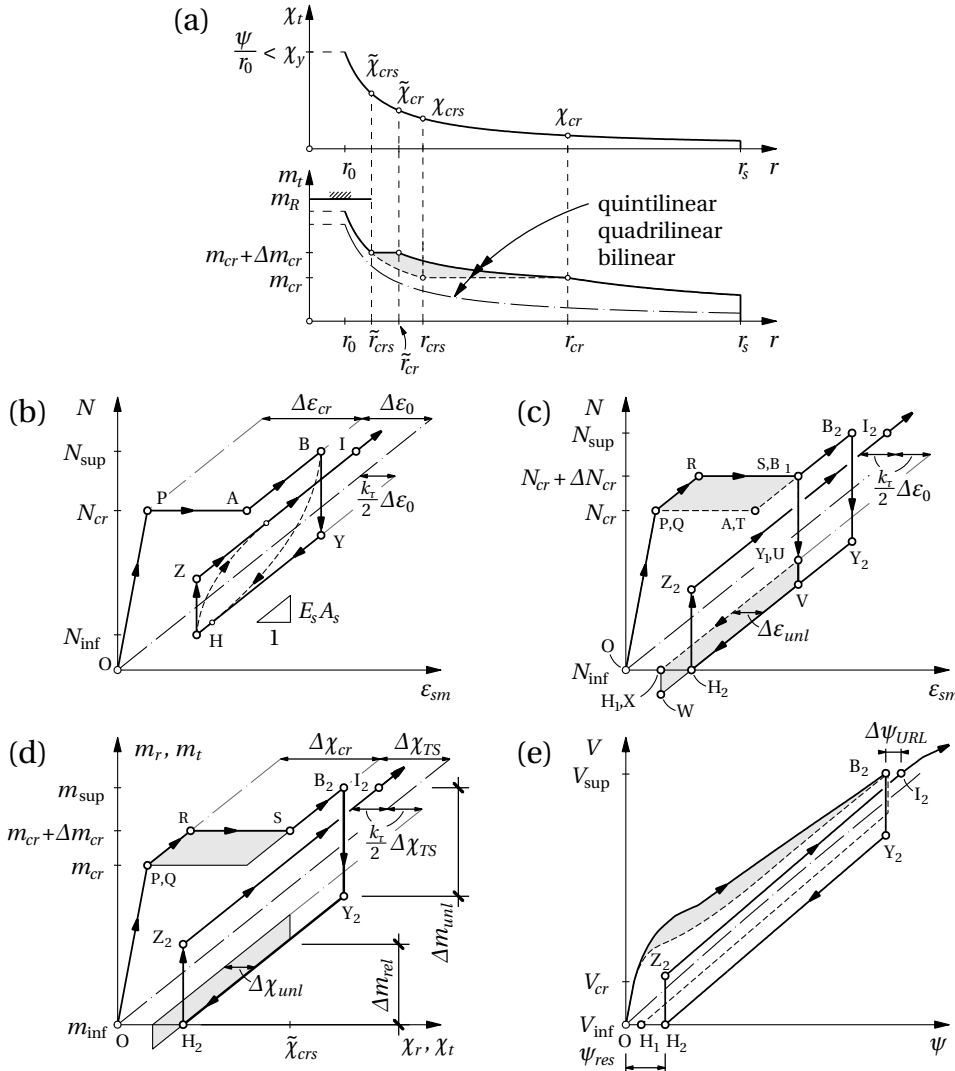


Figure 5.21: (a) Tangential moment distribution along segment (loading in elastic state), (b) simplification of URL load path, (c) elastic URL load path of tension chord, (d) moment–curvature relationship of slab, (e) shear force–rotation curve of slab

Figure 5.21(c) illustrates the modified loading path $OPRB_1$ where point B_1 is at $N_{cr} + \Delta N_{cr}$. Accordingly, the unloading path is now shifted downwards by a constant value $E_s A_s \Delta \varepsilon_{unl}$ (= distance UV) where $\Delta \varepsilon_{unl}$ is determined by equalizing the two grey areas (QRST and UVWX), thus assuming that the fracture energy during loading is the same as the energy required to push the fibers back during unloading. Now unloading takes place along path $B_1 UVH_2$ (at full unloading). $H_1 = X$ is actually shifted horizontally to H_2 and not vertically to W, giving a small error indicated by the extra triangle XWH_2 below the abscissa that is considered in the calculation of $\Delta \varepsilon_{unl}$.

Unloading starting at $B_2 > B_1$ does not provide any supplemental vertical shift. Thus the unloading path $B_2 Y_2 H_2$ runs along the parallel line at a total horizontal distance of $\Delta \varepsilon_{unl} + k_\tau / 2 \cdot \Delta \varepsilon_0$ to the naked steel characteristic down to N_{inf} (point H_2) where a residual elongation of the rebar remains (distance OH_2). The reloading path back to N_{sup} , $H_2 Z_2 I_2$, runs along a parallel line at $k_\tau / 2 \cdot \Delta \varepsilon_0$ distance to the naked steel characteristic, and thus no softening is taken into account in reloading. For reloading the same value of k_τ was assumed as for unloading (see Eq. 5.6). Therefore back at N_{sup} a horizontal gap between I_2 and B_2 of $(1 - k_\tau / 2) \Delta \varepsilon_0$ remains after completion of the URL cycle.

The moment–curvature relationship [Figure 5.21(d)] is modified in the same way. Unloading from m_{sup} to m_{inf} (path $B_2 Y_2 H_2$) is accomplished by an immediate vertical drop of Δm_{unl} , Eq. 5.30, and a subsequent linear decrease with slope EI^H . Reloading (path $H_2 Z_2 I_2$) exhibits a vertical rise of Δm_{rel} , Eq. 5.31, and the same linear increase back to m_{sup} (point I_2), where there also remains a horizontal gap in relation to the initial load path, $\Delta \psi_{URL} = (1 - k_\tau / 2) \Delta \chi_{TS}$.

$$\Delta m_{unl} = EI^H \left[\left(1 + \frac{k_\tau}{2} \right) \Delta \chi_{TS} + \Delta \chi_{unl} \right] \quad (5.30)$$

$$\Delta m_{rel} = EI^H [k_\tau \Delta \chi_{TS} + \Delta \chi_{unl}] \quad (5.31)$$

where

$$\Delta \chi_{unl} = \frac{\Delta m_{cr} \Delta \chi_{cr}}{EI^H \left(\tilde{\chi}_{crs} - \frac{k_\tau}{2} \Delta \chi_{TS} \right)} \quad (5.32)$$

Based on the moment–curvature relationships for the URL cycle $B_2 Y_2 H_2 Z_2 I_2$ load–rotation curves can be calculated, see Figure 5.21(e). It is assumed that the entire prefactor in Eq. 5.29, which takes transverse shear into account, remains constant at its m_{sup} -value. Thus the URL load–rotation curves are also linear. The increase of rotation resulting after the URL cycle of a slab in the cracked elastic state, $\Delta \psi_{URL} = \psi_{I_2} - \psi_{B_2}$, can be determined for a known load difference $V_{sup} - V_{inf}$, resulting in a constant value due to the rigid–fully cracked approximation:

$$\Delta \psi_{URL} = \frac{\left(1 - \frac{k_\tau}{2} \right) \Delta \chi_{TS} r_s}{1 + \ln \left(\frac{r_s}{r_0} \right)} \quad (5.33)$$

Validation with experiments

a) Experimental database

In the literature only a small number of experiments was found with single unloading and reloading cycles before the load was increased up to failure. At ETH Zurich four slabs (P2–3, P5–6) without post-tensioning were tested in the 1970s (Marti et al. 1977; Pralong et al. 1979). All slabs had an octagonal shape, a central column with diameter 300 mm and were loaded by eight cylinders, see Figure 5.22(a). Slabs P2, P3 and P5 had an orthogonal reinforcement layout, P6 included only tangential ring reinforcement, but radially arranged stirrups around the column. Here, a secant rotation was calculated from the average deflection at the slab edge, assuming zero deflection at the column edge. Two of the slabs used in Lips' (2012) investigation on the punching resistance of square slabs with large amounts of shear reinforcement, PF3 and PF5, were also unloaded and reloaded. The layout of the two slabs with orthogonal reinforcement is given in Figure 5.22(b). The slab rotations of the weak axis were measured directly using inclinometers that were installed near the applied load.

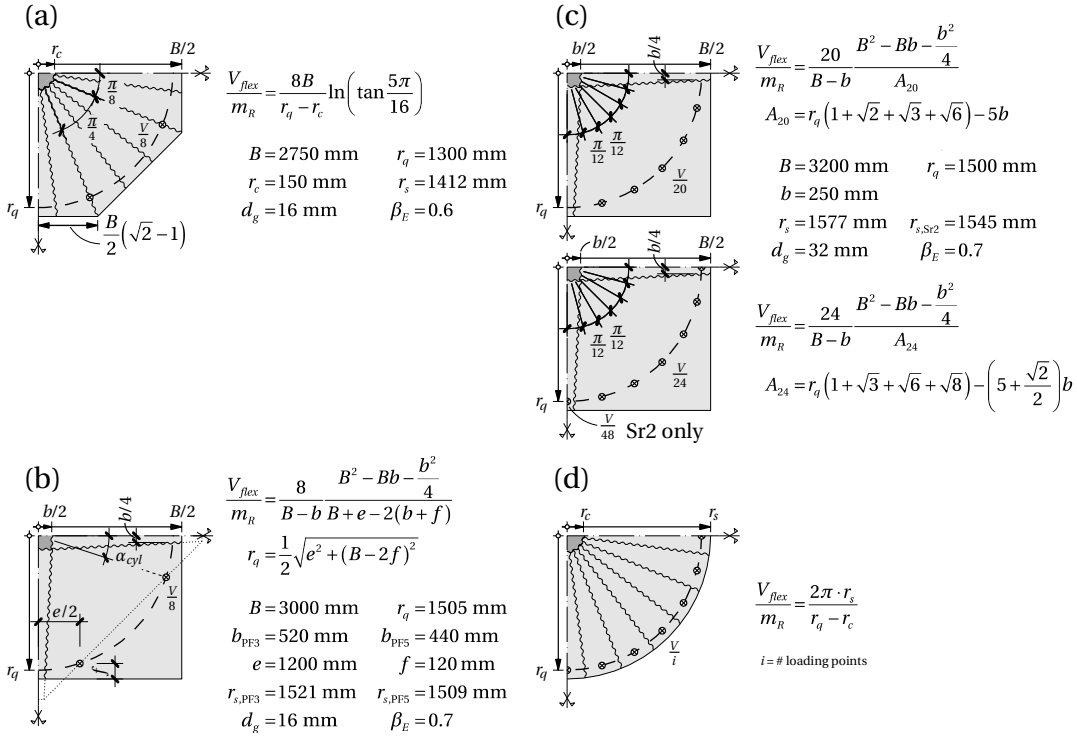


Figure 5.22: Slab dimensions and YLMs: (a) fan mechanism for round column (slabs P2/3/5/6); four-point star mechanisms for (b) eight (PF3/5), (c) 20 (Sd1–2, Sh2–4, Sr1–2) and 24 load points (Sr3); (d) truncated cone mechanism of equivalent circular slab

An experimental campaign on several strengthening systems for existing RC flat slabs was carried out in Chapter 3 and Appendix B. Three slabs, Sh2–4, were strengthened against punching shear by an externally prestressed steel head placed underneath the slab. Another three slabs, Sr1–3, contained non-laminated and prestressed CFRP straps installed crosswise around the column in pre-drilled and pre-cut openings, and anchored on the bottom side

Table 5.1: Slab properties for model validation

| Reference | Slab | unl ^a | rel ^a | h [mm] | d_m [mm] | ρ_m [%] | f_c [MPa] | f_{ct} [MPa] | E_c [GPa] | f_{sy} [MPa] | E_s [GPa] | $\frac{V_{flex}}{m_R}$ [-] | ω_m [-] | κ_V [-] |
|--------------------------|------|------------------|------------------|-------------|---------------|-----------------|----------------|-------------------|-------------------|-------------------|----------------|-------------------------------|-------------------|-------------------|
| Marti et al. (1977) | P2 | yes | yes | 180 | 143 | 1.48 | 37.3 | 3.4 ^b | 37.2 | 558 | 206 | 7.71 | 0.22 | 0.46 |
| | P3 | yes | yes | 180 | 152 | 1.40 | 35.8 | 3.3 ^b | 36.6 | 558 | 206 | 7.71 | 0.22 | 0.46 |
| Pralong et al. (1979) | P5 | yes | yes | 180 | 154 | 1.31 | 27.1 | 2.7 ^b | 37.3 | 515 | 204 | 7.71 | 0.25 | 0.53 |
| | P6 | yes | yes | 180 | 154 | 1.31 | 30.0 | 2.5 ^b | 38.1 | 515 | 204 | 7.71 | 0.22 | 0.48 |
| Lips (2012) | PF3 | yes | yes | 250 | 209 | 1.50 | 37.1 | 3.3 ^c | 33.4 ^c | 583 | 200 | 8.14 | 0.24 | 0.50 |
| | PF5 | yes | yes | 400 | 354 | 1.50 | 33.4 | 3.1 ^c | 32.2 ^c | 580 | 200 | 7.74 | 0.26 | 0.57 |
| Appendix B | Sd1 | yes | yes | 256 | 199 | 1.58 | 51.0 | 3.9 ^b | 38.5 | 517 | 205 | 7.39 | 0.16 | 0.33 |
| | Sd2 | yes | yes | 257 | 202 | 1.56 | 52.2 | 3.9 ^b | 39.5 | 517 | 205 | 7.39 | 0.15 | 0.31 |
| Lips et al. (2014) | Sh2 | yes | no | 260 | 199 | 1.58 | 59.1 | 4.0 ^b | 37.4 | 514 | 205 | 7.39 | 0.14 | 0.28 |
| | Sh3 | yes | no | 260 | 203 | 1.55 | 47.6 | 3.9 ^b | 40.0 | 569 | 205 | 7.39 | 0.19 | 0.38 |
| | Sh4 | yes | no | 255 | 207 | 1.52 | 45.3 | 3.4 ^b | 40.3 | 569 | 205 | 7.39 | 0.19 | 0.40 |
| Section 3.2 | Sr1 | yes | no | 257 | 200 | 1.57 | 48.1 | 3.6 ^b | 41.0 | 517 | 205 | 7.39 | 0.17 | 0.35 |
| | Sr2 | yes | no | 187 | 138 | 1.46 | 43.1 | 3.4 ^b | 35.8 | 521 | 205 | 7.39 | 0.18 | 0.36 |
| | Sr3 | yes | no | 325 | 264 | 1.44 | 44.2 | 3.4 ^b | 35.1 | 525 | 205 | 7.24 | 0.17 | 0.36 |

^a unl = unloading path, rel = reloading path of non-strengthened slabs

^b values from double-punch tests on cylinders ($h = \emptyset = 150$ mm) acc. to Chen (1970); Marti (1989)

^c values calculated using relationships acc. to SIA 262 (2013): $E_c = 10000 \text{ MPa}^{2/3} \cdot \sqrt[3]{f_c}$, $f_{ct} = 0.3 \text{ MPa}^{1/3} \cdot f_c^{2/3}$ (both in MPa)

of the slab by a steel compression frame. The slabs [for properties see Figure 5.22(c)] were preloaded and unloaded before the strengthening systems were installed and applied. Two further slabs, Sd1–2, were investigated without subsequent strengthening, but to quantify the effect of boreholes (required for the strap system) on the punching resistance of the non-strengthened slabs. The slab properties and yield-line mechanisms (YLMs) of all specimens are summarized in Figure 5.22(a)–(c) and Table 5.1. For the MSM the slab and column geometries were transformed to an equivalent circular slab with the same flexural capacity, Figure 5.22(d). For actual circular slabs and columns $\beta_E \approx 0.6$ was used (Muttoni 2008), for square ones $\beta_E \approx 0.7$, see Section 4.3.1. Slab rotations were calculated from deflections measured near the column and the slab edge. The maximum rotation of the weak axis was selected, except for Sr1–3 where only deflections along the strong axis were recorded during preloading.

The zero measurements in the experiments prior to loading define the origin \hat{O} of the load–rotation curves, see Figure 5.23. Thus the dead weight G of the slab and the equipment, and the resulting slab rotation ψ_G had to be added and the coordinate system was shifted from \hat{O} to O . ψ_G was estimated using elasticity theory. Assuming an uncracked behavior of an equivalent circular slab, which is ring-supported at r_c , and ring-loaded along the slab edge with $r_s \approx r_q$, maximum slab rotation at the slab edge is calculated according to Beyer (1956):

$$\psi_G = \frac{3G}{\pi} \frac{1-\nu}{E_c h^3} \frac{r_q^2 - r_c^2}{r_q} \quad (5.34)$$

where ν = Poisson's ratio ≈ 0.2 .

In the following modeled and measured load–rotation curves of non-strengthened slabs are compared in normalized diagrams (see Figs. 5.24 and 5.25) according to Muttoni (2008). On the ordinate the equivalent shear stress, $V/(u_0 d_v)$ is divided by $\sqrt{f_c}$, assumed as being proportional to the concrete shear strength. On the abscissa, the product $\psi d_m k_g$ is plotted.

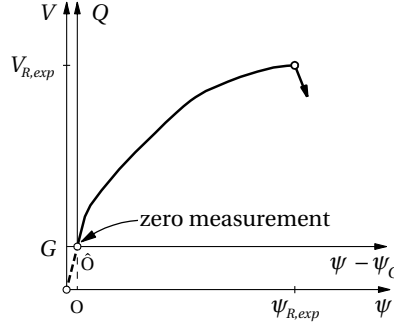


Figure 5.23: Shift of origin for experimental curves

b) Monotonic loading considering concrete softening

In Figure 5.24, the observed monotonic load paths (solid lines) of five slabs are compared to calculated load paths, Eqs. 5.26 and 5.29, without (dotted) and with (dashed) consideration of concrete softening by using the estimation of G_F in Eq. 5.24. The shapes of the dashed curves show a better agreement with the measurements than the dotted curves. For higher applied loads both calculations gradually result in the same rotations, since the stiffening effect due to the bridging fibers is exhausted as soon as all crack widths exceed w_{cr} .

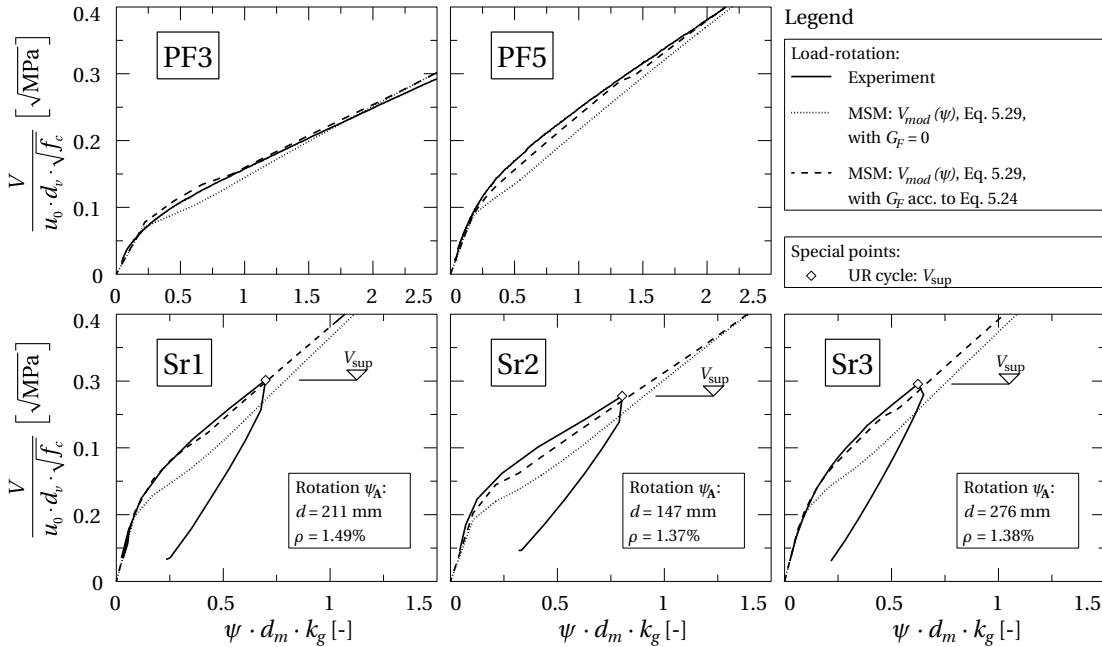


Figure 5.24: Monotonic loading: comparison of quadri- and quintilinear MSM to experimental results

c) Residual rotation after unloading and rotation increase after reloading

Fourteen slabs were completely unloaded to $V = G$, eight of them were reloaded, see Table 5.1. Slab PF3 failed before the URL cycle could be completed. The experimentally obtained paths are displayed in Figure 5.25, together with modeled unloading and reloading paths according to Figure 5.21(e) (dashed curves). In the model the maximum load before unloading, V_{sup} , resulted from adjusting the computational slab rotation to the measured one before unloading the slab. The slopes of the measured URL paths are steeper than the modeled ones because of the rigid–fully cracked approach of the moment–curvature relationship. The residual slab rotations after unloading are underestimated by the model by 15% on average, see Table 5.2. The Coefficient of Variation (COV) of 38%, however, is quite high; it is much lower for the complete data sets of the author’s experiments (13%). The predicted rotation increases after completion of the full URL cycle, according to Eq. 5.33, overestimate the experimental values by 16% on average, the COV is 51%, see Table 5.2. By excluding the URL cycle of P5, the average value decreases to 0.94 with a COV of 15%. In the observed experiments the rotation increases are only 23% (on average) of the residual rotations, see also Table 5.2.

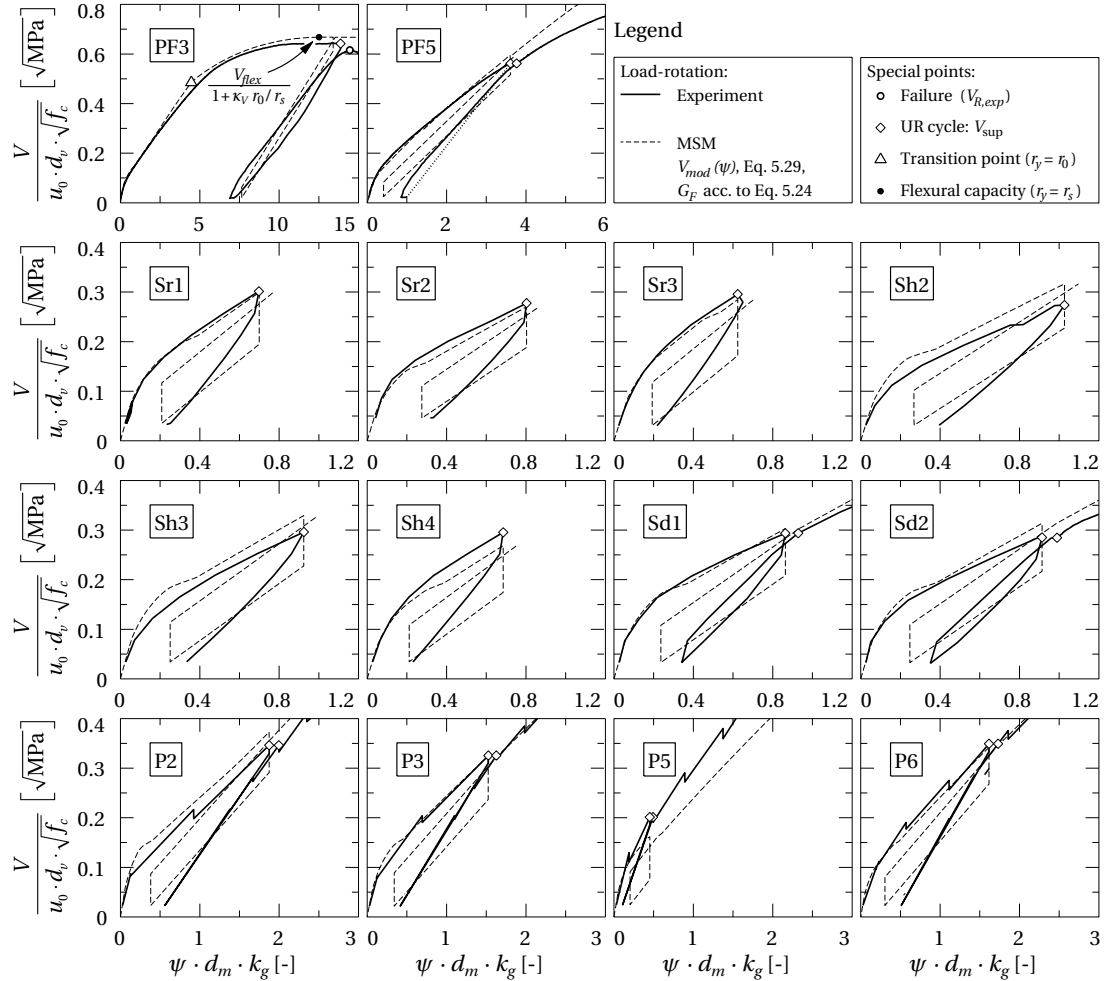


Figure 5.25: Comparison of predicted and observed unloading (and reloading) cycles

Table 5.2: Residual slab rotation ψ_{res} and rotation increase after reloading ($\Delta\psi_{URL,mod}$ according to Eq. 5.33)

| Slab | $\psi_{res,exp}$ [mrad] | $\psi_{res,mod}$ [mrad] | $\frac{\psi_{res,mod}}{\psi_{res,exp}}$ [-] | avg. | COV | $\Delta\psi_{URL,exp}$ [mrad] | $\Delta\psi_{URL,mod}$ [mrad] | $\frac{\Delta\psi_{URL,mod}}{\Delta\psi_{URL,exp}}$ [-] | avg. | COV | $\frac{\Delta\psi_{URL,exp}}{\psi_{res,exp}}$ |
|------------------|----------------------------|----------------------------|--|------|------|----------------------------------|----------------------------------|--|------|------|---|
| P2 | 2.61 | 1.77 | 0.68 | | | 0.57 | 0.48 | 0.84 | | | 0.22 |
| P3 | 1.83 | 1.49 | 0.82 | | | 0.43 | 0.50 | 1.14 | | | 0.23 |
| P5 | 0.47 | 0.88 | 1.84 | | | 0.17 | 0.43 | 2.45 | | | 0.36 |
| P6 | 2.21 | 1.32 | 0.60 | 0.92 | 0.54 | 0.50 | 0.40 | 0.79 | 1.21 | 0.58 | 0.23 |
| PF3 | 22.0 | 24.4 | 1.11 | | | – | 0.40 | – | | | – |
| PF5 | 1.62 | 0.78 | 0.48 | | | 0.30 | 0.25 | 0.84 | | | 0.19 |
| Sd1 | 1.72 | 1.19 | 0.69 | | | 0.33 | 0.35 | 1.08 | | | 0.19 |
| Sd2 | 1.74 | 1.22 | 0.70 | | | 0.38 | 0.36 | 0.96 | | | 0.22 |
| Sh2 | 1.99 | 1.35 | 0.68 | | | – | 0.36 | – | | | – |
| Sh3 | 1.65 | 1.24 | 0.75 | | | – | 0.36 | – | | | – |
| Sh4 | 1.12 | 1.02 | 0.92 | 0.80 | 0.13 | – | 0.33 | – | 1.02 | – | – |
| Sr1 | 1.18 | 1.04 | 0.88 | | | – | 0.35 | – | | | – |
| Sr2 | 2.31 | 2.00 | 0.86 | | | – | 0.46 | – | | | – |
| Sr3 | 0.82 | 0.73 | 0.89 | | | – | 0.30 | – | | | – |
| Total (14 slabs) | | | | 0.85 | 0.38 | Total (7 slabs) | | | 1.16 | 0.51 | 0.23 |

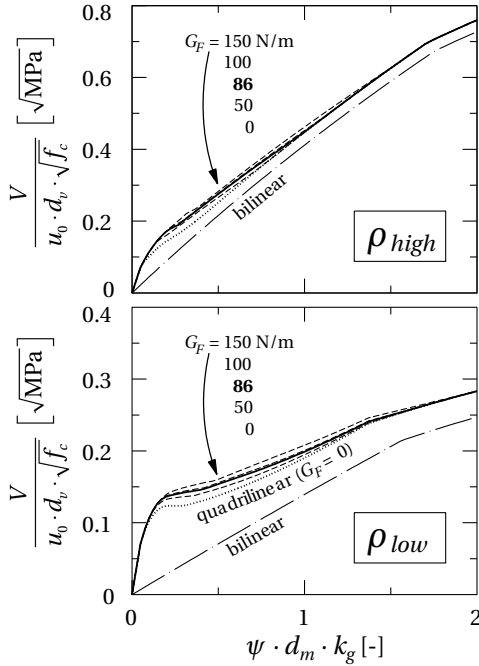
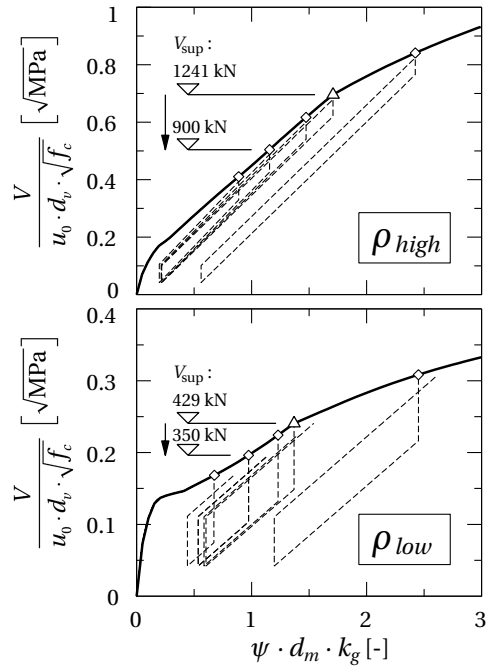
Parametric study

Based on the validated models for the residual rotation and the rotation increase after one URL cycle, a parametric study for non-strengthened and strengthened slabs was performed in order to evaluate the sensitivity of the results to some assumptions that were made in the models. In the non-strengthened case, the following three parameters were investigated: the influence of G_F on the deformation behavior, the influence of V_{sup} on the residual rotation, and the influence of the rotation increase due to an URL cycle, $\Delta\psi_{URL}$, on the punching resistance. Two slabs with the same geometry and material properties ($r_c = 159$ mm, $r_q = 1500$ mm, $r_s = 1575$ mm, $h = 250$ mm, $d_m = 200$ mm, $G = 75$ kN, $f_c = 30$ MPa, $E_c = 35$ GPa, $f_{ct} = 2.9$ MPa, $d_g = 32$ mm, $f_{sy} = 500$ MPa, $E_s = 205$ GPa, $\beta_E = 0.7$), but different reinforcement ratios ($\rho_{high} = 2.1\%$, $\rho_{low} = 0.5\%$) were selected for the first two parameters. For the third parameter ρ (0.5% and 2.1%), d_m (100, 200 and 400 mm, $d/h = 0.8$) and f_c (30 and 60 MPa), and thus also f_{ct} (2.9 and 4.6 MPa) and G_F (86 and 137 N/m), were varied, see Table 5.3.

These parameters were also used for the strengthened case in which slabs were strengthened after a preloading up to V_{R0} and a full unloading down to zero to investigate the maximum possible effect of an URL cycle on the punching resistance of concrete. Because of modified slab properties after strengthening and / or different failure criteria the residual rotation ψ_{res} (= origin of new V – ψ -curve) is the critical parameter instead of $\Delta\psi_{URL}$. Four strengthening cases were investigated: The first one was a duplication and triplication of the support area (increase of the control perimeter, u_0 , and of the flexural capacity, V_{flex}), the second case was a duplication of V_{flex} by neglecting a stiffness increase (i.e. in the case of the application of very thin CFRP sheets, Harajli and Soudki 2003), the third one assumed a duplication of V_{flex}

and a stiffness increase of 50% (e.g. by applying an additional upper concrete layer, Amsler et al. 2014, or an external steelhead placed between column and slab, Lips et al. 2014). In the last case, the effect of a prestressed shear-strengthening system was investigated, which is able to compensate the residual slab rotation, see Figure 3.23. The URL cycle curves of the strengthened slabs were calculated as if they were monotonically loaded and then horizontally shifted by ψ_{res} . In the first three cases, the effect of residual slab rotations on the concrete contribution to the punching resistance, according to Eq. 5.27, was quantified. In the fourth case, the punching resistances, V_{R1} , of the prestressed and non-prestressed systems were compared, both assumed to be reached at $V_{R,crush}$, according to Eq. 5.28, with $k_{sys} = 2.5$, see Section 4.4.3.

The load–rotation curves for different specific fracture energies G_F are compared in Figure 5.26 ($G_F = 86 \text{ N/m}$ according to Eq. 5.24 and $G_F = 0, 50, 100, 150 \text{ N/m}$ were selected, whereas $G_F = 0$ is equivalent to a quadrilinear moment–curvature relationship). The effect of G_F on the deformations is only visible immediately after cracking and gradually disappears as flexural capacity is approached. In the serviceability limit state, it is therefore sufficient to refer to a simple estimation of G_F as in Eq. 5.24. G_F can be neglected in the moment–curvature relationship for the determination of the punching shear capacity.

Figure 5.26: Effect of G_F on V – ψ curveFigure 5.27: Effect of V_{sup} on ψ_{res}

In the experimental validation of the model, V_{sup} was calibrated to start unloading at the same rotation as in the measurements. In some slabs the difference between the calculated V_{sup} and the actual value was more than 15%. The curves in Figure 5.27 illustrate that, as long as no part of the slab's longitudinal reinforcement yields (below the marked triangle), the variation of residual rotation is low. In the case of the slab with ρ_{low} , a decrease of V_{sup} from 429 kN to

350 kN (−18%) reduces ψ_{res} by 11%. For the slab with ρ_{high} a decrease from 1241 kN to 900 kN (−28%) results in almost no reduction of ψ_{res} (−2%).

The effect of a URL cycle on punching resistance is shown in Figure 5.28(a) and (b) for two non-strengthened slabs with different reinforcement ratios ($\rho_{high} = 2.1\%$, $\rho_{low} = 0.5\%$), effective depths ($d_m = 100$ and 400 mm) and concrete compressive strengths ($f_c = 60$ and 30 MPa). The intersection of the load–rotation curve with the failure criterion, Eq. 5.27, denotes the punching resistance, V_{R0} . If the slabs are unloaded and reloaded, rotation ψ_{R0} increases by $\Delta\psi_{URL}$ and, accordingly, V_{R0} decreases. The limit case of a complete loss of bond between concrete and rebar, i.e. setting $k_\tau = 0$ instead of $k_\tau = 1$, doubles $\Delta\psi_{URL}$. Nevertheless, the slab rotations at failure increase by only 4% [Figure 5.28(a)] and 12% [Figure 5.28(b)], and by 7% on average (total) and maximum 14% if considering all parameter combinations, see Table 5.3. The resulting decreases of V_{R0} remain small: 2% and 5% for Figure 5.28(a) and (b), 3% on average (total) and 7% maximum.

In the first strengthening case [see Figure 5.28(c) and (d)] the increase of the column radius, r_c , increases the control perimeter, u_0 , and simultaneously the flexural capacity of the slab by a reduction of the denominator ($r_q - r_c$), see Figure 5.22. ψ_{res} causes practically no resistance decrease (smaller than 5%), see Table 5.3.

Table 5.3: Parametric study: increase of slab rotation and decrease of punching resistance resulting from UR cycle (calculations 5 and 13 correspond to Figure 5.28)

| Parameters | | | | $k_\tau = 1$ | | $k_\tau = 0$ | | $2r_c$ | | $3r_c$ | | $2V_{flex}, EI$ | | $2V_{flex}, 1.5EI$ | |
|---|---------------|----------------|---------------|--------------------------|------------------------|--------------------------|------------------------|--------------------------|------------------------|--------------------------|------------------------|--------------------------|------------------------|--------------------------|------------------------|
| # | ρ [%] | f_c [MPa] | d_m [mm] | $\Delta\psi_{R0}$ [%] | ΔV_{R0} [%] | $\Delta\psi_{R0}$ [%] | ΔV_{R0} [%] | $\Delta\psi_{R1}$ [%] | ΔV_{R1} [%] | $\Delta\psi_{R1}$ [%] | ΔV_{R1} [%] | $\Delta\psi_{R0}$ [%] | ΔV_{R0} [%] | $\Delta\psi_{R0}$ [%] | ΔV_{R0} [%] |
| 1 | 2.1 | 30 | 200 | +3 | −1 | +5 | −1 | +4 | −1 | +3 | −1 | +7 | −2 | +11 | −2 |
| 2 ^a | 2.1 | 30 | 100 | +1 | −1 | +3 | −1 | +6 | −3 | +3 | −2 | +17 | −5 | +25 | −6 |
| 3 | 2.1 | 30 | 400 | +4 | −1 | +8 | −2 | +7 | −2 | +5 | −2 | +10 | −2 | +16 | −3 |
| 4 | 2.1 | 60 | 200 | +3 | −1 | +6 | −2 | +5 | −2 | +3 | −2 | +8 | −2 | +12 | −3 |
| 5 ^a | 2.1 | 60 | 100 | +2 | −1 | +4 | −2 | +7 | −4 | +4 | −3 | +22 | −8 | +32 | −9 |
| 6 | 2.1 | 60 | 400 | +5 | −1 | +9 | −3 | +7 | −3 | +6 | −2 | +11 | −3 | +17 | −4 |
| Average ($\rho = 2.1\%$) | | | | +3 | −1 | +6 | −2 | +6 | −2 | +4 | −2 | +13 | −4 | +19 | −4 |
| Max. $\Delta\psi_R$; min. ΔV_R | | | | +5 | −1 | +9 | −3 | +7 | −4 | +6 | −3 | +22 | −8 | +32 | −9 |
| 11 ^a | 0.5 | 30 | 200 | +3 | −2 | +7 | −4 | +6 | −3 | 0 | 0 | +46 | −17 | +66 | −20 |
| 12 ^a | 0.5 | 30 | 100 | +1 | −2 | +4 | −3 | +1 | 0 | 0 | 0 | +78 | −30 | +100 | −33 |
| 13 ^a | 0.5 | 30 | 400 | +6 | −2 | +12 | −5 | +7 | −3 | +5 | −3 | +15 | −6 | +23 | −7 |
| 14 ^a | 0.5 | 60 | 200 | +4 | −2 | +8 | −5 | 0 | 0 | 0 | 0 | +69 | −26 | +88 | −28 |
| 15 ^a | 0.5 | 60 | 100 | +2 | −2 | +4 | −3 | 0 | 0 | 0 | 0 | +104 | −39 | +128 | −43 |
| 16 ^a | 0.5 | 60 | 400 | +7 | −3 | +14 | −7 | +8 | −5 | +4 | −2 | +32 | −13 | +46 | −15 |
| Average ($\rho = 0.5\%$) | | | | +4 | −2 | +8 | −4 | +4 | −2 | +2 | −1 | +57 | −22 | +75 | −24 |
| Max. $\Delta\psi_R$; min. ΔV_R | | | | +7 | −3 | +14 | −7 | +8 | −5 | +5 | −3 | +104 | −39 | +128 | −43 |
| Average (total) | | | | +3 | −2 | +7 | −3 | +5 | −2 | +3 | −1 | +35 | −13 | +47 | −14 |
| Max. $\Delta\psi_R$; min. ΔV_R | | | | +7 | −3 | +14 | −7 | +8 | −5 | +6 | −3 | +104 | −39 | +128 | −43 |

^a including plastic rotations before unloading (V_{sup} above transition point)

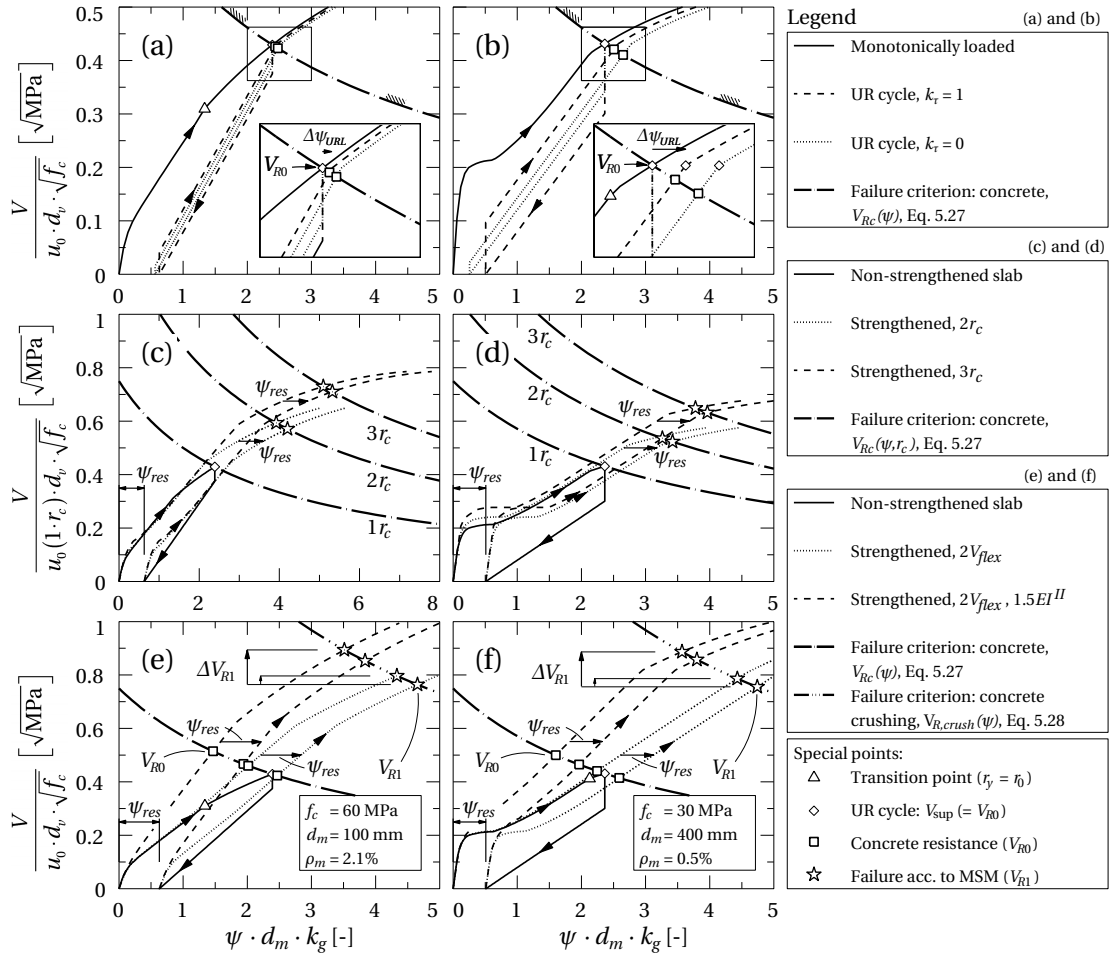


Figure 5.28: Effect of URL cycle on: (a) and (b) V_{R0} of non-strengthened slab, (c) and (d) V_{R1} of strengthened slab (increase of support area), (e) and (f) V_{R0} of strengthened slab (increase of flexural capacity and/or stiffness) and ΔV_{R1} due to prestressed system. The diagrams were evaluated for the parameters indicated in the boxes in (e) and (f), respectively

In the second case with doubled V_{flex} and no flexural stiffness increase, a horizontal shift of the load–rotation curves by ψ_{res} caused by the URL cycle increases ψ_{R0} and thus decreases V_{R0} [see Figure 5.28(e) and (f)]. The amount of increase and decrease, respectively, is influenced by irreversible plastic slab rotations that have occurred before unloading and strengthening in some of the slabs (indicated in Figure 5.28 by triangles, and in Table 5.3). In the case of highly reinforced slabs ($\rho_{high} = 2.1\%$) the reinforcements of the two thin slabs were only plasticized around the column. Thus the rotation increase is 13% on average [22% for the slab in Figure 5.28(e)] and the decrease of the concrete contribution to the punching resistance is less than 8% when compared to $\psi_{res} = 0$ (4% on average). This decrease is much higher for low reinforced slabs ($\rho_{low} = 0.5\%$) with much larger plastic deformations before unloading, especially for the thin slabs. An average decrease of concrete resistance of 22% results [only 6% for the slab in Figure 5.28(f)], with a maximum loss of 39%. If additionally the flexural stiffness

is increased by 50% (third case), the obtained increases of ψ_{R0} are approximately 30% higher; the corresponding reductions of V_{R0} are 10% higher on average compared to those without stiffness increase.

In the fourth case, the applied prestressing force is adjusted in such a manner as to fully compensate ψ_{res} in cases 2 and 3 and thus does not result in a reduced contribution of the concrete to punching resistance. The prestressed system (with $\psi_{res} = 0$) is compared to the non-prestressed one (with $\psi_{res} > 0$). If only V_{flex} is doubled (as in case 2, e.g. using the prestressed CFRP straps of Chapter 3), strap prestressing leads to an average increase of punching resistance, ΔV_{R1} , of 5%, see Figure 5.28(e) and (f). If the prestressed shear-strengthening system further increases slab stiffness by 50% (as in case 3, e.g. by a prestressed external steelhead, Lips et al. 2014), a ΔV_{R1} of 14% results on average.

5.2.5 Conclusions

Using the Modified Sector Model (MSM) load–rotation curves were derived to discuss the effect of unloading and reloading (URL) cycles on the deformation behavior and punching shear resistance of non-strengthened and strengthened flat slabs. A comparison of the model results to the author's and literature experiments, and a parametric study, result in the following conclusions:

- A quintilinear moment–curvature relationship – which takes into account a softening branch in the concrete stress–strain relationship and the tension stiffening effect – together with a URL cycle, modeled as a bilinear envelope assuming full slip reversal, are able to predict residual slab rotations and irreversible rotation increases after a full URL cycle.
- URL cycles increase the slab rotation and thus reduce the punching shear resistance part of the concrete compared to a monotonically loaded slab; the effect however is small. The effect may increase significantly if the slab is strengthened after unloading or for slabs with low reinforcement ratios due to irreversible plastic slab rotations. Prestressing of the strengthening system, however, may compensate the residual slab rotation and thus prevent the loss of punching resistance.
- In the serviceability limit state, slab rotations are more accurately predicted if the concrete softening branch is considered. Approaching the ultimate limit state – for estimation of the punching shear resistance – the effect of concrete softening disappears and may thus be neglected.

Further research is required to take into account time-dependent effects like shrinkage or creep of concrete. These effects may lead to additional deformations and may also result in a decreased punching resistance. In the proposed model this may be considered by the superposition of an additional time-dependent slab rotation, and by a reduction of material properties of concrete.

6 Conclusions and future research

6.1 Conclusions

The load–deformation behavior of flat slabs was analyzed on the basis of the analytical rotation-symmetric sector model by Kinnunen and Nylander (1960) and the assumption of a quadrilinear moment–curvature relationship according to Muttoni (2008), i.e. on a Quadrilinear Sector Model (QSM). A Modified Sector Model (MSM) was developed which considers the influence of shear on flexural behavior. The following main conclusions are drawn:

- The developed model suggests a strength reduction factor for the longitudinal reinforcement crossing the shear crack. This reinforcement has to transmit forces resulting from shear, in addition to forces resulting from bending. The strength reduction factor depends on the mechanical longitudinal reinforcement ratio.
- The consideration of this strength reduction factor in the calculation of the load–rotation curve of slabs according to the MSM leads to a reduction of flexural stiffness, flexural capacity and punching resistance. Compared to the QSM curves a better agreement with experimental curves is achieved, particularly for cases with higher longitudinal reinforcement ratios.

In the last twenty to thirty years an increasing number of reinforced concrete slabs have had to be strengthened against brittle punching shear failure for such reasons as bad detailing, durability deficiencies, or changes of usage leading to a need for increased load-bearing capacity. The efficiency of the available non-prestressed punching strengthening methods is limited; for instance, post-installed shear reinforcement often cannot be sufficiently activated by additional slab deformations before punching failure occurs. On the other hand the prestressing of post-installed shear reinforcement activates the shear-strengthening components immediately after their installation and unloads the slab. The present work analyzed such a strengthening concept in an experimental campaign. This campaign involved a strengthening concept with prestressed carbon fiber-reinforced polymer (CFRP) straps as shear reinforcement:

- Although CFRP is a brittle material, strap prestressing of at least 15% of the tensile strength leads to a significant increase of punching resistance by 67–114% and to an increase of slab deformability: the rotations at failure were 40–110% higher than in the non-strengthened cases.
- The increase of punching shear resistance is similar for all three investigated CFRP strap-anchoring systems – an open system with 1) adhesively-bonded anchors or 2) a steel compression frame mounted underneath the slab around the column, and a closed system with 3) self-anchored straps using a turnbuckle.
- The installed CFRP straps increase the bending resistance of the slab. In accordance with the experimental results a linear dependence of the strap activation on the slab rotation is assumed. The strap activation also depends on the applied prestressing force and on strap stiffness.
- The developed MSM is able to predict the load–rotation responses of flat slabs strengthened with prestressed CFRP straps by considering this increased bending resistance. The agreement of the MSM with the results of the experimental campaign is especially good for the punching resistance (underestimation by 1% with a COV of 5%). The slab rotations at failure are underestimated by 11% (COV: 14%) when considering all slabs (strengthened and non-strengthened), and $7\% \pm 12\%$ for the strengthened cases.

The unloading of an existing flat slab, to activate the subsequently installed strengthening solution during reloading, leads to residual rotations. Punching models based on a rotation-dependent punching shear resistance are able to consider these slab rotations. Thus the load history resulting from a single unloading and reloading (URL) cycle was analytically investigated to quantify its effect on the rotation-dependent punching resistance according to Muttoni (2003, 2008). First the load–deformation behavior of a uniaxial tension chord was analyzed on the basis of the Tension Chord Model (TCM) by Marti et al. (1998). The results were implemented in the MSM, where a quintilinear instead of a quadrilinear moment–curvature relationship was proposed, to take into account an additional contribution of concrete in tension in the fracture process zone according to the Fictitious Crack Model (Hillerborg et al. 1976) via a concrete softening branch after cracking according to Dugdale (1960). Comparisons with experimental results and parametric studies led to the following main conclusions:

- In the serviceability limit state, slab rotations can be more accurately predicted if the concrete softening branch in the crack is considered. This effect gradually disappears when the ultimate limit state is approached.
- URL cycles reduce tension stiffening, which results in additional deformations. Here this is taken into account by an irreversible reduction of the admissible bond shear stress by 50% in the bond stress–slip relationship according to Sigrist (1995).
- The agreement of the quintilinear MSM – including simplified bilinear URL cycle envelopes – with the few available experimental load–rotation curves is acceptable, with

residual slab rotations being underestimated and irreversible rotation increases overestimated by ca. 15%.

- A parametric study shows that the effect of a URL cycle, increasing the slab rotation and thus reducing the portion of the punching shear resistance borne by the concrete, may become significant if the slab is strengthened after unloading. However, the decreased resistance can be compensated by installing a shear-strengthening system using a prestressing method. This was confirmed in the experimental campaign where the residual slab rotations after preloading and unloading of a non-strengthened slab were eliminated during prestressing of the CFRP straps that were installed after unloading.

An investigation of the available punching models, primarily developed for new structures, was carried out, evaluating their applicability to problems specific to the strengthening of existing slabs, as for instance insufficient anchorage of the longitudinal reinforcement or supplementary cut openings or cut reinforcement. The conclusions relating to these problems are as follows:

- Longitudinal tensile reinforcement insufficiently anchored outside the punching zone reduces the flexural stiffness, bending resistance and thus punching resistance. This may be particularly observed for strengthening solutions that increase the control perimeter. Supplementary strengthening measures are necessary to ensure full anchorage of the tensile reinforcement.
- Some strengthening solutions require supplementary cut openings within the punching zone that damage the existing structure before they strengthen it. Existing punching models can consider openings by a reduction of the control section which thus reduces the punching resistance. However, experiments on slabs Sd1–2 did not exhibit a measurable decrease of punching resistance, only a softer slab response compared to the reference slabs without cut openings or cut reinforcement. The location of the boreholes at the column corners seemed to only marginally divert the load transfer toward the column.

The Modified Sector Model developed here successfully reproduces the load–deformation behavior of new and existing reinforced concrete flat slabs by taking into account the contribution of concrete in tension between and inside the cracks. The consideration of a shear effect on flexural behavior eliminates an overestimation of the flexural capacity and consequently punching resistance. A strengthening solution consisting of prestressed CFRP straps used as post-installed shear reinforcement is able to significantly increase the punching resistance of slabs. Furthermore, prestressing of the CFRP straps compensates residual slab rotations due to the load history. The portion of the punching resistance borne by the concrete is thus not reduced.

6.2 Original contributions

A three-level classification was developed, providing a consistent overview of the wide range of analytical models for calculating punching shear resistance.

Partial contributions were made to the development of the previously launched experimental campaign. The measurement data from all experiments was reprocessed for the analysis.

The load–rotation behavior of rotation-symmetric slabs was analyzed in detail. Flexural stiffness reduction factors that take an orthogonal reinforcement layout in rotation-symmetric slabs into account were analytically investigated. A survey was conducted of the common double-symmetric yield-line mechanisms (YLMs) of slabs. Two YLMs were developed: for concentrated column strip reinforcement and for reinforcement with insufficient anchorage outside the punching zone.

An analytical modification of the sector model – the MSM – was developed, taking into account the fact that shear reduces the bending resistance in the column vicinity. The proposed model was validated by seventy-two slab responses obtained from literature.

The structural behavior of the prestressed punching shear-strengthening concept was investigated and implemented into the MSM via an increased bending resistance of the slab, depending on the strap activation. This model was successfully validated by the results of the experimental campaign.

The TCM was analyzed and applied to a uniaxial tension chord under single URL cycles. Such cycles damage the concrete around the ribbed rebar, which was considered by an irreversible reduction of the admissible bond shear stress. Hence, the reduced tension stiffening leads to additional deformations after reloading up to the same load as previously applied. Experimental results validated the proposed bond stress reduction of 50% compared to initial loading in the elastic state.

The findings concerning the uniaxial case were extended to flat slabs. There, an analytical consideration of URL cycles was implemented in the MSM by simplifying a cycle using a bilinear envelope, providing acceptable agreement with experimental results.

A better agreement of the MSM prediction with experimental results in the serviceability limit state was obtained by introducing a quintilinear instead of quadrilinear moment–curvature relationship, considering a concrete softening branch after cracking.

6.3 Recommendations for future research

In the following several recommendations for future developments are given to further enhance the understanding of the punching of new and existing slabs and validate the models presented here for additional applications.

In this research membrane forces were neither considered in the MSM nor in the experimental research in which isolated slab cutouts were analyzed. For the examination of actual slabs, however, membrane action may become significant. More research is required to determine the influence of compressive membrane action around the column that may increase the flexural stiffness, bending and punching resistance. An investigation of the effect of the lateral restraining stiffness of neighboring slab supports on the load–deformation behavior is necessary.

The MSM is valid for internal columns and a rotation-symmetric column, slab and load geometry. The model must be extended for the prediction of the punching resistance of rigidly connected edge or corner columns, wall ends or walls with re-entrant angles.

The load–rotation curves calculated by the MSM were validated by experimental slab responses. Slab rotations at failure and punching resistances were determined for the CFRP strap strengthening system presented in Section 1.2, and compared to experimental results. A validation of the MSM for new slabs with ordinary shear reinforcement is recommended, which requires a model for the activation of shear reinforcement with increasing rotation.

The experimental campaign verified the applicability and efficiency of the CFRP strap-strengthening system. The experimental database should be further extended by additional experiments. It is recommended that the applied prestressing force be varied for different slab thicknesses, and that the influence of different thicknesses of the steel compression frame on the structural behavior be examined. The performance of the strengthening system has to be proven for other slab and column sizes and column geometries.

Insufficient anchorage of the tensile reinforcement around the column is a common problem in existing slabs, and is amplified when strengthening systems are installed to increase the support area. More research is required to better quantify the decrease of punching resistance and analyze the effect of additional post-installed bending reinforcement, for instance by applying externally-bonded reinforcement made of steel or FRP on the slab surface.

A more detailed analysis is required to investigate the effect of supplementary cut openings and / or cut reinforcement within the punching zone of existing slabs on their load–deformation behavior and punching resistance. The most important parameters have to be identified, for instance: the number of holes and / or rebar cuts, their size and distribution around the column, the column geometry, and a potential contribution of the cut reinforcement between the holes.

Long-term effects were excluded in the analysis of the load history of slabs. Effects like creep and shrinkage lead to additional deformations that may also result in decreased punching resistance. These effects can for instance occur with strengthening systems comprising additional upper concrete layers. Few experimental investigations are available and a theoretical and experimental study is therefore recommended to develop accurate estimates of the deformation increases resulting from sustained effects.

Bibliography

- ACI 318 (2011).** *Building Code Requirements for Structural Concrete (ACI 318-11) and Commentary*. American Concrete Institute, ACI Committee 318, Farmington Hills MI, USA, 503 p.
- Adetifa, B. and Polak, M. A. (2005).** Retrofit of Slab Column Interior Connections Using Shear Bolts. *ACI Structural Journal*, 102(2):268–274.
- Alexander, S. D. B. and Simmonds, S. H. (1992).** Bond Model for Concentric Punching Shear. *ACI Structural Journal*, 89(3):325–334.
- Alvarez, M. (1998).** *Einfluss des Verbundverhaltens auf das Verformungsvermögen von Stahlbeton*. PhD thesis ETH Zürich, IBK Bericht Nr. 236. Birkhäuser, Basel, Switzerland, 182 p.
- Amsler, M., Thoma, K., and Heinzmann, D. (2014).** Mit Aufbeton verstärkte Durchstanzplatte: Versuch und Nachrechnungen. *Beton- und Stahlbetonbau*, 109(6):394–402.
- Andersson, J. L. (1963).** Punching of concrete slabs with shear reinforcement. Transactions of the Royal Institute of Technology Stockholm, No. 212, Stockholm, Sweden, 59 p.
- Andrä, H.-P. (1982).** *Zum Tragverhalten des Auflager-Bereichs von Flachdecken*. PhD thesis Universität Stuttgart, Stuttgart, Germany, 149 p.
- Balázs, G. L. (1991).** Fatigue of Bond. *ACI Materials Journal*, 88(6):620–629.
- Barenblatt, G. I. (1962).** The Mathematical Theory of Equilibrium Cracks in Brittle Fracture. *Advances in Applied Mechanics*, 7:55–129.
- Base, G. D. (1959).** Some tests on the punching shear strength of reinforced concrete slabs. Cement and Concrete Association, *Technical Report No. TRA/321*, London, UK, 10 p.
- Baumann, T. (1972).** Zur Frage der Netzbewehrung von Flächentragwerken. *Bauingenieur*, 47:367–377.
- Bažant, Z. P. and Cao, Z. (1987).** Size Effect in Punching Shear Failure of Slabs. *ACI Structural Journal*, 84(1):44–53.
- Bažant, Z. P. and Oh, B. H. (1983).** Crack band theory for fracture of concrete. *Materials and Structures*, 16(93):155–177.

- Bažant, Z. P., Ožbolt, J., and Eligehausen, R. (1994).** Fracture Size Effect: Review of Evidence for Concrete Structures. *ASCE Journal of Structural Engineering*, 120(8):2377–2398.
- Beutel, R. R. K. (2003).** *Durchstanzen schubbewehrter Flachdecken im Bereich von Innenstützen*. PhD thesis RWTH Aachen, Aachen, Germany, 267 p.
- Beyer, K. (1956).** *Die Statik im Stahlbetonbau*. 2nd edition. Springer, Berlin, Germany, 804 p.
- BFS (2013).** Statistisches Lexikon der Schweiz: Jährliche Bau- und Wohnbaustatistik. Bauausgaben und -vorhaben nach Art der Arbeiten [Swiss Statistical Encyclopedia: Annual building and housing statistics. Construction expenditure by type of activity]. Bundesamt für Statistik, Neuchâtel, Switzerland. URL <http://www.bfs.admin.ch/bfs/portal/en/index/infothek/lexikon.html>. Accessed on 2014-11-03.
- Binici, B. and Bayrak, O. (2005a).** Use of Fiber-Reinforced Polymers in Slab-Column Connection Upgrades. *ACI Structural Journal*, 102(1):93–102.
- Binici, B. and Bayrak, O. (2005b).** Upgrading of slab–column connections using fiber reinforced polymers. *Engineering Structures*, 27(1):97–107.
- Birkle, G. (2004).** *Punching of Flat Slabs: The Influence of Slab Thickness and Stud Layout*. PhD thesis University of Calgary, Calgary AB, Canada, 152 p.
- Bollinger, K. (1985).** *Zu Tragverhalten und Bewehrung von rotationssymmetrisch beanspruchten Stahlbetonplatten*. PhD thesis Universität Dortmund, Dortmund, Germany, 118 p.
- Borosnyói, A. and Balázs, G. L. (2005).** Models for flexural cracking in concrete: the state of the art. *Structural Concrete*, 6(2):53–62.
- Bortolotti, L. (1990).** Punching shear strength in concrete slabs. *ACI Structural Journal*, 87(2): 208–219.
- Brändli, W. (1985).** *Durchstanzen von Flachdecken bei Rand- und Eckstützen*. PhD thesis ETH Zürich, IBK Bericht Nr. 146. Birkhäuser, Basel, Switzerland, 102 p.
- Broms, C. E. (2005).** *Concrete flat slabs and footings: Design method for punching and detailing for ductility*. PhD thesis Royal Institute of Technology Stockholm, TRITA-BKN Bulletin 80, Stockholm, Sweden, 114 p.
- Bræstrup, M. W., Nielsen, M. P., Jensen, B. C., and Bach, F. (1976).** Axisymmetric punching of plain and reinforced concrete. Technical University of Denmark, Afdelingen for Bærende Konstruktioner, Report No. R75, Lyngby, Denmark, 33 p.
- Burns, C. (2012).** *Serviceability analysis of reinforced concrete based on the Tension Chord Model*. PhD thesis ETH Zürich, IBK Bericht Nr. 342. vdf Hochschulverlag, Zürich, Switzerland, 147 p.

- CEB (1993).** *CEB-FIP Model Code 1990: Design Code*. Comité Euro-International du Béton. Thomas Telford, London, UK, 437 p.
- Chen, C.-C. and Li, C.-Y. (2005).** Punching Shear Strength of Reinforced Concrete Slabs Strengthened with Glass Fiber-Reinforced Polymer Laminates. *ACI Structural Journal*, 102(4):535–542.
- Chen, W.-F. (1970).** Double-Punch Test for Tensile Strength of Concrete. *Proceedings of the ACI Journal*, 67(12):993–995.
- Desayi, P. and Seshadri, H. K. (1997).** Punching shear strength of flat slab corner column connections. Part 1: Reinforced concrete connections. *Proceedings of the ICE – Structures and Buildings*, 122(1):10–20.
- Di Stasio, J. and van Buren, M. P. (1960).** Transfer of Bending Moment Between Flat Plate Floor and Column. *Proceedings of the ACI Journal*, 57:299–314. Discussion by Kreps R. R. and Reese R. C. in 57:1261–1263.
- Dieterle, H. (1978).** Zur Bemessung von Fundamentplatten ohne Schubbewehrung. *Beton- und Stahlbetonbau*, 73(2):29–37.
- Dragosavić, M. and van den Beukel, A. (1974).** Punching shear. *HERON*, 20(2):1–48.
- Drucker, D. C., Greenberg, H. J., and Prager, W. (1951).** The Safety Factor of an Elastic-Plastic Body in Plane Strain. *Journal of Applied Mechanics*, 18:371–378.
- Drucker, D. C., Prager, W., and Greenberg, H. J. (1952).** Extended Limit Design Theorems for Continuous Media. *Quarterly of Applied Mathematics*, 9(4):381–389.
- Dugdale, D. S. (1960).** Yield of Steel Sheets Containing Slits. *Journal of the Mechanics and Physics of Solids*, 8(2):100–104.
- Ebead, U. and Marzouk, H. (2002).** Strengthening of Two-Way Slabs Using Steel Plates. *ACI Structural Journal*, 99(1):23–31.
- Ebead, U. and Marzouk, H. (2004).** Fiber-Reinforced Polymer Strengthening of Two-Way Slabs. *ACI Structural Journal*, 101(5):650–659.
- El-Enein, H. A., Azimi, H., Sennah, K., and Ghrib, F. (2014).** Flexural strengthening of reinforced concrete slab–column connection using CFRP sheets. *Construction and Building Materials*, 57:126–137.
- El-Salakawy, E. F., Polak, M. A., and Soliman, M. H. (1999).** Reinforced Concrete Slab-Column Edge Connections with Openings. *ACI Structural Journal*, 96(1):79–87.
- El-Salakawy, E. F., Polak, M. A., and Soudki, K. A. (2003).** New Shear Strengthening Technique for Concrete Slab-Column Connections. *ACI Structural Journal*, 100(3):297–304.

- El-Shafiey, T. F. and Atta, A. M. (2011).** Punching strengthening of two-way slabs using a prestressing technique. *In: Grantham, M., Mechtcherine, V., and Schneck, U. (eds.), Concrete Solutions, 4th International Conference on Concrete Repair.* Taylor & Francis Group, London, Dresden, Germany, September 26–28 2011, pp. 177–185.
- Elstner, R. C. and Hognestad, E. (1956).** Shearing strength of reinforced concrete slabs. *Proceedings of the ACI Journal*, 53(1):29–58.
- EN 10083-3 (2006).** *Steels for quenching and tempering – Part 3: Technical delivery conditions for alloy steels.* Comité Européen de Normalisation, Brussels, Belgium, 54 p.
- EN 1992-1-1 (2004).** *Eurocode 2: Design of concrete structures – Part 1-1: General rules and rules for buildings.* Comité Européen de Normalisation, Brussels, Belgium, 225 p.
- EN 1993-1-1 (2005).** *Eurocode 3: Design of steel structures – Part 1-1: General rules and rules for buildings.* Comité Européen de Normalisation, Brussels, Belgium, 91 p.
- Esfahani, M. R., Kianoush, M. R., and Moradi, A. R. (2009).** Punching shear strength of interior slab-column connections strengthened with carbon fiber reinforced polymer sheets. *Engineering Structures*, 31(7):1535–1542.
- Etter, S., Heinzmann, D., Jäger, T., and Marti, P. (2009).** Versuche zum Durchstanzverhalten von Stahlbetonplatten. Institut für Baustatik und Konstruktion, ETH Zürich, *IBK Bericht Nr. 324*, vdf Hochschulverlag, Zürich, Switzerland, 64 p.
- Evans, R. H. and Marathe, M. S. (1968).** Microcracking and Stress–Strain Curves for Concrete in Tension. *Materials and Structures*, 1(1):61–64.
- Faria, D. M. V., Lúcio, V. J. G., and Ramos, A. P. (2009).** Strengthening of reinforced concrete flat slabs using post-tensioning with anchorages by bonding. *In: fib Symposium: Concrete: 21st Century Superhero*, London, UK, June 22–24 2009, 9 p.
- Faria, D. M. V., Lúcio, V. J. G., and Ramos, A. P. (2011).** Strengthening of flat slabs with post-tensioning using anchorages by bonding. *Engineering Structures*, 33:2025–2043.
- Faria, D. M. V., Lúcio, V. J. G., and Ramos, A. P. (2012).** Post-punching behaviour of flat slabs strengthened with a new technique using post-tensioning. *Engineering Structures*, 40: 383–397.
- Feix, J., Wörle, P., and Gerhard, A. (2012).** Ein neuer Ansatz zur Steigerung der Durchstanztragfähigkeit bestehender Stahlbetonbauteile. *Bauingenieur*, 87(4):149–155.
- Fernández Ruiz, M. and Muttoni, A. (2009).** Applications of Critical Shear Crack Theory to Punching of Reinforced Concrete Slabs with Transverse Reinforcement. *ACI Structural Journal*, 106(4):485–494.

- Fernández Ruiz, M., Muttoni, A., and Kunz, J. (2010).** Strengthening of Flat Slabs Against Punching Shear Using Post-Installed Shear Reinforcement. *ACI Structural Journal*, 107(4): 434–442.
- fib (2000).** Bond of reinforcement in concrete. Fédération Internationale du Béton, *fib-Bulletin No. 10*, Lausanne, Switzerland, 427 p.
- fib (2001).** Punching of structural concrete slabs: Technical report. Fédération Internationale du Béton, *fib-Bulletin No. 12*, Lausanne, Switzerland, 307 p.
- fib (2013).** *fib Model Code for Concrete Structures 2010*. Fédération Internationale du Béton. Ernst und Sohn, Berlin, Germany, 402 p.
- FJ. Aschwanden AG (2014).** RINO Durchstanzverstärkung. Product line for strengthening concrete structures. FJ. Aschwanden AG, Lyss, Switzerland. URL <http://aschwanden.com/de/produkte.29/rino.41.html>. Accessed on 2014-11-03.
- Foote, R. M. L., Mai, Y.-W., and Cotterell, B. (1987).** Process Zone Size and Crack Growth Measurement in Fiber Cements. American Concrete Institute, *Special Publication SP 105-3*, Detroit MI, USA, pp. 55–70.
- Fürst, A. (2001).** *Vorgespannte Betonzugglieder im Brückenbau*. PhD thesis ETH Zürich, IBK Bericht Nr. 267. Birkhäuser, Basel, Switzerland, 124 p.
- Gardner, N. J., Huh, J., and Chung, L. (2000).** What Can We Learn from the Sampoong Department Store Collapse? In: Silfwerbrand, J. and Hassanzadeh, G. (eds.), *International Workshop on Punching Shear Capacity on RC Slabs*, TRITA-BKN Bulletin 57, Stockholm, Sweden, June 7–9 2000, pp. 225–233.
- Georgopoulos, T. (1987).** *Durchstanzlast und Durchstanzwinkel über Innenstützen punktförmig gestützter Stahlbetonplatten und deren Sicherung gegen progressiven Kollaps*. PhD thesis Technische Universität München, München, Germany, 197 p.
- Gesund, H. and Kaushik, Y. P. (1970).** Yield Line Analysis of Punching Failures in Slabs. *IABSE Publications*, 30:41–60.
- Gomes, R. B. (1991).** *Punching resistance of reinforced concrete flat slabs with shear reinforcement*. PhD thesis The Polytechnic of Central London, London, UK, 185 p.
- Gomes, R. B. and Regan, P. E. (1999a).** Punching Resistance of RC Flat Slabs with Shear Reinforcement. *ASCE Journal of Structural Engineering*, 125(6):684–692.
- Gomes, R. B. and Regan, P. E. (1999b).** Punching strength of slabs reinforced for shear with offcuts of rolled steel I-section beams. *Magazine of Concrete Research*, 51(2):121–129.
- Goto, Y. (1971).** Cracks Formed in Concrete Around Deformed Tension Bars. *Proceedings of the ACI Journal*, 68(4):244–251.

- Graf, O. (1938).** Versuche über die Widerstandsfähigkeit von allseitig aufliegenden dicken Eisenbetonplatten unter Einzellasten. Deutscher Ausschuss für Eisenbeton, Vol. 88, Ernst und Sohn, Berlin, Germany, 26 p.
- Göricke, M. (1999).** *Additives Tragmodell zur Beschreibung des Durchstanzwiderstandes von Flachdecken*. PhD thesis Technische Universität Berlin, Berlin, Germany, 165 p.
- Grudemo, Å. (1979).** Microcracks, Fracture Mechanism and Strength of the Cement Paste Matrix. *Cement and Concrete Research*, 9(1):19–33.
- Guandalini, S. (2005).** *Poinçonnement symétrique des dalles en béton armé*. PhD thesis École Polytechnique Fédérale de Lausanne, Thèse 3380, Lausanne, Switzerland, 179 p.
- Guandalini, S., Burdet, O. L., and Muttoni, A. (2009).** Punching Tests of Slabs with Low Reinforcement Ratios. *ACI Structural Journal*, 106(1):87–95.
- Guidotti, R. (2010).** *Poinçonnement des planchers-dalles avec colonnes superposées fortement sollicitées*. PhD thesis École Polytechnique Fédérale de Lausanne, Thèse 4812, Lausanne, Switzerland, 191 p.
- Gvozdev, A. A. (1938).** Определение величины разрушающей нагрузки для статически неопределимых систем, претерпевающих пластические деформации. [The Determination of the Value of the Collapse Load for Statically Indeterminate Systems Undergoing Plastic Deformation]. In: Galerkin, B. G. (ed.), *Proceedings of the Conference on Plastic Deformations*, USSR Academy of Sciences, Department of Technical Sciences, Moscow-Leningrad, USSR, December 1936; published in 1938, pp. 19–30. Translated by: Haythornthwaite, R. M. (1960), *International Journal of Mechanical Sciences*, 1(4):322–335.
- Hallgren, M. (1996).** *Punching Shear Capacity of Reinforced High Strength Concrete Slabs*. PhD thesis Royal Institute of Technology Stockholm, TRITA-BKN Bulletin 23, Stockholm, Sweden, 206 p.
- Hallgren, M. and Kinnunen, S. (1991).** Punching shear tests on circular high strength concrete slabs without shear reinforcement. *Nordic Concrete Research*, 10:37–47.
- Hanson, N. W. and Hanson, J. M. (1968).** Shear and moment transfer between concrete slabs and columns. Journal of the PCA Research and Development Laboratories, *Bulletin D129*, Skokie IL, USA, 16 p.
- Harajli, M. H. and Soudki, K. A. (2003).** Shear Strengthening of Interior Slab–Column Connections Using Carbon Fiber-Reinforced Polymer Sheets. *ASCE Journal of Composites for Construction*, 7(2):145–153.
- Hassanzadeh, G. (1996).** Förstärkning av brobaneplattor på pelare med hänsyn till genomstansning: Redovisning av provningar. Kungliga Tekniska Högskolan Stockholm, *TRITA-BKN Bulletin 41*, Stockholm, Sweden, 134 p.

- Hassanzadeh, G. and Sundquist, H. (1998).** Strengthening of bridge slabs on columns. *Nordic Concrete Research*, 21(1):23–34.
- Hawkins, N. M. and Corley, W. G. (1971).** Transfer of unbalanced moment and shear from flat plates to columns. American Concrete Institute, *Special Publication SP 30–7*, Detroit MI, USA, pp. 147–176.
- Heilmann, H. G., Hilsdorf, H., and Finsterwalder, K. (1969).** Festigkeit und Verformung von Beton unter Zugspannungen. Deutscher Ausschuss für Stahlbeton, *Vol. 203*, Ernst und Sohn, Berlin, Germany, 94 p.
- Heinzmann, D., Etter, S., Villiger, S., and Jäger, T. (2012).** Punching Tests on Reinforced Concrete Slabs with and without Shear Reinforcement. *ACI Structural Journal*, 109(6): 787–794.
- Herwig, A. and Motavalli, M. (2012).** Axial Behavior of Square Reinforced Concrete Columns Strengthened with Lightweight Concrete Elements and Unbonded GFRP Wrapping. *ASCE Journal of Composites for Construction*, 16(6):747–752.
- Higgins, D. D. and Bailey, J. E. (1976).** Fracture measurements on cement paste. *Journal of Materials Science*, 11(11):1995–2003.
- Hill, R. (1951).** On the state of stress in a plastic-rigid body at the yield point. *Philosophical Magazine Series 7*, 42:868–875.
- Hill, R. (1952).** A note on estimating yield-point loads in plastic-rigid body. *Philosophical Magazine Series 7*, 43:353–355.
- Hillerborg, A. (1983).** Analysis of one single crack. In: Wittmann, F. H. (ed.), *Fracture Mechanics of Concrete*. Elsevier, Amsterdam, the Netherlands, pp. 223–249.
- Hillerborg, A., Modéer, M., and Petersson, P.-E. (1976).** Analysis of crack formation and crack growth in concrete by means of fracture mechanics and finite elements. *Cement and Concrete Research*, 6(6):773–781.
- Hordijk, D. A. (1992).** Tensile and Tensile Fatigue Behaviour of Concrete; Experiments, Modelling and Analyses. *HERON*, 37(1):1–79.
- Hughes, B. P. and Chapman, G. P. (1966).** The complete stress–strain curve for concrete in direct tension. *RILEM Bulletin, New Series*, 30:95–97.
- Häusler, F. S. (2009).** Zum maximalen Durchstanzwiderstand von Flachdecken mit und ohne Vorspannung. PhD thesis RWTH Aachen, Aachen, Germany, 213 p.
- Ingvarsson, H. (1977).** Betongplattors hållfasthet och armeringsutformning vid hörnpelare [Load-bearing capacity of concrete slabs and arrangement of reinforcement at corner columns]. Kungliga Tekniska Högskolan Stockholm, *Meddelande Nr. 122*, Stockholm, Sweden, 143 p.

- Johansen, K. W. (1943).** *Brudlinieteorier*. Jul. Gjellerup, København, Denmark, 189 p.
- Johansen, K. W. (1962).** *Yield-line Theory*. Cement and Concrete Association, London, UK, 181 p.
- Kanellopoulos, A. (1986).** *Zum unelastischen Verhalten und Bruch von Stahlbeton*. PhD thesis ETH Zürich, IBK Bericht Nr. 153. Birkhäuser, Basel, Switzerland, 86 p.
- Kaufmann, W. (1998).** *Strength and Deformations of Structural Concrete Subjected to In-Plane Shear and Normal Forces*. PhD thesis ETH Zürich, IBK Bericht Nr. 234. Birkhäuser, Basel, Switzerland, 147 p.
- Keller, T. (2003a).** Strengthening of concrete bridges with carbon cables and strips. In: Tan, K. H. (ed.), *6th International Symposium on Fibre Reinforced Polymer (FRP) Reinforcement for Concrete Structures (FRPRCS-6)*, Singapore, July 8–10 2003, pp. 1331–1340.
- Keller, T. (2003b).** Use of Fibre Reinforced Polymers in Bridge Construction. International Association for Bridge and Structural Engineering, *Structural Engineering Documents No. 7*, IABSE, Zürich, Switzerland, 131 p.
- Keller, T. (2010).** *Reinforcement element for absorbing forces of concrete slabs in the area of support elements*. European Patent Office, No. EP2236686(A1), October 10 2010.
- Keller, T. (2013).** *Reinforcing element for absorbing forces in concrete elements supported by supporting elements*. European Patent Office, No. EP2489808(B1), September 4 2013.
- Keller, T., Kenel, A., and Koppitz, R. (2013).** Carbon Fiber-Reinforced Polymer Punching Reinforcement and Strengthening of Concrete Flat Slabs. *ACI Structural Journal*, 110(6): 919–927.
- Kenel, A. (2002).** *Biegetragverhalten und Mindestbewehrung von Stahlbetonbauteilen*. PhD thesis ETH Zürich, IBK Bericht Nr. 277. vdf Hochschulverlag, Zürich, Switzerland, 115 p.
- Kenel, A. and Marti, P. (2002).** Faseroptische Dehnungsmessungen an einbetonierten Bewehrungsstäben. ETH Zürich, *IBK Bericht Nr. 271*, vdf Hochschulverlag, Zürich, Switzerland, 93 p.
- Kenel, A., Nellen, P., Frank, A., and Marti, P. (2005).** Reinforcing Steel Strains Measured by Bragg Grating Sensors. *ASCE Journal of Materials in Civil Engineering*, 17(4):423–431.
- Kinnunen, S. (1963).** Punching of concrete slabs with two-way reinforcement. Transactions of the Royal Institute of Technology Stockholm, No. 198, Stockholm, Sweden, 108 p.
- Kinnunen, S. and Nylander, H. S. E. (1960).** Punching of concrete slabs without shear reinforcement. Transactions of the Royal Institute of Technology Stockholm, No. 158, Stockholm, Sweden, 112 p.

- Kobarg, J. (1986).** *Ein inkrementelles Stahlbetonverbundgesetz unter Berücksichtigung von Stahldehnung und Querdruck*. PhD thesis Universität Karlsruhe, Fortschrittberichte VDI Reihe 4, Nr. 76. VDI Verlag, Düsseldorf, Germany, 197 p.
- Koppitz, R., Kenel, A., and Keller, T. (2013).** Punching shear of RC flat slabs – Review of analytical models for new and strengthening of existing slabs. *Engineering Structures*, 52: 123–130.
- Koppitz, R., Kenel, A., and Keller, T. (2014a).** Punching shear strengthening of flat slabs using prestressed carbon fiber-reinforced polymer straps. *Engineering Structures*, 76:283–294.
- Koppitz, R., Kenel, A., and Keller, T. (2014b).** Effect of punching shear on load–deformation behavior of flat slabs. *Engineering Structures*, 80:444–457.
- Koppitz, R., Kenel, A., and Keller, T. (2014c).** Tension Chord Model Modification for Uniaxial Unloading and Reloading in Elastic and Plastic States. *ASCE Journal of Structural Engineering*, 140(10):04014077. Erratum in 140(10):08014002.
- Kupfer, H. B. (1964).** Erweiterung der Mörsch’schen Fachwerkanalogie mit Hilfe des Prinzips vom Minimum der Formänderungsenergie. Comité Euro-International du Béton, *CEB-Bulletin No. 40*, Lausanne, Switzerland, pp. 44–57.
- Lawler, N. and Polak, M. A. (2011).** Development of FRP Shear Bolts for Punching Shear Retrofit of Reinforced Concrete Slabs. *ASCE Journal of Composites for Construction*, 15(4): 591–601.
- Lees, J. M. and Winistörfer, A. U. (2011).** Nonlaminated FRP Strap Elements for Reinforced Concrete, Timber, and Masonry Applications. *ASCE Journal of Composites for Construction*, 15(2):146–155.
- Lees, J. M., Winistörfer, A. U., and Meier, U. (2002).** External Prestressed Carbon Fiber-Reinforced Polymer Straps for Shear Enhancement of Concrete. *ASCE Journal of Composites for Construction*, 6(4):249–256.
- Leonhardt, F. (1978).** *Vorlesungen über Massivbau. Vierter Teil: Nachweis der Gebrauchsfähigkeit*. 2nd edition. Springer, Berlin, Germany, 194 p.
- Lim, F. K. and Rangan, B. V. (1995).** Studies on concrete slabs with stud shear reinforcement of edge and corner columns. *ACI Structural Journal*, 92(5):515–525.
- Lips, S. (2012).** *Punching of Flat Slabs with Large Amounts of Shear Reinforcement*. PhD thesis École Polytechnique Fédérale de Lausanne, Thèse 5409, Lausanne, Switzerland, 217 p.
- Lips, S., Fernández Ruiz, M., and Muttoni, A. (2012).** Experimental Investigation on Punching Strength and Deformation Capacity of Shear-Reinforced Slabs. *ACI Structural Journal*, 109(6):889–900.

- Lips, S., Koppitz, R., Kenel, A., and Keller, T. (2014).** New Punching Strengthening Systems for Flat Slabs. *In: 4th International fib Congress*, Mumbai, India, February 10–14 2014, 11 p.
- Long, A. E. and Bond, D. (1967).** Punching failure of reinforced concrete slabs. *Proceedings of the Institution of Civil Engineers*, 37(1):109–135. Discussion by Regan, P. E. in 39(1):151–158.
- Luo, Y. H. and Durrani, A. J. (1995a).** Equivalent beam model for flat-slab buildings – Part I: Interior connections. *ACI Structural Journal*, 92(1):115–122.
- Luo, Y. H. and Durrani, A. J. (1995b).** Equivalent beam model for flat-slab buildings – Part II: Exterior connections. *ACI Structural Journal*, 92(2):250–257.
- Mainz, J. (1993).** *Modellierung des Verbundtragverhaltens von Betonrippenstahl*. PhD thesis Technische Universität München, Berichte aus dem Konstruktiven Ingenieurbau Nr. 3/93, München, Germany, 157 p.
- Marti, P. (1989).** Size Effect in Double-Punch Tests on Concrete Cylinders. *ACI Materials Journal*, 86(6):597–601.
- Marti, P. (1990).** Design of Concrete Slabs for Transverse Shear. *ACI Structural Journal*, 87(2): 180–190. Discussion by Adebar, P. in 88(1):117–118.
- Marti, P. (1999).** *Stahlbeton Grundzüge I. Vorlesungsautographie*. Institut für Baustatik und Konstruktion, ETH Zürich, Zürich, Switzerland, 106 p.
- Marti, P. and Thürlimann, B. (1977).** Fließbedingung für Stahlbeton mit Berücksichtigung der Betonzugfestigkeit. *Beton- und Stahlbetonbau*, 72(1):7–12.
- Marti, P., Pralong, J., and Thürlimann, B. (1977).** Schubversuche an Stahlbeton-Platten. Institut für Baustatik und Konstruktion, ETH Zürich, *Bericht Nr. 7305-2*, Birkhäuser, Basel, Switzerland, 123 p.
- Marti, P., Alvarez, M., Kaufmann, W., and Sigrist, V. (1998).** Tension Chord Model for Structural Concrete. *Structural Engineering International*, 8(4):287–298.
- Marti, P., Alvarez, M., Kaufmann, W., and Sigrist, V. (1999).** Tragverhalten von Stahlbeton. ETH Zürich, *IBK Spezialpublikation Nr. SP-008*, Institut für Baustatik und Konstruktion, Zürich, Switzerland, 301 p.
- Martin, H., Schießl, P., and Schwarzkopf, M. (1980).** Berechnungsverfahren für Rißbreiten aus Lastbeanspruchung. *Forschung Straßenbau und Straßenverkehrstechnik, Heft 309*, Bundesministerium für Verkehr, Abteilung Straßenbau, Bonn, Germany, pp. 34–66.
- Martinez-Cruzado, J. A., Qaisrani, A.-N., and Moehle, J. P. (1994).** Post-tensioned flat plate slab-column connections subjected to earthquake loading. *In: 5th U.S. National Conference on Earthquake Engineering*, Vol. 2, Chicago IL, United States, July 10–14 1994, pp. 139–148.

- Masterson, D. M. and Long, A. E. (1974).** The punching strength of slabs, a flexural approach using finite elements. American Concrete Institute, *Special Publication SP 42-32*, Detroit MI, USA, pp. 747–768.
- Meier, U. and Winistörfer, A. U. (1998).** *Multilayer Traction Element in the Form of a Loop*. European Patent Office, No. EP0815329(B1), January 7 1998.
- Meisami, M. H., Mostofinejad, D., and Nakamura, H. (2013).** Punching shear strengthening of two-way flat slabs using CFRP rods. *Composite Structures*, 99:112–122.
- Menétrey, P. (1996).** Analytical Computation of the Punching Strength of Reinforced Concrete. *ACI Structural Journal*, 92(5):503–511.
- Menétrey, P. and Brühwiler, E. (1997).** Punching shear strengthening of reinforced concrete: experimental and analytical investigations. In: Forde, M. C. (ed.), *7th International Conference on Structural Faults and Repair*, Edinburgh, Scotland, July 8 1997, pp. 451–458.
- Moe, J. (1961).** Shearing strength of reinforced concrete flat slabs and footings under concentrated loads. Journal of the PCA Research and Development Laboratories, *Bulletin D47*, Skokie IL, USA, 130 p.
- Muttoni, A. (2003).** Schubfestigkeit und Durchstanzen von Platten ohne Querkraftbewehrung. *Beton- und Stahlbetonbau*, 98(2):74–84.
- Muttoni, A. (2008).** Punching Shear Strength of Reinforced Concrete Slabs without Transverse Reinforcement. *ACI Structural Journal*, 105(4):440–450.
- Muttoni, A. and Schwartz, J. (1991).** Behaviour of Beams and Punching in Slabs without Shear Reinforcement. In: *IABSE Colloquium “Structural Concrete”*, Vol. 62, Stuttgart, Germany, pp. 703–708.
- Muttoni, A., Fernández Ruiz, M., and Kunz, J. (2008).** Nachträgliche Durchstanzbewehrung zur Verstärkung von Stahlbetonflachdecken. *Bauingenieur*, 83:503–511.
- Narasimhan, N. (1971).** *Shear reinforcement in reinforced concrete column heads*. PhD thesis Imperial College of Science and Technology, London, UK, 267 p.
- Narui, S. (1977).** *Tragfähigkeit von Flachdecken an Rand- und Eckstützen. Ultimate shear capacity of edge column-slab-connections*. PhD thesis Universität Stuttgart, Stuttgart, Germany, 306 p.
- Nielsen, M. P. (1999).** *Limit Analysis and Concrete Plasticity*. 2nd edition. CRC Press, Boca Raton FL, USA, 908 p.
- Nölting, D. (1984).** *Das Durchstanzen von Platten aus Stahlbeton: Tragverhalten, Berechnung, Bemessung*. PhD thesis Technische Universität Braunschweig, Braunschweig, Germany, 174 p.

- Petersson, P.-E. (1981).** Crack growth and development of fracture zones in plain concrete and similar materials. Lund Institute of Technology, *Report TVBM-1006*, Lund, Sweden, 174 p.
- Pfyl, T. (2003).** *Tragverhalten von Stahlfaserbeton*. PhD thesis ETH Zürich, IBK Bericht Nr. 279. vdf Hochschulverlag, Zürich, Switzerland, 139 p.
- Pfyl, T. and Marti, P. (2001).** Versuche an stahlfaserverstärkten Stahlbetonelementen. ETH Zürich, *IBK Bericht Nr. 268*, Birkhäuser, Basel, Switzerland, 137 p.
- Pöllet, L. (1983).** *Untersuchung von Flachdecken auf Durchstanzen im Bereich von Eck- und Randstützen*. PhD thesis RWTH Aachen, Aachen, Germany, 190 p.
- Polak, M. A. and Bu, W. (2013).** Design Considerations for Shear Bolts in Punching Shear Retrofit of Reinforced Concrete Slabs. *ACI Structural Journal*, 110(1):15–25.
- Pralong, J. (1982).** *Poinçonnement symétrique des planchers-dalles*. PhD thesis ETH Zürich, IBK Bericht Nr. 131. Birkhäuser, Basel, Switzerland, 118 p.
- Pralong, J., Brändli, W., and Thürlimann, B. (1979).** Durchstanzversuche an Stahlbeton- und Spannbetonplatten. Institut für Baustatik und Konstruktion, ETH Zürich, *Bericht Nr. 7305-3*, Birkhäuser, Basel, Switzerland, 89 p.
- Ramberg, W. and Osgood, W. R. (1943).** Description of stress-strain curves by three parameters. National Advisory Committee for Aeronautics, *Technical Note No. 902*, Washington D.C., USA, 28 p.
- Rangan, B. V. and Hall, A. S. (1983).** Moment and shear transfer between slab and edge column. *ACI Structural Journal*, 80(3):183–191.
- Rankin, G. I. B. and Long, A. E. (1987).** Predicting the enhanced punching strength of interior slab-column connections. *Proceedings of the Institution of Civil Engineers*, Pt. 1, 82(4): 1165–1186.
- Regan, P. E. and Bræstrup, M. W. (1985).** Punching Shear in Reinforced Concrete: A state-of-the-art report. Comité Euro-International du Béton, *CEB-Bulletin No. 168*, Lausanne, Switzerland, 232 p.
- Rehm, G. (1961).** Über die Grundlagen des Verbundes zwischen Stahl und Beton. Deutscher Ausschuss für Stahlbeton, *Vol. 138*, Ernst, Berlin, Germany, 59 p.
- Rehm, G. and Martin, H. (1968).** Zur Frage der Rißbegrenzung im Stahlbetonbau. *Beton- und Stahlbetonbau*, 63(8):175–182.
- Reimann, H. (1963).** *Zur Bemessung von dünnen Plattendecken auf Stützen ohne Kopf gegen Durchstanzen*. PhD thesis Universität Stuttgart, Stuttgart, Germany, 157 p.

- Richart, F. E. and Kluge, R. W. (1939).** Tests of reinforced concrete slabs subjected to concentrated loads. University of Illinois, Engineering Experiment Station, *Bulletin No. 314*, Urbana IL, USA, 78 p.
- Rostásy, F. S., Koch, R., and Leonhardt, F. (1976).** Zur Mindestbewehrung für Zwang von Außenwänden aus Stahlleichtbeton. Deutscher Ausschuss für Stahlbeton, *Vol. 267*, Ernst und Sohn, Berlin, Germany, pp. 5–83.
- Sawczuk, A. and Jaeger, T. (1963).** *Grenztragfähigkeits-Theorie der Platten*. Springer, Berlin, Germany, 522 p.
- Schaumann, E., Vallée, T., and Keller, T. (2009).** Modeling of Direct Load Transmission in Lightweight-Concrete-Core Sandwich Beams. *ACI Structural Journal*, 106(4):435–444.
- Schießl, P. (1989).** Grundlagen der Neuregelung zur Beschränkung der Rißbreite. Deutscher Ausschuss für Stahlbeton, *Vol. 400*, Beuth, Berlin, Germany, pp. 157–175.
- Shehata, I. A. E. M. (1985).** *Theory of Punching in Concrete Slabs*. PhD thesis The Polytechnic of Central London, London, UK, 257 p.
- Shehata, I. A. E. M. (1990).** Rational Method for Designing RC Slabs to Resist Punching. *ASCE Journal of Structural Engineering*, 116(7):2055–2060.
- Shehata, I. A. E. M. and Regan, P. E. (1989).** Punching in R.C. slabs. *ASCE Journal of Structural Engineering*, 115(7):1726–1740.
- Sherif, A. G. (1996).** *Behaviour of reinforced concrete flat slabs*. PhD thesis University of Calgary, Calgary AB, Canada, 397 p.
- Shima, H., Chou, L.-L., and Okamura, H. (1987).** Micro and macro models for bond in reinforced concrete. *Journal of the Faculty of Engineering, The University of Tokyo, Series B*, 39(2):133–194.
- Shima, H., Kanakubo, T., Uchida, Y., and Watanabe, K. (2011).** Technical committee on bond models and their applications for numerical analyses. Japanese Concrete Institute, *Committee Report JCI-TC092A, Digest Edition*, pp. 25–48.
- SIA 262 (2013).** *Betonbau*. Schweizerischer Ingenieur- und Architektenverein, Zürich, Switzerland, 102 p.
- SIA Dokumentation D0226 (2008).** *Tragsicherheit von Einstellhallen*. Schweizerischer Ingenieur- und Architektenverein, Zürich, Switzerland, 105 p.
- Siao, W. B. (1994).** Punching Shear Resistance of Flat Slabs: A Beam-Strip Analogy. *ACI Structural Journal*, 91(5):594–604.
- Sigrist, V. (1995).** *Zum Verformungsvermögen von Stahlbetonträgern*. PhD thesis ETH Zürich, IBK Bericht Nr. 210. Birkhäuser, Basel, Switzerland, 159 p.

- Sissakis, K. and Sheikh, S. A. (2007).** Strengthening Concrete Slabs for Punching Shear with Carbon Fiber-Reinforced Polymer Laminates. *ACI Structural Journal*, 104(1):49–59.
- Staller, M. A. (2001).** Analytische und numerische Untersuchungen des Durchstanztragverhaltens punktgestützter Stahlbetonplatten. Deutscher Ausschuss für Stahlbeton, *Vol. 515*, Beuth, Berlin, Germany, 155 p.
- Stamenković, A. and Chapman, J. C. (1972).** Local strength of flat slabs at column heads. Construction in Industry Research and Information Association (CIRIA), *Report 39*, London, UK, 81 p.
- Talbot, A. N. (1913).** Reinforced concrete wall footings and concrete footings. University of Illinois, Engineering Experiment Station, *Bulletin No. 27*, Urbana IL, USA, 114 p.
- Tassinari, L. (2011).** *Poinçonnement non symétrique des dalles en béton armé*. PhD thesis École Polytechnique Fédérale de Lausanne, Thèse No. 5030, Lausanne, Switzerland, 163 p.
- Teng, S., Cheong, H. K., Kuang, K. L., and Geng, J. Z. (2004).** Punching Shear Strength of Slabs with Openings and Supported on Rectangular Columns. *ACI Structural Journal*, 101(5):678–687.
- Theodorakopoulos, D. D. and Swamy, R. N. (2002).** Ultimate punching shear strength analysis of slab-column connections. *Cement & Concrete Composite*, 24:509–521.
- Trunk, B. G. (1999).** *Einfluß der Bauteilgröße auf die Bruchenergie von Beton*. PhD thesis ETH Zürich, Zürich, Switzerland, 155 p.
- Villiger, S. (2009).** *Durchstanzverhalten von Stahlbetonplatten*. Master's thesis ETH Zürich, Zürich, Switzerland, 99 p.
- Vocke, H. (2002).** *Zum Durchstanzen von Flachdecken im Bereich von Rand- und Eckstützen*. PhD thesis Universität Stuttgart, Stuttgart, Germany, 228 p.
- Weibull, W. (1939).** A statistical theory of the strength of materials. The Royal Swedish Institute for Engineering Research, *No. 151*, Stockholm, Sweden, 45 p.
- Winistörfer, A. U. (1999).** *Development of non-laminated advanced composite straps for civil engineering applications*. PhD thesis University of Warwick, Coventry, UK, 170 p.
- Wittmann, F. H., Rokugo, K., Brühwiler, E., Mihashi, H., and Simonin, P. (1988).** Fracture energy and strain softening of concrete as determined by means of compact tension specimens. *Materials and Structures*, 21(1):21–32.
- Wood, J. G. M. (2003).** Pipers Row Car Park, Wolverhampton: Quantitative Study of the Causes of the Partial Collapse on 20th March 1997. British Health and Safety Executive (HSE), *Final Report*, 197 p.

- Zaglool, E. R. F. and de Paiva, H. A. R. (1973).** Strength analysis of corner column-slab connections. *Journal of the Structural Division, Proceedings of the ASCE*, 99(ST 1):53–71.
- Zanuy, C., Albajar, L., and de la Fuente, P. (2010).** On the cracking behaviour of the reinforced concrete tension chord under repeated loading. *Materials and Structures*, 43(5):611–632.
- Zhu, Y. (1991).** *Evaluation of bond strength between new and old concrete by means of fracture mechanics method*. PhD thesis Royal Institute of Technology Stockholm, TRITA-BST Bulletin 157, Stockholm, Sweden, 112 p.

Notation

Abbreviations

| | |
|-------|---|
| Avg. | Average |
| CBM | Crack Band Model |
| CFRP | Carbon Fiber-Reinforced Polymer |
| COV | Coefficient of Variation |
| CSCT | Critical Shear Crack Theory |
| FCM | Fictitious Crack Model |
| FRP | Fiber-Reinforced Polymer |
| GFRP | Glass Fiber-Reinforced Polymer |
| ICS | Image Correlation System |
| LBT | Lower-Bound Theorem of Plasticity |
| LCFT | Linear Compression Field Theory by Kupfer |
| LS | Load Stage |
| LVDT | Linear Variable Differential Transformer |
| MSM | Modified Sector Model |
| NLFEA | Nonlinear Finite Element Analysis |
| PA12 | Thermoplastic Polyamide 12 |
| PES | Thermoplastic Polyethersulfone |
| QSM | Quadrilinear Sector Model |
| RC | Reinforced Concrete |
| St. | Stirrup |
| TCM | Tension Chord Model |
| TS | Tension Stiffening |
| UBT | Upper-Bound Theorem of Plasticity |
| URL | Unloading and Reloading |
| YLM | Yield-Line Mechanism |
| YLT | Yield-Line Theory |

Roman capital letters

| | |
|------------------------|---|
| A | main axis in direction of 4 th reinforcement layer = strong axis |
| <i>A</i> | area |
| <i>A_{add}</i> | area prop. to higher deformations after reloading (modified TCM, Section 5.1.3) |

| | |
|---------------------|--|
| A_c | concrete cross-sectional area |
| A_p | CFRP cross-sectional area = $b_p \cdot t_p$ |
| A_{res} | area proportional to residual crack opening (modified TCM, Section 5.1.3) |
| A_s | reinforcing steel cross-sectional area |
| $A_{t,ef}$ | effective tension area (tension chord) |
| B | main axis in direction of 3 rd reinforcement layer = weak axis |
| B | side length of slab |
| C_a | compressive force of steel frame (per unit width) |
| $C_{V_{R,exp,2}}$ | compressive force in bottom compression ring at second peak load (cantilever model, Section 3.1.6) |
| E_c | concrete Young's modulus |
| E_p | CFRP Young's modulus |
| $E_p A_p$ | axial CFRP strap stiffness |
| E_s | reinforcing steel Young's modulus |
| E_{sh} | reinforcing steel hardening modulus |
| EI^I | uncracked flexural slab stiffness per unit width = $E_c h^3 / 12$ |
| EI^{II} | cracked flexural slab stiffness per unit width |
| G | dead weight |
| G_F | specific fracture energy |
| L | length, span width, initial length of beam element |
| $L_{b,eff}$ | effective anchorage length of reinforcement |
| $L_{bd,net}$ | required length for full anchorage of reinforcement |
| M | bending moment |
| N | axial force |
| N_{cr} | cracking load |
| N_{max} | maximum axial force |
| N_R | axial resistance |
| N_{sup}, N_{inf} | upper and lower bounds of axial force (URL cycle) |
| N_{tang} | tangential force in steel frame |
| P | average prestressing force (CFRP plates and straps) |
| P_0 | applied (initial) prestressing force |
| P_{flex} | strap force at which $\psi = \psi_{flex}$ |
| P_u | CFRP plate or strap resistance |
| $P_{u,max}$ | resistance of largest strap with 2×50 loops |
| $P_{V_{R,exp}}$ | prestressing force at peak load |
| $P_{V_{R,exp,1/2}}$ | prestressing force at first/second peak load (Section 3.1) |
| Q | single load |
| Q_{max} | maximum load |
| Q_y | load at which yield strength of reinforcing steel is exceeded |
| T | torsion, tensile force |
| T_s, T_p | tensile forces of reinforcement and strap (per unit width) |
| T_{sup} | tensile force of radial longitudinal reinforcement, Eq. 4.6 |

| | |
|----------------------|---|
| V | shear force |
| V_c | shear force transmitted in concrete to support (Eq. 3.1) = $V - V_p$ |
| $V_c, V_{R,exp}$ | shear force transmitted in concrete to support at peak load |
| $V_c, V_{R,exp,1/2}$ | shear force transmitted in concrete to support at first/second peak load (Section 3.1) |
| V_{cr} | cracking load |
| V_{flex} | flexural capacity of non-strengthened slab |
| V_{flex}^+ | flexural capacity of strengthened slab |
| V_{mod} | shear force (MSM), = $f(\psi)$ |
| V_{mod}^+ | shear force (strengthened slab, MSM), = $f(\psi)$ |
| V_p | vertical component of prestressing forces (Eq. 3.1) = $8P \sin \beta_p$ |
| $V_p, V_{R,exp}$ | vertical component of prestressing forces at peak load |
| $V_p, V_{R,exp,1/2}$ | vertical component of prestressing forces at first/second peak load (Section 3.1) |
| V_{pu} | vertical component of strap resistances = $8P_u \sin \beta_p$ |
| $V_{R,crush}$ | crushing resistance of concrete, = $f(\psi)$ |
| $V_{R,exp}$ | experimental punching shear resistance of strengthened slab = $V_{R,exp,1}$ in Section 3.1 |
| $V_{R,in}$ | punching failure inside shear-reinforced area, = $f(\psi)$ |
| $V_{R,out}$ | punching failure outside shear-reinforced area, = $f(\psi)$ |
| $V_{R,pred,1}$ | empirical prediction of first peak load (Eq. 3.6) |
| V_{R0} | predicted punching shear resistance of concrete (non-strengthened slab) or portion of punching shear resistance borne by concrete |
| V_{R1} | predicted punching shear resistance (strengthened slab) |
| V_{Rc} | failure criterion (CSCT), = $f(\psi)$ |
| V_{Rp} | shear resistance of CFRP straps, = $f(\psi)$ |
| V_{ser} | service load |
| V_{skt} | shear force (CSCT), = $f(\psi)$ |
| V_{sup}, V_{inf} | upper and lower bounds of shear force (URL cycle) |

Roman lowercase letters

| | |
|------------|---|
| a_s | reinforcing steel cross-sectional area (per unit width) |
| b | side length of square column |
| b_a | width of steel compression frame |
| b_p | width of CFRP plate, sheet or strap |
| c_s | coefficient for cold-formed steel stress-strain relationship (Eq. 5.14) |
| d | effective depth |
| d_g | maximum aggregate size |
| d_m | average effective depth of both orthogonal directions = $\frac{d_x + d_y}{2}$ |
| d_p | effective depth of CFRP strap $\approx h$ |
| d_v | shear-resisting effective depth |
| d_x, d_y | effective depths in x - and y -direction |
| f_{ay} | yield strength of structural steel |

| | |
|---------------------|--|
| f_{bd} | design value of bond stress |
| f_c | cylinder concrete compressive strength ($h = 300 \text{ mm}$, $\emptyset = 150 \text{ mm}$) |
| $f_{c,eff}$ | effective value of concrete compressive strength (Chapter 2) $= k_c f_c$ |
| $f_{c,V_{R,exp,2}}$ | stress in concrete compression ring at second peak load (cantilever model, Section 3.1.6) |
| f_{ct} | concrete tensile strength |
| f_{pk} | tensile strength of CFRP, 5% fractile |
| f_{pu} | tensile strength of CFRP, mean value |
| $f_{s0.2}$ | yield strength of cold-formed reinforcing steel (0.2% plastic strain) |
| f_{sd} | design value of yield strength $= f_{sy}/\gamma_s$ |
| f_{su} | ultimate (rupture) strength of reinforcing steel |
| f_{sy} | yield strength of reinforcing steel |
| h | beam or slab thickness |
| k_σ | maximum stress factor (modified TCM, Eq. 5.7) |
| $k_{\sigma,adm}$ | admissible stress factor |
| k_τ | bond stress factor |
| k_c | reduction factor of concrete compressive strength |
| k_g | factor to take crack roughness into account (CSCT) $= \frac{48}{16 \text{ mm} + d_g}$ |
| k_{sys} | empirical factor to take performance of shear reinforcement system into account |
| k_U | minimum stress factor (modified TCM, Eq. 5.8) |
| l_l | base length of long LVDTs, Pfyl's tests (Pfyl and Marti 2001) $= 2\,000 \text{ mm}$ |
| l_m | base length of medium LVDTs, Pfyl's tests (Pfyl and Marti 2001) $= 1\,000 \text{ mm}$ |
| l_p | CFRP strap length |
| l_s | base length of short LVDTs, Pfyl's tests (Pfyl and Marti 2001) $= 200 \text{ mm}$ |
| m | bending moment (per unit width) |
| m_{cr} | cracking moment (per unit width) |
| m_R | bending resistance (average of both rebar directions $= \sqrt{m_{Rx} m_{Ry}}$) |
| m_R^+ | bending resistance of strengthened slab |
| m_{Rx}, m_{Ry} | bending resistances in x - and y -direction |
| m_r, m_t | radial and tangential moments (per unit width) |
| m_{sup}, m_{inf} | upper and lower bounds of bending moment (URL cycle) |
| n | modular ratio $= E_s/E_c$ |
| r | radius (from slab center) |
| r_0 | radius of critical shear crack (CSCT) $= r_c + d_m$ |
| r_1 | radius of resultant shear force crossing the crack (Lips 2012) |
| r_2 | radius of critical shear crack (Lips 2012) |
| r_c | radius of (equivalent) circular column |
| r_{cr} | radius of cracked zone |
| \tilde{r}_{cr} | radius of cracked zone at critical crack width w_{cr} |
| r_{crs} | radius of zone in which cracking is stabilized (at m_{cr}) |
| \tilde{r}_{crs} | radius of zone in which cracking is stabilized (at $m_{cr} + \Delta m_{cr}$) |
| r_q | radius of load introduction at perimeter |

| | |
|------------------|---|
| r_s | (equivalent) radius of circular isolated slab element = slab radius |
| r_y | radius of yielded zone |
| s | spacing of reinforcing bars |
| s_{r0} | maximum crack spacing |
| s_{rm} | average crack spacing |
| t | direction of parallel cracks (LCFT) |
| t_a | thickness of steel compression frame |
| t_p | total thickness of CFRP plate, sheet or strap |
| u_0 | control perimeter for punching shear resistance at distance $d_v/2$ to area of support = $\pi (2r_c + d_v)$ |
| v_r | (radial) shear force per unit width |
| w | vertical deflection, crack width |
| $w_{\mathbf{B}}$ | vertical deflection in direction \mathbf{B} |
| w_{cr} | critical crack width where concrete tensile strength is exhausted (Section 5.2) |
| w_m | vertical deflection at midspan |
| $w_{m,u}$ | vertical deflection at midspan at ultimate load |
| w_p | vertical deflection at penetration point of strap at lower slab surface |
| x | horizontal coordinate (axial direction), depth of compression zone |
| x^{II} | depth of compression zone in cracked state |
| x_c | depth of equivalent concrete stress block = $0.85x$ |
| x_s | length of slip reversal |
| x_{sU} | length of slip reversal after unloading |
| y | horizontal coordinate (transverse direction) |
| z | vertical coordinate, lever arm of internal forces |

Greek capital letters

| | |
|----------------------------|---|
| Δ | deviation |
| $\Delta..$ | increment |
| ΔL | elongation of beam element |
| ΔN_{cr} | axial force increase resulting from specific fracture energy |
| ΔP | increase of prestressing force during loading = $P - P_0$ |
| $\Delta P_{V_{R,exp,1/2}}$ | increase of prestressing force at first/second peak load (Section 3.1) |
| ΔV_{R0} | predicted difference of punching shear resistance or portion of punching shear resistance borne by concrete |
| ΔV_{R1} | predicted difference of punching shear resistance (strengthened slab) |
| Δl_p | strap elongation |
| Δm_{cr} | moment increase resulting from specific fracture energy |
| Δm_{rel} | moment offset of reloading path |
| Δm_{unl} | moment offset of unloading path |
| $\Delta \varepsilon$ | strain increment (TCM, Eq. 5.4) |
| $\Delta \varepsilon_0$ | characteristic tension stiffening effect (TCM) = $2\lambda \cdot \Delta \varepsilon$ |
| $\Delta \varepsilon_{cr}$ | strain offset |

| | |
|------------------------|---|
| $\Delta\epsilon_{unl}$ | additional tension stiffening for unloading (tension chord) |
| $\Delta\varphi$ | opening angle of slab segment in sector model |
| $\Delta\chi_{cr}$ | curvature offset |
| $\Delta\chi_m$ | tension stiffening curvature offset (Marti 1999; Burns 2012) |
| $\Delta\chi_{TS}$ | tension stiffening curvature offset (CSCT) |
| $\Delta\chi_{unl}$ | additional tension stiffening for unloading (slab) |
| $\Delta\psi_{R0}$ | predicted slab rotation increase at failure (non-strengthened slab) |
| $\Delta\psi_{R1}$ | predicted slab rotation increase at failure (strengthened slab) |
| $\Delta\psi_{URL}$ | increase of slab rotation after complete URL cycle |
| $\Delta\psi_{URL,exp}$ | experimental increase of slab rotation after complete URL cycle (Section 5.2) |
| $\Delta\psi_{URL,mod}$ | predicted increase of slab rotation after complete URL cycle (Section 5.2) |

Greek lowercase letters

| | |
|-----------------------------|--|
| α | angle, prestressing level = P_0/P_u |
| α_{cyl} | angle of loading cylinder to main axis |
| α_{YL} | angle of yield-line to main axis |
| β_E | reduction factor of steel Young's modulus |
| $\beta_{E\varphi}$ | directional axial stiffness reduction factor |
| β_{EI} | reduction factor of flexural stiffness |
| $\beta_{EI\varphi}$ | directional flexural stiffness reduction factor |
| β_p | borehole or CFRP plate / strap inclination |
| γ_c | partial resistance factor for concrete |
| γ_s | partial resistance factor for reinforcing and prestressing steel |
| δ | bond slip = relative displacement between steel and concrete |
| δ_u | slip at which at which ultimate (rupture) strength of rebar is exceeded |
| δ_y | slip at which at which yield strength of rebar is exceeded |
| ϵ_1, ϵ_2 | maximum and minimum principal strains |
| ϵ_c | concrete strain |
| $\epsilon_{c,el}$ | concrete strain in elastic part of beam |
| $\epsilon_{c,inf,tang}$ | tangential in-plane concrete (compressive) strain |
| $\epsilon_{c,inf,tang,1/2}$ | tangential concrete (compressive) strain at first/second peak load (Section 3.1) |
| ϵ_s | steel strain |
| ϵ_{sm} | averaged steel strain over crack element |
| ϵ_{su} | steel strain at ultimate stress |
| ϵ_{sy} | steel strain at yielding stress |
| ζ | coefficient, YLMs (d) and (e) in Appendix C |
| η_δ | degree of slip reversal (modified TCM, Eq. 5.11) |
| η_{TS} | residual tension stiffening factor (modified TCM, Eq. 5.13) |
| θ_r | crack inclination |
| κ_p | reduction factor |
| κ_s | coefficient for cold-formed steel stress–strain relationship (Eq. 5.14) |
| κ_V | strength reduction factor for reinforcement inside shear crack (MSM, Eq. 4.8) |

| | |
|----------------------|---|
| λ | coefficient for crack spacing = s_{rm}/s_{rm0} |
| ν | Poisson's ratio |
| ξ | coefficient (modified TCM, Eq. 5.12) |
| ξ_p | compliance factor of CFRP strap strengthening system |
| ρ, ρ_s | geometrical reinforcement ratio (of reinforcing steel) |
| ρ_{eff} | fictitious reinforcement ratio weighting reinforcing and prestressing steel (Chapter 2) |
| ρ_m | average reinforcement ratio of both orthogonal directions = $\sqrt{\rho_x \rho_y}$ |
| ρ_p | reinforcement ratio of prestressing steel |
| $\rho_{s,ef}$ | reinforcement ratio relating to effective tension area according to <i>fib</i> Model Code 2010 (<i>fib</i> 2013), Figure 7.6-4 |
| ρ_x, ρ_y | reinforcement ratios in x - and y -direction |
| σ | normal stress |
| σ_1, σ_2 | maximum and minimum principal stresses |
| σ_{adm} | admissible stress (Chapter 2) |
| σ_c | concrete stress |
| σ_s | steel stress |
| σ_{sr} | steel stress at crack edge |
| σ_{sr0} | steel crack stress |
| τ | shear stress |
| τ_b | bond shear stress between steel and concrete |
| τ_{b0} | initial bond stress for elastic reinforcement (TCM) = $2f_{ct}$ |
| τ_{b1} | initial bond stress after onset of yielding (TCM) = f_{ct} |
| τ_{bR} | bond shear stress for reloading |
| τ_{bU} | bond shear stress for unloading |
| φ | direction of applied stress (LCFT) |
| χ | curvature |
| χ_{cr} | curvature at cracking |
| $\tilde{\chi}_{cr}$ | curvature at critical crack width w_{cr} |
| χ_{crs} | curvature at stabilized crack phase (at m_{cr}) |
| $\tilde{\chi}_{crs}$ | curvature at stabilized crack phase (at $m_{cr} + \Delta m_{cr}$) |
| χ_r, χ_t | radial and tangential curvatures |
| χ_y | curvature at yielding of reinforcing steel |
| ψ | slab rotation outside column region |
| ψ_A | slab rotation in direction A |
| ψ_B | slab rotation in direction B |
| ψ_{flex} | slab rotation at which V_{flex} is reached = $r_s \cdot \chi_y$ |
| ψ_G | elastic rotation under dead weight |
| ψ_m | average slab rotation |
| $\psi_{R,exp}$ | experimental slab rotation at punching shear resistance |
| ψ_{R0} | predicted slab rotation at punching shear resistance (non-strengthened slab) |
| ψ_{R1} | predicted slab rotation at punching shear resistance (strengthened slab) |

Notation

| | |
|------------------------------|---|
| ψ_{res} | residual slab rotation after unloading |
| $\psi_{res,exp}$ | experimental residual slab rotation after unloading (Section 5.2) |
| $\psi_{res,mod}$ | predicted residual slab rotation after unloading (Section 5.2) |
| ω | mechanical reinforcement ratio = $\rho f_{sy}/f_c$ |
| ω_m | average reinforcement ratio of both orthogonal directions = $\rho_m f_{sy}/f_c$ |
| $\omega_{min}, \omega_{max}$ | minimum and maximum mechanical reinforcement ratios |

Other symbols

| | |
|-------------|----------------------|
| 1, 2 | principal directions |
| \emptyset | diameter |



Appendices

A Strengthening system references

The following tables give a brief summary of the presented strengthening solutions for existing flat slabs, classified in four categories:

Table A.1: Overview: Column enlargement

| Reference | Description |
|--|--------------------------|
| Martinez-Cruzado et al. (1994) | Concrete column capital |
| Hassanzadeh (1996); Hassanzadeh and Sundquist (1998) | Shotcrete column capital |
| Hassanzadeh (1996); Hassanzadeh and Sundquist (1998) | Steel collar |

Table A.2: Overview: Increase of bending resistance

| Reference | Description | Bond |
|---------------------------|------------------------------|-------|
| Harajli and Soudki (2003) | CFRP sheets | Epoxy |
| Ebead and Marzouk (2004) | CFRP plates | Epoxy |
| Ebead and Marzouk (2004) | GFRP plates | Epoxy |
| Chen and Li (2005) | GFRP plates (entire surface) | Epoxy |
| Esfahani et al. (2009) | CFRP sheets | ? |
| El-Enein et al. (2014) | CFRP sheets | Epoxy |

Table A.3: Overview: Local slab prestressing by prestressed shear reinforcement

| Reference | Description | Bond |
|---------------------------|--|---------------|
| Faria et al. (2009, 2011) | Steel strands, inclined borehole (11°) | Epoxy |
| Chapter 3 | CFRP straps, inclined borehole (34°) | End-anchorage |

Table A.4: Overview: Post-installed shear reinforcement

| Reference | Description | Bond |
|--|---|----------------------|
| Martinez-Cruzado et al. (1994) | Top and bottom steel drop panels around column with steel bolts | Epoxy |
| Ebead and Marzouk (2002) | Top and bottom steel drop panels around column with steel bolts | Epoxy |
| Ebead and Marzouk (2004) | Top and bottom CFRP sheets (drop panels) around column with steel bolts | ? |
| Hassanzadeh (1996); Hassanzadeh and Sundquist (1998) | Inclined boreholes (45°) with steel bolts up to level of tensile reinforcement only | Grout |
| Menétrey and Brühwiler (1997) | Vertical boreholes with steel bolts (some are prestressed) | Epoxy or unbounded |
| El-Salakawy et al. (2003) | Vertical boreholes with steel bolts | ? |
| Binici and Bayrak (2005a,b) | Vertical boreholes with closed CFRP stirrups | Epoxy |
| Adetifa and Polak (2005) | Vertical boreholes with steel bolts | ? |
| Sissakis and Sheikh (2007) | Vertical boreholes with CFRP stirrups | Epoxy |
| Muttoni et al. (2008); Fernández Ruiz et al. (2010) | Inclined boreholes (45°) with steel bolts up to level of tensile reinforcement only | Epoxy |
| Lawler and Polak (2011) | Vertical boreholes with GFRP bolts | ? |
| El-Shafiey and Atta (2011) | Vertical boreholes (PVC ducts) with prestressed steel bolts | Cementitious grout |
| Feix et al. (2012) | Vertical boreholes with “concrete screws” made of steel up to level of tensile reinforcement only | Form closure of hole |
| Meisami et al. (2013) | Vertical boreholes with bolts made of CFRP or steel | Epoxy |

B Summary experimental campaign

B.1 Overview

Sixteen full-scale concrete slabs were tested within this research project. All slabs had the same plan dimensions ($3.2 \text{ m} \times 3.2 \text{ m}$), the same bending reinforcement ratio ($\rho_m \approx 1.5\%$) and were supported by a central column ($0.25 \text{ m} \times 0.25 \text{ m}$). The reinforcement layout was orthogonal and parallel to the slab edges. A graphical overview of the campaign is presented in Figure B.1.

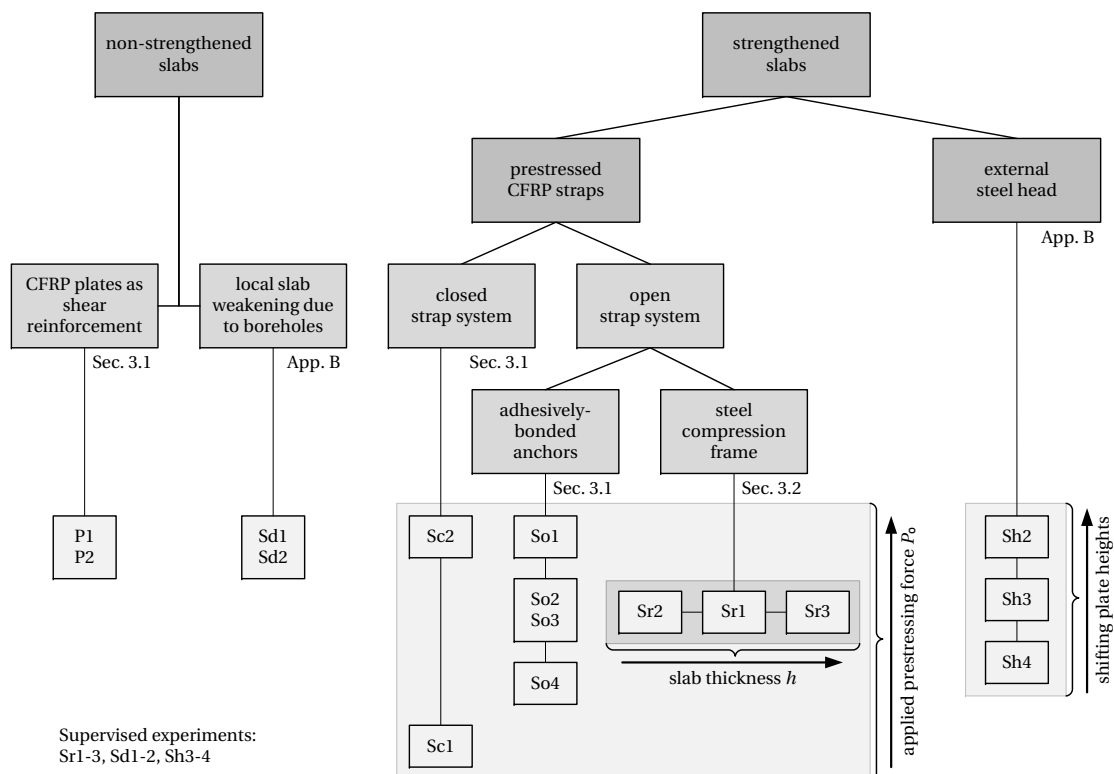


Figure B.1: Overview of experimental campaign with varied parameters

In a first series (Section 3.1), CFRP elements were installed to reinforce new or strengthen existing RC slabs against punching shear failure. Two slabs (P1–2) included non-prestressed flexible plates as shear reinforcement for new slabs, another six slabs (So1–4 and Sc1–2) contained non-laminated and prestressed straps installed crosswise around the column in pre-drilled and pre-cut openings. The straps of the first four slabs were anchored underneath the slab by adhesively-bonded steel anchors, the ones of the latter two slabs were self-anchored in a closed configuration using a turnbuckle. The efficiency of the strap systems was investigated for different applied strap prestressing forces. The slab thickness was constant ($h = 260$ mm).

A second series (Section 3.2) was used to investigate another strap anchoring system: a steel compression frame instead of adhesively-bonded anchors. The efficiency of the two anchoring systems was compared. Before the strengthening system was installed and the straps were prestressed, the slabs were preloaded up to service loads and completely unloaded afterwards. The slab thickness was varied from 180 to 320 mm (Sr1–3).

Two additional slabs (Sd1–2) were cast to investigate the effect of cut longitudinal reinforcement and boreholes (required for the CFRP strap systems) on the punching resistance of the non-strengthened slab [Figure B.2(a)–(b)]. An alternative strengthening system was investigated with slabs Sh2–4 by means of a prestressed external steel head placed between the central column and the slab [Figure B.2(c)–(d)]. The steel head system itself is not part of this research project, but provides additional preloading and unloading curves prior to the installation of the strengthening system. In Section 5.2 these curves are compared to the analytical prediction and the main parameters of Sh2–4 are thus also included in the summary in Table B.1.

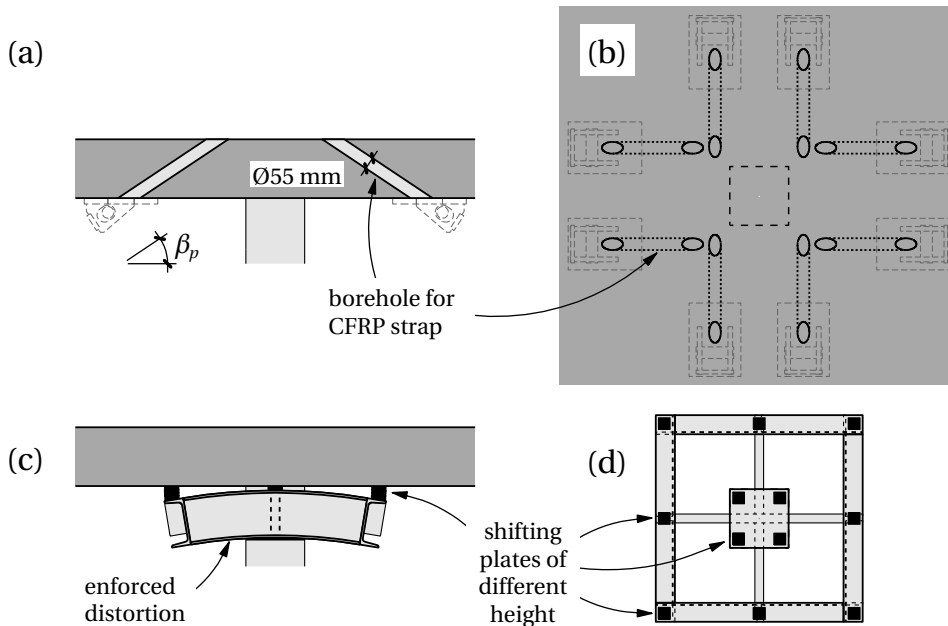


Figure B.2: Boreholes for CFRP strap systems: (a) section and (b) plan views. Steel head strengthening system: (c) section and (d) plan views of cut column head

Various measurements were taken, such as the applied load, vertical displacements along both main axes, surface deformations, change in slab thickness, and forces acting in the CFRP reinforcement. In Section B.2 a brief summary of the experimental results is given.

Table B.1: Specimen overview with relevant parameters. $d_g = 32$ mm, $E_s = 205$ GPa, f_{ct} from double-punch tests on cylinders ($h = \varnothing = 150$ mm) and cubes (side length 150 mm) according to Chen (1970); Marti (1989)

| Slab | h [mm] | d_m [mm] | ρ_m [%] | G [kN] | A_p [mm ²] | P_0 [kN] | $\alpha = \frac{P_0}{P_u}$ [%] | l_p [mm] | f_c [MPa] | f_{ct} [MPa] | E_c [GPa] | f_{sy} [MPa] | f_{pu} [MPa] | E_p [GPa] |
|------|-------------|---------------|-----------------|-------------|-----------------------------|---------------|-----------------------------------|---------------|----------------|-------------------|----------------|-------------------|-------------------|----------------|
| P1 | 256 | 195 | 1.61 | 76 | 60 | – | – | – | 30.3 | 2.5 | 30.7 | 514 | 3100 | 165 |
| P2 | 256 | 200 | 1.57 | 76 | 60 | – | – | – | 31.3 | 2.8 | 30.8 | 514 | 3100 | 165 |
| So1 | 260 | 194 | 1.62 | 79 | 375 | 318 | 47 | 1.76 | 39.9 | 3.3 | 33.9 | 514 | 1820 | 132 |
| So2 | 260 | 199 | 1.58 | 79 | 248 | 220 | 49 | 1.88 | 40.7 | 3.2 | 33.7 | 514 | 1820 | 132 |
| So3 | 260 | 204 | 1.54 | 78 | 188 | 225 | 66 | 1.86 | 40.3 | 3.4 | 33.0 | 514 | 1820 | 132 |
| So4 | 260 | 199 | 1.58 | 78 | 375 | 102 | 15 | 1.89 | 40.9 | 3.6 | 34.9 | 514 | 1820 | 132 |
| Sc1 | 255 | 204 | 1.54 | 80 | 375 | 32 | 5 | 1.85 | 51.5 | 3.7 | 38.8 | 514 | 1820 | 132 |
| Sc2 | 255 | 199 | 1.58 | 78 | 375 | 278 | 41 | 2.15 | 56.6 | 4.2 | 40.4 | 514 | 1820 | 132 |
| Sr1 | 257 | 200 | 1.57 | 80 | 375 | 203 | 30 | 1.97 | 48.1 | 3.6 | 41.0 | 517 | 1820 | 120 |
| Sr2 | 187 | 138 | 1.46 | 60 | 375 | 199 | 29 | 1.66 | 43.1 | 3.4 | 35.8 | 521 | 1820 | 120 |
| Sr3 | 325 | 264 | 1.44 | 98 | 375 | 208 | 31 | 2.19 | 44.2 | 3.4 | 35.1 | 525 | 1820 | 120 |
| Sd1 | 256 | 199 | 1.58 | 77 | – | – | – | – | 51.0 | 3.9 | 38.5 | 517 | – | – |
| Sd2 | 257 | 202 | 1.56 | 77 | – | – | – | – | 52.2 | 3.9 | 39.5 | 517 | – | – |
| Sh2 | 260 | 199 | 1.58 | 78 | – | – | – | – | 59.1 | 4.0 | 37.4 | 514 | – | – |
| Sh3 | 260 | 203 | 1.55 | 79 | – | – | – | – | 47.6 | 3.9 | 40.0 | 569 | – | – |
| Sh4 | 255 | 207 | 1.52 | 79 | – | – | – | – | 45.3 | 3.4 | 40.3 | 569 | – | – |

B.2 Summary of results

Sd1–2 and all slabs of the two experimental series failed in punching. Table B.2 presents the experimentally obtained punching resistances (first peak) and the slab rotations along the weak axis **B** at failure. The results are normalized according to Muttoni (2008), as described in detail in Section 3.2.4. The normalized failure points are graphically displayed in Figure B.3, together with the concrete failure criterion of a non-strengthened slab without shear reinforcement, $V_{Rc}(\psi)$, according to Eq. 4.3.

| Slab | Symbol | $\frac{V_{R,exp}}{u_0 d_v \sqrt{f_c}}$ [$\sqrt{\text{MPa}}$] | $\psi_B d_m k_g$ [-] |
|------|--------|---|-------------------------|
| P1 | ● | 0.52 | 1.46 |
| P2 | ● | 0.56 | 1.75 |
| So1 | △ | 0.98 | 4.10 |
| So2 | △ | 0.86 | 4.01 |
| So3 | △ | 0.84 | 3.99 |
| So4 | △ | 0.86 | 4.27 |
| Sc1 | □ | 0.49 | 2.15 |
| Sc2 | □ | 0.76 | 3.92 |
| Sr1 | ◇ | 0.88 | 3.45 |
| Sr2 | ◇ | 0.83 | 4.94 |
| Sr3 | ◇ | 0.78 | 2.57 |
| Sd1 | ● | 0.51 | 2.30 |
| Sd2 | ● | 0.49 | 2.34 |

Table B.2: Overview of experimental results

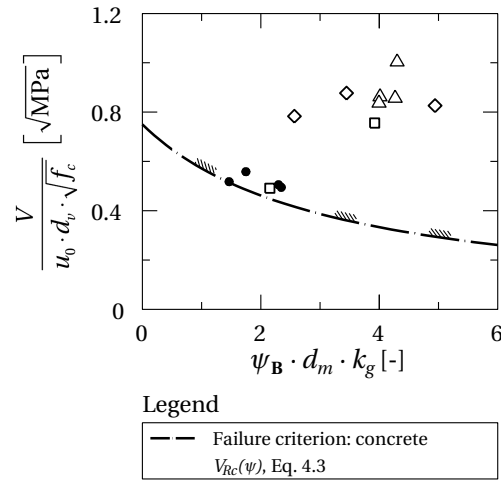


Figure B.3: Normalized punching resistance vs. normalized slab rotation for the investigated specimens

Figure B.4 summarizes the normalized load–rotation and strap force–rotation curves of all slabs loaded up to failure ($P_{u,max} = 683 \text{ kN}$ is the resistance of the largest CFRP strap). Further to the discussion in Chapter 3 it can be stated that, compared to P1–2, Sd1–2 exhibited a higher increase of slab rotation before failure, but the punching resistance was approximately equal. The diversion of the load transfer toward the column seemed to be small due to the concentration of the boreholes at the column corners, at approximately 45° to the main axes. The slightly prestressed CFRP straps in Sc1 were significantly activated after the first peak only [Figure 3.14]. Thus the first peak punching resistance corresponds to the resistance of a non-strengthened slab. As stated in Section 3.1.5, p. 40, the decrease of measured strap forces during loading of Sc2 can be explained by significant friction forces at the deviators on the lower slab surface. The effective strap force in the inclined borehole probably increased with additional slab rotations.

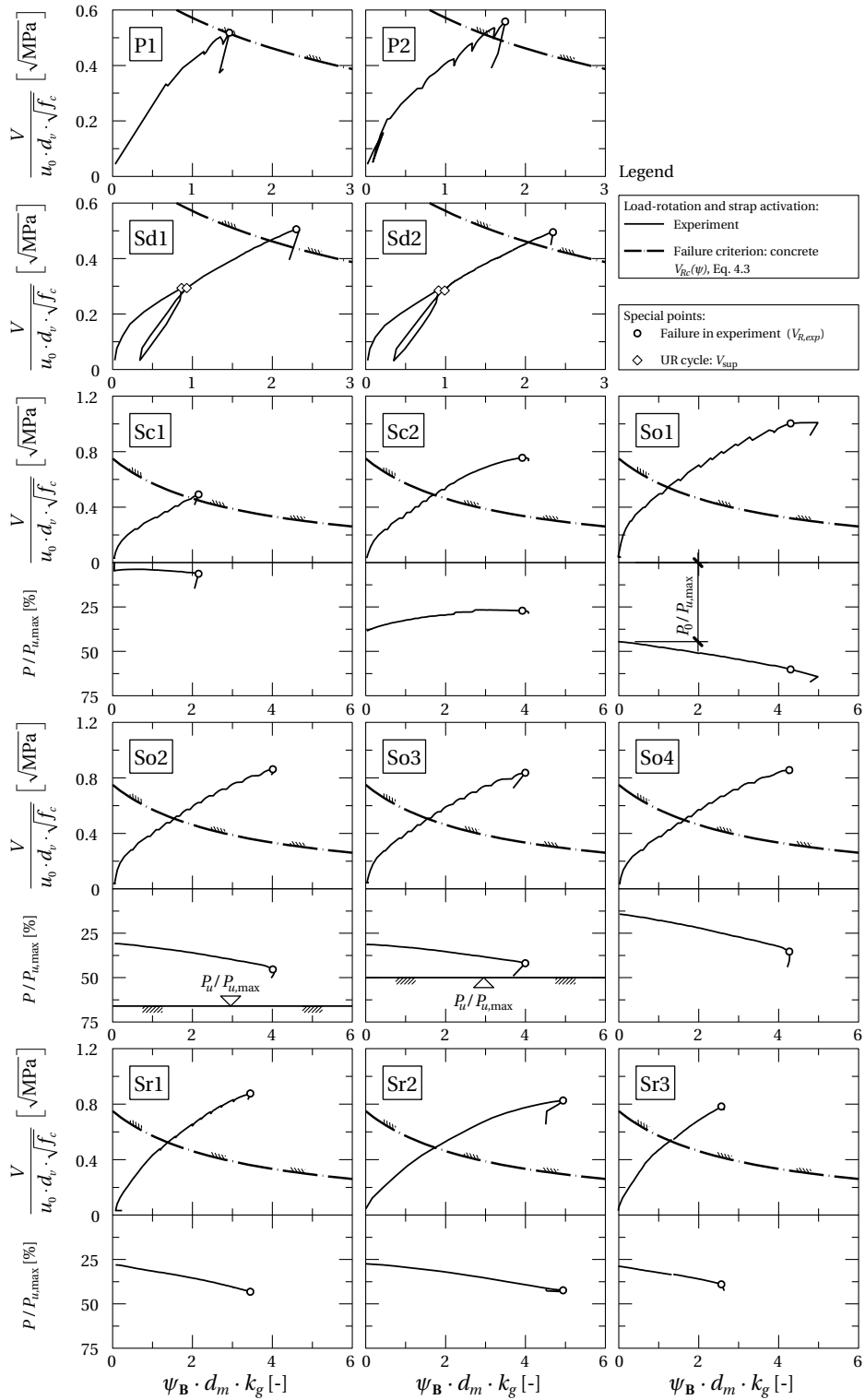


Figure B.4: Normalized load-rotation and strap force activation-rotation curves of tested slabs in Table B.2

C Flexural capacity of slabs

The sector model proposals, see Chapter 4 and Figure 2.6, are primarily valid for rotation-symmetric slabs in which a yield-line mechanism (YLM) in the form of a truncated cone develops when flexural capacity is reached. Thus other slab, column and loading geometries, as well as the support conditions, have to be adapted to an equivalent circular slab with slab radius r_s , column radius r_c and load application at radius r_q . Square columns with side lengths b are replaced by circular ones with the same perimeter, as suggested by Kinnunen and Nylander (1960). Various ways of determining the slab radius of the equivalent circular slab were proposed. A reasonable suggestion is setting the flexural capacity of the actual slab shape (considering double-symmetric mechanisms) equal to the equivalent circular one (Guandalini 2005; Lips 2012), thus the same amount of virtual work has to be done by the internal and external forces. A YLM – kinematically compatible to the actual slab, column and load geometry – resulting in the smallest flexural capacity (= equivalent slab radius) has to be found. Table C.1 summarizes the common double-symmetric yield-line mechanisms. The YLMs of subfigures (a)–(c) and (g)–(j) were reported elsewhere; (d) and (e) were developed here, (f) follows from (c), and (k)–(n) are based on (j), considering different numbers of loading points.

Table C.1: Yield-line mechanisms for: (a)–(e) circular column, (f)–(n) square column

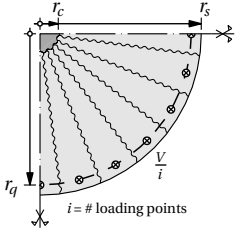
| Yield-line mechanism | Formula | References and comments |
|--|--|--|
| <p>(a)</p>  <p>$i = \# \text{ loading points}$</p> | $\frac{V_{flex}}{m_R} = \frac{2\pi r_s}{r_q - r_c}$ $= \frac{2\pi r_q}{r_q - r_c} \quad \text{for } r_q = r_s$ $= 2\pi \quad \text{for single load}$ | <p>Guandalini (2005); Nielsen (1999) for $r_q = r_s$; Sawczuk and Jaeger (1963) for single load</p> |

Table C.1: (continued)

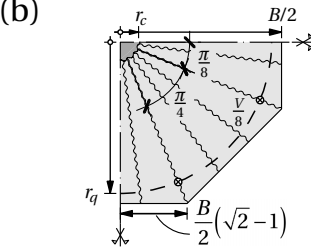
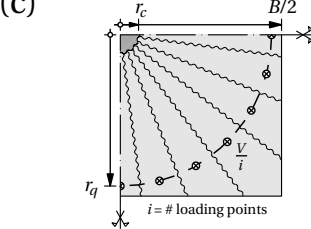
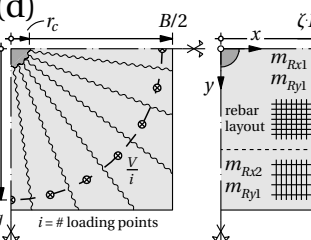
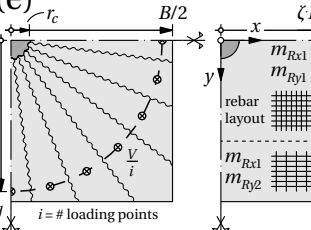
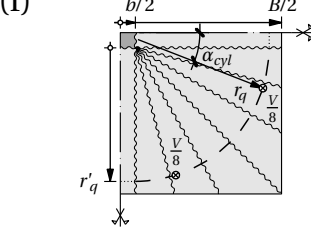
| Yield-line mechanism | Formula | Ref. and comm. |
|---|--|---|
| (b)  | $\frac{V_{flex}}{m_R} = \frac{8B}{r_q - r_c} \ln \left(\tan \frac{5\pi}{16} \right)$ | Sawczuk and Jaeger (1963) for single load |
| (c)  | $\frac{V_{flex}}{m_R} = \frac{8}{r_q - r_c} \frac{B}{2} \ln (\sqrt{2} + 1)$ $= \frac{4B}{r_q} \ln (\sqrt{2} + 1) \quad \text{for single load}$ | Sawczuk and Jaeger (1963) for single load |
| (d)  | $V_{flex} = \frac{2B}{r_q - r_c} (A_1 \cdot A_2 + A_3)$ $A_1 = m_{Rx1} - m_{Rx2} + m_{Ry1} - m_{Ry2}$ $A_2 = \zeta \cdot \ln \left(\frac{1}{\zeta} + \sqrt{\frac{1}{\zeta^2} + 1} \right)$ $A_3 = \ln (\sqrt{2} + 1) \cdot (m_{Rx2} + m_{Ry2})$ | For concentrated column strip reinforcement |
| (e)  | $V_{flex} = \frac{2B}{r_q - r_c} (A_1 \cdot A_4 + A_3)$ $A_1 = m_{Rx1} - m_{Rx2} + m_{Ry1} - m_{Ry2}$ $A_4 = \ln \left(\zeta + \sqrt{\zeta^2 + 1} \right)$ $A_3 = \ln (\sqrt{2} + 1) \cdot (m_{Rx2} + m_{Ry2})$ | For too short anchorage; or for FRP laminates between 0 and $\zeta \cdot \frac{B}{2}$ |
| (f)  | $\frac{V_{flex}}{m_R} = \frac{8}{r'_q} \left[\frac{b}{2} + \frac{B-b}{2} (\sqrt{2} + 1) \right]$ $r'_q = \sqrt{\left[r_q \cos (\alpha_{cyl}) - \frac{b}{2} \right]^2 + \left[r_q \sin (\alpha_{cyl}) - \frac{b}{2} \right]^2}$ | 8 loading cylinders |

Table C.1: (continued)

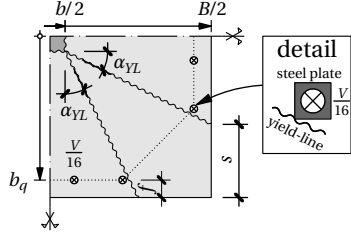
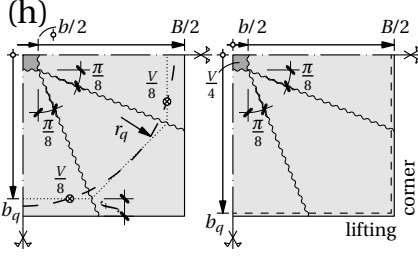
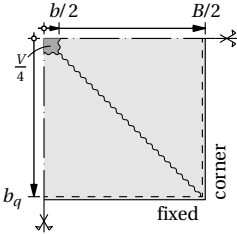
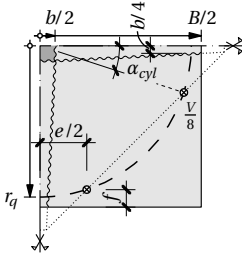
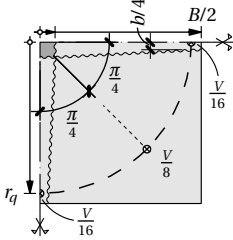
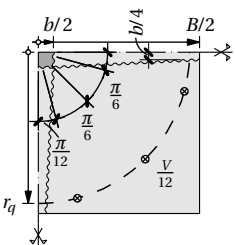
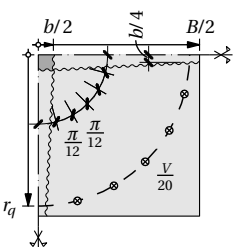
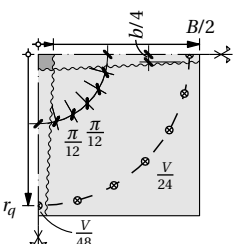
| Yield-line mechanism | Formula | Ref. and comm. |
|--|--|---|
| <p>(g)</p>  | $\frac{V_{flex}}{m_R} = \frac{16}{2b_q - b} \left[\frac{b}{2} + \frac{(B-b)^2}{2(B-b-s)} - s \right]$ $s = \frac{B-b}{2} (1 - \tan \alpha_{YL})$ $b_q = \frac{B}{2} - f$ | <p>If load geometry requires $\alpha_{YL} > \pi/8$; Elstner and Hognestad (1956) for $b_q = \frac{B}{2}$</p> |
| <p>(h)</p>  | $\frac{V_{flex}}{m_R} = \frac{16}{2b_q - b} \left[\frac{b}{2} + \frac{B-b}{2} 2(\sqrt{2}-1) \right]$ $= 8 \left[\frac{B}{B-b} + 2\sqrt{2}-3 \right] \quad \text{for } b_q = \frac{B}{2}$ $b_q = \frac{B}{2} - f$ | <p>Minimum at $\alpha_{YL} = \pi/8$; Guandalini (2005); Sawczuk and Jaeger (1963) for single load</p> |
| <p>(i)</p>  | $\frac{V_{flex}}{m_R} = \frac{8B}{2b_q - b}$ $= \frac{8B}{B-b} \quad \text{for } b_q = \frac{B}{2}$ | <p>Elstner and Hognestad (1956) for $b_q = \frac{B}{2}$</p> |
| <p>(j)</p>  | $\frac{V_{flex}}{m_R} = \frac{8}{B-b} \frac{B^2 - Bb - \frac{b^2}{4}}{B + e - 2(b+f)}$ $= \frac{4}{B-b} \frac{B^2 - Bb - \frac{b^2}{4}}{r_q (\cos \alpha_{cyl} + \sin \alpha_{cyl}) - b}$ $\alpha_{cyl} = \arctan \left(\frac{e}{B-2f} \right)$ $r_q = \frac{1}{2} \sqrt{e^2 + (B-2f)^2}$ | <p>8 loading cylin- ders; Guidotti (2010)</p> |
| <p>(k)</p>  | $\frac{V_{flex}}{m_R} = \frac{8}{B-b} \frac{B^2 - Bb - \frac{b^2}{4}}{A_8}$ $A_8 = \sqrt{2} r_q - \frac{2+\sqrt{2}}{4} b$ | <p>8 loading cylin- ders</p> |

Table C.1: (continued)

| Yield-line mechanism | Formula | Ref. and comm. |
|--|--|----------------------|
| (l)  | $\frac{V_{flex}}{m_R} = \frac{12}{B-b} \frac{B^2 - Bb - \frac{b^2}{4}}{A_{12}}$ $A_{12} = r_q (\sqrt{2} + \sqrt{6}) - 3b$ | 12 loading cylinders |
| (m)  | $\frac{V_{flex}}{m_R} = \frac{20}{B-b} \frac{B^2 - Bb - \frac{b^2}{4}}{A_{20}}$ $A_{20} = r_q (1 + \sqrt{2} + \sqrt{3} + \sqrt{6}) - 5b$ | 20 loading cylinders |
| (n)  | $\frac{V_{flex}}{m_R} = \frac{24}{B-b} \frac{B^2 - Bb - \frac{b^2}{4}}{A_{24}}$ $A_{24} = r_q (1 + \sqrt{3} + \sqrt{6} + \sqrt{8}) - \left(5 + \frac{\sqrt{2}}{2}\right)b$ | 24 loading cylinders |

D Reduction factor of flexural stiffness

In Figure 4.6(b) β_{EI} is displayed neglecting compression reinforcement. If on the other hand, an orthotropic compression reinforcement is considered in the m - χ -relationship, the flexural stiffness reduction will be intensified. Figure D.1 illustrates this effect for a constant β_E and evaluating the following two equations:

$$x^H = (\rho + \rho') \beta_E n d \left(\sqrt{1 + \frac{2}{\beta_E n} \frac{\rho + \rho' \frac{d'}{d}}{(\rho + \rho')^2}} - 1 \right) \quad (D.1)$$

where $\rho' = a'_s/d$ geometrical longitudinal compression reinforcement ratio with effective depth d' , and:

$$EI^H = \beta_E E_s \left[\frac{(x^H)^3}{2\beta_E n} \left(\frac{h}{2x^H} - \frac{1}{3} \right) + \rho d^3 \left(1 - \frac{x^H}{d} \right) \left(1 - \frac{h}{2d} \right) + \rho' d^3 \left(\frac{x^H}{d} - \frac{d'}{d} \right) \left(\frac{h}{2d} - \frac{d'}{d} \right) \right] \quad (D.2)$$

instead of Eqs. 4.22 and 4.23 to consider ρ' . It is shown that compression reinforcement results in a smaller increase of β_{EI} with increasing reinforcement ratio, ρ .

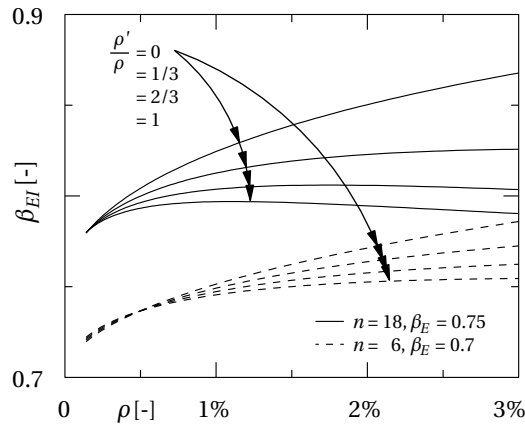


Figure D.1: $\beta_{EI} = \frac{EI^H(\beta_E)}{EI^H(\beta_E=1)}$ acc. to Eq. D.2 with $\frac{d}{h} = 0.8$, $\frac{d'}{h} = 0.2$

E Modified Sector Model: Validation

In addition to Figure 4.7 the predicted load–rotation curves according to the MSM (Eq. 5.29, G_F according to Eq. 5.24) and QSM (Eq. 4.1) are compared to other experimental results documented in literature in Section E.1. These specimens include non-strengthened flat slabs with and without shear reinforcement. Slabs with a constant reinforcement ratio and an orthogonal layout are considered, with emphasis on high mechanical reinforcement ratios. For each experimental series the minimum YLM used according to Appendix C is denoted. For circular columns and load application $\beta_E = 0.6$, for square columns $\beta_E = 0.7$ was applied. The strength reduction factor, κ_V , was calculated according to Eq. 4.8.

In Section E.2 the MSM is compared to the measured results for all slabs of this experimental campaign, in addition to the comparison of series So and Sr in Figure 4.11.

E.1 Experiments from literature

Seventy-two specimens of the following experimental series were selected for a graphical validation of the Modified Sector Model:

- Sixteen experiments by Lips (2012); Lips et al. (2012)
- Four experiments by Guidotti (2010)
- Three experiments at ETH Zurich by Etter et al. (2009); Heinzmann et al. (2012)
- Ten experiments by Guandalini (2005); Guandalini et al. (2009)
- Six experiments by Hallgren (1996)
- Twelve experiments by Gomes (1991); Gomes and Regan (1999a,b)
- Six experiments by Kinnunen and Nylander (1960)
- Fifteen experiments by Elstner and Hognestad (1956)

Experiments by Lips (2012)

Sixteen experiments were carried out on square slabs, four (PL1, PL3–5) without and all others with punching shear reinforcement, either corrugated double-headed studs (PL6–12) or cages of continuous stirrups (PF1–5), see properties in Table E.1 and comparison with the calculations in Figure E.1. Different column sizes, slab thicknesses, and the extent of the two shear reinforcement systems were investigated. The slab rotation of the weak axis was directly measured using inclinometers, installed near the applied load.

Table E.1: Properties of specimens by Lips (2012), $\beta_E = 0.7$, $d_v = d_m$, YLM acc. to Table C.1(j)

| Slab | B | b | h | d_m | ρ_m | r_q | d_g | f_c | f_{ct}^a | E_c^a | f_{sy} | E_s^c | $\frac{V_{flex}}{m_R}$ | κ_V |
|------|------|------|------|-------|----------|-------|-------|-------|------------|---------|------------------|---------|------------------------|------------|
| | [mm] | [mm] | [mm] | [mm] | [%] | [mm] | [mm] | [MPa] | [MPa] | [GPa] | [MPa] | [GPa] | [-] | [-] |
| PL1 | 3000 | 130 | 250 | 193 | 1.63 | 1505 | 16 | 36.2 | 3.3 | 33.1 | 583 | 200 | 6.48 | 0.56 |
| PL3 | 3000 | 520 | 250 | 197 | 1.60 | 1505 | 16 | 36.5 | 3.3 | 33.2 | 583 | 200 | 8.14 | 0.54 |
| PL4 | 3000 | 340 | 320 | 267 | 1.58 | 1505 | 16 | 30.5 | 2.9 | 31.2 | 562 ^b | 200 | 7.29 | 0.63 |
| PL5 | 3000 | 440 | 400 | 353 | 1.51 | 1505 | 16 | 31.9 | 3.0 | 31.7 | 580 | 200 | 7.74 | 0.60 |
| PL6 | 3000 | 130 | 250 | 198 | 1.59 | 1505 | 16 | 36.6 | 3.3 | 33.2 | 583 | 200 | 6.48 | 0.54 |
| PL7 | 3000 | 260 | 250 | 197 | 1.60 | 1505 | 16 | 35.8 | 3.3 | 33.0 | 583 | 200 | 6.96 | 0.55 |
| PL8 | 3000 | 520 | 250 | 200 | 1.57 | 1505 | 16 | 36.0 | 3.3 | 33.0 | 583 | 200 | 8.14 | 0.54 |
| PL9 | 3000 | 340 | 320 | 266 | 1.59 | 1505 | 16 | 32.1 | 3.0 | 31.8 | 562 ^b | 200 | 7.29 | 0.60 |
| PL10 | 3000 | 440 | 400 | 343 | 1.55 | 1505 | 16 | 33.0 | 3.1 | 32.1 | 580 | 200 | 7.74 | 0.59 |
| PL11 | 3000 | 260 | 250 | 201 | 1.56 | 1505 | 16 | 34.2 | 3.2 | 32.5 | 554 | 200 | 6.96 | 0.54 |
| PL12 | 3000 | 260 | 250 | 201 | 1.56 | 1505 | 16 | 34.6 | 3.2 | 32.6 | 554 | 200 | 6.96 | 0.53 |
| PF1 | 3000 | 130 | 250 | 209 | 1.50 | 1505 | 16 | 31.1 | 3.0 | 31.4 | 583 | 200 | 6.48 | 0.61 |
| PF2 | 3000 | 260 | 250 | 208 | 1.51 | 1505 | 16 | 30.4 | 2.9 | 31.2 | 583 | 200 | 6.96 | 0.63 |
| PF3 | 3000 | 520 | 250 | 209 | 1.50 | 1505 | 16 | 37.1 | 3.3 | 33.4 | 583 | 200 | 8.14 | 0.51 |
| PF4 | 3000 | 340 | 320 | 274 | 1.54 | 1505 | 16 | 32.5 | 3.1 | 31.9 | 562 ^b | 200 | 7.29 | 0.58 |
| PF5 | 3000 | 440 | 400 | 354 | 1.50 | 1505 | 16 | 33.4 | 3.1 | 32.2 | 580 | 200 | 7.74 | 0.57 |

^a values calculated using relationships acc. to SIA 262 (2013): $E_c = 10000 \text{ MPa}^{2/3} \cdot \sqrt[3]{f_c}$, $f_{ct} = 0.3 \text{ MPa}^{1/3} \cdot f_c^{2/3}$ (both in MPa)

^b 531 MPa ($\emptyset 20$), 580 MPa ($\emptyset 26$), weighted by a_s

^c value fixed by Lips (2012)

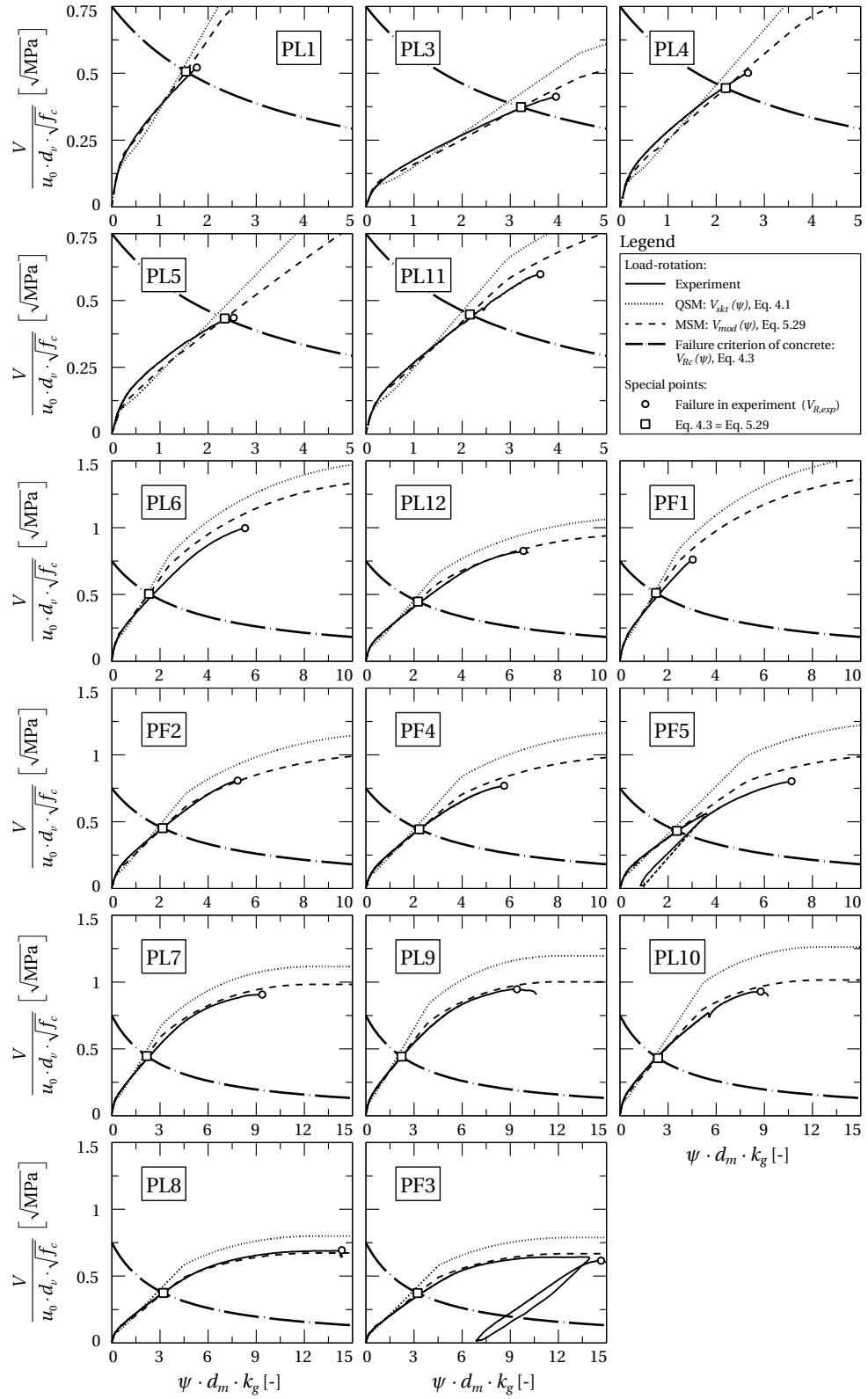


Figure E.1: Specimens by Lips (2012): MSM, QSM and experimental results

Experiments by Guidotti (2010)

Guidotti carried out four experimental series on square slabs. He focused on the slab–column joint in the flat slab between an upper and lower column (to simulate multi-story buildings), which has to bear the upper column load in addition to shear and bending moments caused by loads applied on the slab. Series II was tested without column loads, but varying the type of concrete used (ordinary vibrated concrete and self-compacting concrete, SCC), the maximum aggregate size, and the bending reinforcement ratio. The slab rotation of the weak axis was directly measured using inclinometers, installed near the applied load. Here, only the experiments with vibrated concrete are displayed in Table E.2 and Figure E.2.

Table E.2: Properties of specimens by Guidotti (2010), $\beta_E = 0.7$, $d_v = d_m$, YLM acc. to Table C.1(j)

| Slab | B | b | h | d_m | ρ_m | r_q | d_g | f_c | f_{ct}^a | E_c | f_{sy} | E_s^b | $\frac{V_{flex}}{m_R}$ | κ_V |
|------|------|------|------|-------|----------|-------|-------|-------|------------|-------|----------|---------|------------------------|------------|
| | [mm] | [mm] | [mm] | [mm] | [%] | [mm] | [mm] | [MPa] | [MPa] | [GPa] | [MPa] | [GPa] | [-] | [-] |
| PG19 | 3000 | 260 | 247 | 206 | 0.78 | 1505 | 16 | 46.2 | 3.2 | 32.7 | 510 | 205 | 6.96 | 0.16 |
| PG20 | 3000 | 260 | 245 | 201 | 1.56 | 1505 | 16 | 51.7 | 3.4 | 33.9 | 551 | 205 | 6.96 | 0.35 |
| PG23 | 3000 | 260 | 250 | 199 | 0.81 | 1505 | 32 | 41.0 | 3.0 | 32.2 | 510 | 205 | 6.96 | 0.18 |
| PG24 | 3000 | 260 | 249 | 194 | 1.62 | 1505 | 32 | 39.8 | 2.9 | 31.9 | 551 | 205 | 6.96 | 0.47 |

^a values from direct tension tests

^b value fixed by Guidotti (2010)

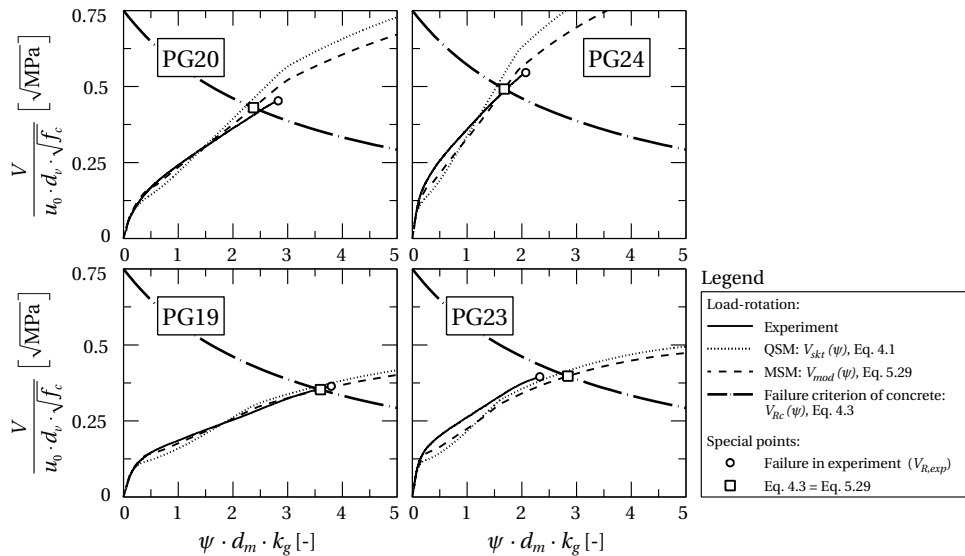


Figure E.2: Specimens by Guidotti (2010): MSM, QSM and experimental results

Experiments at ETH Zurich in 2009

Three experiments on square slabs were carried out by Etter et al. (2009) and Heinzmann et al. (2012), see Table E.3. Slab SP1 was a reference slab without shear reinforcement. SP2 and SP3 were reinforced with corrugated double-headed shear studs, which were placed locally around the column (SP2) or over the entire slab (SP3). Here, the slab rotation was determined by calculating the secant rotation from four (near the weak axis) deflection measuring points, located at 1.7 m from the slab center, and from another two inductive transducers measuring the support deformation. The comparison to the model is illustrated in Figure E.3.

Table E.3: Properties of specimens by Etter et al. (2009), $\beta_E = 0.6$, $d_v = d_m$,
YLM acc. to Table C.1(c)

| Slab | B | r_c | h | d_m | ρ_m | r_q | d_g | f_c | f_{ct}^a | E_c | f_{sy} | E_s | $\frac{V_{flex}}{m_R}$ | κ_V |
|------|------|-------|------|-------|----------|-------|-------|-------|------------|-------|----------|-------|------------------------|------------|
| | [mm] | [mm] | [mm] | [mm] | [%] | [mm] | [mm] | [MPa] | [MPa] | [GPa] | [MPa] | [GPa] | [-] | [-] |
| SP1 | 4100 | 200 | 350 | 294 | 1.21 | 1962 | 32 | 35.5 | 3.0 | 33.1 | 577 | 209 | 8.20 | 0.41 |
| SP2 | 4100 | 200 | 350 | 294 | 1.21 | 1962 | 32 | 34.5 | 3.3 | 35.2 | 577 | 209 | 8.20 | 0.42 |
| SP3 | 4100 | 200 | 350 | 294 | 1.21 | 1962 | 32 | 33.4 | 3.3 | 33.8 | 577 | 209 | 8.20 | 0.43 |

^a values from double-punch tests on cylinders ($h = \varnothing = 150\text{mm}$) acc. to Chen (1970); Marti (1989)

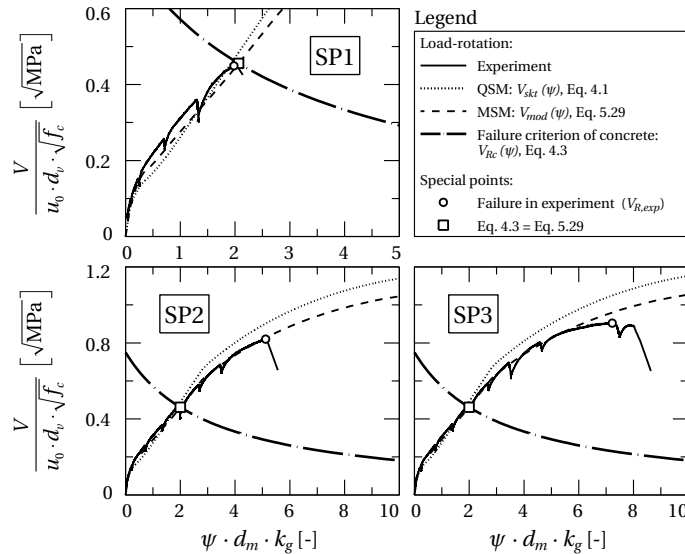


Figure E.3: Specimens by Etter et al. (2009): MSM, QSM and experimental results

Experiments by Guandalini (2005)

An experimental series on square slabs (default side length $B = 3\text{ m}$) with varying bending reinforcement ratio was carried out. Additionally the scale of the slabs was varied from 2:1 ($B = 6\text{ m}$) to 1:2 ($B = 1.5\text{ m}$). The slabs contained no shear reinforcement. The slab rotation of the weak axis was directly measured using inclinometers, installed near the applied load. The parameters are summarized in Table E.4 and the experimental results are displayed in Figure E.4.

Table E.4: Properties of specimens by Guandalini (2005), $\beta_E = 0.7$, $d_v = d_m$,
YLM acc. to Table C.1(j)

| Slab | B | b | h | d_m | ρ_m | r_q | d_g | f_c | f_{ct}^a | E_c | f_{sy} | E_s^b | $\frac{V_{flex}}{m_R}$ | κ_V |
|------|------|------|------|-------|----------|-------|-------|-------|------------|-------|----------|---------|------------------------|------------|
| | [mm] | [mm] | [mm] | [mm] | [%] | [mm] | [mm] | [MPa] | [MPa] | [GPa] | [MPa] | [GPa] | [-] | [-] |
| PG1 | 3000 | 260 | 250 | 210 | 1.50 | 1505 | 16 | 27.7 | 2.0 | 25.7 | 573 | 205 | 6.96 | 0.69 |
| PG2b | 3000 | 260 | 250 | 210 | 0.25 | 1505 | 16 | 40.5 | 3.0 | 34.7 | 552 | 205 | 6.96 | 0.04 |
| PG3 | 6000 | 520 | 500 | 464 | 0.32 | 2845 | 16 | 32.4 | 2.1 | 31.8 | 520 | 205 | 7.35 | 0.09 |
| PG4 | 3000 | 260 | 250 | 210 | 0.25 | 1505 | 4 | 32.2 | 2.0 | 27.3 | 541 | 205 | 6.96 | 0.06 |
| PG5 | 3000 | 260 | 255 | 210 | 0.33 | 1505 | 16 | 29.3 | 2.3 | 26.8 | 555 | 205 | 6.96 | 0.10 |
| PG6 | 1500 | 130 | 125 | 96 | 1.46 | 752 | 16 | 34.7 | 2.4 | 33.7 | 526 | 205 | 6.96 | 0.47 |
| PG7 | 1500 | 130 | 125 | 100 | 0.75 | 752 | 16 | 34.7 | 2.4 | 33.7 | 550 | 205 | 6.96 | 0.24 |
| PG8 | 1500 | 130 | 140 | 102 | 0.32 | 752 | 16 | 34.7 | 2.4 | 33.7 | 525 | 205 | 6.96 | 0.06 |
| PG9 | 1500 | 130 | 140 | 102 | 0.25 | 752 | 16 | 34.7 | 2.4 | 33.7 | 525 | 205 | 6.96 | 0.04 |
| PG10 | 3000 | 260 | 255 | 210 | 0.33 | 1505 | 16 | 28.5 | 2.2 | 29.5 | 577 | 205 | 6.96 | 0.11 |

^a values from direct tension tests on cylinders ($h = 320\text{ mm}$, $\emptyset = 160\text{ mm}$)

^b value fixed by Guandalini

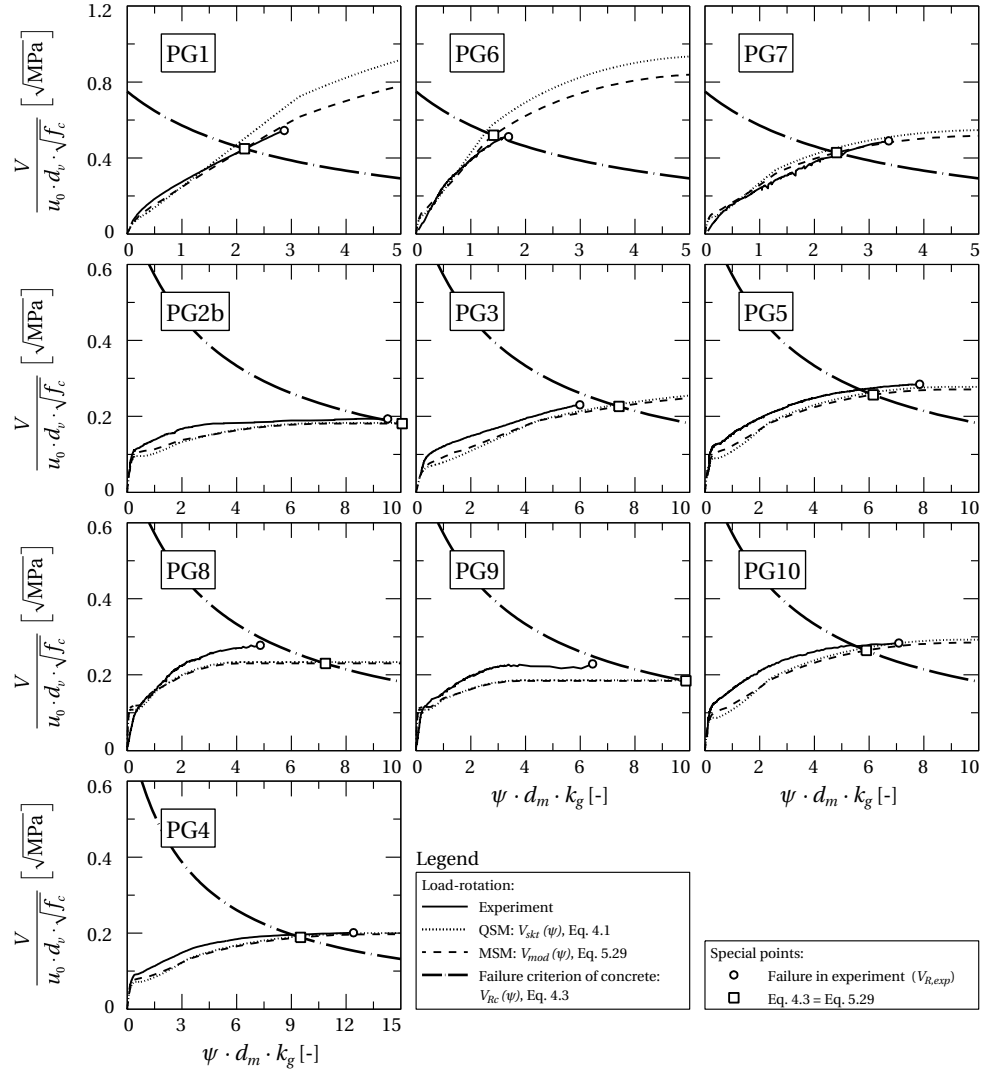


Figure E.4: Specimens by Guandalini (2005): MSM, QSM and experimental results

Experiments by Hallgren (1996)

Hallgren carried out an experimental series on circular flat slabs with high-strength concrete and varying bending reinforcement with an orthogonal layout, see Table E.5. Excluded from the analysis here are three slabs containing bent-up bars as shear reinforcement that locally increase the longitudinal reinforcement ratio in the column vicinity, and slab HSC6 for which the measurement data was lost during the test (Hallgren 1996). The angle of rotation was determined by Hallgren from the inclination of the rigid slab sector outside the shear crack (observed rotations on opposite column sides) and directly displayed in his Figure 4-7 (Hallgren 1996; all experiments) and in his Fig. 2 (Hallgren and Kinnunen 1991; HSC0 and HSC1). The experimental curves are compared to the model in Figure E.5.

Table E.5: Properties of specimens by Hallgren (1996), $\beta_E = 0.6$, $d_v = d_m$,
YLM acc. to Table C.1(a)

| Slab | r_s | r_c | h | d_m | ρ_m | r_q | d_g^b | f_c | f_{ct}^d | E_c | f_{sy} | E_s | $\frac{V_{flex}}{m_R}$ | κ_V |
|---------------------|-------|-------|------|-------|----------|-------|---------|-------------------|------------|-----------|----------|------------------|------------------------|------------|
| | [mm] | [mm] | [mm] | [mm] | [%] | [mm] | [mm] | [MPa] | [MPa] | [GPa] | [MPa] | [GPa] | [-] | [-] |
| HSC0 | 1270 | 125 | 240 | 200 | 0.81 | 1200 | 18 | 93.7 ^c | 4.5 | 51.0 | 643 | 215 ^e | 7.42 | 0.09 |
| HSC1 | 1270 | 125 | 245 | 200 | 0.81 | 1200 | 18 | 91.3 | 6.9 | 42.9 | 627 | 215 ^e | 7.42 | 0.09 |
| HSC2 | 1270 | 125 | 240 | 194 | 0.83 | 1200 | 18 | 85.7 | 5.7 | 37.2 | 620 | 215 ^e | 7.42 | 0.10 |
| HSC4 | 1270 | 125 | 240 | 200 | 1.19 | 1200 | 18 | 91.6 | 6.6 | 41.3 | 596 | 195 | 7.42 | 0.14 |
| N/HSC8 ^a | 1270 | 125 | 242 | 198 | 0.81 | 1200 | 18 | 29.9/94.9 | 3.2/6.9 | 29.2/43.5 | 631 | 213 | 7.42 | 0.09 |
| HSC9 | 1270 | 125 | 239 | 202 | 0.33 | 1200 | 18 | 84.1 | 6.7 | 39.0 | 634 | 231 | 7.42 | 0.02 |

^a high-strength concrete in column vicinity only

^b $d_g = 18$ mm used in calculation despite provisions for high-strength concrete according to SIA 262 (2013)

^c $f_{c,cube} = 112.9$ MPa (side length 150 mm), $f_c \approx 0.83 f_{c,cube}$

^d splitting tests on cubes (side length 150 mm)

^e values not measured, average taken from measured E_s of HSC3s,6,7s,8,9 (Ø16)

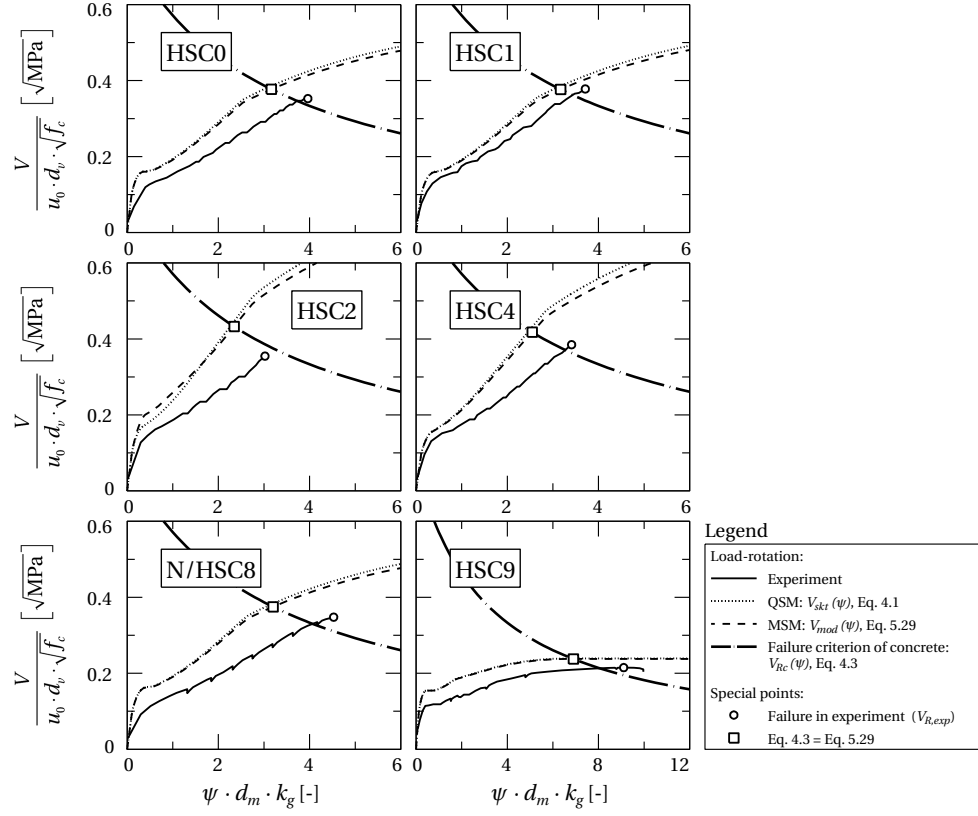


Figure E.5: Specimens by Hallgren (1996): MSM, QSM and experimental results

Experiments by Gomes (1991)

Twelve square flat slabs were tested to investigate the influence of shear reinforcement on the punching resistance. Short off-cuts of steel I-beams were used as shear reinforcement in all slabs except slabs S1 and S1A, which were reference slabs without shear reinforcement. The slab rotation of the weak axis was determined here by calculating the secant rotation from deflection measuring points given in Gomes (1991), located at 1.2 m and 0.9 m, respectively, from the slab center. The experimental campaign is summarized in Table E.6 and displayed in Figure E.6.

Table E.6: Properties of specimens by Gomes (1991), $\beta_E = 0.7$, $d_v = d_m$,
YLM acc. to Table C.1(g)

| Slab | B | b | h | d_m | ρ_m | r_q | d_g | f_c^a | f_{ct}^b | E_c^c | f_{sy} | E_s^d | $\frac{V_{flex}}{m_R}$ | κ_V |
|------|------|------|------|-------|----------|-------|-------|---------|------------|---------|----------|---------|------------------------|------------|
| | [mm] | [mm] | [mm] | [mm] | [%] | [mm] | [mm] | [MPa] | [MPa] | [GPa] | [MPa] | [GPa] | [-] | [-] |
| S1 | 3000 | 200 | 200 | 159 | 1.27 | 1425 | 20 | 41.7 | 3.4 | 34.7 | 680 | 195 | 7.64 | 0.43 |
| S1A | 3000 | 200 | 200 | 159 | 1.27 | 1425 | 20 | 42.7 | 3.3 | 34.9 | 680 | 195 | 7.64 | 0.43 |
| S2 | 3000 | 200 | 200 | 153 | 1.32 | 1425 | 20 | 35.8 | 3.0 | 32.9 | 680 | 195 | 7.64 | 0.53 |
| S3 | 3000 | 200 | 200 | 158 | 1.27 | 1425 | 20 | 40.7 | 3.4 | 34.4 | 670 | 195 | 7.64 | 0.44 |
| S4 | 3000 | 200 | 200 | 159 | 1.27 | 1425 | 20 | 33.3 | 3.1 | 32.2 | 670 | 195 | 7.64 | 0.54 |
| S5 | 3000 | 200 | 200 | 159 | 1.27 | 1425 | 20 | 36.0 | 3.5 | 33.0 | 670 | 195 | 7.64 | 0.49 |
| S6 | 3000 | 200 | 200 | 159 | 1.27 | 1425 | 20 | 38.8 | 3.5 | 33.8 | 670 | 195 | 7.64 | 0.46 |
| S7 | 3000 | 200 | 200 | 159 | 1.27 | 1425 | 20 | 35.1 | 3.0 | 32.7 | 670 | 195 | 7.64 | 0.51 |
| S8 | 3000 | 200 | 200 | 159 | 1.27 | 1425 | 20 | 35.4 | 3.4 | 32.8 | 670 | 195 | 7.64 | 0.50 |
| S9 | 3000 | 200 | 200 | 159 | 1.27 | 1425 | 20 | 41.5 | 3.0 | 34.6 | 670 | 195 | 7.64 | 0.44 |
| S10 | 3000 | 200 | 200 | 154 | 1.31 | 1425 | 20 | 36.6 | 3.0 | 33.2 | 670 | 195 | 7.64 | 0.51 |
| S11 | 3000 | 200 | 200 | 154 | 1.31 | 1425 | 20 | 35.9 | 3.1 | 33.0 | 670 | 195 | 7.64 | 0.52 |

^a compressive tests on cubes (side length 150 mm), $f_c \approx 0.83 f_{c,cube}$

^b splitting tests on cylinders ($h = 300$ mm, $\varnothing = 150$ mm)

^c values calculated using relationships acc. to SIA 262 (2013): $E_c = 10000 \text{ MPa}^{2/3} \cdot \sqrt[3]{f_c}$ (in MPa)

^d graphically determined by author from Figure 3.3 in Gomes (1991)

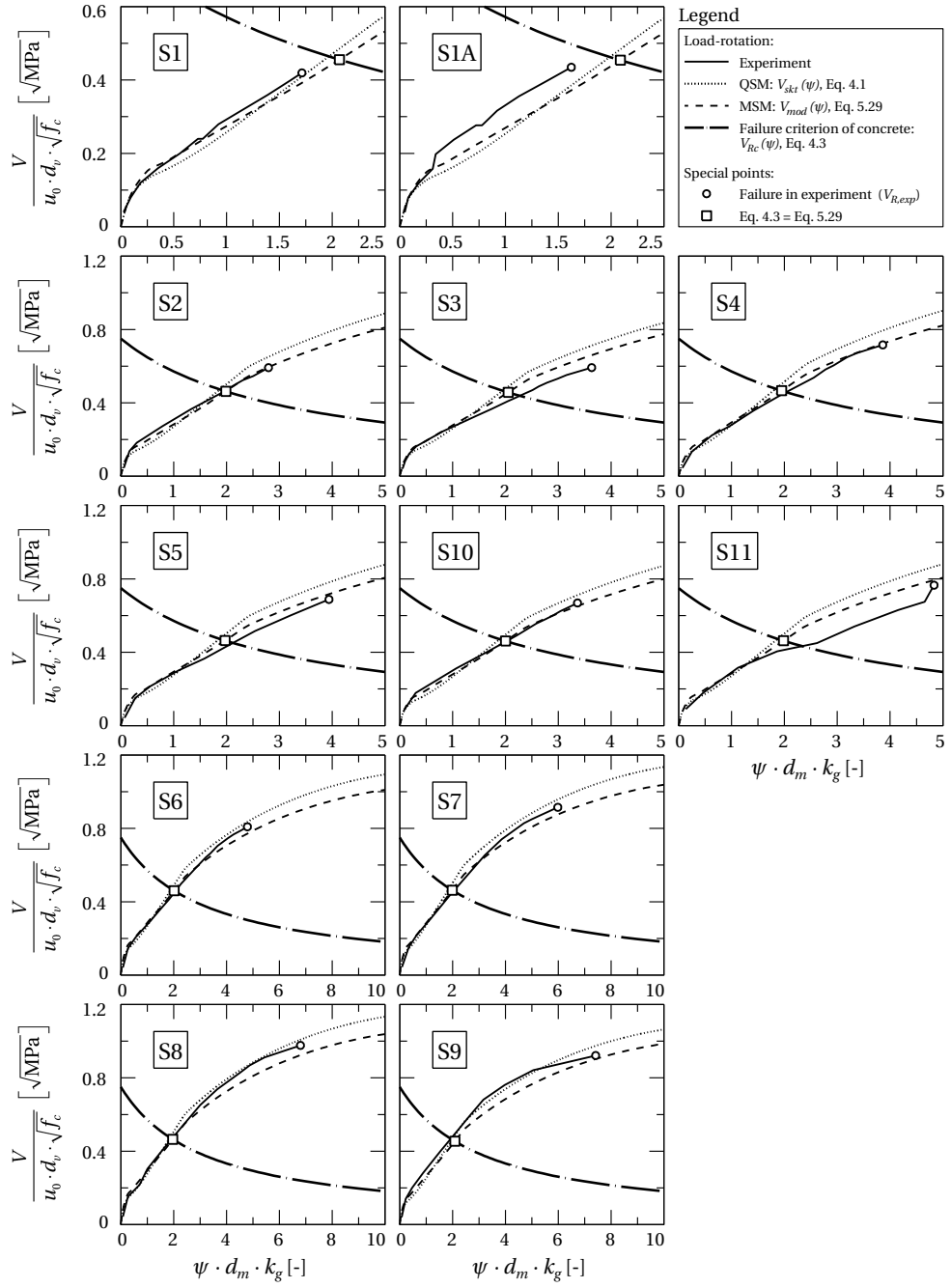


Figure E.6: Specimens by Gomes (1991): MSM, QSM and experimental results

Experiments by Kinnunen and Nylander (1960)

Kinnunen and Nylander carried out an experimental series on 43 circular slab cutouts. They varied the column size, ratio, and layout of the longitudinal reinforcement (ring, tangential and radial, orthogonal, concentrated around column). The angle of rotation of the slab portion outside the shear crack was determined by Kinnunen and Nylander as secant rotation from the observed deflections of the slab and was directly displayed in the figures. Six experiments were selected for the comparison (constant reinforcement ratio, orthogonal layout), see Table E.7 and Figure E.7.

Table E.7: Properties of specimens by Kinnunen and Nylander (1960), $\beta_E = 0.6$, $d_v = d_m$, YLM acc. to Table C.1(a)

| Slab | r_s [mm] | r_c [mm] | h [mm] | d_m [mm] | ρ_m [%] | r_q [mm] | d_g [mm] | f_c^a [MPa] | f_{ct}^b [MPa] | E_c^b [GPa] | f_{sy} [MPa] | E_s [GPa] | $\frac{V_{flex}}{m_R}$ [–] | κ_V [–] |
|----------|---------------|---------------|-------------|---------------|-----------------|---------------|---------------|------------------|---------------------|------------------|-------------------|----------------|-------------------------------|-------------------|
| IA15a-5 | 920 | 75 | 149 | 117 | 0.79 | 855 | 32 | 27.3 | 2.7 | 30.1 | 441 | 206 | 7.41 | 0.24 |
| IA15a-6 | 920 | 75 | 151 | 118 | 0.78 | 855 | 32 | 26.7 | 2.7 | 29.9 | 454 | 206 | 7.41 | 0.25 |
| IA30a-24 | 920 | 150 | 158 | 128 | 1.01 | 855 | 32 | 26.9 | 2.7 | 29.9 | 456 | 206 | 8.20 | 0.34 |
| IA30a-25 | 920 | 150 | 154 | 124 | 1.04 | 855 | 32 | 25.6 | 2.6 | 29.5 | 451 | 206 | 8.20 | 0.37 |
| IA30d-32 | 920 | 150 | 155 | 123 | 0.48 | 855 | 32 | 26.8 | 2.7 | 29.9 | 448 | 206 | 8.20 | 0.13 |
| IA30d-33 | 920 | 150 | 156 | 125 | 0.47 | 855 | 32 | 27.1 | 2.7 | 30.0 | 461 | 206 | 8.20 | 0.13 |

^a compressive tests on cubes (side length 150 mm), $f_c \approx 0.83 f_{c,cube}$

^b values calculated using relationships acc. to SIA 262 (2013): $E_c = 10000 \text{ MPa}^{2/3} \cdot \sqrt[3]{f_c}$, $f_{ct} = 0.3 \text{ MPa}^{1/3} \cdot f_c^{2/3}$ (both in MPa)

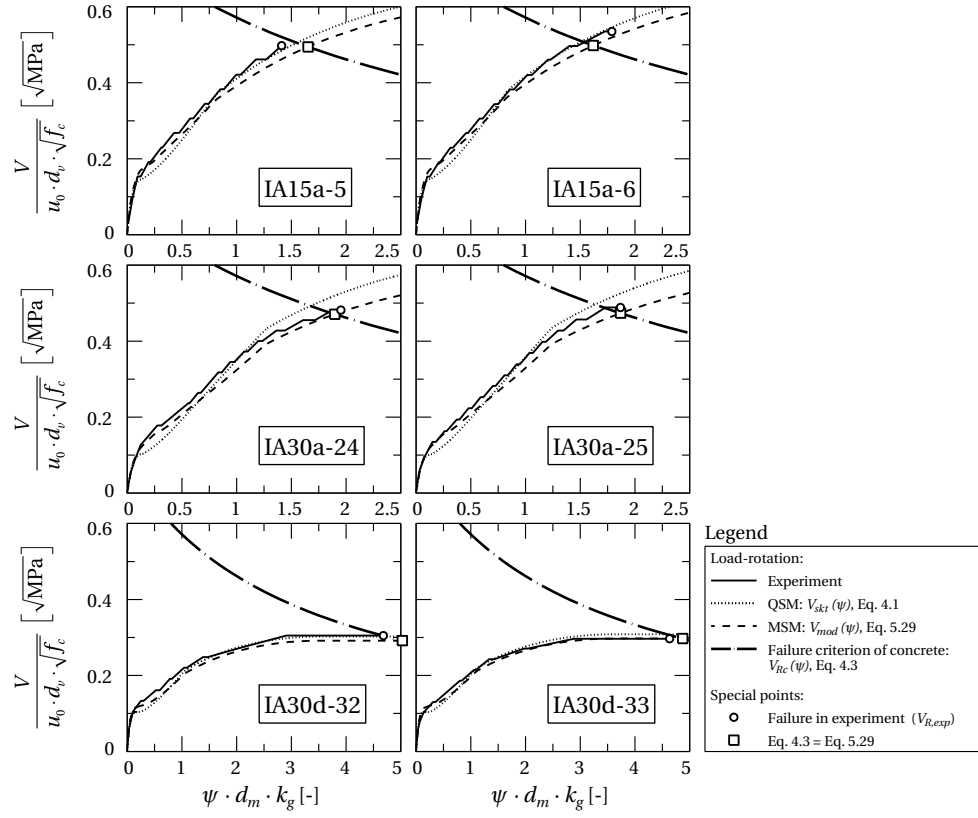


Figure E.7: Specimens by Kinnunen and Nylander (1960): MSM, QSM and experimental results

Experiments by Elstner and Hognestad (1956)

A total of 39 experiments on 1.83-m (6-ft) square slabs were carried out to investigate the effect of different concrete compressive strengths, bending reinforcement ratios, reinforcement concentration around the column, column size and conditions of slab support. Nine slabs included shear reinforcement. The slabs were supported by “ 2×1 -in. maple strips” on a steel frame. For lack of more detailed information Staller (2001) assumed a clear span of 1.78 m (5 ft 10 in.), following Base’s (1959) procedure in similar experiments. A secant rotation was calculated here from the recorded deflections at the central square column assuming zero deflection of the supported edges. Fifteen experiments were selected for the comparison, see Table E.8 and Figure E.8¹.

Table E.8: Properties of specimens by Elstner and Hognestad (1956), $\beta_E = 0.7$, $d_v = d_m$, YLM acc. to Table C.1(h)

| Slab | B | b | h | d_m | ρ_m | r_q | d_g | f_c | f_{ct}^a | E_c^a | f_{sy} | E_s^b | $\frac{V_{flex}}{m_R}$ | κ_V |
|------|------|------|------|-------|----------|-------|-------|-------|------------|---------|----------|---------|------------------------|------------|
| | [mm] | [mm] | [mm] | [mm] | [%] | [mm] | [mm] | [MPa] | [MPa] | [GPa] | [MPa] | [GPa] | [-] | [-] |
| A1a | 1829 | 254 | 152 | 118 | 1.17 | 890 | 25 | 14.1 | 1.7 | 24.1 | 332 | 200 | 8.17 | 0.56 |
| A2c | 1829 | 254 | 152 | 114 | 2.48 | 890 | 25 | 37.4 | 3.4 | 33.5 | 321 | 200 | 8.17 | 0.44 |
| A7b | 1829 | 254 | 152 | 114 | 2.48 | 890 | 25 | 27.9 | 2.8 | 30.3 | 321 | 200 | 8.17 | 0.60 |
| A3a | 1829 | 254 | 152 | 114 | 3.72 | 890 | 25 | 12.8 | 1.6 | 23.4 | 321 | 200 | 8.17 | 1.00 |
| A3d | 1829 | 254 | 152 | 114 | 3.72 | 890 | 25 | 34.5 | 3.2 | 32.6 | 321 | 200 | 8.17 | 0.75 |
| A4 | 1829 | 356 | 152 | 118 | 1.17 | 890 | 25 | 26.1 | 2.6 | 29.7 | 332 | 200 | 8.85 | 0.28 |
| A13 | 1829 | 356 | 152 | 121 | 0.54 | 890 | 25 | 26.2 | 2.6 | 29.7 | 294 | 200 | 8.85 | 0.08 |
| B1 | 1829 | 254 | 152 | 114 | 0.49 | 890 | 38 | 14.2 | 1.8 | 24.2 | 324 | 200 | 8.17 | 0.18 |
| B2 | 1829 | 254 | 152 | 114 | 0.49 | 890 | 38 | 47.6 | 3.9 | 36.2 | 321 | 200 | 8.17 | 0.02 |
| B4 | 1829 | 254 | 152 | 114 | 1.00 | 890 | 38 | 47.7 | 3.9 | 36.3 | 303 | 200 | 8.17 | 0.09 |
| B9 | 1829 | 254 | 152 | 114 | 2.02 | 890 | 38 | 43.9 | 3.7 | 35.3 | 341 | 200 | 8.17 | 0.31 |
| B11 | 1829 | 254 | 152 | 114 | 3.02 | 890 | 38 | 13.5 | 1.7 | 23.8 | 409 | 200 | 8.17 | 1.00 |
| B14 | 1829 | 254 | 152 | 114 | 3.02 | 890 | 38 | 50.5 | 4.1 | 37.0 | 325 | 200 | 8.17 | 0.40 |
| B10 | 1829 | 254 | 152 | 114 | 2.02 | 890 | 38 | 46.4 | 3.9 | 35.9 | 335 | 200 | 8.17 | 0.28 |
| B12 | 1829 | 254 | 152 | 114 | 3.02 | 890 | 38 | 45.8 | 3.8 | 35.8 | 332 | 200 | 8.17 | 0.45 |

^a values calculated using relationships acc. to SIA 262 (2013): $E_c = 10000 \text{ MPa}^{2/3} \cdot \sqrt[3]{f_c}$, $f_{ct} = 0.3 \text{ MPa}^{1/3} \cdot f_c^{2/3}$ (both in MPa)

^b assumption

¹ Elstner and Hognestad (1956) reported that slabs failing in flexure (A13, B1, B2 and B4) had ca. 10–20% larger failure loads than those calculated by the YLT. They attributed the increased flexural capacity to membrane action and hardening of the tensile reinforcement.

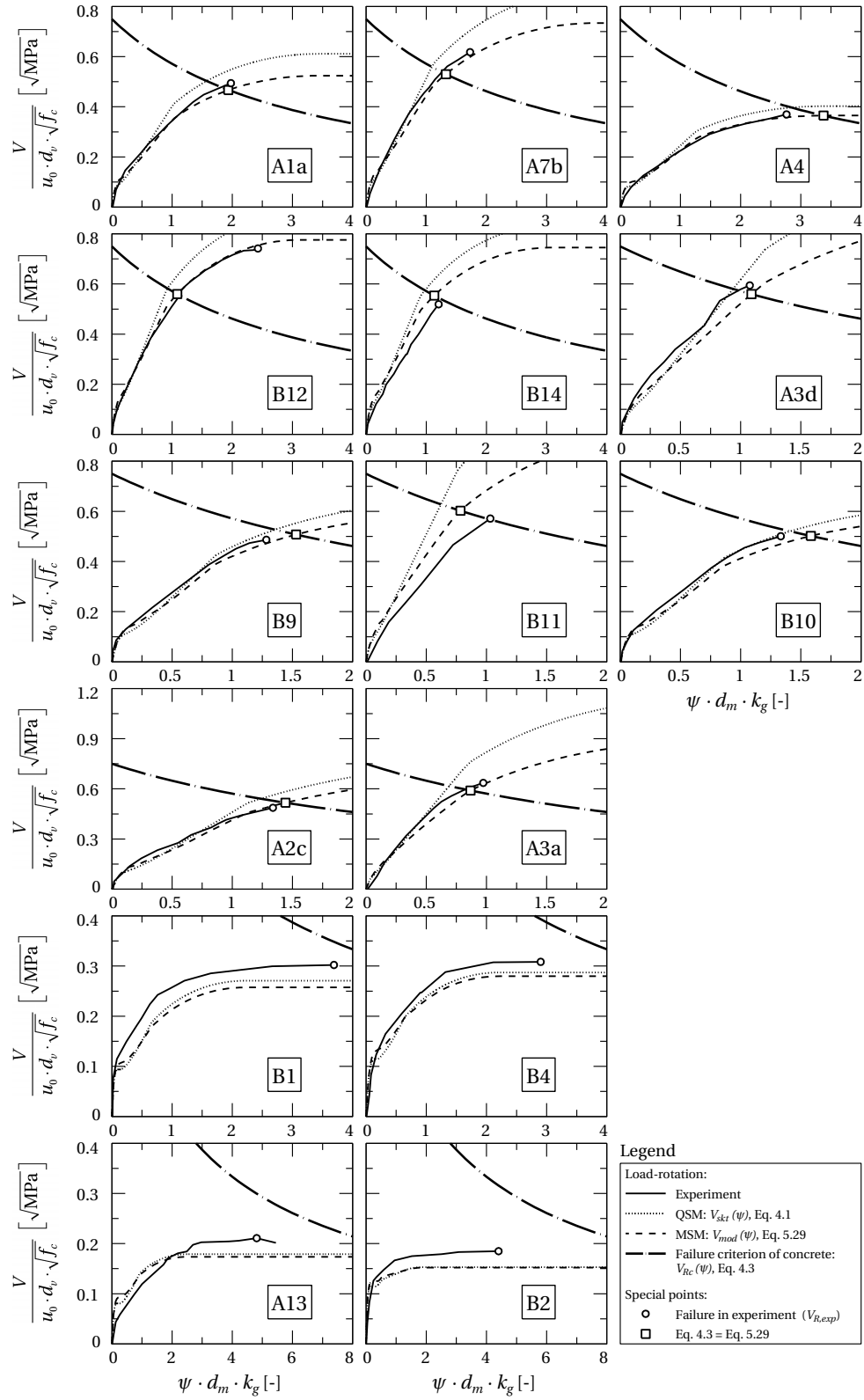


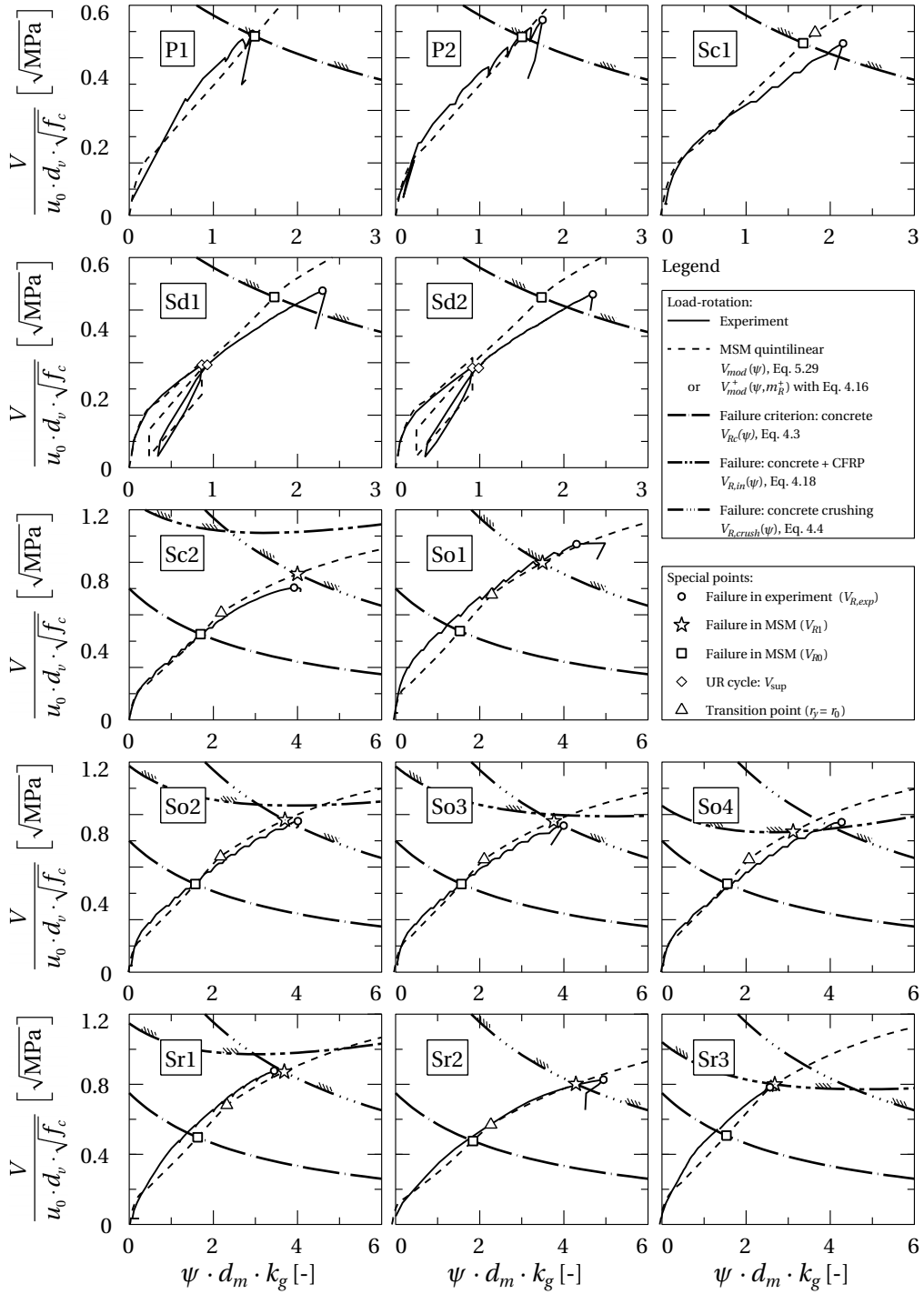
Figure E.8: Specimens by Elstner and Hognestad (1956): MSM, QSM and experimental results

E.2 Experimental campaign

The Modified Sector Model was validated with the two slab series So and Sr in Section 4.4.4. In the following the experimental load–rotation curves of the series P, Sd and Sc are also compared to the predicted MSM curves, see Table E.9 and Figure E.9. The MSM curves are calculated according to Eq. 5.29 with the bending resistance according to Eqs. 4.16 or 4.25, respectively, and considering G_F according to Eq. 5.24. The CFRP plates in slabs P1–2 were ineffective, and thus their resistance, $V_{Rp}(\psi)$, is neglected in the calculation. Since the boreholes did not reduce the punching resistance, the critical section in the slabs Sd1–2 is not reduced. However, the greater increase of slab rotation compared to P1–2 is not covered by the model (underestimation of ψ_{R0} by ca. 25%). Slab Sc2 is also modeled as non-strengthened because the CFRP straps were significantly activated after the first peak load. The agreement between modeled and measured punching resistance is good for both cases, the non-strengthened ($V_{R0}/V_{R,exp}$) and strengthened ($V_{R1}/V_{R,exp}$), with a total average value of 0.99. The MSM underestimates slab rotations at failure by 11% (total) with a COV of 14%. The underestimation is smaller for the strengthened slabs, $7\% \pm 12\%$.

Table E.9: Experimental punching resistances and slab rotations at failure (see Table B.2), increase of bending resistance and comparison of predicted and experimental results

| Slab | $\frac{V_{R,exp}}{u_0 d_v \sqrt{f_c}}$ [$\sqrt{\text{MPa}}$] | $\psi d_m k_g$ [–] | $\frac{V_{R0}}{V_{R,exp}}$ [–] | $\frac{\psi_{R0}}{\psi_{R,exp}}$ [–] | $\frac{m_R^+}{m_R}$ [–] | $\frac{V_{R1}}{V_{R,exp}}$ [–] | $\frac{\psi_{R1}}{\psi_{R,exp}}$ [–] |
|-----------------------------------|---|-----------------------|-----------------------------------|---|----------------------------|-----------------------------------|---|
| P1 | 0.52 | 1.46 | 0.99 | 1.02 | – | – | – |
| P2 | 0.56 | 1.75 | 0.91 | 0.86 | – | – | – |
| So1 | 0.98 | 4.10 | – | – | 1.31 | 0.91 | 0.85 |
| So2 | 0.86 | 4.01 | – | – | 1.20 | 1.01 | 0.92 |
| So3 | 0.84 | 3.99 | – | – | 1.16 | 1.03 | 0.94 |
| So4 | 0.86 | 4.27 | – | – | 1.19 | 0.94 | 0.73 |
| Sc1 | 0.49 | 2.15 | 1.00 | 0.78 | – | – | – |
| Sc2 | 0.76 | 3.92 | – | – | 1.25 | 1.10 | 1.02 |
| Sr1 | 0.88 | 3.45 | – | – | 1.31 | 0.99 | 1.07 |
| Sr2 | 0.83 | 4.94 | – | – | 1.57 | 0.97 | 0.87 |
| Sr3 | 0.78 | 2.57 | – | – | 1.23 | 1.02 | 1.05 |
| Sd1 | 0.51 | 2.30 | 0.96 | 0.75 | – | – | – |
| Sd2 | 0.49 | 2.34 | 0.98 | 0.74 | – | – | – |
| Average | | | 0.97 | 0.83 | | 1.00 | 0.93 |
| COV | | | 0.04 | 0.14 | | 0.06 | 0.12 |
| Average (V_{R0} and V_{R1}) | | | | | | 0.99 | 0.89 |
| COV | | | | | | 0.05 | 0.14 |

Figure E.9: Comparison of experiments with model curves, $\beta_E = 0.7$

In Figure 4.11 the modeled and experimental strap activation curves were graphically compared. Figure E.10 provides a quantification (average \pm standard deviation) of calculated strap force, P_{mod} , according to Eq. 4.14 vs. the measured one, P_{exp} , at several load stages $V/V_{R,exp}$. The linear approximation generally overestimates the strap activation (modeled slab behavior is softer than in experiment) by ca. 10%; towards failure the overestimation decreases to 1.04. The standard deviation increases from 5% to 8% at failure.

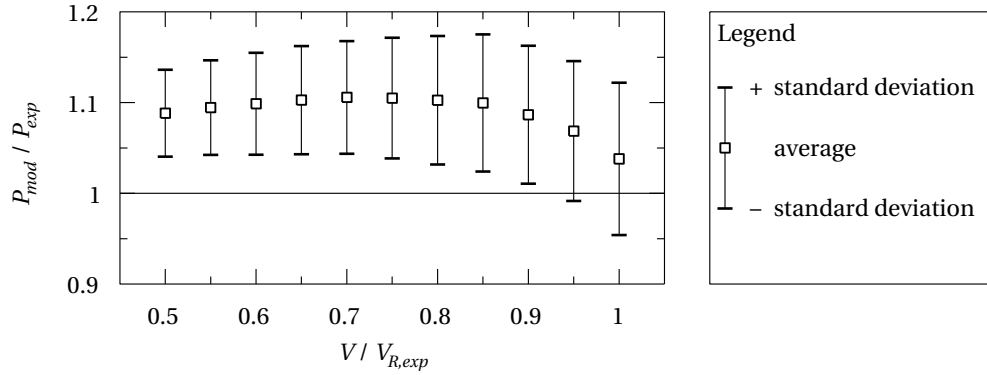


Figure E.10: P_{mod} vs. P_{exp} (average \pm standard deviation) at several load stages $V/V_{R,exp}$

F Effect of crack spacing on tension stiffening loss

The effect of different bond stress factors, k_τ , on the degree of slip reversal, η_δ , and the residual tension stiffening factor, η_{TS} , is illustrated in Figure 5.7 for different minimum stress factors, k_U , and maximum crack spacing ($\lambda = 1$). Smaller crack spacings result in an earlier reaching of a full slip reversal ($\eta_\delta = 1$), and thus in a lower η_{TS} . However, cases for $\lambda < 1$ can be transformed to cases where $\lambda = 1$ by adjusting k_U :

$$k_U(\lambda) = 1 + \lambda \cdot [k_U(\lambda = 1) - 1] \quad (\text{E.1})$$

Thus, for example a minimum crack spacing ($\lambda = 0.5$) induces the same tension stiffening loss for half the amount of unloading, compared to $\lambda = 1$. In Figure E.1 the parameter setting $\lambda = 1$, $k_U = 0.5$ is equivalent to $\lambda = 0.5$ and $k_U = 0.75$, for instance.

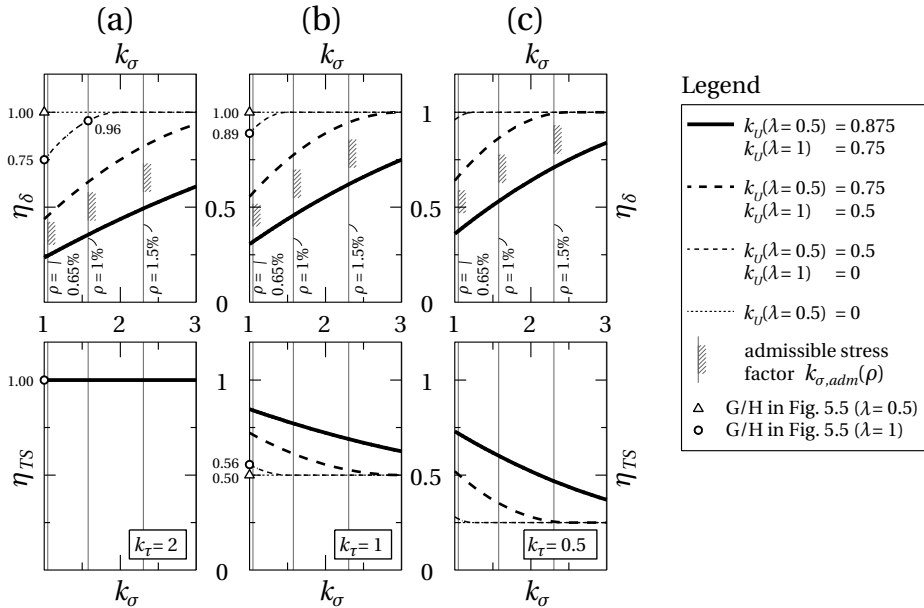


Figure E.1: Effect of λ on degree of slip reversal η_δ and residual tension stiffening factor η_{TS} for: (a) $k_\tau = 2$, (b) $k_\tau = 1$ and (c) $k_\tau = 0.5$

The parameters of the example in Figure 5.5 are again used: $k_\sigma = 1$, $k_U = 0$, $\rho = 1$. The resulting values for η_δ and η_{TS} are indicated in Figure F.1(a)–(b) for $k_\tau = 2$ and 1, respectively (amendment to Figure 5.7). $\lambda = 0.5$ leads to a full slip reversal in both cases (plotted triangles in Figure F.1) where for maximal crack spacing ($\lambda = 1$) $\eta_\delta = 0.75$ and 0.89 is derived, respectively (circles in the diagram). For $k_\tau = 2$ full slip reversal is impossible to achieve (see intersection between curve and vertical line for $k_{\sigma,adm} = 1.58$ at $\eta_\delta = 0.96$). Remaining tension stiffening lies between 0.56 and 0.50 for $k_\tau = 1$, depending on λ as a function of the effective average crack spacing.

Curriculum Vitae

Personal details

| | |
|-----------------------------|-------------------------------------|
| Name | Robert Koppitz |
| Address | Probusweg 1 8057 Zürich |
| E-mail address | robert.koppitz@gmx.ch |
| Date and place of birth: | 30.08.1985 in Mutlangen, Germany |
| Place of origin: | Tscheppach (SO) |
| Nationalities: | Swiss and German |



Education

| | |
|-------------------|--|
| 09/2010 – present | École Polytechnique Fédérale de Lausanne PhD candidate, Composite Construction Laboratory (CCLAB) |
| 09/2008 – 07/2010 | Swiss Federal Institute of Technology Zurich Master of Science in Civil Engineering with Majors in Structural Engineering and in Geotechnical Engineering |
| 10/2004 – 09/2007 | Swiss Federal Institute of Technology Zurich Bachelor of Science in Civil Engineering |
| 08/2000 – 08/2004 | Kantonsschule Solothurn Matura graduation, Mathematics and Natural Sciences Profile with emphasis on Physics and Applications of Mathematics |

Professional experience

| | |
|---|---|
| 08/2010 – present | HSR Rapperswil University of Applied Sciences Research and Teaching Assistant, Institute for Civil and Environmental Engineering (IBU) |
| 03/2010 – 06/2010 and 09/2008 – 06/2009 | Swiss Federal Institute of Technology Zurich Tutorial Assistant in “Structural Concrete II” and in “Structural Analysis I & II”, Institute of Structural Engineering (IBK) |
| 10/2007 – 09/2008 | BSB + Partner, Ingenieure und Planer AG, Biberist Internship, Divisions of Structural and of Civil Engineering |

Language skills

| | |
|---------|-----------------|
| German | native language |
| English | very good |
| French | good |

Publications

Journal papers

- Koppitz, R., Kenel, A., and Keller, T. (2013). Punching shear of RC flat slabs – Review of analytical models for new and strengthening of existing slabs. *Engineering Structures*, 52: 123–130.
- Keller, T., Kenel, A., and Koppitz, R. (2013). Carbon Fiber-Reinforced Polymer Punching Reinforcement and Strengthening of Concrete Flat Slabs. *ACI Structural Journal*, 110(6):919–927.
- Koppitz, R., Kenel, A., and Keller, T. (2014). Tension Chord Model Modification for Uniaxial Unloading and Reloading in Elastic and Plastic States. *ASCE Journal of Structural Engineering*, 140(10):04014077.
- Koppitz, R., Kenel, A., and Keller, T. (2014). Punching Shear Strengthening of Flat Slabs using Prestressed Carbon Fiber-Reinforced Polymer Straps. *Engineering Structures*, 76: 283–294.
- Koppitz, R., Kenel, A., and Keller, T. (2014). Effect of punching shear on load–deformation behavior of flat slabs. *Engineering Structures*, 80:444–457.
- Koppitz, R., Kenel, A., and Keller, T. Effect of load history on punching shear resistance of flat slabs. *Engineering Structures*, submitted in October 2014, revised in January 2015.

Conference papers

- Koppitz, R., Keller, T., and Kenel, A. (2013). Punching Shear Strengthening of Reinforced Concrete Flat Slabs with Carbon Fiber-Reinforced Polymer Reinforcement. *In*: Barros, J. and Sena-Cruz, J. (eds.), 11th International Symposium on Fiber Reinforced Polymer for Reinforced Concrete Structures (FRPRCS-11), Guimarães, Portugal, June 26–28 2013, 8 p.
- Lips, S., Koppitz, R., Kenel, A., and Keller, T. (2014). New Punching Strengthening Systems for Flat Slabs. *In*: 4th International *fib* Congress, Mumbai, India, February 10–14 2014, 11 p.
- Lips, S., Koppitz, R., Kenel, A., and Keller, T. (2014). Neue vorgespannte Durchstanzverstärkungssysteme für Flachdecken (New prestressed punching strengthening systems for flat slabs). *In*: Betonbau in der Schweiz, Schweizer Gruppe der *fib*, 2014, 171–175.